Universidad de Concepción
Facultad de Ciencias Físicas y Matemáticas
Programa de Doctorado en Ciencias Físicas

Dwarf ellipticals
(Enanas elipticas)

Tesis para optar al grado academico de
Doctora en Ciencias Físicas por

Fernanda Cecilia Urrutia Zapata

Supervisor: Dr. Michael Fellhauer

Co-Supervisor: Dr. Pavel Kroupa

Concepción, Chile
Abril 2024

Agradecimientos

Me gustaría agradecer a todas las personas que me apoyaron durante estos años de estudios. A mis compañeros y amigos con los que nos dimos fuerzas y ánimo para seguir adelante y terminar esta importante etapa.

Agradezco a Dios.

Agradezco a mi familia, a mi mamá, Norma Zapata, mi hermana, Francisca Urrutia y por supuesto a mi perrita Femy por acompañarme durante largas noches de producción.

Agradezco a mis profesores que me enseñaron e instruyeron con paciencia durante todos mis años universitarios. En especial a mi profesor tutor Michaell Fellhauer que me impulsó e insentivó a avanzar cada vez más en mi desarrollo como cientifica, durante todos mis años de estudios de postgrado. También al profesor Dominik Schleicher que siendo parte del Theory group siempre me ha apoyado, por cualquier medio posible. También agradezco a mi co-tutor Dr. Pavel Kroupa por apoyarme en mi visita a Alemania para intercambio cientifico y para aprender a usar PoR.

Agradezco enormemente la ayuda de mis compañeros Diego Matus y Alex Alarcon que siempre estuvieron ahí para apoyarme, ayudarme y guiarme durante mis estudios.

Agradesco a la Universidad de Concepción a Dirección de Postgrado, a el programa de ANID becas doctorado nacional 21190614 y FONDECYT por la ayuda financiera brindada durante estos años.

Abstract

Dwarf elliptical (dE) galaxies are at the low-luminosity end of the elliptical galaxy sequence, characterized by smaller sizes and lower luminosities compared to typical elliptical galaxies. A common method of distinguishing between a normal elliptical galaxy and a dwarf galaxy is through its absolute magnitude, with a commonly used limit of -18 mag. Below masses compared to dwarf ellipticals are found Ultra compact dwarf galaxies (UCDs). UCDs are extended objects(EOs) with high mass, typically characterized by a lower mass limit of 2×10^6 $M_\odot$. Their luminosities are above the brightest known star clusters (SCs), and their effective radii range between 10 and 100 parsecs. Thus, while they are larger, brighter, and more massive than star clusters, they remain more compact than typical dwarf galaxies of comparable luminosity.

In our study we investigate the possibility of dE galaxies losing their components in the tidal stripping and truncation scenario, leaving their dense central cluster on the type of orbits on which UCDs are found. I.e, a dE,N galaxy with a dense core gets partly destroyed by the gravitational forces of one or many bigger galaxies. Only the compact central part survives as UCD. It is important to test if this can be done in Lambda cold dark matter (LCDM), in where each dE galaxy has its own Navarro-Frenk-White halo with the preinfall properties as given by the theory, on how to associate a baryonic galaxy with a dark matter halo.

So, in this work, our aim is to address the questions of whether the dark matter halo can be stripped, as assumed in previous studies, and whether then the stellar body of the dE galaxy can also be stripped, resulting in UCDs in the orbits where we observe them?

Resumen

Las galaxias elípticas enanas (dE) se encuentran en el extremo de baja luminosidad de la secuencia de galaxias elípticas, caracterizadas por tamaños más pequeños y luminosidades más bajas en comparación con las típicas galaxias elípticas. Un método común para distinguir entre una galaxia elíptica normal y una galaxia enana es a través de su magnitud absoluta, con un límite comúnmente utilizado de -18 mag.

Por debajo de las masas de dEs se encuentran las galaxias enanas ultra compactas (UCDs). Las UCDs son objetos extendidos con alta masa, típicamente caracterizados por un límite de masa inferior de 2×10^6 $M_\odot$. Sus luminosidades están por encima de los cúmulos de estrellas (SCs) más brillantes conocidos, y sus radios efectivos oscilan entre 10 y 100 pc. Por lo tanto, aunque son más grandes, más brillantes y más masivos que los SCs, siguen siendo más compactos que las galaxias enanas típicas de luminosidad comparable.

En nuestro estudio investigamos la posibilidad de que las galaxias dE pierdan sus componentes con el "Tidal stripping and truncation scenario", dejando su denso núcleo central en el tipo de órbitas en las que se encuentran las UCDs. Esto es, una galaxia dE,N con un núcleo denso es parcialmente destruida por las fuerzas gravitatorias de una o varias galaxias más grandes. La parte central compacta sobrevive como UCD. Es importante probar si esto se puede hacer en el modelo Lambda cold dark matter(LCDM), donde cada galaxia dE tiene su halo Navarro-Frenk-White con propiedades preinfall según lo dado por la teoría, en sobre cómo asociar una galaxia bariónica con un halo de materia oscura. Entonces, en este trabajo, nuestro objetivo es abordar las preguntas: ¿Puede el halo de materia oscura ser desprendido?, como se asume en estudios previos, y luego, ¿Puede el cuerpo estelar de la galaxia dE también ser desprendido resultando en UCDs en las órbitas donde los observamos?.

Contents

List of Figures

List of Tables

Chapter 1

Introduction

1.1 Extended Objects.

In the last decades, a huge sample of object with different sizes, masses, and luminosities have been observed, with a variety of characteristics from extended to compact objects.

Fig. 1.1 shows a size-luminosity diagram where Star Clusters(SCs) and Extended Objects(EOs) are plotted as black circles and the early-type galaxies are shown as open circles. The median effective radius per luminosity bin for the SCs is given as yellow squares.

Extended objects with masses comparable to normal globular clusters are called extended clusters (ECs). There is not a physical size demarcation between SCs and ECs but an effective radius(r_{eff}) of 10 pc is seen as a reasonable limit (van den Bergh & Mackey 2004). Objects with bigger masses and luminosities above the known GCs are named ultra compact dwarf galaxies (UCDs). Both objects are named extended stellar dynamical objects (EOs).

Extended clusters are metal-poor clusters, they are like globular clusters but with r_{eff} up to 10 pc. Fig. 1.2 shows the effective radius against the total V-band luminosity of 835 extended objects, taken from the catalog of Brüns (2013), in early-type and late-type galaxies. Also the position of the EC and UCDs are labeled in the graphic.

The magnitudes for most of these objects are in the range of $M_V = -5$ to -13 mag . At M_V = -8.5 mag the number of objects decreases in comparison to lower and higher

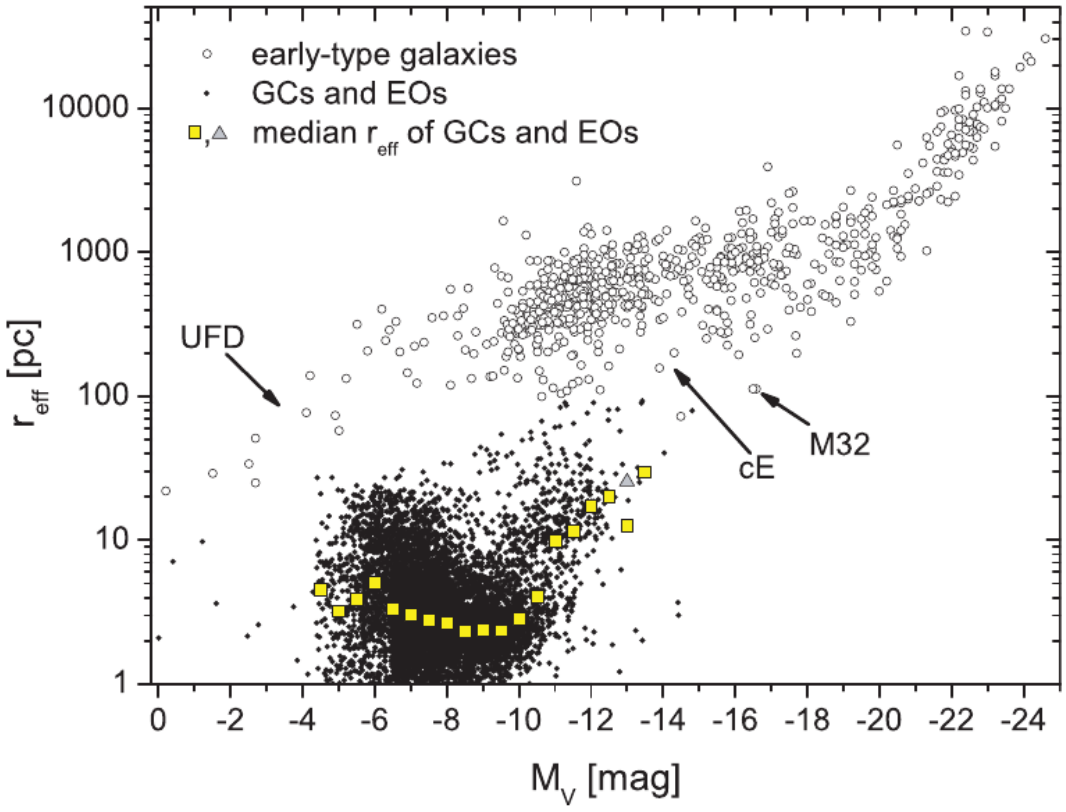

Figure 1.1: Size Luminosity diagram. SCs and EOs are plotted as black circles and the early-type galaxies are shown as open circles. The median effective radius for SCs and EOs per luminosity bin is given as yellow squares.
The position that compact ellipticals occupy in this graphic is labeled with their prototype example M32. Also the position of ultra faint dwarf galaxy (UFD) found in the Milky Way is labeled. The grey triangle shows the median effective radius, when the 6 exceptionally bright compact SCs with luminosities between $M_V = -12.5$ and M_V=-14.5 and an effective radii velow 4 pc were removed in the bin at M_V= -13.0 mag. Image taken by Brüns (2013).

luminosities. Also a correlation between the luminosity and the upper size limit is observed.

ECs are mainly found in the outer parts of the galaxy. The median Galactic distance of all SCs of the Milky Way (SCs and ECs) is about 5 kpc but, if we only consider the ECs we find a median galactic distance of 72 kpc. The most extended EC of the Milky Way is Palomar14 with an effective radius of 27 pc.

In the same size region we found Faint Fuzzies(FFs). FFs were discovered by Larsen

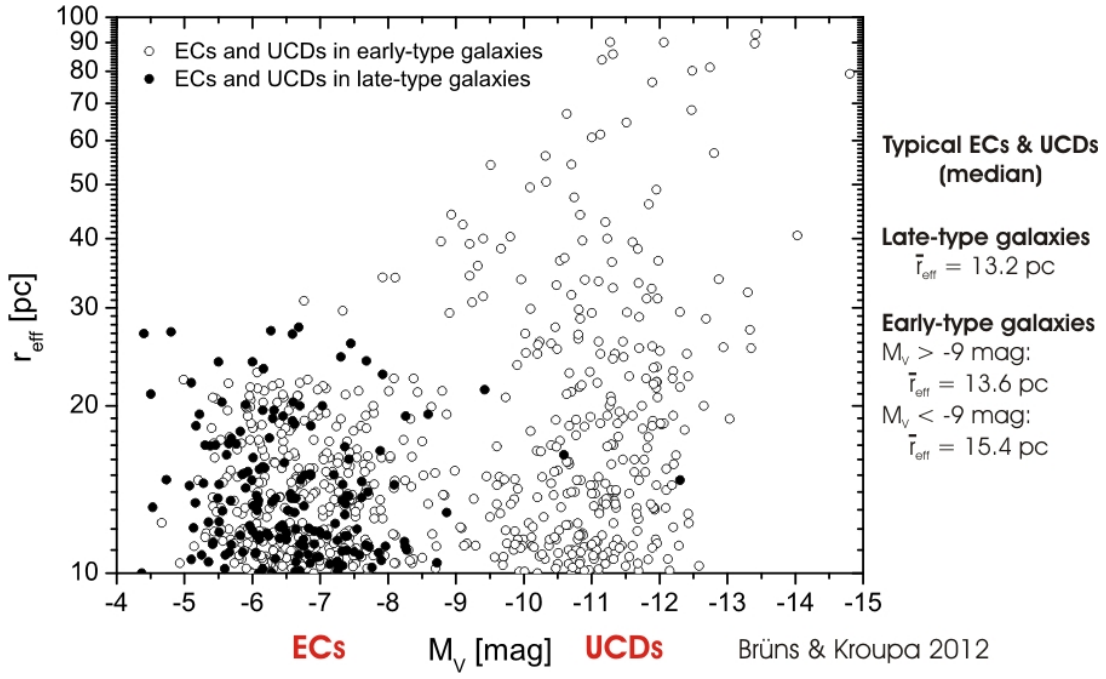

Figure 1.2: Luminosity(M_V)-size diagram. EOs in early-type galaxies are represented by open circles, and EOs in late-type galaxies, by black circles. Image taked by Brüns & Kroupa 2012.

& Brodie (2000) when they observed extended star clusters co-rotating with the disk of the lenticular galaxy NGC1023. Fig. 1.3 shows this galaxy, the black line marks the orientation of the galaxy, and the black circles denote different distances to the center of the galaxy, i.e. 2, 4, 6, 8, 10 and 12 kpc. The boxes mark the image that Larsen & Brodie (2000) used to detect Faint Fuzzies(FF). The green and white crosses mark the confirmed FF and the remaining candidates from Larsen & Brodie (2000), respectively.

They observed the galaxy and found a bimodal color distribution. They called some of these objects Faint Fuzzies(FF) due to their faint and extended appearance. The blue sample of SCs in NGC1023 is metal-poor having effective radii on average of about 2.0 pc and the red sample of SCs is metal-rich with an average radius of 1.7 pc (West et al. 2004). The blue and red sample of SCs have a different range of sizes. The blue clusters are smaller than 7 pc, while the red clusters reach a size of 18 pc. Objects bigger than 7 pc are generally fainter than the red compact objects.

After Brodie & Larsen (2002) performed spectroscopic observations of the SCs in

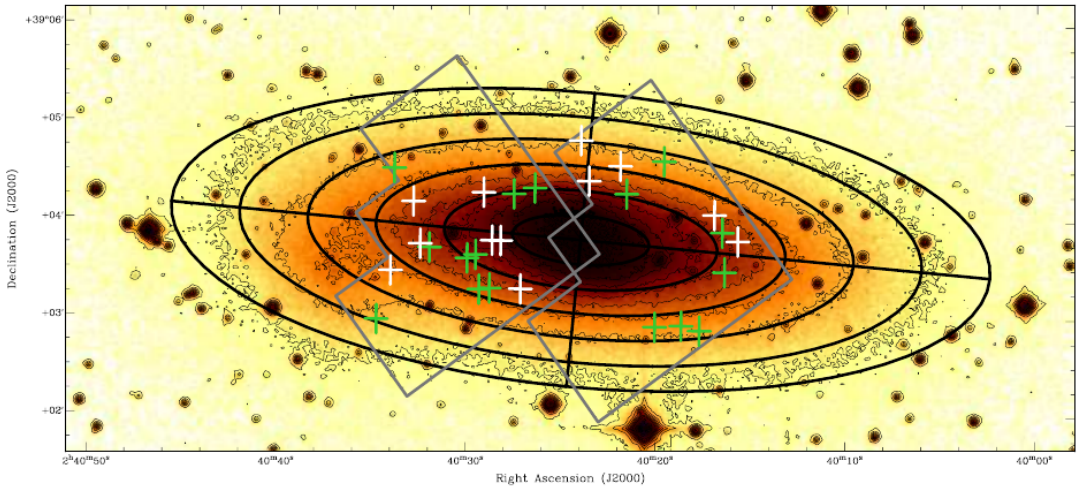

Figure 1.3: Digitized Sky Survey (DDS) image of the galaxy NGC 1023. The black line marks the orientation of the galaxy, and the black circles are different distance to the center of the galaxy i.e 2, 4, 6, 8, 10 and 12 kpc. The boxes marks the image that Larsen & Brodie (2000) used to detect Faint Fuzzy(FF). The green and white crosses mark the confirmed FF and the remaining candidates from Larsen & Brodie (2000), respectively. Image taken from Brüns (2013).

NGC1023 they found that the extended and faint objects show signs of co-rotation with the disk of the galaxy, but the sample of compact red objects didn't show this behavior, they concluded that FFs and the rest of the sample of SCs are separate populations, and only the FFs are associated with the disk.
According to Larsen & Brodie (2000) the range of effective radii of FFs spans from 7 pc to 13.4 pc with a median of 10.7 pc, and the luminosity ranges from 21.4 mag to 25 mag.

They averaged all FF spectra in order to obtain a high signal to noise ratio to estimate the age of FFs. The found age seems to be older than 7-8 Gyr.
A couple of years later Burkert et al. (2005) analyzed the distribution and radial velocities of the FFs in NGC1023, and found that FFs are remnants of a past gravitational interaction forming a structure like a ring.

FFs and halo ECs are very difficult to distinguish because of the similar structural parameters. They are difficult to detect but today this types of galactic systems have been

observed in other galaxies, like for example the lenticular galaxy NGC 1380 (Chies-Santos et al. 2007) and also in other types of galaxies like the dwarf irregular galaxy NGC5195 (Lee et al. 2005).

Going to higher masses ultra compact dwarf galaxies (UCDs) are found. They are extended objects with a high mass. As the object in Fig. 1.1 are part of a continuum there is no clear division between each class, but observers apply a lower mass limit of 2×10^6 $M_\odot$ for UCDs (e.g. Mieske et al. 2008).

Hilker et al (1999) and Drinkwater et al.(2000) discovered these particular objects in the Fornax cluster. While the effective radii range between 10 to 100 pc, their luminosities are higher than the brightest known SCs. So they are brighter, larger and more massive than SCs but more compact than typical dwarf galaxies of comparable luminosity.

Fig. 1.4 is a representative image of the comparison between the sizes of an UCD and the Milky Way.

The most extended UCD is VUCD7, with an effective radius of 93.2 pc(Evstigneeva et al. 2008) and a mass of 8.8×10^7 $M_\odot$(Evstigneeva et al. 2007). This object was discovered in the outer halo of the elliptical galaxy M87 of the Virgo cluster.

Most of these objects seems to be older than 8 Gyr, and there is only a few of them youngers.

Maraston et al (2004) found a very young version of this type of objects named W3, with an age between 300 and 500 Myr, a mass of about 8×10^7 $M_\odot$ and an effective radius of 17.5 pc, W3 is a massive star cluster in the galaxy NGC7252.

Norris & Kannappan (2011) found in the galaxy NGC4546 an example of an UCDs with an intermediate age of 3.4 Gyr having an effective radius of 25.5 pc and a mass of 3×10^7 $M_\odot$.

For several years these object have been studied because of the controversy of their formation and the nature of these objects. First, the structural parameters place them between the known SCs and dwarf galaxies. Because of this discussion Kissler-Patig (2004) named them ultra-diffuse star clusters considering this object more like SCs. One year later Hasegan et al. (2005) proposed the name dwarf-globular transition object, even

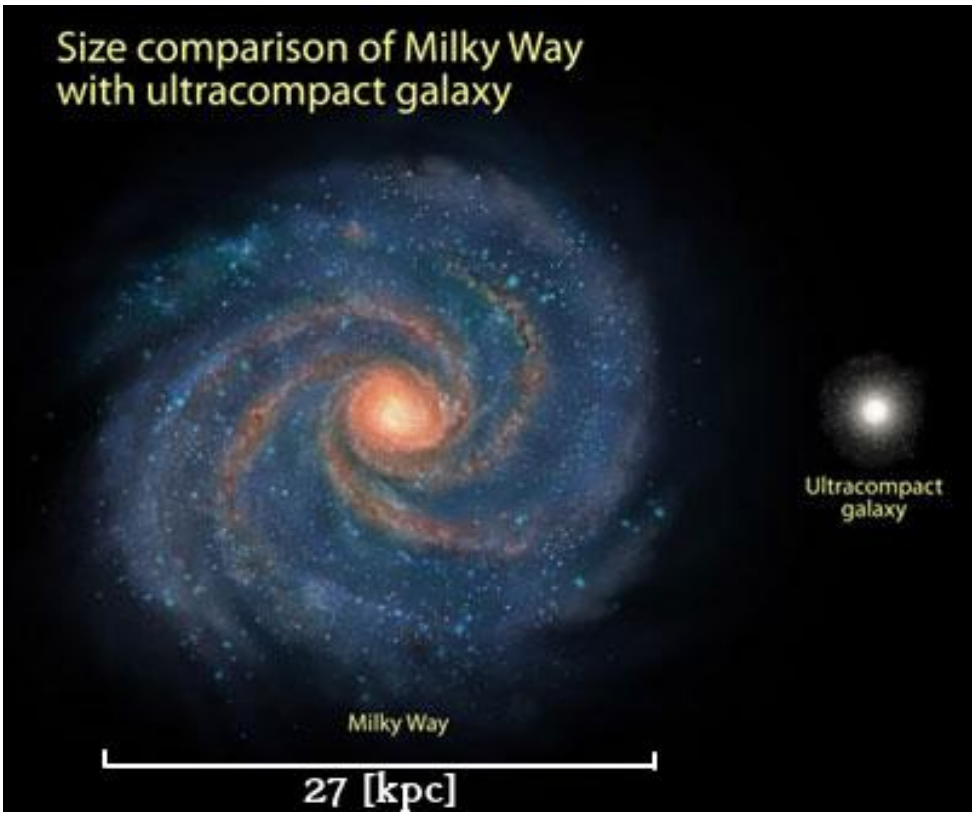

Figure 1.4: This is a representative image of the size of an UCD compared to the Milky way. Credit: NASA, ESA, A. Feild (STScI) and P. van Dokkum (Yale).

though the most known and common way to call these objects is ultra compact dwarf galaxies.

In the luminosity size diagram shown in Fig. 1.5 the position of different EOs is labeled. Until 2013, there was a gap shown in the figure. This zone called 'avoided zone' (Hwang et al 2011) was filled in 2013 when Forbes et al. found objects around the early-type galaxies NGC4278, NGC4649 and NGC4697. These objects are shown as blue and red symbols (corresponding to a division in color (g–z) = 1.1, equivalent to metallicity [Fe/H] = -1). The diagram shows that the more luminous and bigger objects located in the right size of the diagram are blue, and on the left side, objects with low luminosities are red. Different dashed lines denote lines of constant surface density.

The formation scenario of these objects have been in debate for the past decades and it

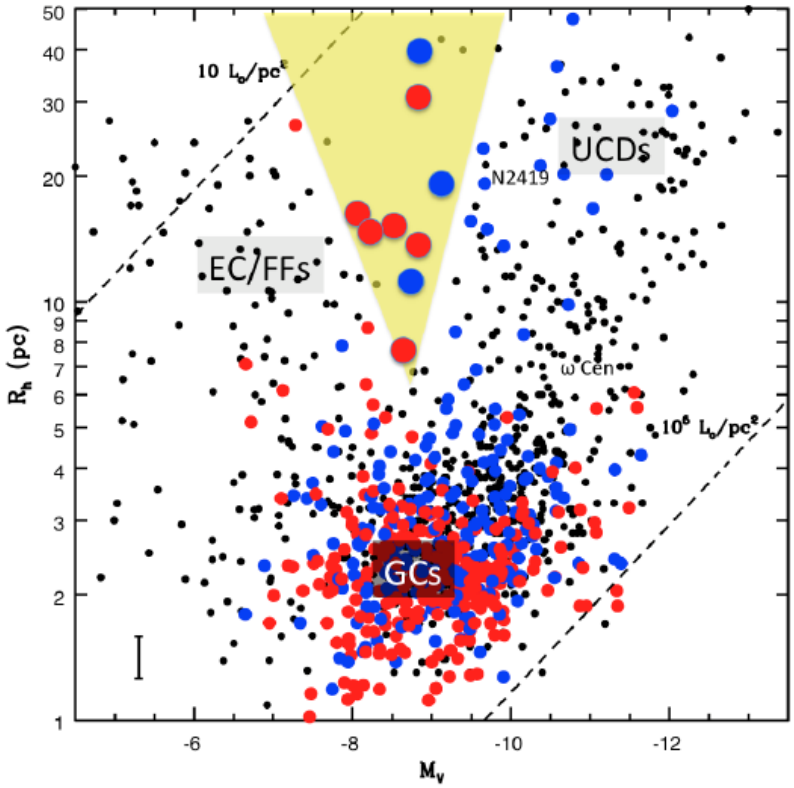

Figure 1.5: Size-luminosity diagram. The position of EOs is labeled. The avoidance zone (Hwang et al 2011) is shown with the objects found by Forbes et al (2013). Circles blue and red corresponding to a division at color(g–z) = 1.1, equivalent to metallicity [Fe/H] = -1. and different dashed lines denote lines of constant surface density. Image taken from Forbes et al 2013.

is still a huge topic of discussion today. The scenarios of formation can be subdivided into two groups. There is the group of astronomers who claim that the scenario of formation contain a galaxy origin and there is the group who thinks they have a star cluster origin.

An example for the scenarios with a galaxy origin is the galaxy threshing scenario, which describes a nucleated small galaxy interacting with bigger galaxies (typically early-type galaxies). The interaction between the small and the bigger galaxy results in the loss of almost all stars of the main body except for the nucleus of the smaller galaxy (Bekki et al. 2001).

There are also people that catalog UCDs like remnants of primordial compact galaxies (Drinkwater et al. 2004).

Scenarios with a SC origin are where the UCDs are the result of the merger of SCs in a Cluster Complex (CC) (Fellhauer & Kroupa 2002b,a), this is called the Merging Star Cluster Scenario(see section 1.5). Or where UCDs are the natural massive end of the distribution of SCs (Mieske et al. 2002).

Reaching the low mass end of the elliptical sequence we found Compact ellipticals (cEs). cEs have very similar parameters as EOs but they have values of r_{eff} between 100 to 1000 pc and a mass between 10^8 and 10^{10} $M_\odot$ (Anna Ferré-Mateu et al. 2017). The prototype galaxy for this type of galaxies is the Local Group dwarf galaxy M32 (Huxor et al 2013). They are a very rare class of galaxies. They have very small effective radii compared to their high central surface brightnesses (Faber 1973) resulting in a highly compact object, as shown in Fig. 1.1. The position that compact ellipticals take in this graphic is labeled with their prototype example M32.

The position of known compact ellipticals tells us that they are usually not isolated in the field, but they are close to massive galaxies in groups or clusters. Huxor et al (2011) found two cEs, which show evidence of formation resulting from ongoing tidal stripping of more massive progenitors, but there are examples of isolated cEs, like cE0 (CSCG 063-062) (Huxor et al 2013).
Until a few years ago the numbers of cEs identified until a distance of 100 Mpc was only a few dozen, in the last years this number has increase considerably(e.g Ferré-Mateu et al. 2017, Janz et al.2016 and references therein)

Just like UCDs the formation scenario of these systems can be subdivided into two scenarios. The first scenario has a galactic origin, having these systems originating from interaction between galaxies with a giant companion which leads to the tidal stripping and truncation scenario (Faber 1973) very similar to the galaxy threshing scenario.

This scenario of stripping may have an origin either as a bulge of a partially stripped disk galaxy (e.g Bekki et al. 2001) or as a elliptical galaxy truncated with a dense core (e.g King 1962; Faber 1973).

Wirth & Gallagher (1984) and Kormendy et al. (2009) considered cEs as systems

with an intrinsic origin due to the fact that they are the natural extension of the class of elliptical galaxies to smaller sizes and lower luminosities.

According to Kormendy & Bender (2012) there has to be another scenario of formation for these types of galaxies. They argue against the stripping scenario as: "not all cEs are companions of massive galaxies; many dSph galaxies are companions to massive galaxies yet are not truncated; bulges also sit at the compact end of the scaling relations for elliptical galaxies but are not truncated; and that unlike globular clusters, the exemplars for ideas of tidal truncation, the dark matter halo of a dwarf galaxy will quickly lead to a merger with its massive host."

There are examples of observed cEs that show evidence of formation resulting from the tidal and striping scenario, for example Huxor et al. (2011) report two cEs were the tidal tails are clearly visible, but there are also samples of cEs isolated, the first isolated cE was found by Huxor et al (2013). Its isolated position suggests that tidal stripping and truncation scenario is not the only way to form cEs, but there has to be an alternative channel to form cEs.
This alternative channel was probed to work in Urrutia Zapata et al (2019). In this work the merging star cluster scenario is testing for higher masses and sizes than the ones for the simulations of UCDs. The early Universe might have produced sufficiently strong star bursts to form systems containing SCs which merge into cEs. (see section 1.4 and 1.5).

1.2 Dwarf elliptical galaxies

Dwarf ellipticals (dEs) galaxies are in the low luminosity end of the elliptical sequence, having smaller sizes and lower luminosities than normal elliptical galaxies. A way to differentiate if a elliptical galaxy is a normal elliptical galaxy or a dwarf galaxy is its absolute magnitude, a limit of -18 mag is commonly used (Sandage & Binggeli 1984). There is evidence to believe that these two types of "apparently" different objects are indeed an extension of each other.(e.g. W Graham 2005.)

Considering the luminosity-size diagram of EOs Fig. 1.1 below magnitudes of -18 mag we have smooth-profile of two classes of systems,

- Compact galaxies: Galaxies with small r_{eff} for their level of central surface brightness, given a high compactness, like M32. (The systems studied in Urrutia Zapata et al 2019.)

- diffuse galaxies with low central surface brightnesses, where the Local Group dwarf spheroidals(dSph) are located.

dE and dSph are difficult to demarcate, i.e. where ends one type of objects and where starts the other. Again there is not a universally accepted definition, so it may vary between one author and another. Both objects have smooth, low surface brightness, and this makes the differentiation of them very difficult or leads to confusion over if these objects are similar systems or not. Because they both are smooth, low surface brightness galaxies. Considering this, dSph could be classified as a subgroup of dE.

The differentiation of dEs and bright elliptical galaxies in the elliptical sequence is not just a nomination, they are indeed different types of systems (Wirth & Gallagher 1984; but see Graham 2002a). This is supported by the way to describe their surface brightness, dwarf elliptical galaxies have a nearly flat radial profile, and are well described with a King model with a small concentration index or an exponential function(Faber & Lin 1983; Binggeli, Sandage, & Tarenghi 1984) and bright ellipticals are better described by a de Vaucouleurs' (1948, 1959) $R^{1/4}$- profile.

Regarding the formation of these galaxies, apparently they are the natural extension

of the elliptical sequence to lower masses and sizes, but the differences between this two object have shown strong evidence on the presumption of that they are indeed different objects and that they have different physical evolution.
The standard model present dEs like the result of the gravitational collapse of primordial density fluctuations(e.g. Press & Schechter 1974). But other authors claim that they could be the evolution of tidal dwarf galaxies(TDGs) (J. Dabringhausen and P. Kroupa 2013.) (see Section 1.3).

If we talk about morphological features their luminosities range from $M_B \approx$ -18 to -8, but they are usually in the range of $M_B \approx$ -18 to -14. Their mean surface brightness increases with luminosity.

There are some characteristics of dE that allows a morphological classification (Sandage & Binggeli 1984):

- Nucleus (dE,N): Usually bright dwarf galaxies show apparent central nucleus. When this morphological behaviour is exhibited the dE is named dE,N. The brightest nucleus can have a 20% of the total brightness of the dE galaxy. The ratio between nucleated and normal dE decreases with luminosity, faint dE usually do not have a nucleus (Sandage et al 1985b).

- Dwarf S0 (dS0): Is a variation of dE. They are inhomogeneous and very uncommon to find. The surface brightness of dS0 is low. And one of the most important reason to call them a different type of galaxy is the direct evidence of a disk or two components in the radial intensity distribution(Sandage & Binggeli 1984) but there are other reasons like twisted isophotes or high apparent flattening (Binggeli & Cameron 1991)

- Huge, low surface brightness: They are big systems with low surface brightness and with almost no gradient. Commonly they are classified along the dE/Irregulars transition, because they are outside the dE sequence. Fig.1.6 shows clearly that dE and Irregular are in the same M_B - μ plane of normal E's and bulges (Binggeli, B. 1994).

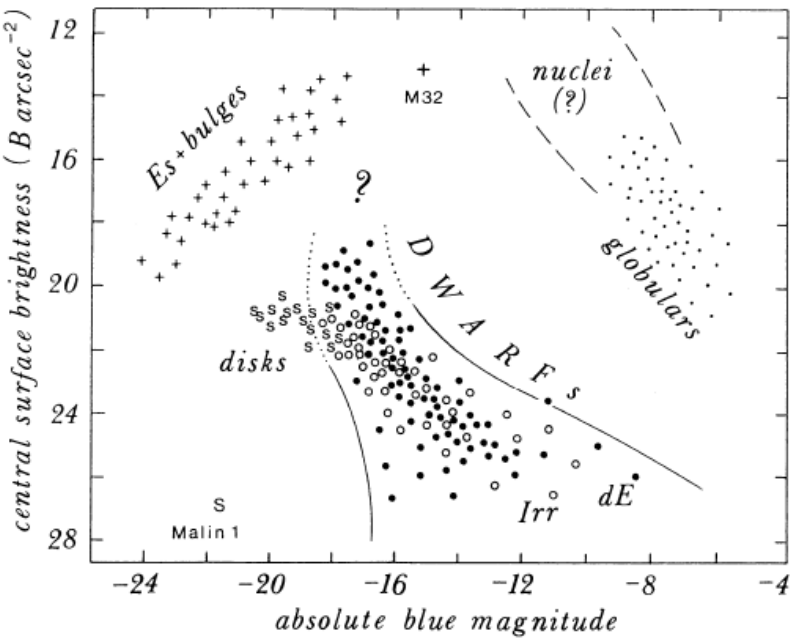

Figure 1.6: Central surface brightness against blue magnitude (M_B- μ plane) for stellar systems. Image taken from Binggeli, B. (1994).

In the scheme of Fig. 1.7. is shown the previous classification in relation with different object in the Hubble sequence. The circles and the numbers represent the major classes objects of the Atlas of Sandage & Binggeli (1984).

1.3 Tidal dwarf galaxies

Tidal dwarf galaxies (TDGs) were first observed in the catalog Arp (1996). TDGs appear to have filamentary structure. These structures connect interacting galaxies and are caused by the tidal forces as shown N-body simulations(Toomre & Toomre 1972).

TDGs are predicted in a lot of numerical calculations of encounters of galaxies. These galaxies have been observed e.g. "The Mice" galaxies and the "Antennae" galaxies. These bridges of matter can be understood by the gravitational force that exercise two or more encountering galaxies on each other (Toomre & Toomre 1972).

The potential of the background can form fully compressive tides. Compressive tides develop regions with starburst and after that contribute to the surviving of these regions

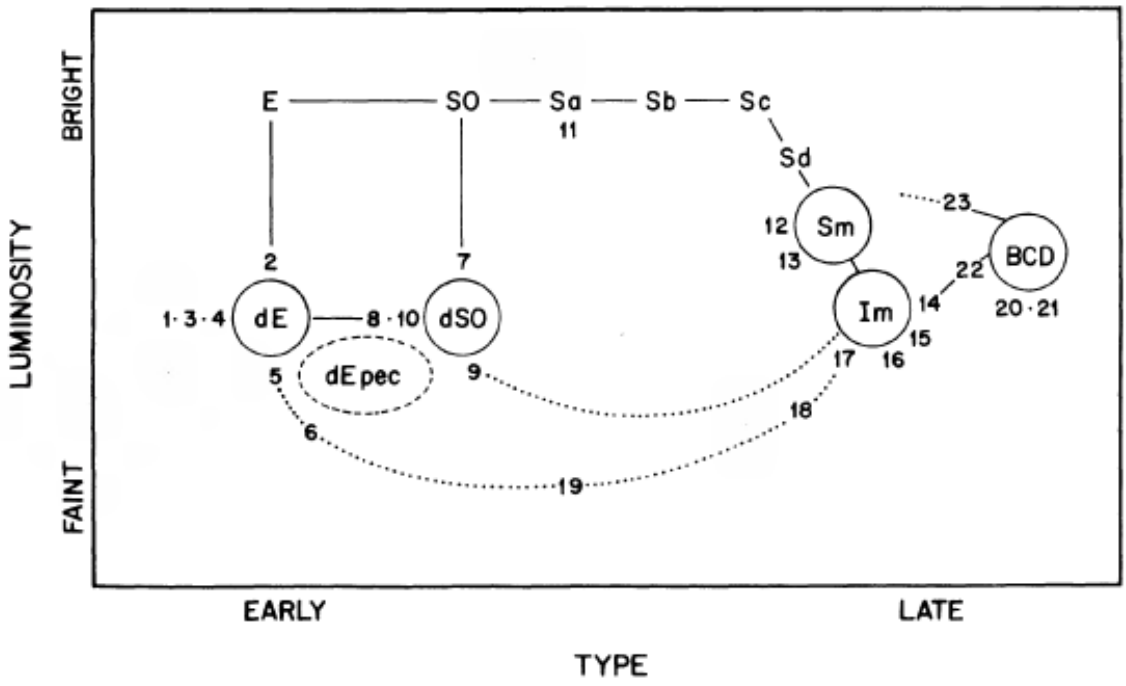

Figure 1.7: Relation of the different objects taken by the atlas of Sandage & Binggeli (1984). The Hubble sequence is shown in the principal first line of objects. A possible connection between early and late type of dwarfs is shown in dotted lines.

after the formation of star clusters and tidal dwarf galaxies. These compressive regions keep together clusters that would disappear in the formation stage because of the expulsion of gas(Renaud, F. et al 2008). The features and future of these regions have been studies in N-body calculations by many works e.g. Renaud. et al (2008), Duc & Renaud (2013), Renaud et al (2014).

Renaud et al (2008) studied the Antennae system and found very good agreement between their result -the position of these compression regions and the duration of their time-life- with the observational data. Their study theoretically show that the star clusters stay together even with SFHs lower than 10%.

After, Renaud et al (2009) extended their study to explore a bigger range of parameters. They claim that "neither the importance of the compressive tides ($\approx$15% of the stellar mass) nor their duration ($\approx 10^7$ yr) is strongly affected by changes in the progen-

itors' configurations and orbits"(Renaud et al 2009).

To increase the accuracy in the results of the these types of studies, the simulations have shown the entire evolution of the environment where the star clusters evolve, because of the very strong dependence of this evolution on the strength of the tidal field.

Ploeckinger et al 2014 perform hydrodynamics simulations to explore the early chemo dynamical evolution. They consider different models considering an IMF for the TDGs, filled or an IMF truncated at a maximal star mass m_{max}.

Both models start with an initial starburst and their dynamical evolution is followed with a self-regulated and continous star formation. The models evolve into dwarf galaxies with similar masses in gas and stars. They claim that TDGs can survive the early stage of a strong starburst (considering stellar feedback processes, ram pressure winds, and its dark matter halo, between others), no matter which shape of IMF, even if they do not have a stabilizing dark matter halo themself (Ploeckinger et al 2014).

Then, in an extension of their study Ploeckinger et al., 2015 they explore the evolution of different models, but now, on the long-term evolution of TDG with different SFHs, chemical enrichment, and rotation curves, resulting in different initial metallicities and considering an external tidal field or not.

All models in their study evolve into a stage of equilibrium and self-regulation of star formation. None of the simulations show a disrupted object even considering extreme feedback. The presence of compressive tides show clearly an increase of the SFRs and a compaction on the shape of the TDGs. Fig. 1.8 expose models with compressive tides : TDG-p and TDG-r, compared to isolated model: TDG-t. Top panel: SFRs for models TDG-t, TDG-p and TDG-r, shown in red, green and blue, respectively. Bottom panels: evolution of chemical abundances of star clusters in models TDG-t, TDG-p, and TDG-r for top to bottom. This evolution is presented as a 2D histogram displaying [O/Fe] ratio against the clusters' formation time in the simulation. Each pixel represents the stellar mass at t = 25 Myr $\times$[O/Fe] = 0.025, color-coded accordingly. Additionally, data points illustrate the mass-weighted, logarithmic average, along with standard deviation error bars, calculated within 100 Myr time bins. Nevertheless, none of the rotation curves

match the high real values of the observational data.

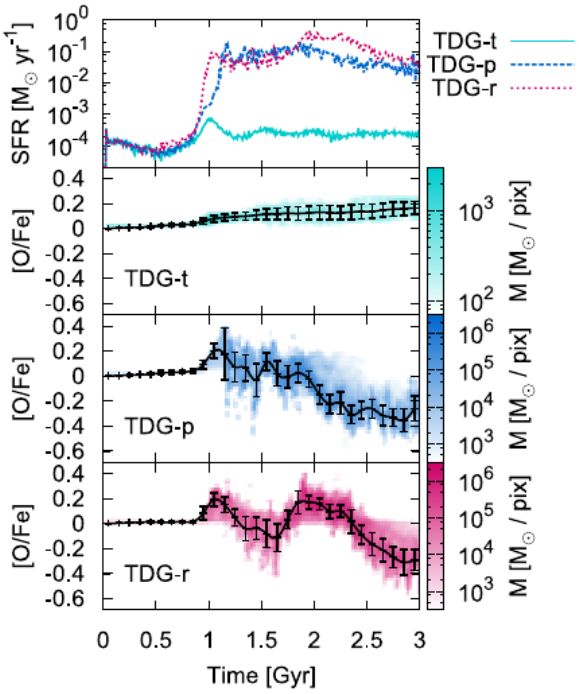

Figure 1.8: Top panel: SFRs for models TDG-t, TDG-p and TDG-r, shown in red, green and blue, respectively. Bottom panels: evolution of chemical abundances of star clusters in models TDG-t, TDG-p, and TDG-r for top to bottom. This evolution is presented as a 2D histogram displaying [O/Fe] ratio against the clusters' formation time in the simulation. Each pixel represents the stellar mass at t = 25 Myr $\times$[O/Fe] = 0.025, color-coded accordingly. Additionally, data points illustrate the mass-weighted, logarithmic average, along with standard deviation error bars, calculated within 100 Myr time bins. Image taken from Ploeckinger et al., 2015.

Many authors claim that these systems do not contain dark matter(e.g. Kroupa 2012, Dabringhausen and P. Kroupa, (2013)).

Renaud et al 2016 perform hydrodynamical simulations without dark matter. Instead they use an alternative theory name Modified Newtonian Dynamics (MOND), consisting in the modification of the normal Newton laws in regions with low acceleration (see section 1.6). Their study observes the evolution of interacting galaxies considering the star formation and stellar feedback.

They conclude that similar morphologies of systems can be obtained with the Newtonian treatment of gravity and with MOND. But, the last one requires a much slower orbital velocity for the systems (see Fig 1.9).

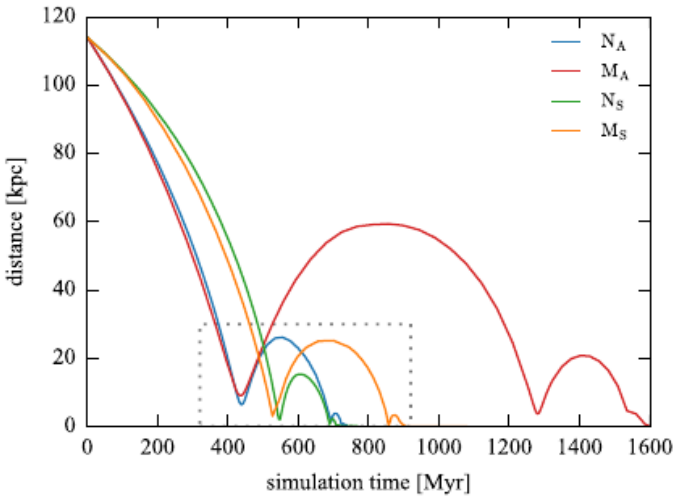

Figure 1.9: Evolution of the distance between the interacting galaxies. 'N' and 'M' represent a Newtonian treatment and Mondian dynamics, respectively. 'A' indicates the orbit of the Antennae model of Renaud et al.(2015a), and 'S' stand for Slow initial velocities.

Since Holmert 1941, the formation scenario of these types of system has been testing by several simulation studies. According to J. Dabringhausen and P. Kroupa, (2013) dE galaxies could be ancient tidal dwarf galaxies, because of their similar masses and sizes, this is shown in Fig. 1.10, which contains an estimates of the final radii of TDGs after their gas is expelled against their mass. In some places they overlap with dSph and dE. The large error bars are probably from the poor knowledge on how star formation and mass loss will influence the future evolution of the gas-rich present-day TDG candidates until they possibly resemble old, gas-poor dEs.

As TDGs formed from progenitors with stars already existing, their gas is already enriched by the stars of the galaxies, so this causes clear increase of the metallicities of these systems compared to the dwarf galaxies of similar luminosities.

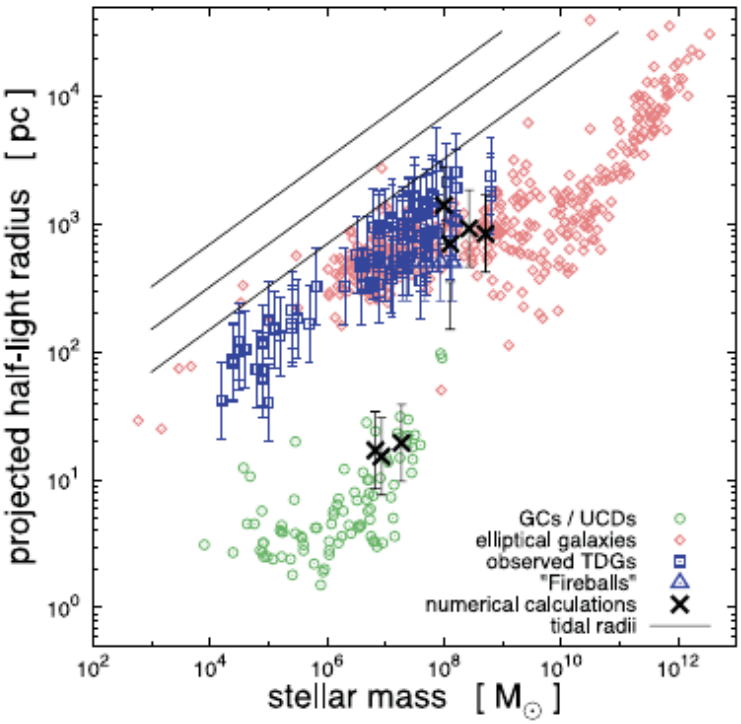

Figure 1.10: Estimates of the final radii of TDGs after their gas is expelled against their mass, in some places they overlap with dSph and dE. Image taken from J. Dabringhausen and P. Kroupa (2013).

1.4 Cluster complex (CC)

Young massive star clusters (YMSCs) have been observed in different types of galaxies. They sometimes form in groups called Cluster Complexes(CCs). These groups contain from a few to hundreds of YMSCs. The mass inside a CC is the sum of the mass of all YMSCs and the diameter of these systems is between a few hundred pc to ∼1 kpc. Most of the observed CCs seems to have a concentration of YMSCs in the central part and a few to hundred of star clusters in the vecinity surrounding the center(Bastian et al. 2005).

CCs have been observed in different environments. Fig. 1.11 shows the Antennae galaxies(NGC4038 + NGC4039). This system, at a distance of 20 Mpc contains two spiral galaxies undergoing a collision, which resulted in a strong starburst. The gravitational forces, caused by the interaction, create 'shock waves' in the gas and the compression of

molecular clouds leads to the formation of YMSC in CCs.

The Hubble Space Telescope (HST) takes images of the Antennae galaxies and reveals clusters of many dozens and possibly hundreds of young compact massive star clusters -the CC- within projected regions spanning about 100 to 500 pc (Whitmore & Schweizer 1995).

These concentrations of YMSCs in the Antennae are called knots. The second brightest knot in this system -Knot S- has a r_{eff} of 155 pc and a total luminosity of $M_V = -15.8$ mag (Whitmore et al. (1999)). Fig. 1.11.b shows this Knot. The blue circle is the r_{eff} and the black circle is the radius of 450 pc used by Whitmore et al. (1999) to derive the total luminosity.

The age of knot S derived by Whitmore et al. 1999 is about 7 Myr, this involves a mass-to-light ratio of $log_{10}(M/L_V) = -1.6$ (Bruzual & Charlot 2003), this particular low mass-to-light ratio leads to a total mass of 4.5×10^6 $M_\odot$.

The white circle in Fig. 1.11.b denotes the central object in the Knot S, having 1/3 of the total mass and a size of 18 pc (Bastian et al. 2013). In the vicinity of this central object there are 94 objects, 33 of these objects are brighter than $M_V = -9$ mag or more massive than 3.8×10^3 $M_\odot$ (Whitmore et al. 2010).

An example of the formation of a CC in a spiral galaxy is shown in Fig. 1.12. The image shows M51, a grand-design spiral galaxy and its neighbor galaxy called NGC5195. The formation takes place during an interaction with the small companion galaxy.

11 CCs have been found in the disk of M51 connected to the spiral arms of the disk, with sizes in the range of 85 and 240 pc, with ages younger than 10 Myr, and with the mass in the range of 0.3–3×10^5 $M_\odot$ (Bastian et al. 2005). An example of a CC is shown in the zoom of one arm.

In Fig.1.13 we show the Tadpole galaxy. Here you can see an example of the formation of CCs in tidal tails. The blow-up picture in the lower left, shows the most luminous, biggest and most massive CC. This CC has a total luminosity of -14.45 mag, an effective

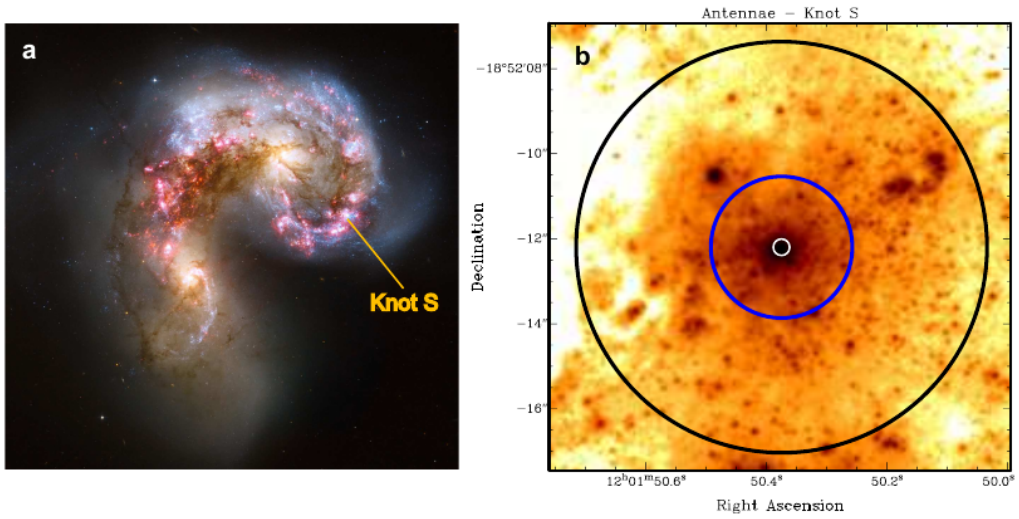

Figure 1.11: Antennae galaxies(NGC 4038 + NGC 4039), spiral galaxies interacting. (4.a) Image of the central part of the system. The position of Knot S is labeled. (4.b) A HST ACS image in the F435W band of knot S. It is possible to see an object already formed in the center. The circles in white (18 pc), blue(155 pc) and black(450 pc), denote the center object of the CC, the effective radius of the CC and the radius used to derive the luminosity (by Whitmore et al (1999)), respectively. Image taken from Brüns (2013), the data used in the plot was taken from the Hubble Legacy Archive.

radius of 160 pc and a mass of the order of 10^6 $M_\odot$ (Tran et al 2003). The projected distance to the center is around 60 kpc and the age is 4.5 Myr. Considering this, and the position in the tidal tail, Tran et al (2003) demonstrated that the CC formed within the tidal tail.

1.5 Merging Star Cluster Scenario

A mechanism for the formation of massive and extended star clusters was proposed by Kroupa (1998) who studied the likely fate of such CCs, and their possible relationship to spheroidal dwarf galaxies. He simulated the dynamical evolution of CCs using a collisionless method, for the duration of 95 Myr and showed that in a CCs with a high density of star clusters the merger of these SCs is very likely. It leads to the formation of a central stellar system that is more extended than the individual star clusters (by one to

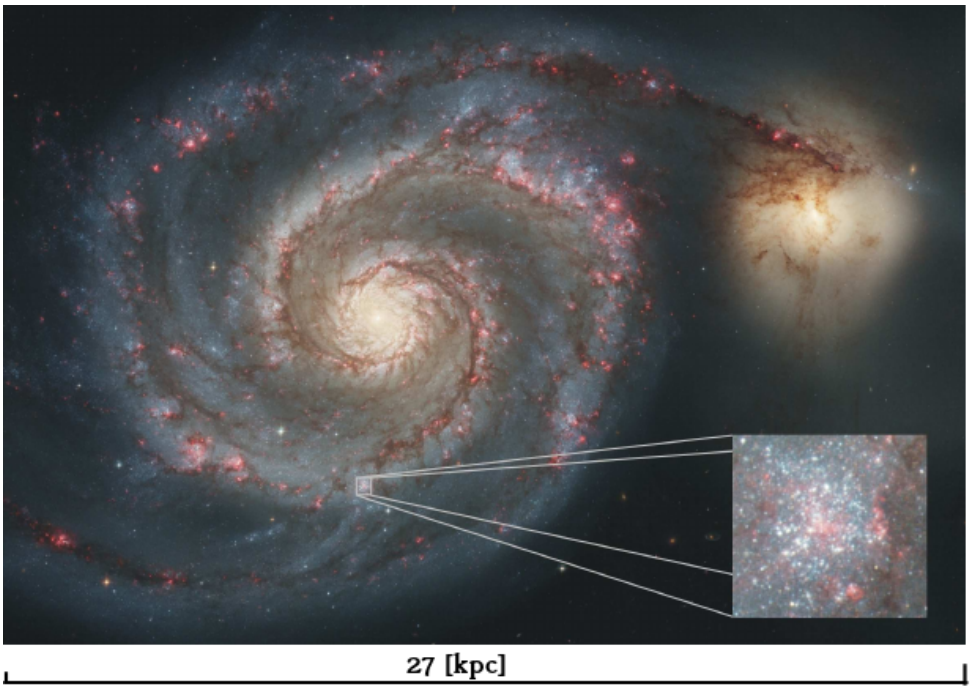

Figure 1.12: Formation of CC in a spiral galaxy forming during an interaction with a small companion galaxy (Like Whirlpool galaxy). An example of a CC is shown in the zoom of one arm. Figure is based on images taken from the HST public picture database.

two orders of magnitude). This central stellar system its called the merger object.

This scenario is called “merging star cluster scenario” and it contains essentially no dark matter apart from stellar remnants. The influence of orbital and internal parameters on the rate and timescales in the merger process was studied in Fellhauer et al (2002). They show that with the right set of parameters corresponding to self-consistent dynamical models, the simulation could end up with a dwarf galaxy, this opens up a formation channel for long-lived dwarf satellite galaxies. An important conclusion was obtained in this work: ”as long as the super-cluster is smaller than its tidal radius, almost all clusters merge”.

Afterwards, Fellhauer & Kroupa (2002a, 2002b) simulated different sets of parameters to show the evolution of CCs in a tidal field. They probe that the YMSCs in a CCs merge on a few supercluster crossing times in the merging star cluster scenario, and the merger object have the same observational parameters of FFs and UCDs, respectively. So

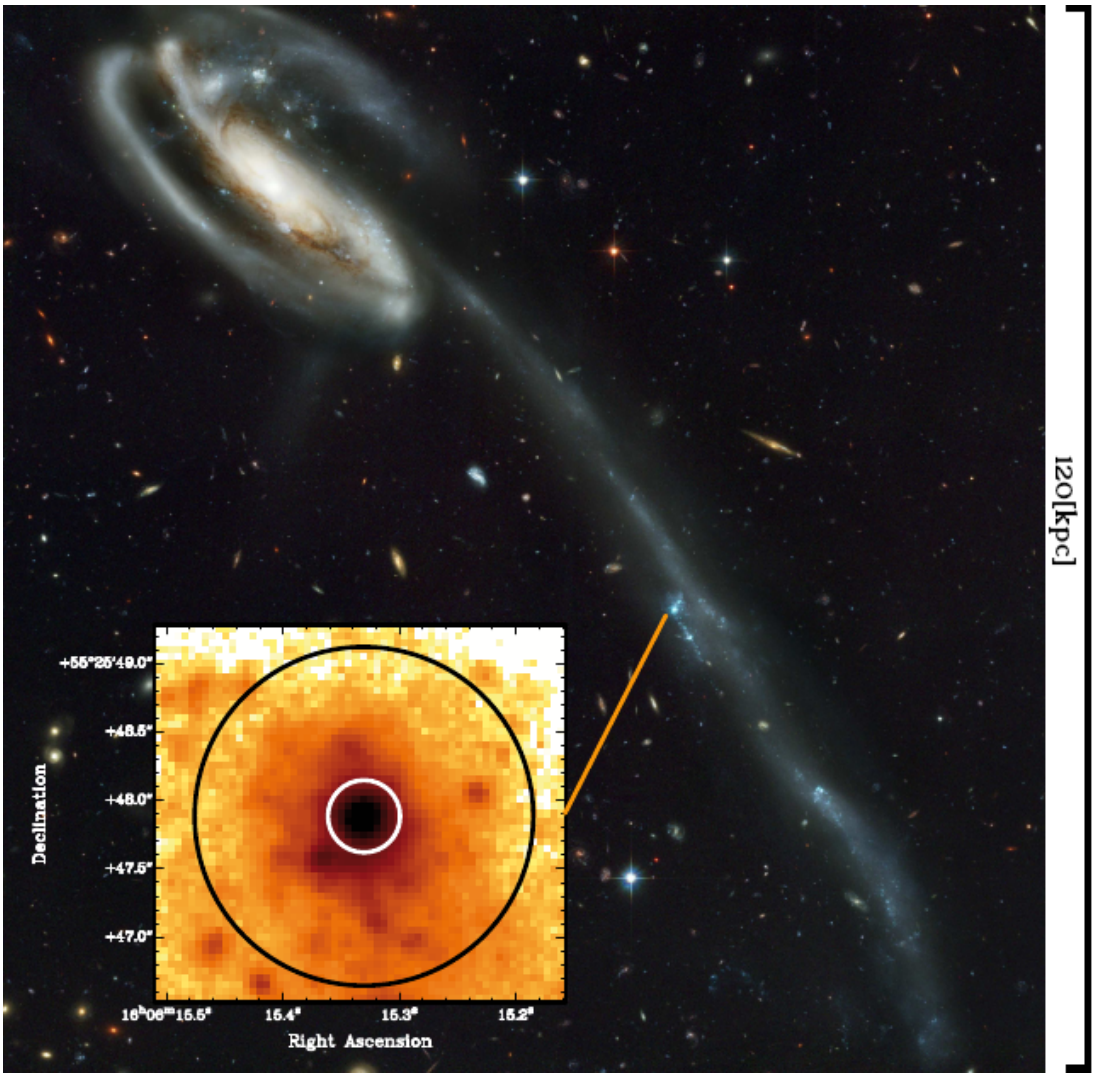

Figure 1.13: The main figure is taken from the HST public picture database and the enlargement is based on HST ACS data in the F435W band, taken from the Hubble Legacy Archive. TIt is possible to see an example of CC that forms within a tidal tail in Tadpole Galaxy (USC10214). The blow-up picture shown the biggest, most luminous and massive CC, which has an effective radius of 160 pc (white circle) and a mass of the order 10^6 $M_{\odot}$. The scale of the image is 120 x 120 [kpc]. The black circle (750 pc) covers the total extend of the CC. Image taken from Brüns (2013).

they claim that the merging star cluster scenario is able to produce merger objects with structural parameters similar to FFs and UCDs after a dynamical evolution of several Gyrs.

Brüns (2013) in her PhD thesis, did an extensive and detailed study of the merging star cluster scenario for the formation of ECs, FFs and UCDs. She simulated for several Gyrs a huge range of masses an sizes of CCs, with different orbital parameters. In the table 6.23 we show the main parameters of her simulations, to investigate if the CCs are the progenitor of FFs and UCDs. She varies these different set parameters and compares the merger object obtained with the observations. To do this, she uses the values of M/L=2.3 for FF as no observational constrains on the M/L ratio of FFs were available. This value was observed by Pryor & Meylan 1993 for 56 SC in the Milky Way.
For UCD she uses the value for M/L=3 as an intermediate value between the typical mass to light ratios of about 2 and 4 of SCs and UCDs.
Usually the YMSC are modeled as Plummer spheres(Plummer 1911). An important parameter in the studies of these systems is the Filling Factor parameter or α parameter which is defined as the ration between the Plummer radius of the SC($R_{\rm pl}^{\rm SC}$) and the Plummer radius of the cluster complex($R_{\rm pl}^{\rm CC}$). So this parameter tells us how densely filled the system is:

$$\alpha = \frac{R_{pl}^{SC}}{R_{pl}^{CC}} \tag{1.1}$$

One of the most important results found by Brüns (2013) is that the type of the merger object depends mainly on the initial CC size, the initial CC mass, and the external tidal field.

Those 3 parameters are combined in the β parameter defined by the ratio between the cut off radius ($R_{\rm pl}^{\rm cc}$) and the tidal radius of the CC ($R_{\rm t}^{\rm cc}$):

$$\beta = \frac{R_{\rm pl}^{\rm cc}}{R_{\rm t}^{\rm cc}} \tag{1.2}$$

The tidal radius depends on the CC mass and the strength of the tidal field, given by:

$$R_{\rm t}^{\rm cc} = \left[\frac{M_{\rm cc}}{3M_{\rm gal}}\right]^{1/3} R_{\rm peri} \tag{1.3}$$

Here $M_{\rm cc}$ is the mass of the CC, and $M_{\rm gal}$ is the mass of the host galaxy, and $R_{\rm peri}$ is the distance to the host galaxy of the CC, also in case of the eccentric orbits the tidal radius

	FF	UCD
N_0^{cc}	20	32
α	0.008	0.4,0.2,0.1,0.05,0.025
R_{pl}^{cc}[pc]	85 - 240	10,20,40,80,160,240,360
$M_{cc}[M_\odot]$	$10^4 - 10^5$	$10^{5.5} - 10^8$
M/L	2.3 (Pryor & Meylan 1993)	3

Table 1.1: Main parameters of the simulations of Brüns (2013), to investigate the fate of different sets of CCs to studies if they are progenitors of FFs and UCDs. In the table ,N_0^{sc} is the number of particles in each SC, N_0^{cc} is the number of SCs in the simulation, α is the filling factor, R_{pl}^{cc} is the size of the cluster complex, "grids" is the number of grids in the simulations, M_{cc} is the total mass in the simulation and M/L is the mass to light ratio. Source: From Urrutia Zapata (2018).

is estimated at perigalacticon(R_{peri}). The tidal radius is defined as the radius where the attractive force of the CC on a particle equals the pulling force of the external analytical potential(Brüns (2013)).

Brüns found that the merging of star clusters in CCs are a possible formation channel for ECs, FFs and UCDs. Comparing the results of the simulations with observations, she found that the CC models evolve into stable objects having structural parameters comparable to those of the observed objects.
"So, they are all part of the same formation process and they are, therefore united under the name "Extended Stellar Dynamical Objects".

The diagram in Fig. 1.14 shows the fate of the final object considering the characteristic and parameters of the simulated system -compact or extended CC-.

Urrutia Zapata et al. (2019) show that, similar to the merging star cluster scenario, the merger of objects immediately smaller than cEs, could end up in the formation of an object with the effective radius (r_{eff}), central velocity dispersion (σ_0), central surface brightness (Σ_0) and ellipticity (ϵ) matching with the observed cEs. This opened up the new formation channel for this types of galaxies, one with an UCDs origin.

Urrutia Zapata et al. (2019) model the evolution of very massive CCs with masses

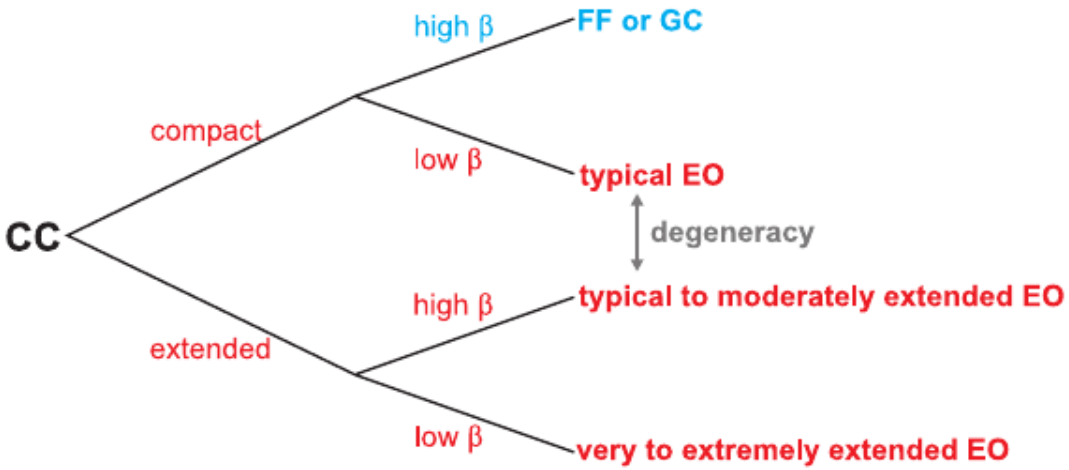

Figure 1.14: Diagram of the destiny of compact or extended CC according to the characteristic and parameters of the simulation. The colors represent the position in the simulated host galaxy. Blue represents simulations in the disk and in the inner parts of the halo of the galaxies and red the simulations in the outer parts of the halo of the galaxies. Image taken from Brüns (2013).

R_{gal} kpc]	R_{pl}^{sc} [pc]	R_{pl}^{cc} [pc]	N_0
20	4	50	64
60	10	100	128
100	20	200	

Table 1.2: Parameters varied in the 162 simulations.The distance to the center of the galaxy of the CC (R_{gal}), the Plummer radius of the SCs/UCDs (R_{pl}^{sc}), the Plummer radius of the CC (R_{pl}^{cc}) and the initial number of "UCDs" in the CC (N_0). Source: From Urrutia Zapata (2018).

of 10^9 $M_\odot$. SCs/UCDs are modeled as a Plummer spheres with radius R_{pl}^{sc} = 4, 10 or 20 pc using 100,000 particles in each SC/UCDs. The SCs are positionated inside the CC, following a Plummer distribution with radius R_{pl}^{cc} = 50, 100 or 200 pc at different distances to the host galaxy R_{gal} = 20, 60 or 100 kpc. These main parameters used by Urrutia Zapata et al. (2019) are displayed in Table 1.2.

The total number of simulations performed is 162. They simulate each combination

of parameters shown in Tab 1.2 using three different random seeds for the positions and velocities of the SCs inside the CC.

Almost all sets of parameters used in the study lead to objects similar to cEs. In Fig. 1.15 we compare our results with data from various observations plotting total brightness against effective radius. Our simulations have effective radii similar to M32 and total masses similar to the mean value of compact ellipticals. Please note that we have used a generic M/L ratio of unity and therefore we overestimate the total luminosity of our objects. Furthermore, as we keep the mass of our CC constant and almost all SC/UCDs end up in the merger object, almost all of our results show approximately the same absolute magnitude. Monachesi et al 2012 found two different stellar populations observing M32. Our simulations treat only the dynamics of the systems, so the metallicities are not included. This is because our particles are representations of the phase-space and not actual stars. We think that in the early Universe strong star-bursts form massive CCs that can re-accrete the expelled gas, seen e.g. as H-alpha bubbles around the CCs in the Antennae (e.g. Whitmore et al 1999), forming a second generation of stars.

Alarcon et al (2018) simulated systems in a very similar way, their simulations shown SCs dissolved to form a dSph, but in a dark matter halo. In his research different SFH are studied and the results and conclusions do not change when they adopt a star formation history into their models. So, we are confident that if our scenario includeds a SFH, it would also show no significant differences.

An important consideration in the study of the formation of cE by the merging star cluster scenario, is that none of the authors mentioned in this chapters claim that the merging star cluster scenario is the **only** way to form these EOs, we have to consider the existence of other tested formation scenarios like the tidal stripping and truncation scenario (Faber 1973) 2001) or cEs could have an intrinsic origin due the natural extension of the class of elliptical galaxies to smaller values of sizes luminosities (Wirth & Gallagher 1984). But the conclusions of Urrutia Zapata et al. 2019 opens up a new and alternative formation scenario for cE.

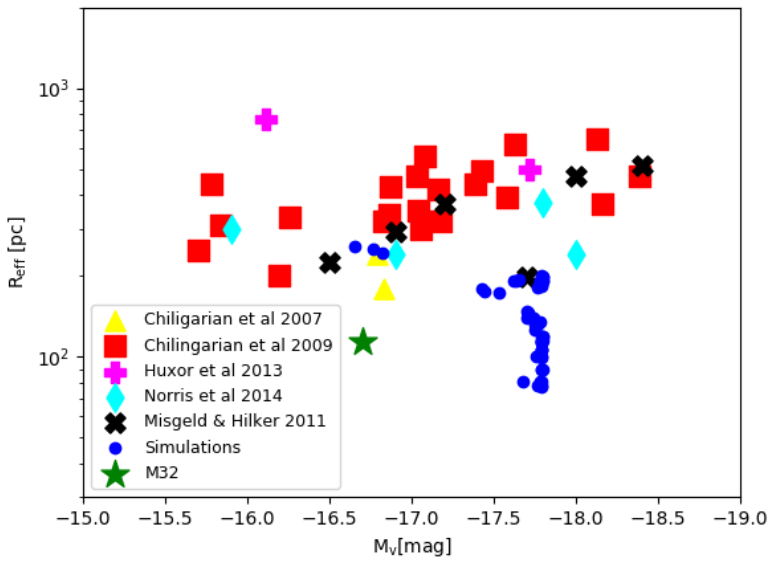

Figure 1.15: Absolute Magnitude vs. effective radius of observed cEs and our simulations. The green star denotes M32. The symbols are the different observational values taken from Chilingarian et al. (2007) (yellow triangles), Chilingarian et al. (2009) (red squares), Huxor et al. (2013) (magenta plus), Misgeld & Hilker (2011) (black crosses) and Norris et al. (2014) (cyan diamonds). The blue circles are our simulation results. Note that in order to determine the absolute magnitude we applied a generic M/L-ratio of unity, i.e. our objects should be less bright in reality. Further- more, all our models have the same initial mass, therefore the final mass (or brightness) is also almost the same. Image taken from Urrutia Zapata, F. et al (2019).

1.6 LCDM vs. MOND.

Well known is the problem of the rotation curve of disc galaxies in the Universe. The quantity of stars or luminous mass predicts a rotation velocity, calculated using the Newtons laws, that is much smaller that the measured one. Fig. 1.16 shows the behaviour of the rotation curve, the observed mass tells us that the velocity should follow the A line for example, but the measured velocity is bigger represented by the B line.

To solve this problem, the hypothesis of the existence of particle dark matter(DM) was born. One possibility is DM is considered like a Weakly Interacting Massive Particle (WIMP) and is a non-baryonic particle, which means that is not composed primarily of

baryons, i.e. the normal known matter composed by atoms. The study of dark matter is very poor and difficult to probe and until this day is debated in the community. Two considerations of dark matter are known , the cold dark matter and the hot dark matter.

Lambda cold dark matter(LCDM) is the standard dark energy plus cold dark matter model of cosmology, and cold refers to the fact that the dark matter moves slowly compared to the speed of light.

In the cold dark matter theory, structure grows hierarchically, with small objects collapsing under their self-gravity first and merging in a continuous hierarchy to form larger and more massive objects, so bottom-up, the opposite to consider the dark matter as hot, where the particles move with relativistic velocities and the structures of the formation are top-down, so in the beginning there were big systems which start to fragment into smaller objects (see Fig. 1.17).

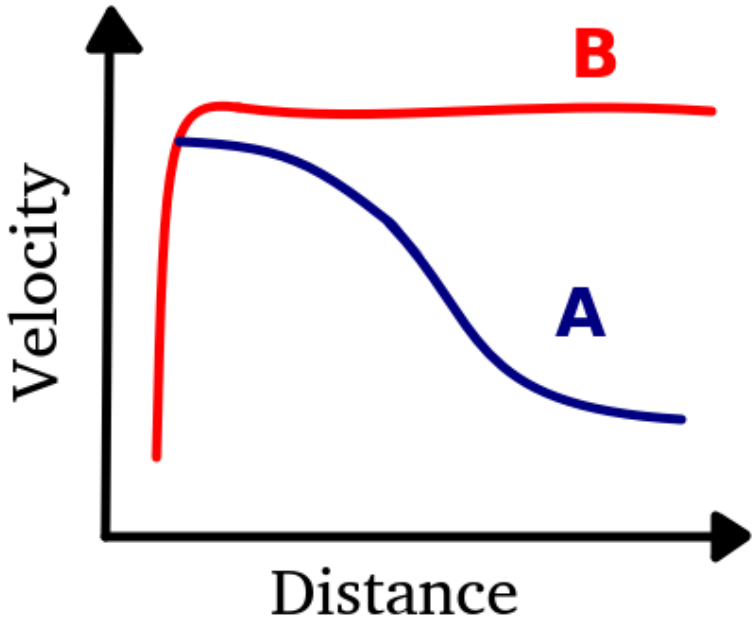

Figure 1.16: Rotation curve of galaxies. The velocities of the stars depending on their distance to the center of the galaxy. The A line represent the theoretical curve calculated with the Newtons equations and the B line is the observed curve. Source: this work

Modified Newtonian Dynamics(MOND), is an alternative to the theory of dark matter in terms of explaining why galaxies do not appear to obey the currently understood laws

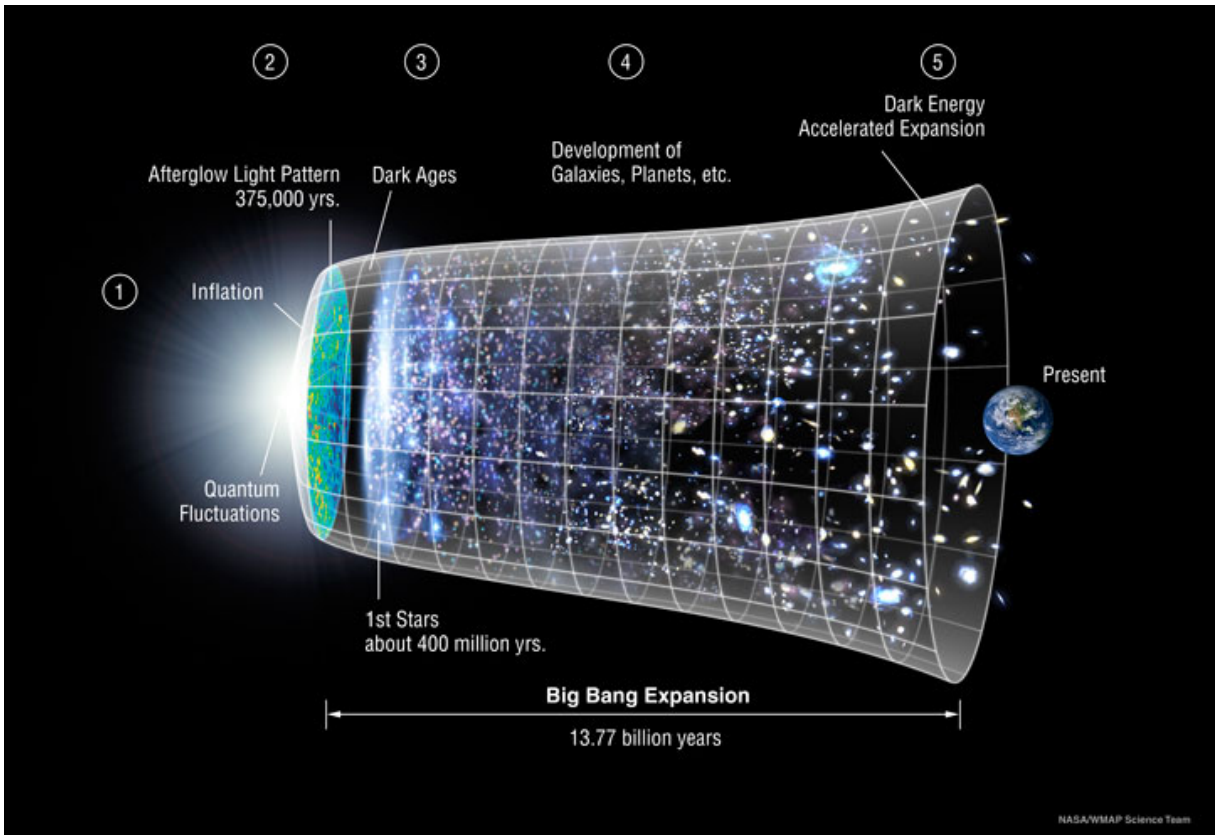

Figure 1.17: Lambda Cold dark matter model(LCDM). Adaptation of original NASA WMAP Science Team image.

of physics(see Fig.1.16). MOND is a theory that proposes a modification of Newton's laws to account for observed properties of galaxies.

It was created in 1982 and published in 1983 by Mordehai Milgrom. The basic premise of MOND is that while Newton's laws have been extensively tested in nearby high-acceleration environments like the Solar System and on Earth, they have not been verified in regions with extremely low acceleration, such as for stars in the outer parts of galaxies. So maybe that is the reason of the discrepancy on the predicted and observed line in rotation curves.

In the standard second law of Newton, the force is equal to mass multiplied by acceleration. The second law modified by Milgrom is written in the following way:

$$m_{\mathrm{g}}\mu(a/a_0)a = F \tag{1.4}$$

$$\mu(x \gg 1) \approx 1 \quad \text{for} \quad \mathrm{x} \gg 1$$

$$\mu(x \ll 1) \approx x \quad \text{for} \quad \text{x} \ll 1$$

$$x = \frac{a}{a_0}$$

Here F is the Newtonian force, m_g is the object's (gravitational) mass, a is its acceleration, μ(x) is an as-yet unspecified function (known as the "interpolating function"), and a_0 is a new fundamental constant which marks the transition between the Newtonian and deep-MOND regimes.

With empiric approximations and in the MOND regime we obtain the following relation for an object of mass M:

$$\frac{GMm_\text{g}}{r^2} = m_\text{g}\frac{\left(\frac{v^2}{r}\right)^2}{a_0} \Rightarrow v^4 = GMa_0 \tag{1.5}$$

In the following years after the first paper presenting MOND in 1983 different implementations of this theory, relativistic and non-relativistic, have been developed.

Most known theories are the following two:

1. **AQUAL**: The traditional and most known formulation, from 1984 (Bekenstein & Milgrom (1984)). In this formulation the non-linear Poisson equation that is needed is :

$$\bigtriangledown \cdot \left(\mu\left(\frac{|\bigtriangledown \phi|}{a_0}\right)\bigtriangledown \phi\right) = 4G\pi\rho \tag{1.6}$$

with a_0 the MOND acceleration parameter and with $\mu(x)$ the interpolation function that marks the transition between the Newtonian and the MONDian regime. To achieve the basic formulation to obtain the accelerations in the weak gravity range for MOND and the Newtonian gravity in the strong range for the gravity μ has to satisfy : μ(x) eq.1.4.

2. **QUMOND**: A latter formulation presented in Milgrom (2010). This formulation was developed by Milgrom for computational purpose, the non-linearity of the formulation of 1984 makes the process to solve the equation 1.6 difficult. In this later formulation only linear differential equations(with one nonlinear, algebraic step) is needed to solve.

In the QUMOND formulation the equation gotten from the nonlinear generalization that is need to solve is:

$$\rho' = \frac{1}{4\pi G}\bigtriangledown \cdot \left(\nu'\left(\frac{|\bigtriangledown \phi_N|}{a_0}\right)\bigtriangledown \phi_N\right) \tag{1.7}$$

with ϕ_N the Newtonian potential and ν' the interpolated function for the QUMOND description, this function now has to satisfy: $\nu'(y) \to 0$ when y$\gg$ 1 and $\nu'(y) \to y^{-1/2}$

when $y \ll 1$ to recover the ratio of the Newtonian gravitational acceleration. The ν' function corresponding to our μ function is given by:

$$\nu' = \frac{1}{2}\sqrt{1+\frac{4}{y}} - \frac{1}{2} \tag{1.8}$$

This is related to ν, the inverse of the μ, by $\nu = \nu' + 1$.

This equation satisfies all the standard conservation laws, and is easier to apply.

1.7 Outline of Thesis

Chapter 1 provides the theoretical framework for our study, then in Chapter 2 we present and explain the codes used in our research, followed by Chapter 3, which focuses on the formation of UCDs. In this chapter, each dE galaxy is associated with its own NFW halo, with pre-infall properties as predicted by the theory. Our objective is to investigate whether the dark matter halo can be stripped away, followed by the potential stripping of the stellar body of the dE galaxy, resulting in the observed UCDs. To achieve this, we first test the initial conditions and the code, and then perform 11 sets of different simulations with varying parameters to study their behavior over 10 Gyr of simulation in different orbits. In Chapter 4, we conduct additional simulations first we performs simulations inspired by the parameters investigated by Pfeffer & Baumgardt (P&B), but considering a dark matter halo, then we explore the transformation of dEs into UCDs within the framework of MOND, and a set of simulations in where we consider extreme orbits where satellites enter the dark matter halo from outside at varying angles, aiming to understand the behavior of dark matter halos under such conditions. Finally, Chapter 5 presents the discussion and conclusions. Chapter 6 contains the appendix, where all tables are shown.

Chapter 2

Codes

2.1 Superbox

SUPERBOX is a particle-mesh code with high resolution sub-grids and a nearest grid point (NGP) force-calculation scheme based on the second derivatives of the potential. This code uses moving subgrids to track and resolve high-density peaks in the particle distribution. This code is efficient in various ways, for example:

- The code is very efficient in memory because SUPERBOX uses only one set of grids to treat galaxies in succession.
- It avoids the limitation in spatial resolution of the standard particle mesh codes, because of they employ only a single grid.
- The computational overhead is kept as low as possible.

SUPERBOX implements a fast low-storage Fast Fourier Transformation (FFT) algorithm, which gives the possibility to work with millions of particles on regular computers. The basic idea implemented in SUPERBOX is to increase the resolution only at places where it is necessary, simultaneously keeping the computational overhead as small as possible. Using a fixed NGP force-calculation scheme, the accuracy is increased by linear force interpolation to the exact position of the particle inside a cell.

SUPERBOX works with 5 grids with 3 different resolutions and provides two higher-resolution levels of sub-grids, which stay focused on the galaxy. The medium-resolution grid contains an entire galaxy(R_{out}), and the high-resolution grid treats its core (R_{core}). Another important feature of this code is that the CPU-time scales both linearly with the particle number N_p, and with the number of grid-cells $N_{gc} = N^3$. A disadvantage of this grid-based method, is the dependency on the geometry of the grid but if we increase the spatial resolution, the geometry of the cells becomes less important.

In the particle-mesh technique the density of the particles is derived on a grid. This grid contains the simulation area, and the Poisson's equation

$$\bigtriangledown^2\Phi = 4\pi G\rho \tag{2.1}$$

in where Φ is the potential, G is the gravitational constant and ρ is the density, is solved on these grid-based density ρ_{ijk} to get the grid-based potential, Φ_{ijk}, using the FFT method and a suitable Green's function.

- Suitable Green's function: The usual geometry of the grid in a particle-mesh code is Cartesian and cubic. The simplest Green's function, which describes the distances between cells is,

$$H_{ijk} = \frac{1}{i^2 + j^2 + k^2} \quad i, j, k = 0, ...N \tag{2.2}$$

$$H_{000} = \frac{4}{3} \tag{2.3}$$

  where the grid-cells have unit length and N is the number of grid-cells per dimension. N has to be a power of two. The value of H_{000} is undefined, and usually $H_{000} = H_{100}$ (see e.g. Sellwood 1987).

- Deriving the density-grid: Locate each particle according to its position (x, y, z) in a grid. To assign the mass of the particle to the density-grid covering the simulation there are two possibilities:

  1. Nearest-grid-point scheme (NGP): assigns the whole mass of the particle to the grid-cell. All particles belonging to one galaxy have the same mass i.e. the ratio between the total mass of the galaxy and the number of particles.

2. Cloud-in-cell scheme (CIC): assigns a radius of half a cell length to each particle, and the mass of the particle is now distributed to the cell the particle is in and the surrounding cells according to the actual deviation of the particle position with respect to the center of the cell, however this is unnecessary, since the number of particles is large. This possibility improves momentum and energy conservation.

In order to allow a faster assignment of the densities, SUPERBOX still uses the NGP scheme, Fig. 2.1 is a 2D scheme showing how this assignment looks like.

- The FFT - algorithm: This algorithm gives the exact solution of the grid-based potential for a periodical system. For an isolated system, the size of the density-array has to be doubled ($2n$), filling all inactive grid cells with a value of zero. And extending the Green's function in the empty regions, using:

$$\begin{aligned} H_{2n-i,j,k} &= H_{2n-i,2n-j,k} \\ &= H_{2n-i,j,2n-k} \\ &= H_{2n-i,2n-j,2n-k} \\ &= H_{i,2n-j,k} \\ &= H_{i,2n-j,2n-k} \\ &= H_{i,j,2n-k} \\ &= H_{i,j,k} \end{aligned}$$

this provides the isolated solution of the potential in the simulated area between $i, j, k = 0$ and $n - 1$. To keep storage as slim as possible, only a 2n $\times$ 2n $\times$ n-array is used for transforming the densities, and a (n + 1) $\times$ (n + 1) $\times$ (n + 1)-array for the Green's function.

- Derivation of the forces: to obtain the forces according to each particle SUPERBOX uses the discrete numerical differentiation of the potential, in the grid-based potential of our simulation area.

- Integrating the particles: the orbits of the particles are integrated forward in the time using the leap frog algorithm. SUPERBOX uses a fixed global time-step (the same

time-step for all particles which stays constant during the whole simulation). This process is very fast and accurate for a grid-based code, has good energy conservation properties and it is time-reversible.

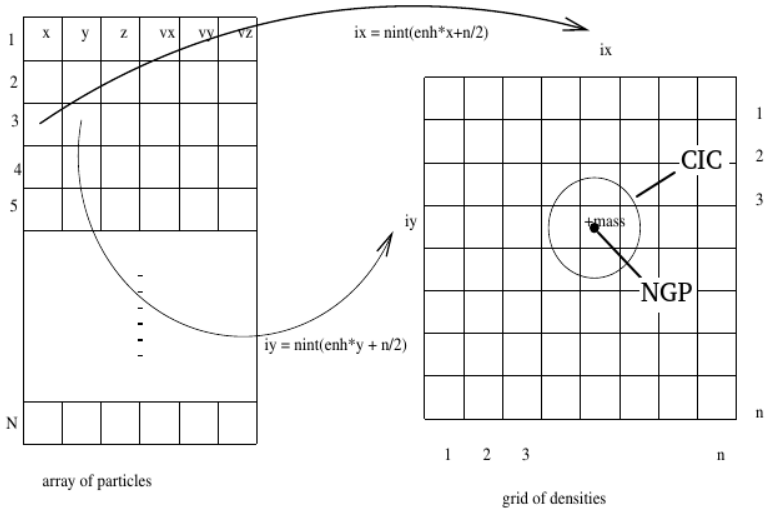

Figure 2.1: Two dimensional scheme that show the deriving density grid out of the particle positions. Image taken from Fellhauer et al (2000).

Fig. 2.2 is a float chart of SUPERBOX taken by Fellhauer et al (2000). This float chart shows step by step how SUPERBOX works.

An important property of SUPERBOX is the multi-grid structure. For each object, five grids with 3 different resolutions are used, this is possible by invoking the additivity of the potential. Fig. 2.3 is a scheme of this grids. The five grids are as follows:

- Grid 1: is the high-resolution grid which resolves the center of the galaxy. It has a length of $2 \times R_{\text{core}}$ in one dimension, with R_{core} the radius of high resolution grid centered in the object. In evaluating the densities, all particles of the galaxy within $r \leq R_{\text{core}}$ are stored in the grid.

- Grid 2: has an intermediate resolution to resolve the galaxy as a whole. The length is $2 \times R_{\text{core}}$, but only particles with $r \leq R_{\text{core}}$ are stored here, i.e. the same particles as are also stored in grid 1.

- Grid 3: has the same size and resolution as a grid 2, but only contains particles with $R_{\text{core}} < r \leq R_{\text{out}}$.

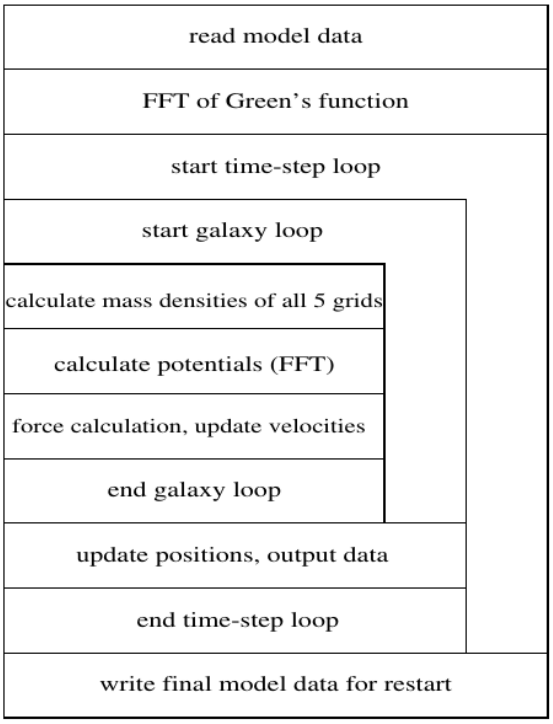

(a) Floart chart

Figure 2.2: Float chart of SUPERBOX. Image taken from Fellhauer et al (2000).

- Grid 4: has the size of the whole simulation are, i.e. local universe with $2 \times R_{\rm system}$, and has the lowest resolution. It is fixed. Only particles of the galaxy with $r \leq R_{\rm out}$ are stored in grid 4.
- Grid 5: has the same size and resolution of grid 4. This grid treats the escaping particles of a galaxy, and contains all particles with $r > R_{\rm out}$.

Grids 1, 2 and 3 are focused on the common center of the galaxy and move with it through the local universe. All grids have the same number of cells per dimension, given by n, for all galaxies. Each of the grids has its associated potential Φ_i, with $i = 1, 2, ..., 5$ computed by the particle-mesh technique. To calculate the acceleration:

- For a particle in the range $r \leq R_{\rm core}$ the potentials of the grids 1,3 and 5 are used.
- For a particle with $R_{\rm core} < r \leq R_{\rm out}$, the potentials of grids 2,3 and 5 are combined.
- If $r > R_{\rm out}$ then the acceleration is calculated from the potentials of grids 4 and 5.

- A particle with $r > R_{\text{system}}$ is removed from the computation.

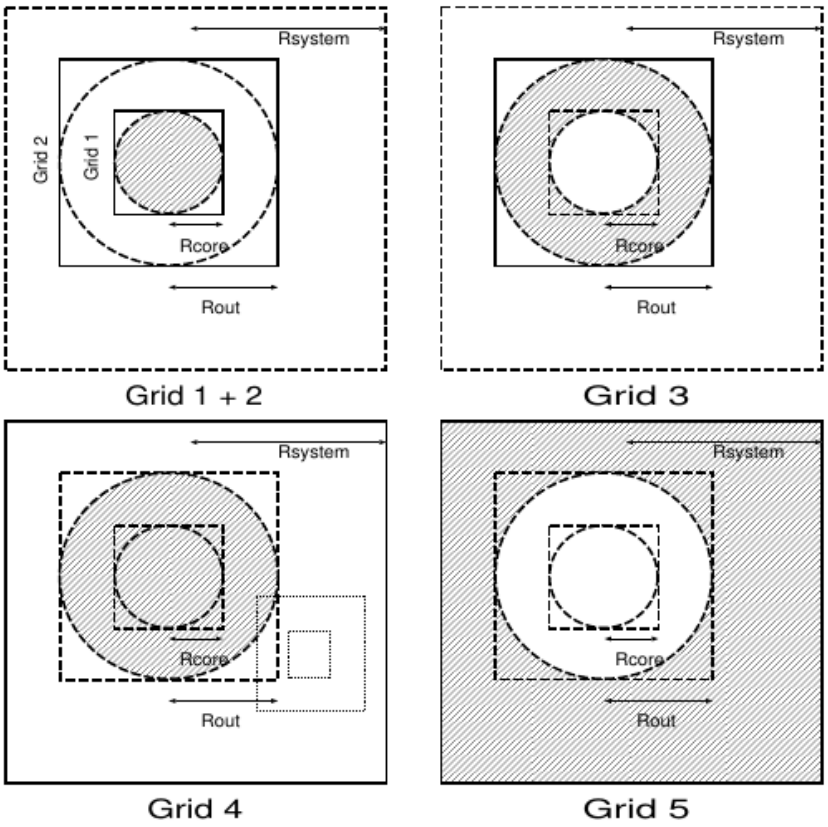

Figure 2.3: Multi-Grid structure of SUPERBOX. Image taken from Fellhauer et al. (2000).

2.2 Phantom of RAMSES(PoR)

One of the few codes to work with the Milgromian dynamics is Phantom of RAMSES (PoR) developed by Fabian Lughausen, Benoit Famaey, and Pavel Kroupa in 2014 (Lughausen et al. 2014), and is a customized version of RAMSES (parallel adaptive mesh refinement code). PoR is based on the modified Poisson equation (see M. Milgrom 2010). Some of the advantages of PoR are:

- Includes particles and gas dynamics.
- High spatial resolution of complex systems due to the adaptive mesh refinement technique.
- Allows the direct comparison between MOND and Newtonian simulations.
- Is suited for different systems such as isolated and interacting ones, as well as the formation of structures in a cosmological context.

One of the theories of MOND is called quasi-linear formulation of MOND (QUMOND). Considering the Poisson equation as:

$$\bigtriangledown^2\Phi(x) = 4\pi G(\rho_b(x) + \rho_{\rm ph}(x)) \tag{2.4}$$

ρ_b representing the baryonic density, Φ the total potential, $\rho_{\rm ph}(x)$ is an additional matter density distribution. Considering this functions the classical equation for the Newtonian potential is given by $\bigtriangledown^2\phi(x) = 4\pi G\rho_b(x)$ and the additional potential $\Phi_{\rm ph}(x)$ yields to the 'Phantom Dark Matter'(PDM) density given as $\bigtriangledown^2\Phi_{\rm ph}(x) = 4\pi G\rho_{\rm ph}(x)$. So the total gravitational potential is given by $\Phi = \phi + \Phi_{\rm ph}$, which is the classical Newtonian part ϕ plus an additional Milgromian part $\Phi_{\rm ph}$.

$$\rho_{\rm ph} = \frac{\bigtriangledown \cdot [\nu(|\bigtriangledown \phi(x)|/a_0) \bigtriangledown \phi(x)]}{4\pi G} \tag{2.5}$$

The computational time and resources increase when a code passes the limits of $N = 10^6$ particles, making it difficult to work with a regular laptop but in collisionless systems where the relaxation time scales are longer than a Hubble time(i.e. galaxies), the potential becomes smoother and direct N-body forces can be neglected. So we can

obtain the accelerations for a larger number of particles, considering several simplifications. In these codes the technique consists of mapping the position and masses of the particles on a discrete grid to determine the smoothed matter density distribution $\rho_b(x)$ of the particles. Using this value we can solve the Poisson equation $\bigtriangledown^2\phi(x) = 4\pi G\rho_b(x)$ to obtain the potential ϕ. We can obtain the acceleration from $a(x) = -\bigtriangledown\phi(x)$, then this acceleration is interpolated at the position to the individual particles to obtain equations of motion of each particle and integrate them.

As PoR is a customed version of RAMSES, it implements an adaptive mesh refinement (AMR) strategy. This code works with grids that are recursively cell-by-cell and level-by-level refined. If the cell passes a certain, pre-defined particle number density, the cell is splitted up into 2^3 sub-cells. So we can use large simulation areas and conserve a high resolution where we want to. The code can be used very efficiently for cosmological simulations, galaxy-galaxy interactions, satellite galaxies of a bigger host galaxy, among others. To solve the Poisson equation the codes uses a multi-grid relaxation scheme as described in section 2.2.1, the residual $\bigtriangledown^2\phi - 4\pi G\rho$ is minimized using the Gauss-Seidel method. This code is very efficiently working with large numbers of particles because the convergence rate does not depend on the number of cells.
This code allows the direct and easy comparison between a Newtonian and a Milgromian simulation, by setting a flag in the project configuration file. We can decide if we want a Newtonian force, a Milgromian force or the two of them. With this comparison allowed by PoR we can analyze and find the most important differences given in the results and the behaviour of the objects in the simulation.

2.2.1 The Poisson solver

To solve equation 2.4 we need to solve two linear differential equations and one algebraic step, in the following way :

- We obtain the Newtonian potential ϕ and its gradient solving the classical Poisson equation $\bigtriangledown^2\phi(x) = 4\pi GH\rho_b(x)$ from the distribution of matter. And the boundary con-

dition $\phi(r) = -GM_b/r$ is applied, with M_b the total baryonic mass, and r the distance to the center.

-Then the PDM density ρ_{ph} is calculated with the following discrete scheme:

$$\begin{aligned}\rho_{\rm ph}^{i,j,k} = \frac{1}{4\pi G h} \quad [\quad & \nu_{\rm B_x}(\bigtriangledown\phi)_{\rm B_x,x} - \nu_{\rm A_x}(\bigtriangledown\phi)_{\rm A_x,x} + \nu_{\rm B_y}(\bigtriangledown\phi)_{\rm B_y,y} \\ - \quad & \nu_{\rm A_y}(\bigtriangledown\phi)_{\rm A_y,y} + \nu_{\rm B_z}(\bigtriangledown\phi)_{\rm B_z,z} - \nu_{\rm A_z}(\bigtriangledown\phi)_{\rm A_z,z}]\end{aligned} \tag{2.6}$$

Here the PDM is approximate to the center of the (i,j,k) grid cell at the position $x_{i,j,k}$, and:

ϕ: is the Newtonial potential computed in the first step.

h: is the cell width.

$\nu_{\rm A_x}$: is the value of $\nu(|\bigtriangledown\phi|/a_0)$ at the point $\rm A_x$.

$(\bigtriangledown\phi)_{\rm A_x,x}$: is the x-component of the $\bigtriangledown\phi$ at the point $\rm A_x$ and is approximate as following:

$$(\bigtriangledown\phi)_{\rm A_x,x} = \frac{\phi^{-2,0,0} - 27\phi^{-1,0,0} + 27\phi^{0,0,0} - \phi^{1,0,0}}{24h}$$

$$(\bigtriangledown\phi)_{\rm A_x,y} = 0.5\left[(\bigtriangledown\phi)_{\rm y}^{-1,0,0} + (\bigtriangledown\phi)_{\rm y}^{0,0,0}\right] \tag{2.7}$$

$$(\bigtriangledown\phi)_{\rm A_x,z} = 0.5\left[(\bigtriangledown\phi)_{\rm z}^{-1,0,0} + (\bigtriangledown\phi)_{\rm z}^{0,0,0}\right]$$

and considering:

$$\begin{aligned}(\bigtriangledown\phi)_{\rm y}^{i,j,k} &= \frac{\phi^{0,-2,0} - 8\phi^{0,-1,0} + 8\phi^{0,1,0} - \phi^{0,2,0}}{12h} \\ (\bigtriangledown\phi)_{\rm z}^{i,j,k} &= \frac{\phi^{0,0,-2} - 8\phi^{0,0,-1} + 8\phi^{0,0,1} - \phi^{0,0,2}}{12h}\end{aligned} \tag{2.8}$$

This scheme is illustrated in Fig. 2.4 and can be used for the other points analogously. The Newtonian potential is interpolated from the next coarse grid level.

- Finally the Poisson equation is solved but now considering the two matter components as shown in equation (2.4). To solve this equation and obtain Φ we consider the boundary condition $\Phi(r) = (GM_b a_0)^{1/2}\ln(\rm r)$ which is true considering $|\bigtriangledown\phi(r)|/a_0 \ll 1$.

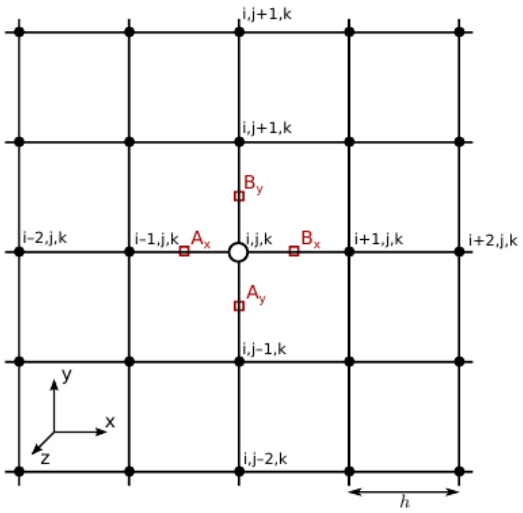

Figure 2.4: Scheme of how PoR works in the x-y plane. The values of ν are evaluated at A and B points. Image taken from Lüghausen et al. (2014a)

PoR is very efficient because we can use several existing Poisson solvers and of existing grid-based codes but it can not be implemented into codes which requires to linearly add accelerations, this holds for tree-codes and the ones that use nested grids like SUPERBOX.

2.3 RAyMOND

RAyMOND on the other hand has 2 formulations of MOND.
1. First the traditional formulation of MOND a fully non-linear aquadratic Lagrangian (AQUAL) formulation from 1984 (Bekenstein & Milgrom (1984))-RAMSES is easily adaptable to this- but the nonlinearity of this formulation limits the numerical techniques that may be used in a computational solver.
2. And a later formulation by Milgrom 2010, often referred to a quasi-linear simulations called QUMOND. This formulation works with the standard Poisson equation and use an additional density component the 'phantom dark matter' (PDM) distribution explained in the previous section. In QUMOND we solve only linear differential equations, with one nonlinear, algebraic step. This second formulation is easier to apply.

The goal is being able to explore MONDian galactic dynamics in more physically realistic settings, involving important processes in the Universe like galaxy mergers, tidal stripping and ram-pressure stripping. To do that the N-body-hydrodynamics adaptive mesh refinement (AMR) code RAMSES (Teyssier 2002) is modified to implement the two formulations of MOND previously explained. RAMSES works with an iterative Gauss–Seidel solver accelerated in a multigrid scheme to solve the Newtonian Poisson equation.

2.3.1 AQUAL

For the first formulation, the non-linear Poisson equation that RAyMOND has to solve is eq 1.6. To achieve the basic formulation to obtain the accelerations in the weak gravity range for MOND and the Newtonian gravity in the strong range, μ has to satisfy : μ(x) eq.1.4 RAyMOND use the simple formulation for the interpolated function:

$$\mu(x) = \frac{x}{1+x} \tag{2.9}$$

and sets the acceleration parameter as a_0=1.2 $\times$ 10^{-10} m s^{-2}.

The Gauss–Seidel solver in RAMSES uses a standard 6-point stencil as shown in Fig. 2.5.

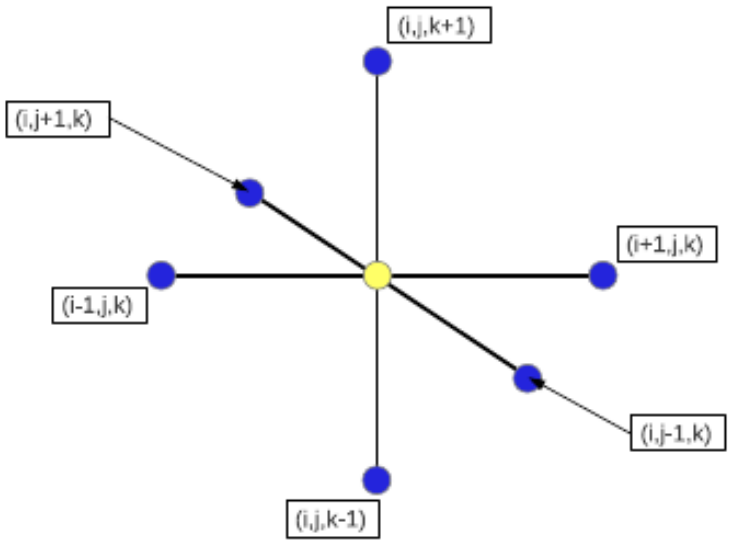

Figure 2.5: Standard 6-point stencil used in RAMSES. Image taken from Candlish, G. N. et al (2015).

This stencil is used to update the value of ϕ at the central grid point considering the average the other six grid points around it. RAyMOND modifies the standard 6-point stencil to use an extended stencil of points around each grid point in the calculation of ϕ, just like the procedure of Brada & Milgrom (1999), see Fig. 2.6.

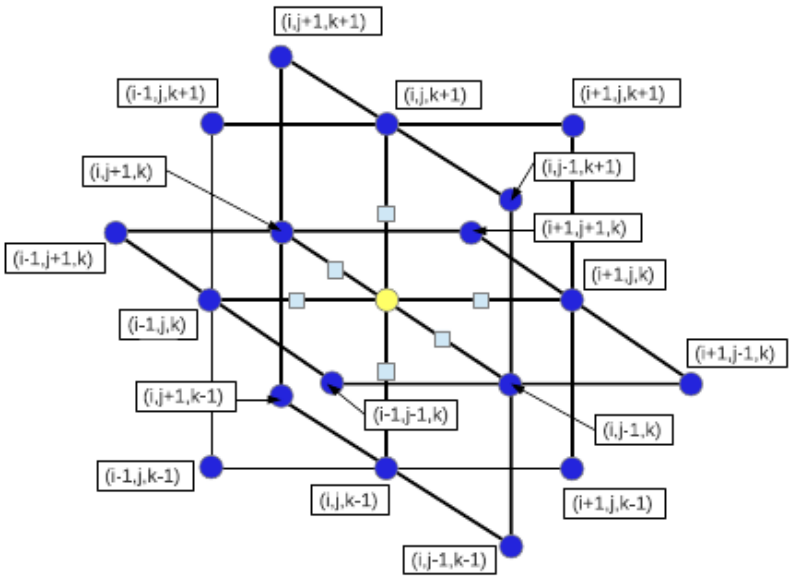

Figure 2.6: 18-point stencil used for RAyMOND. Image taken from Candlish, G. N. et al (2015).

The following expression gives the updated ϕ:

$$\begin{aligned}\phi_{i,j,k} &= (\mu_{i+1/2,j,k}\phi_{i+1,j,k} + \mu_{i-1/2,j,k}\phi_{i-1,j,k} + \mu_{i,j-1/2,k}\phi_{i,j-1,k} \\ &+ \mu_{i,j+1/2,k}\phi_{i,j+1,k} + \mu_{i,j,k-1/2}\phi_{i,j,k-1} + \mu_{i,j,k+1/2}\phi_{i,j,k+1} - 4\pi dx^2\rho_{i,j,k})/\sum_N \mu_N\end{aligned} \tag{2.10}$$

The μ function has to be evaluated in the middle of the grid points (see the squares in Fig. 2.6. This evaluation requires a finite difference calculation of the gradient of ϕ at the grid points around the central grid point, this requires the extended stencil shown in Fig. 2.6. The dependence of μ on ϕ leads to a ϕ dependence in the coefficients used in the RAMSES solver, and thus a non-lineal behaviour. When μ is equal to 1 the Newtonian version of the Gauss-Siedel is recovered.

The extended stencil requires a modification of RAMSES, as we now need the ϕ values at diagonal neighbors, such as $\phi_{i+1,j+1,k}$. RAyMOND use the existing linked list architecture to obtain the points required. To obtain the diagonal points RAyMOND uses the neighbors of neighbors.

The computational mesh is structured in levels of refinement,- the higher levels corresponding to more refinement-, at each level, the mesh is organized into 'grids' and 'cells'.

Each grid contains eight cells in three dimensions, four cells in two dimensions and two cells in one dimension- A grid at one level corresponds to a cell at a lower level of refinement-.

The neighboring grids of a refined cell are referenced pointers for each cell and then reached from the parent grid, then a leapfrog is used to find the diagonal point, if there isn't this first neighboring cell, instead of moving one level of the mesh hierarchy RAMSES moves two of these levels and if the diagonal cell does not exist, the code interpolates ϕ from the next coarsest level. This technique is used in a 'fully threaded tree' data structure (Khokhlov 1998).

Multrigrid algorithm of RAMSES.

The multrigrid algorithm of RAMSES can be briefly described as :

1. RAMSES starts with an initial guess of ϕ.
2. Pre-smoothing: The iterative process updates this initial ϕ on the fine mesh.
3. The error given by the residual, is calculated on the fine mesh.
4. Restriction step: the values of these errors are moved to the coarse mesh. Then an average of the fine grid point values that surround a coarse grid point is assigned to the coarse grid point.
5. Correction: The correction to the fine solution is calculate in the coarse mesh, using the coarse version of the iterative process.
6. Then the coarse correction is interpolated back to the fine mesh and added to the fine solution.
7. Post-smoothing: The iterative process updates the corrected fine solution.

RAyMOND has to modify the previous multigrid algorithm, to do this, there are different approaches, but RAyMOND uses the full approximation storage scheme (Trottenberg et al. 2001). So RAyMOND has to calculate the full solution of the non-linear Poisson equation in all course levels and not only in the coarse levels like in the Newtonian codes. The differences are that RAyMOND restricts the initial fine solution after smoothing,

and calculates the full coarse solution using the restricted fine solution, instead of just the correction. This solution is then subtracted from the coarse solution to find the errors.

2.3.2 QUMOND

For computational purposes, this formulation amounts to solving the Poisson equation twice, using the modified density distribution in the second step(so this does not require to modify the Gauss–Siedel solver). As this uses the usual linear Poisson equation, standard numerical techniques may be applied for this version of MOND, albeit with an additional step of calculating the density distribution. To calculate the density field Raymond use the finite-difference extended stencil described in the previous section.
In the QUMOND formulation Raymond has to solve, for the PDM, the equation 1.7. Considering the ν' function as given by 1.8.

This formulation is easier to apply in the sense of that we do not need to use the iterative scheme to converge to the result, instead we can obtain ρ from (2.5). Then we add the additional density contribution to the density field of the system, finally Raymond solve the standard Poisson equation a second time to obtain the potential.

The multrigrid scheme only requires minor modifications to solve the Poisson equation with the appropriate density field. The memory used for this version of the code increases a little because RAyMOND introduces new arrays to file the MONDian potential and the 'PDM' density.

The execution time of the code has also been demonstrated to be as fast as may be expected, considering the complexity of MOND. The AQUAL version is four times slower than RAMSES, and the QUMOND version is about two times slower. Several tests have confirmed that RAyMOND is able to evolve, in a stable way, considering the MOND laws, dispersion-supported and rotation-supported stellar systems. And a very useful skill of this code is the possibility to compare the different formulations, as Raymond allows the direct comparison between simulations in RAMSES (Newtonian version), and RAyMOND (in the AQUAL and QUMOND formulations).

Chapter 3

Formation of UCDs in LCDM

As explained in Section 1.1 the formation of UCDs has been debated for a few decades. It has been shown that the merging star cluster scenario is able to produce UCDs (see. e.g Fellhauer & Kroupa 2002b and Brüns et al, 2009). Many believe that UCDs are the remnants of larger objects that have been stripped down into these compact and luminous systems (see e.g. Bekki et al., 2001; Bekki et al., 2003). This stripping process occurs when they pass near more massive systems, such as galaxy clusters, and are subjected to their strong tidal gravitational fields. In this section, we explore the possibility of forming enough UCDs through tidal stripping of dwarf ellipticals in a Virgo-like galaxy cluster using numerical simulations within the framework of the LCDM theory. In this scenario, each dE galaxy has its own NFW halo to study whether the dark matter halo can be stripped, and then if the baryonic component of the galaxy can be stripped, resulting in the formation of UCDs consistent with observational data. Our study investigates a scenario similar to that proposed by Pfeffer & Baumgart (2013), but in their simulations, they assume the dark matter halo to already be stripped.

3.1 First simulations (Testing the initial conditions)

In our initial approach, we utilize different task on SUPERBOX to obtain critical parameters for the simulations, such as the dynamical friction parameter, optimal grid settings, and initial velocities of the objects required for the orbits analyzed in this chapter, among

others. In this section we present the simulation setup, parameters and orbits, with their respective conclusions. Finally, we include an examination of the nucleus of the orbiting objects, for which we present a study detailing the most optimal grid parameters for this component.

3.1.1 Setup

We perform simulations with the particle-mesh code SUPERBOX (see section 2.1). Our simulations consist of two objects, a DM halo representing a Virgo-like galaxy cluster including a luminous central galaxy and an infalling nucleated dwarf elliptical made out of a DM halo also including a luminous part as a spherical envelope.
i.e. the simulations host 4 objects:

1. The DM halo of the galaxy cluster, modeled as a NFW distribution with the following parameters which are kept constant for all simulations:
   $R_{s,GC} = 32$ kpc, $R_{200,GC}$=983 kpc and $M_{DM,GC} = 10^{14}$, 10^{15} $M_\odot$.

2. The central galaxy of the galaxy cluster is represented by a Plummer sphere using:
   $R_{pl,GC}$=16.22 kpc and $M_{pl,GC} = 10^{12}$, 10^{14} $M_\odot$.
   Again these parameters stay constant for all simulations.

3. The DM halo of the dE galaxy is modeled as a NFW distribution. In the simulations we vary the parameters as follows:
   $r_{s,dE} = 4$ kpc, $r_{200,dE}$=1, 9.83, 21.19 kpc and $M_{DM,dE} = 10^8$, 10^9 $M_\odot$.

4. The luminous envelop of the dE galaxy is modeled as a Plummer sphere with parameters:
   $R_{pl,dE}$=0.85, 1 kpc and $M_{pl,dE} = 10^7$, 10^8, 10^9 $M_\odot$

In this section, the dark matter component of the satellite and the host are self-consistent objects, so dynamical friction is properly taken into account.

First we explore the behaviour of our simulations using live objects for the central big object, and then we model this object analytically in SUPERBOX. So, in this section the host galaxy has a live dark matter halo, and the satellite (Envelope+Nucleus+DM

halo) also, so the dynamical friction of the orbit is properly taken into account. We utilize different models for distinct components of the object: the Plummer model for the baryonic part and the Navarro–Frenk–White profile for the dark matter component.

Plummer Model

This spherical model, developed by Plummer in 1911, naturally appears from the exploration of the distribution of stars within globular clusters.
The density profile is given by:

$$\rho_{pl} = \frac{3M}{4\pi a^3}\left(1+\frac{r^2}{a^2}\right)^{-5/2} \tag{3.1}$$

Here, M is the total mass, a is the scale length and r is the radius.
The potential of the Plummer model is given by:

$$\Phi_{pl} = -\frac{GM}{\sqrt{r^2+a^2}} \tag{3.2}$$

Navarro–Frenk–White profile

The Navarro–Frenk−White profile (NFW) was named after the authors Julio Navarro, Carlos Frenk and Simon White (Navarro, J. et al 1996). In their study they perform N-body simulations and fit the DM halos in the standard CDM cosmology.

The density profile is given by:

$$\rho_{\mathrm{NFW}}(r) = \frac{\rho_0}{\frac{r}{R_s}\left(1+\frac{r}{R_s}\right)^2} \tag{3.3}$$

Here ρ_0 is the central density and R_s is the scale length radius.

The potential of the NFW profile is :

$$\Phi_{\mathrm{NFW}}(r) = -\frac{4\pi G\rho_0 R_s^3}{r} ln\left(1+\frac{r}{R_s}\right) \tag{3.4}$$

In Figure 3 of Navarro et al. (1996), fitting data is shown using a model proposed by Navarro et al. (1995c):

$$\frac{\rho_{\mathrm{NFW}}(r)}{\rho_{crit}} = \frac{\delta_c}{\frac{r}{R_s}\left(1+\frac{r}{R_s}\right)^2} \tag{3.5}$$

Where,

$$R_s = \frac{r_{200}}{c} \tag{3.6}$$

and ρ_{crit} is the critical density given by:

$$\rho_{crit} = \frac{3H^2}{8\pi G} \tag{3.7}$$

c (the 'concentration on the halo) and δ_c (the characteristic overdensity) are dimensionless parameters, that have to do with that the mean density within the radius r_{200} has to be $200 \times \rho_{crit}$.:

$$\delta_c = \frac{200}{3} \frac{c^3}{ln(1+c) - \frac{c}{1+c}} \tag{3.8}$$

The mass of the halo is given by:

$$M_{200} = 200\ \rho_{crit}\ r_{200}^3\ \frac{4\pi}{3} \tag{3.9}$$

3.1.2 Parameters and orbits

As an initial approach, we vary the number of particles, the scale length of the halo, the Plummer radius of the baryonic part, as well as the mass and the grids to explore different resolutions and to test how different the merging times are - this gives information on how well-resolved the dynamical friction is.

To explore the merger rates we perform first simulations with circular orbits, with the dE orbiting the big object representing the galaxy cluster. These orbits are obtained following the orbital velocity equation :

$$v^2 = GM\left(\frac{2}{r} - \frac{1}{a}\right) \tag{3.10}$$

Where v is the orbital velocity, G is the gravitational constant, M is the mass of the central object, r is the radius of the orbit and a is the semi-major axis of the trajectory. For a circular orbit the a value is fixed to be r so :

$$v^2 = \frac{GM}{r} \tag{3.11}$$

The velocities for a circular orbit are displayed in Table 3.1. In the table, "Mass" represents the mass of the host object, "Radius" indicates the distance to the center of

Mass[$\odot$]	10^{14}	10^{15}	10^{14}
Radius[kpc]	100	100	200
Velocity[km s^{-1}]	2074	6574	1467

Table 3.1: Velocities of the orbiting object for a circular orbit. Mass is the mass of the host object, Radius is the distance to the center of the orbiting object and Velocity is the initial velocity for a circular orbit. Source: this work.

the orbiting object, and "Velocity" denotes the initial velocity required for the orbiting object to follow a circular orbit.

The parameters are varied to explore the behaviour of the objects in the simulation shown in Table 3.2. The dark matter halo and baryonic part of the big object, representing a Virgo like galaxy cluster, are named haloH and PlummerH, respectively (Host). And the dark matter halo and the baryonic part of the dwarf elliptical are named as haloO and PlummerO, respectively (Orbiting).

Object	Particles [10^6]	Scale length [kpc]	R_{200} [kpc]	Mass [$\odot$]	Grid 1 [kpc]	Grid 2 [kpc]	Grid 3 [kpc]
haloH	10	32	983	10^{15}, 10^{14}	50	250	1500
PlummerH	10	16.22		10^{14}, 10^{12}	30, 15	200, 90	1500
haloO9	1, 10	1	1	10^9	0.5, 0.9, 15, 20	1, 10, 40, 70	1500
haloO7	10	4	9.83	10^8	8	30	1500
haloO8	10	4	21.19	10^9	3	50	1500
halo12	10	1	9.83	10^8	0.9	40	1500
PlummerO2	10	1		10^7	0.5	5	1500
PlummerO3	10	0.85		10^8	0.5	5	1500
PlummerO4	10	1		10^8	0.5	5	1500
PlummerO5	10	0.85		10^7	0.5	5	1500
PlummerO6	10	0.85		10^9	0.5	5	1500

Table 3.2: Parameters of the simulations for the ' Testing stage'. The dark matter halo and baryonic part of the host big object representing the Virgo like galaxy cluster, are named haloH and PlummerH, respectively (Host). And the dark matter halo and the baryonic part of the dwarf elliptical are representing as haloO and PlummerO, respectively (Orbiting). Source: this work.

Results

In the simulations, we determine whether the objects merge using a distance criterion; if the distance between objects is sufficiently small, we consider them to be one object. Or, if the mass of the orbiting object during the simulation decreases to less than 10% of its initial mass due to a destroyed and dissolved process of the small galaxy into the host galaxy.

The merger time rates according to different resolutions and distance of the center of the host galaxy are shown in Table 3.3, columns represent the initial distance of the orbiting object (Radial distance), the initial velocity of the object ($v_{initial}$), the 3 different resolution grids (Grid 1, 2, 3) and the time that requires the orbiting object to merger with the central object (T_{merger}). For cases where the objects do not merge, the last column presents the percentage of particles bound to the object at that specified time. All the

Plummer parts have grids of 0.5, 5 and 1500 [kpc], for the grid 1, 2 and 3, respectively. The values for the grids displayed in the table are those set in the simulation.

Sim	Radial Distance [kpc]	$v_{initial}$ [km s^{-1}]	Grid 1 [kpc]	Grid 2 [kpc]	Grid 3 [kpc]	T_{merger} [Myr]
Sim6	100	2084.48	0.5	10	1500	117
Sim9	500	927.5	20	40	1500	228364(16%)
Sim9b	500	927.5	0.5	40	1500	84641
Sim10	100	2074.12	20	40	1500	149
Sim11	200	1466.62	20	40	1500	727
Sim12	700	783.94	20	40	1500	226212(33%)
Sim13	900	691.37	20	40	1500	255363(49%)

Table 3.3: Merger time rates according to different resolutions and distance of the center of the host galaxy. Columns represent the initial distance of the orbiting object (Radial distance), the initial velocity of the object ($v_{initial}$), the 3 different resolution grids (Grid 1, 2, 3) and the time that requires the orbiting object to merger with the central object (T_{merger}). Source: this work.

We can deduce the optimal grid parameters as follows:

- For the Plummer component, the recommended grid sizes are 0.5 kpc for grid 1 and 5 kpc for grid 2.
- For the dark matter component, the grid selection goes from 0.5 to 20 for grid 1 and 10 to 40 for grid 2.

These grids may vary in the next chapters based on different masses within each object. For grid 3, a fixed size of 1500 kpc is recommended. Simulations with large circular orbits indicate that the dynamical friction could not be sufficiently strong to merge the objects within a realistic time frame.

3.1.3 Finding the grids of the nucleus of dE

We explore different grid configurations for the nucleus of the dEs to determine the optimal parameters for r_{pl}= 0.01 [kpc] and Mass=2.56 $\times 10^6[\odot]$. Details of all test simulations can be found in Table 3.4 and Table 3.5. The columns present the simulation name, different grid levels, and the behavior of the Lagrangian radius plot, respectively. Additionally, simulation names are appended with 'a' for dt=0.15, 'b' for dt=0.1, and 'c' for dt=0.8. The simulation that show better behaviour for the Lagrangian radius plot after some Gyr is 'Plnucleus12b' with grid 1= 0.001, grid 2= 0.1, grid 3= 1500 and a dt of 0.1 [Myr]. So all our simulations contain this object in the center of the baryonic part of the dE. Also, the time step (dt) for all simulations is set to 0.1 [Myr].

Sim	Grid 1 [kpc]	Grid 2 [kpc]	grid 3 [kpc]	behaviour
Plnucleus1	0.1	5	1500	bad
Plnucleus2	0.01	5	1500	NaN
Plnucleus3	0.005	5	1500	Nan
Plnucleus4	0.005	1	1500	medium
Plnucleus5	0.005	20	1500	Nan
Plnucleus6(b)	0.005	2	1500	Nan
Plnucleus7(b)	0.008	1	1500	medium
Plnucleus8	0.005	3	1500	Nan
Plnucleus9(b)	0.008	1.5	1500	bad
Plnucleus10	0.005	0.1	1500	bad
Plnucleus11	0.008	0.1	1500	bad
Plnucleus12(b)(c)	0.001	0.1	1500	bad(Good)(Nan)
Plnucleus13	0.005	0.5	1500	bad
Plnucleus14	0.008	0.5	1500	bad
Plnucleus15	0.008	0.08	1500	bad
Plnucleus16(b)(c)	0.009	0.9	1500	medium(medium)(bad)
Plnucleus17	0.01	0.1	1500	bad

Table 3.4: The parameters for these simulations are: r_{pl}=0.01 [kpc], Mass=$2.56x10^6 M_\odot$. Columns are the name of the simulation, the different grid levels and the behavior of the Lagrangian radius plot, respectively. Also in the name of the simulation "a" is associated a dt=0.15, (b) dt=0.1, and (c) dt=0.8. Source: this work

Sim	Grid 1 [kpc]	Grid 2 [kpc]	grid 3 [kpc]	behaviour
Plnucleus18(b)(c)	0.01	1	1500	medium
Plnucleus19(b)	0.005	0.05	1500	bad
Plnucleus20	0.009	1	1500	medium
Plnucleus21	0.009	1.5	1500	bad
Plnucleus22	0.001	1	1500	Nan
Plnucleus23	0.0009	1	1500	Nan
Plnucleus24(c)	0.005	0.8	1500	medium(bad)
Plnucleus25	0.001	0.9	1500	Nan
Plnucleus26	0.0008	1	1500	Nan
Plnucleus27	0.0008	0.8	1500	Nan
Plnucleus28(c)	0.005	0.9	1500	medium(bad)
Plnucleus29	0.001	0.8	1500	medium
Plnucleus30(b)	0.01	0.05	1500	bad
Plnucleus31c	0.01	0.9	1500	bad
Plnucleus32b(c)	0.009	0.8	1500	medium(bad)
Plnucleus33c	0.009	0.7	1500	bad
Plnucleus34c	0.01	0.7	1500	bad
Plnucleus35c	0.01	0.8	1500	bad
Plnucleus36b(c)	0.005	0.7	1500	medium(bad)

Table 3.5: In this simulations the parameters are: Plummer radius=0.01 kpc, Mass=2.56x10^6. Columns are the name of the simulation, the different grid levels and the behavior of the Lagrangian radius plot, respectively. Also in the name of the simulation "a" is associated a dt=0.15, (b) dt=0.1, and (c) dt=0.8. Source: this work.

3.2 Simulations dEs-UCDS

3.2.1 Setup

Our simulations have two main objects, the larger object representing the galaxy cluster which is the host and the smaller satellite which is the dE.
he central large object is set by an analytical potential of the dark matter part (NFW profile) and the baryonic part(Plummer profile) also the dynamical friction that experiences the orbiting object is added in an analytical form in SUPERBOX.

The simulations in this section have an orbiting object composed of a dark matter component (NFW profile) and a baryonic component (Plummer profile), consisting of a nucleus and an 'envelope' of stars.
The parameters varied to explore the behaviour of the objects in the simulation are shown in Table 3.7. The dark matter halo and baryonic part of the big object, representing a Virgo like galaxy cluster, are named haloH and PlummerH, respectively (Host). And the dark matter halo, the nucleus and the envelope part of the dE are named as haloO, Nucleus and PlummerO, respectively (Orbiting). The nucleus parameters are labels as P_{nucleus}.
Similar to section 3.3 of W. Oehm et al (2017) the correlation between the masses of the baryonic component and the dark matter (DM) halo of the satellite was determined according to Behroozi, Wechsler, and Conroy (2013). In their study, a ratio of the order of 100:1 is observed, as depicted in the left panel of fig 7, illustrating the derived stellar mass as a function of halo mass (Behroozi, Wechsler, and Conroy 2013).
On the relations of the masses for the nucleus and the envelope part of the satellite we consider the relation showed in fig 19 of R.Capuzzo-Dolcetta & I. Tosta e Melo 2017, were a relation of the order of 1:100 is also showed.

The components of the two objects and the varied parameters are displayed in summary Table 3.7.

Object	Particles[10^6]	Scale length[kpc]	R_{200}[kpc]	Mass[$\odot$]	Grid 1	Grid 2	Grid 3
haloH		32	983	10^{14}			
PlummerH		16.22		10^{12}			
haloc9	10	1	21.19	10^9	0.9	40	1500
halo07	10	4	9.83	10^8	8	30	1500
halo08	10	4	21.19	10^9	3	50	1500
halo12	10	1	9.83	10^8	0.9	40	1500
halo13	2	1	45.66	10^{10}	0.9	50	1500
haloc14	2	1	21.19	10^9	0.9	40	1500
halo15	2	1	9.83	10^8	0.9	40	1500
halo16	2	4	21.19	10^9	3	50	1500
halo17	2	4	45.66	10^{10}	3	50	1500
Plummer02	10	1		10^7	0.5	5	1500
PlummerO3	10	0.85		10^8	0.5	5	1500
PlummerO4	10	1		10^8	0.5	5	1500
PlummerO5	10	0.85		10^7	0.5	5	1500
PlummerO7	2	0.85		10^8	0.5	5	1500
PlummerO8	2	0.85		10^7	0.5	5	1500
Plummer09	2	1		10^7	0.5	5	1500
Plummer10	2	1		10^8	0.5	5	1500
$P_{nucleus}$	1	0.01		2.56×10^6	0.01	0.1	1500

Table 3.6: Parameters of the object in the simulations UCD-dEs. The dark matter halo, and baryonic part of the host big object representing the Virgo like galaxy cluster, are named haloH and PlummerH, respectively, and are set up analytically in SUPERBOX. The dark matter halo, the nucleus and the envelope part of the dwarf elliptical are named as haloO, Nucleus and PlummerO, respectively. Source: this work.

		Particles[10^6]	Scale length[kpc]	Mass[$M_\odot$]
Host	DM_{NFW}		32	10^{14}
	$Baryonic_{Plummer}$		16.22	10^{12}
dE	DM_{NFW}	2, 10	1, 4	10^8, 10^9, 10^{10}
	$Envelope_{Plummer}$	2, 10	0.85, 1	10^7, 10^8
	$Nucleus_{Plummer}$	1	0.01	2.56×10^6

Table 3.7: Parameters for all the components on the simulation, Host show the parameters for the Virgo like galaxy cluster, the DM part and the baryonic part. dE show the parameters for the three component of the dE, the DM part, the envelope part and the nucleus. Source: this work.

3.2.2 Orbits and parameters of simulations

We want to investigate elliptical orbits with different pericenter distance.
In order to obtain the initial velocity that the dwarf elliptical has to have we consider the conservation of the energy in the extremes.

$$
\begin{aligned}
E_p &= E_a \\
\frac{v_p^2}{2} + \Phi(r_p) &= \frac{v_a^2}{2} + \Phi(r_a) \\
\frac{1}{2}(v_p^2 - v_a^2) &= \Phi(r_a) - \Phi(r_p) \\
\frac{L^2}{r_p^2} - \frac{L}{r_a^2} &= 2(\Phi(r_a) - \Phi(r_p)) \\
L^2(\frac{r_a^2 - r_p^2}{r_p^2 r_a^2}) &= 2(\Phi(r_a) - \Phi(r_p)) \\
L^2 &= \frac{2(\Phi(r_a) - \Phi(r_p))(r_p^2 r_a^2)}{r_a^2 - r_p^2} \\
L &= r_p r_a \sqrt{\frac{2(\Phi(r_a) - \Phi(r_p))}{r_a^2 - r_p^2}} \\
v_0 = \frac{L}{r_a} &= r_p \sqrt{\frac{2(\Phi(r_a) - \Phi(r_p))}{r_a^2 - r_p^2}}
\end{aligned}
$$

With the radius at the apocenter (r_{apo}), pericenter (r_{peri}), and the potential that the orbiting object experiences($\Phi(r)$) we can obtain the initial velocity(v_0). The potential at a fixed radius is the sum of the NFW potential and the Plummer potential at that radius. For this values we obtain the velocities presented in Table 3.8.

r_a[kpc]	250	250	250	250	250	250	250	250	250
r_p[kpc]	240	200	100	50	20	10	5	2	0.5
Velocity[km s^{-1}]	954.07	865.73	605.89	387.57	190.52	103.7	54.41	22.5	5.68

Table 3.8: Initial Velocities of the orbiting object for a elliptical orbit at a fixed apocenter (r_a) and pericenter (r_p) distance. Source: this work.

The parameters of the simulations are displayed in Table 3.9 and Table 3.10. In Table 3.9 the dark matter part and 'envelope' of the dwarf galaxy are built by 10.000.000 particles and the nucleus by 1.000.000 and in Table 3.10 the dark matter part and 'envelope' of the dwarf galaxy are built by 2.000.000 particles and the nucleus by 1.000.000. The $r_{nucleus,pl} = 0.01$ [kpc] and the $Mass_{nucleus} = 2.56 \times 10^6 M_\odot$ in all simulations. Also for all sets of parameters we perform 3 simulations of each 9 different pericenter distances for the orbits: 240, 200, 100, 50, 20, 10, 5, 2, 0.5 [kpc]. The apocenter distance is 250 [kpc] in all orbits. You can see the simulations parameters in more detail in Appendix section 6.1. In the tables we show the scale length, the R_{200}, and the Mass of the dark matter halo followed by the plummer radius (r_{pl}), and the mass of the envelope.

he satellites b, j, and k closely resemble dEs, exhibiting correct ratios between the dark matter (DM) halo and the envelope (100:1), as reported by Behroozi, Wechsler, & Conroy (2013), as well as between the nucleus and the envelope (1:100), according to R. Capuzzo-Dolcetta & I. Tosta e Melo (2017). Other satellites are studied to expand the parameter range of mass and size, with the goal of replicating various small stellar systems.

Sim	DM halo Scale length [kpc]	R_{200} [kpc]	Mass $M_\odot$	Plummer r_{pl} [kpc]	Mass $M_\odot$
C	1	9.83	10^8	0.85	10^7
D	1	21.19	10^9	0.85	10^7
E	4	21.19	10^9	0.85	10^7
F	4	21.19	10^9	1	10^7
G	1	21.19	10^9	0.85	10^8
H	4	21.19	10^9	0.85	10^8
I	4	21.19	10^9	1	10^8

Table 3.9: Simulation parameters, the dark matter part and 'envelope' of the dwarf galaxy is built by 10.000.000 particles and the nucleus by 1.000.000. The $r_{nucleus,pl} = 0.01$ [kpc] and the $Mass_{nuclei} = 2.56 \times 10^6 M_\odot$ in all simulations. Also for all sets of parameters we perform 3 simulations of each 9 different pericenter distances for the orbits: 240, 200, 100, 50, 20, 10, 5, 2, 0.5 [kpc]. The apocenter distance is 250 [kpc] in all orbits. Source: this work.

Sim	DM halo Scale length [kpc]	R_{200} [kpc]	Mass $M_\odot$	Plummer r_{pl} [kpc]	Mass $M_\odot$
a	1	45.66	10^{10}	0.85	10^7
b	1	45.66	10^{10}	0.85	10^8
c	1	9.83	10^8	0.85	10^7
d	1	21.19	10^9	0.85	10^7
e	4	21.19	10^9	0.85	10^7
f	4	21.19	10^9	1	10^7
g	1	21.19	10^9	0.85	10^8
h	4	21.19	10^9	0.85	10^8
i	4	21.19	10^9	1	10^8
j	4	45.66	10^{10}	0.85	10^8
k	4	45.66	10^{10}	1	10^8

Table 3.10: Simulation parameters, the dark matter part and 'envelope' of the dwarf galaxy is built by 2.000.000 particles and the nucleus by 1.000.000. The $r_{nucleus,pl} = 0.01$ [kpc] and the $Mass_{nucleus} = 2.56 \times 10^6 M_\odot$ in all simulations. Also for all sets of parameters we perform 3 simulations of each 9 different pericenter distances for the orbits: 240, 200, 100, 50, 20, 10, 5, 2, 0.5 [kpc]. The apocenter distance is 250 [kpc] in all orbits. Source: this work.

3.2.3 Results

In most simulations the dark matter halo of the orbiting galaxy gets stripped first by the host galaxy and then the baryonic part begins to get stripped.
To determine when a component of the orbiting dwarf is regarded as completely stripped or destroyed, we apply the criterion that the bound particles determined by SUPERBOX are below 10%.

Also, we consider a lower mass limit for UCDs of $2{\times}10^6 M_\odot$ (Hasegan et al 2005). So, in our simulations the nucleus has to have at least 78% of the initial mass.
You can see the result of each simulation individually in the Appendix section 6.2.

Table 3.11, Table 3.12, Table 3.13 and Table 3.14 display the results of each set of simulations. Sets 'a', 'b', 'j', and 'k' represent combinations of three simulations, each with the same parameters but different seed numbers for statistical analysis. All other sets (from "c" to "i"), show the combination of 4 simulations (3 simulations with initial number of particles of 2.000.000 in the dark matter part and in the envelope of the dE, and 1 simulation with initial number of 10.000.000 particles from the same two components). Columns shown (in order), simulation time when the dark matter halo gets destroyed, the percent of the envelope part when the dark matter halo is destroyed and then the same but for the baryonic part (envelope plus nucleus), the time when the Plummer envelope gets destroyed. Then time when the object begins to be an UCDs in the simulation, the mass of the object, the position, mass to light ratio and % of the dark matter content of the object.

Sim	haloc $T_{0.1}^{DM}$ [Myr]	$M_{T_{0.1}^{DM}}^{envelope}$ %	$M_{T_{0.1}^{DM}}^{Plummer}$ %	Envelope $T_{0.1}^{envelope}$ [Myr]	Initial T [Myr]	UCDs M 10^6 $M_\odot$	Posi [kpc]	M/L	% DM_0 %
a240$^+$	9995	7	23	4938±43	9995	10^3	250	342.62	10
a200$^+$	4526±5	8	26	2971±87	4526±5	10^3	249±1	307.97	10
a100$^+$	1233±1	7±1	26±1	1133±24	1233±1	10^3	99±1	307.1±5.4	10
a50	924±1	10±1	28±1	982±10	982±10	803.2 ± 0.3	109±11	227.34	8
a20$^+$	771±1	8	27	526±14	771±1	10^3	214±1	300.9	10
a10$^+$	700±1	5±1	24	294±2	700±1	10^3	236	334.3±6.5	10
a5$^+$	667	3	23	291±2	667	10^3	242	353.8	10
a2$^+$	535±182	2±1	22±1	291±2	535±182	10^3	175±121	371.3±8	10
a0.5$^+$	310	1	21	291±2	310	10^3	1	372.2±7.3	10
b240*	-								
b200*	7416±33	50	51						
b100*	1649±1	48	49						
b50	998±1	48	49	6893±15	6893±15	102.2 ± 0.2	212±7	8.26	0.9
b20	797	47±1	48±1	2947±4	2947±4	92.5	124±5	7.39	0.8
b10	706±1	37±1	39±1	2125±1	2125±1	92.5	107±12	7.39	0.8
b5	668±1	28	30	1627±4	1627±4	92.5	139±4	7.38	0.8
b2	352±35	22±1	24±1	1132±5	1132±5	112.5	227±2	8.97	1
b0.5	310±1	17±3	19±3	917	917	112.5	14±2	8.97	1
c240*	1488±3	40	52						
c200	1293±2	38	50	7716±94	7716±94	5.5	245±3	1.56	2
c100	950±1	31	45	1882±8	1882±8	5.7 ± 0.4	190±10	1.56	2
c50	790±1	23±1	38±1	1036	1036	5.7 ± 0.4	54±1	1.56	2
c20$^+$	1151±305	7±8	26±6	923±1	1151±305	11 ± 3.6	205±86	3.8±1.5	8±4
c10	643±1	11	29	663±1	663±1	11.5	247±1	3.26	8
c5	305	26	41	458±2	458±2	10.5	195±2	2.98	7
c2	305	25±1	40±1	311	311	6.8 ± 0.5	3±1	1.9±0.1	3.3±0.5
c0.5	305	24	39	310	310	6.2 ± 1	1	1.7±0.3	3±1

Table 3.11: Results of simulations from Table 6.4. Columns shown (in order), simulation time when the dark matter halo gets destroyed, percent of the envelope part when the dark matter halo is destroyed, percent of the baryonic part (envelope plus nucleus) when the dark matter halo is destroyed, time when the Plummer envelope gets destroyed. Then time when the object begins to be an UCDs in the simulation, mass of the object, position, mass to light ratio and % of dark matter content of the object. Source: this work.

Sim	haloc $T_{0.1}^{DM}$ [Myr]	$M_{T_{0.1}^{DM}}^{envelope}$ %	$M_{T_{0.1}^{DM}}^{Plummer}$ %	Envelope $T_{0.1}^{envelope}$ [Myr]	Initial T [Myr]	UCDs M 10^6 $M_\odot$	Posi [kpc]	M/L	% DM_0 %
d240	1742±9	28±1	42	5723±581	5723±581	23.5	246±6	6.65	2
d200	1379±3	22	38	4022±124	4022±124	23.5	208±15	6.65	2
d100	991±1	19	35	1748±20	1748±20	42.8 ± 1.5	238±5	11.6±1.4	3.8±0.5
d50	842±1	14±1	31±1	1017±1	1017±1	33.5	72±2	9.48	3
d20	734±1	11	29	835±2	835±2	43.5	175±2	12.31	4
d10$^+$	689	8	27	493±1	689	103.3	241	30.99	10
d5$^+$	665±1	4	23	471±1	665±1	102.7 ± 0.5	245	35.1	10
d2$^+$	647±1	2	22	306±1	647±1	102.9 ± 0.4	247	35.2±3.5	10
d0.5$^+$	307	7±4	26±3	306	307	103.4 ± 0.1	8±2	30.3±0.4	10
e240	1007±7	59	67	4829±210	4829±210	8.3 ± 0.5	249±1	2.3±0.1	0.5±0.1
e200	948±9	55±1	64±1	3269±62	3269±62	11.3 ± 0.5	246±2	3.2±0.1	0.8±0.1
e100	876±1	38	50	1568±31	1568±31	43.5	243±1	12.31	4
e50	808	30±1	42±4	1425±1	1425±1	93.5	248	26.46	9
e20$^+$	1329±24	5±2	24±2	1265±10	1329±24	103 ± 0.2	244±3	34.1±2	10
e10$^+$	724±1	6±1	25±1	656±2	724±1	103.1 ± 0.1	231	33.2±0.5	10
e5$^+$	705	2±1	22±1	549±3	705	102.7 ± 0.1	236	37.9±0.7	10
e2$^+$	694±11	0.8	21	311	694±11	102.6 ± 0.1	238±3	39.2±0.2	10
e0.5$^+$	695±1	0.3	20	310	695±1	102.5	238	39.99	10
f240	999±7	50	60	3438±61	3438±61	10.5	250±1	3	0.7
f200	938±11	45±1	56±1	2440±36	2440±36	13.3 ± 0.5	235±5	3.8±0.1	1±0.1
f100	876±1	27	42	1221±5	1221±5	11.5	100±1	3.26	0.8
f50	808±1	20±1	36±1	1040±207	1040±207	38.5±30	177±46	10.9±8.5	3.5±3
f20$^+$	1316±29	4±2	23±1	796±2	1316±29	102.9±0.2	246±3	35.8±2.1	10
f10$^+$	723	3	23	610±1	723	102.8	231	36.28	10
f5$^+$	705	1	21	312	705	102.6	236±1	38.95	10
f2$^+$	693±11	0.6	21±1	309	693±11	102.8±0.4	238±3	37.2±4.7	10
f0.5$^+$	695±1	0.2	20	309	695±1	102.4±0.3	238	40.14	10

Table 3.12: Results of simulations from Table 6.5. Same columns of the previous Table 3.11. Source: this work.

Sim	haloc $T_{0.1}^{DM}$ [Myr]	$M_{T_{0.1}^{DM}}^{envelope}$ %	$M_{T_{0.1}^{DM}}^{Plummer}$ %	Envelope $T_{0.1}^{envelope}$ [Myr]	Initial T [Myr]	UCDs M 10^6 $M_\odot$	Posi [kpc]	M/L	% DM_0 %
g240*									
g200*	4875±19	69	70						
g100*	1673±19	58	59						
g50	985±1	58	59	5828±20	5828±20	29.3 ± 0.5	169±15	1.79	1
g20	766±1	49±1	50±1	2235±1	2235±1	30±0.6	26±1	1.79	1
g10	693	41	42	1565±1	1565±1	30.5	10±1	1.79	1
g5	533±123	36±4	37±3	1230±1	1230±1	32.5	248	2.59	2
g2	310	37±1	39±1	926	926	22.5	11±2	1.79	1
g0.5	309	40	41	490±4	490±4	42.5	215±2	3.39	3
h240*	1847±8	86±1	86±1						
h200*	1415±50	85	85						
h100	935±3	76	77	5775±21	5775±21	18.5	249±1	1.47	0.6
h50	770±2	64	65	2123±4	2123±4	32.3±0.5	248±1	2.4±0.4	1.8±0.5
h20	1309±1	13	15	1387±2	1387±2	80±5	228±1	6.4±0.4	6.8±0.5
h10	574±7	40	41	1010±6	1010±6	19.5	120±8	1.55	0.7
h5	730±1	13	15	816±3	816±3	22.5	172±2	1.79	1
h2$^+$	696±17	3±1	5±1	554±1	696±17	104.2 ± 1.3	237±5	21.1±2.3	10
h0.5$^+$	696±1	0.9	3	352±1	696±1	103.4	237	30.11	10
i240*	1831±13	81	81						
i200*	1426±4	80±1	80±1						
i100	926±2	69	70	3952±15	3952±15	20.5 ± 0.1	191±56	1.6	0.8±0.1
i50	768±1	55	56	1729±2	1729±2	19.5	60±2	1.55	0.7
i20$^+$	1308	7	9	1264±1	1308	109.5	247	11.48	10
i10	601±2	30	32±1	929	929	19.5	30±5	1.55	0.7
i5$^+$	722±16	6±1	8±1	662±1	722±16	108.9 ± 0.5	228±6	12.4±0.6	10
i2$^+$	682	2	4	480±1	682	104.5	237±8	23.05	10
i0.5$^+$	696±1	0.7	3	329	696±1	103.2 ± 0.1	237	33.4±0.6	10

Table 3.13: Results of simulations from Table 6.6. Same columns of the previous Table 3.11 and Table 3.12. Source: this work.

Sim	haloc $T_{0.1}^{DM}$ [Myr]	$M_{T_{0.1}^{DM}}^{envelope}$ %	$M_{T_{0.1}^{DM}}^{Plummer}$ %	Envelope $T_{0.1}^{envelope}$ [Myr]	Initial T [Myr]	UCDs M 10^6 $M_\odot$	Posi [kpc]	M/L	% DM_0 %
j240*	1638±2	74±1	75±1						
j200*	1349±1	73	74						
j100*	958±1	72	73						
j50	809±1	69	70	3843±8	3843±8	22.5	53±4	1.79	0.1
j20	710	64±1	65±1	2221±2	2221±2	22.5	34±5	1.79	0.1
j10	668	59±1	60±1	1560±2	1560±2	13.7 ± 0.7	10±1	1.1±0.1	0.02
j5	638±1	49	50	1215±6	1215±6	145.8 ± 57.7	246	11.6±4.6	1.3±0.6
j2	306	55	56	923±1	923±1	22.5	6±1	1.79	0.1
j0.5	306	55	56	563±2	563±2	412.5	241±1	32.91	4
k240*	1630±2	67	68						
k200*	1340±1	67±1	67						
k100	955±1	65	66	8693±29	8693±29	19.4 ± 5.3	120±14	1.5±0.4	0.07±0.06
k50	808±1	61	62	3073±13	3073±13	22.5	119±12	1.79	0.1
k20	710	57	58	1918±5	1918±5	212.5	247±2	16.95	2
k10	668	51	52	1529±2	1529±2	22.5	64±3	1.79	0.1
k5	640±1	38±1	40	1012±4	1012±4	55.8 ± 5.8	138±4	4.5±0.5	0.4±0.1
k2	306	47±1	48±1	902±1	902±1	25.8 ± 5.8	51±3	2.1±0.5	0.1±0.1
k0.5	306	47	48	467±5	467±5	312.5	201±4	24.93	3

Table 3.14: Results of simulations from Table 6.7. Same columns of the previous Table 3.11, Table 3.12 and Table 3.13. Source: this work.

Orbits of UCDs

In Fig. 3.1, we show the initial time when we obtain an UCD in the simulations against the pericenter of the orbit of the dE.

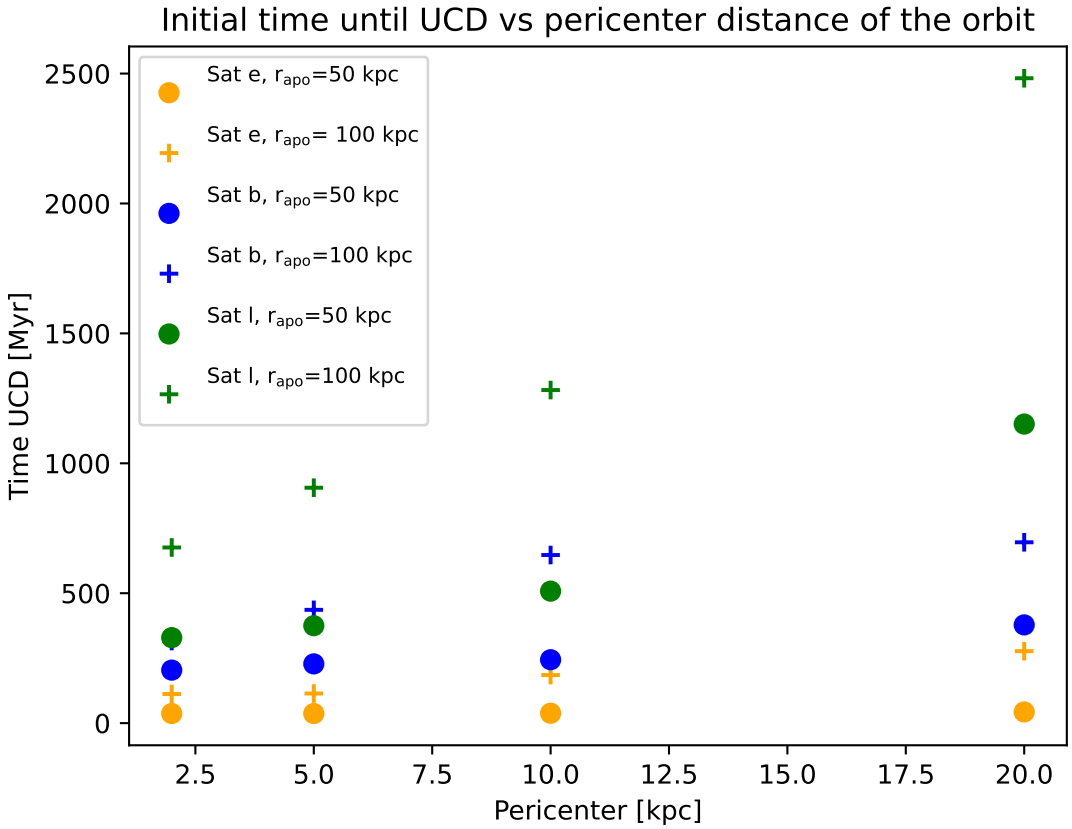

Figure 3.1: Initial time when we obtain an UCD in the simulations against the pericenter distance of the orbit of the dE. The label indicates the mass of the dark matter halo, the mass of the Plummer envelope, and the scale length radius of the dark matter, and the Plummer radius of the envelope. Data from Table 3.11, Table 3.12, Table 3.13 and Table 3.14. Source: this work.

As the dark matter halo is predominantly stripped first in the majority of simulations, it becomes evident that the crucial parameters influencing the outcome are those associated with the Plummer envelope. Simulations with smaller masses tend to be more susceptible to destruction. Simulations with the largest dark matter and Plummer envelope masses do not appear in the upper regions of the graphs, particularly at larger pericenter distances.

This observation implies that satellites with the highest mass values for the satellite and those with the more circular orbits (larger pericenter) do not transform into UCDs

over a 10 Gyr simulation period. If we see Fig. 3.1, it is apparent that, among the initial 9 sets of simulations with different pericenters, those with pericenter of 0.5, 2, 5, 10, 20, and 50 kpc consistently evolve into UCDs. However, as we reach pericenter distances of 100, 200, and 240 kpc, more massive satellites do not have sufficient time to undergo the UCD transformation.

If we analyze the sizes of different satellite components, the envelope is the most important for the evolution of the simulation, followed by the dark matter part. Larger sizes contribute to a less compact object, making it more susceptible to earlier destruction during the simulation. Therefore, the order of importance for the parameters is as follows: the mass of the Plummer envelope (larger masses require more time for UCD formation), followed by the r_{eff} of the Plummer envelope (larger sizes result in a less compact object that is more easily destroyed), and finally, the size of the dark matter part.

If we compare simulations from the 'b' satellite from Table 3.10 (Dark matter mass: $10^{10}[M_{\odot}]$, Scale Length: 1 [kpc], and envelope mass:$10^{8}[M_{\odot}]$, r_{eff}:0.85 [kpc]), with simulations with the 'f' satellite (Dark matter mass: $10^{9}[M_{\odot}]$, Scale Length: 1 [kpc] and envelope mass:$10^{8}[M_{\odot}]$, r_{eff}:0.85 [kpc]), where the only difference lies in the dark matter mass, we observed nearly identical results for the smallest pericenter distances, particularly in the time it takes for the dE to transform into an UCD. However, as pericenter values increase, distinctions become apparent, with simulations featuring a more massive dark matter halo take longer to transition a dE into an UCD.

Another interesting result is, simulations involving the 'a' satellite (Dark matter mass: $10^{10}[M_{\odot}]$, Scale Length: 1 [kpc], and envelope mass:$10^{7}[M_{\odot}]$, r_{eff}:0.85 [kpc]) generally exhibit the Plummer part being destroyed earlier than the dark matter halo, and in some instances, simultaneously. This behaviour may be attributed to the significant difference between the masses of the dark matter halo ($10^{10}M_{\odot}$) and Plummer-envelope part($10^{7}M_{\odot}$). The occurrence of this unusual behaviour is observed in some instances of other sets of satellites, but only for orbits with smaller pericenters. This may be attributed to the high potential experienced by the satellite as it travels through the densest part of the host, leading to a rapid loss of particles.

If we analyze when we successfully obtain an UCD in Fig 3.1 it is useful to demarcate 3 regions in the plot. First, in the lower segment, we encounter objects exhibiting smaller effective radii similar to globular clusters, potentially leading to misidentification. Second, satellites situated in the upper parts of the plot do not have enough time to transition into UCDs within the 10 Gyr simulation period. Finally, the third region are the objects located in the central part of the plot, which can be designated as UCDs

Fig. 3.2 shows the pericenter value of the orbit against the position when the satellite begins to be an UCD. It does not show a clear correlation between that two parameters but one interesting thing to notice is shown more clearly in the histogram Fig. 3.3. Here it is clearly shown that in most of the simulations the satellite turns into an UCD at a distance close to the center of the host -due to the strong potential in that area-, and in the outer part of the orbit, this is near to the apocenter values, this is because according to the second law of Kepler the velocity of the object is smaller near to the apocenter so the probability to obtain the object is larger in that position, because objects spend most of their time around the apocenter.

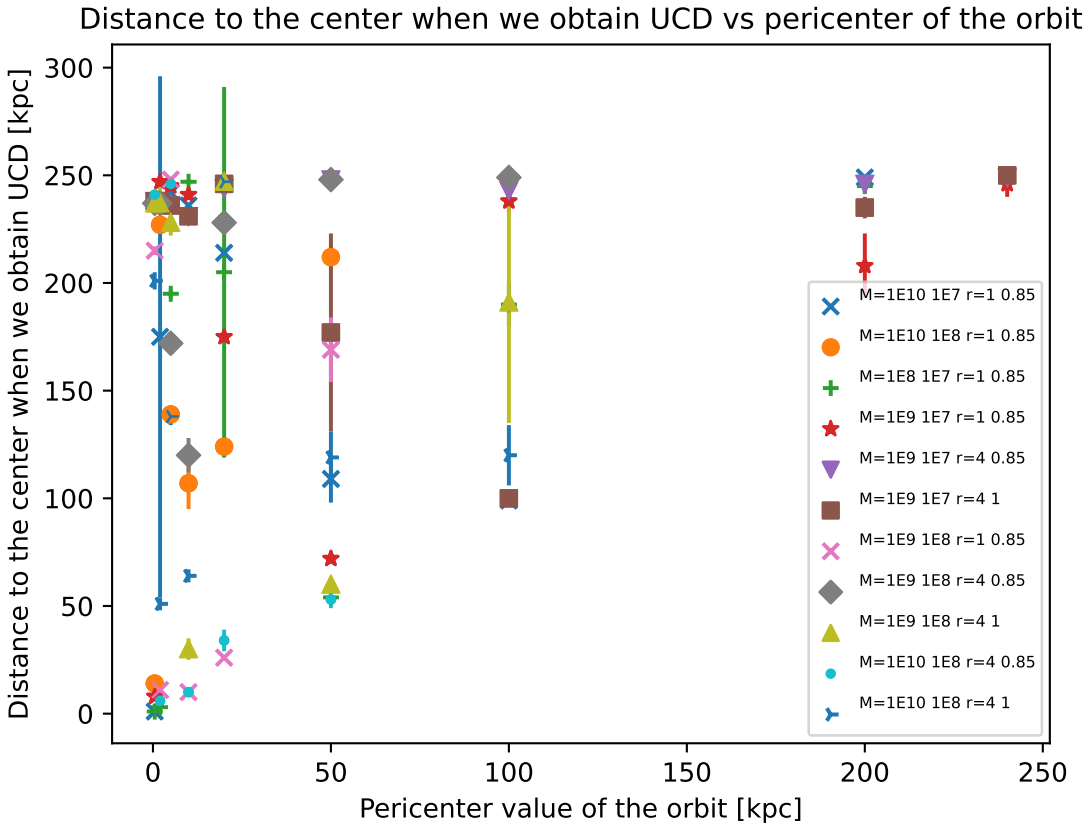

Figure 3.2: Pericenter value of the orbit against the position when the satellite begins to be an UCD. Data from Table 3.11, Table 3.12, Table 3.13 and Table 3.14. Source: this work.

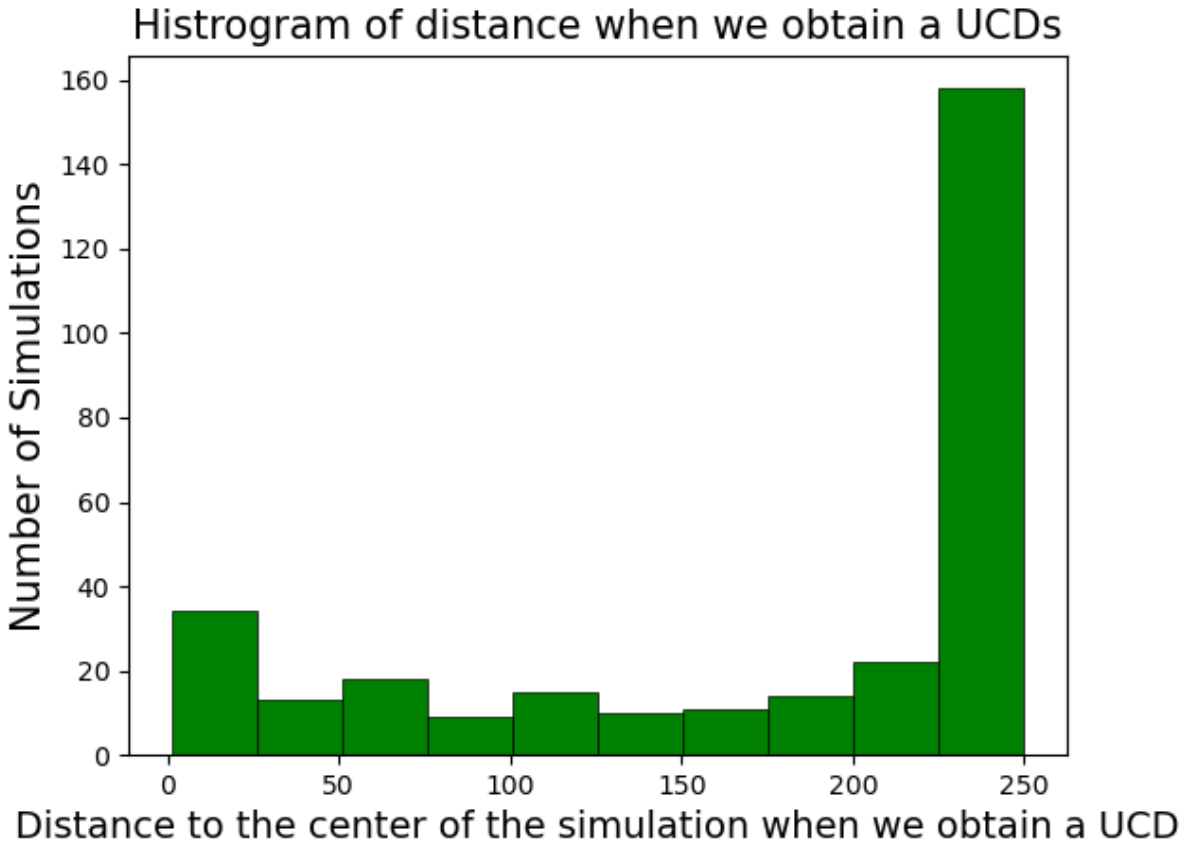

Figure 3.3: Histogram of pericenter value of the distance to the center of the host galaxy at the time the object get stripped into an UCD. Data from Table 3.11, Table 3.12, Table 3.13 and Table 3.14. Source: this work.

In summary: in most simulations, the dE,N turns into an UCD and the DM halo gets stripped first. Further evolution is governed by the parameters of the stellar envelope. Massive dE,N either need close pericenter passages or very long evolution times to turn into UCDs(see Fig. 3.1).
On eccentric orbits, objects spend most of their orbital period close to apocenter. So even though it is the pericentric passages that do the damage to our objects, the objects need time to lose mass and transform into UCDs further out i.e. closer to their apocenter(see Fig. 3.2). Also most UCDs are found close to the apocenter distance today (see Fig. 3.3). We see the following order of importance of our starting parameters: pericenter distance, mass of stellar envelope, size of stellar envelope, size of DM halo.

DM halo

Now, if we analyze the behaviour of the masses and time of the dark matter content of the satellite we can plot in Fig. 3.4, the time when the dark matter part of the dE is destroyed against the pericenter distance of the galaxy in each orbit.

An evident trend is apparent with larger pericenter values in the orbit, where we observe a latest destruction of the DM halo of the satellite. This delay can be attributed to the fact that, similar to the envelope, most destruction occurs near the host where the density is higher. Then, the mass of the halo is the second more important parameters to determinate the time when the halo gets destroyed. Higher masses result in later destruction of the halo. Additionally, the scale length of the halo becomes important; larger scale lengths (4 [kpc]) lead to earlier destruction compared to smaller scale lengths (1 [kpc]). This is due to the fact that, the two objects have the same mass, so objects with larger scale lengths have lower densities compared to the ones with smaller scale lengths.

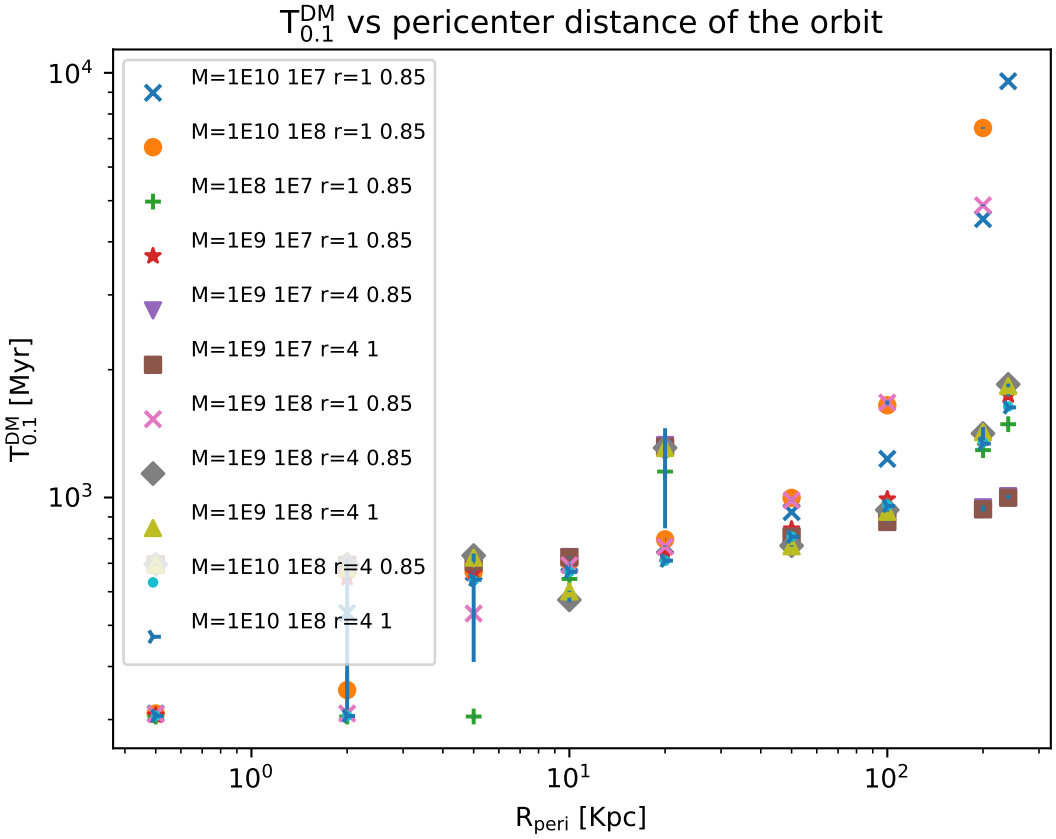

Figure 3.4: Time when the dark matter halo of the dE is destroyed vs pericenter of the orbit. Data from Table 3.11, 3.12, 3.13 and 3.14. Source: this work.

Analyzing the nucleus mass when the dark matter halo is destroyed, we observe that the nucleus retains between 98% and 99% of its initial mass/particles. Moreover, the dark matter component's mass becomes negligible once the UCD forms. The particles of the nucleus begins to be stripped mostly while the envelope mass is being stripped, and once the envelope is destroyed, the nucleus starts to experience the maximum stripping effect, causing its mass to decline more rapidly until the end of the simulation.

UCDs getting destroyed

Table 3.15 shows the time when the object has a mass below the UCD limit ($2 \times 10^6 M_\odot$), the distance from the host center, the mass-to-light (M/L) ratio, and the percentage of initial dark matter content remaining. Notably, all simulations in this table have a

pericenter distance of 0.5 [kpc]. The position when the UCDs reaches the lower mass limit is near to the center where the density of the host is bigger. This is because most particles in the nucleus are very bound and the loss of the particles (so the mass) occurs mostly when the satellite passes near the center of the potential, i.e. is in pericenter distance. Further away the object loses considerably less particles, per time.
When our objects have masses below the UCDS threshold we note that the DM particles are 100% stripped implying a M/L ratio of 1.

Sim	Nucleus T [Myr]	Final Posi [kpc]	UCDs M/L	% DM_0 %
Sima	6424	13	1	0
Simb	6448	21	1	0
Simc	6527	1	1	0
Simd	7717	3	1	0
Sime	6151	60	1	0
Simf	5921	50	1	0
Simg	7141	17	1	0
Simh	6508	3	1	0
Simi	6510	15	1	0

Table 3.15: We present the propoerties of the object when it reaches the lower mass limit for UCDs (in order): Time , distance to the center of the host, M/L ratio and % of the initial content of dark matter in the satellite. Source: this work.

Other characteristic of the UCD (shape, r_{eff}, Σ_0, σ_0)

Next criteria to see if we have an UCDs is to analyze the shape and internal parameters like r_{eff}, Σ_0, σ_0.

The data points for r_{eff}, Σ_0 and σ_0 are obtained with an IDL script. We give to the script in IDL the position and velocities of every particles in the final object. This IDL script take the position of all particles in the final object and make a position map count-

ing the number of particles inside each pixel, which gives us the mass/arcsec^2. With the M/L that we choose in the script (in this case 1), we transform these values to luminosities and magnitudes. In this way IDL is able to make diagrams of surface brightness with color bars.
This IDL script also produces radial profiles of surface brightness and line of sight velocity dispersion, taking the medium value inside concentric circles that begins in the center of the object (0 pc) and increase its radius, until a chosen distance in the script (in this case 1.5 kpc).

In Fig 3.5, we present three examples illustrating the characteristics of the final object up to a radius of 1.5 kpc. The only difference between the three subfigures is the pericenter distance of the orbit. The upper figure shows an example of a satellite that, after 10 Gyr, is no longer an UCD (lower left side of Fig. 3.1). The middle figure shows an example of an UCD (middle part of Fig. 3.1), while the bottom figure shows an example of an object transitioning into an UCD after 10 Gyr of simulation (upper right part of Fig 3.1).
Each figure consists of three panels: the left panel displays the shape of the final object with a color bar indicating the magnitude of the surface brightness, the center panel shows the surface brightness as a function of radius/distance from the centre of the satellite, and the right panel presents the velocity dispersion. The pericenter distance of the orbit (R_{peri}) and the simulation time at which the dE transitions into an UCD (T_{int}^{UCD}) are shown under each set of images.
The first upper subfigure shows an object that can be considered as a globular cluster based on its structural parameters. This is because, although the dE transitions into an UCD 467 [Myr] after starting the simulation (this is shortly after the first pericenter passage (CPP)) the satellite undergoes an additional 15 CPPs during the rest of the simulation. This leads to a significant loss of mass, resulting in the parameters we observe at the end of the simulations. In the middle panel, we observe an UCD located 220 [kpc] away from the center of the host galaxy. This UCD has experienced 14 close pericenter passages before showing the structural parameters illustrated in the figure. In the last bottom figure, the satellite gets his DM halo destroyed , but it did not loose the 90 % of

the initial bound particles of the envelope during the 10 Gyr duration of the simulation. The presence of tidal tails around the object indicates that the stripping process is still occurring. The position of this object is 247 [kpc], so it is very close to its apocenter, which can be clearly seen in the figure of the following section of Tidal Tail. Additional examples can be found in Appendix 6.3.

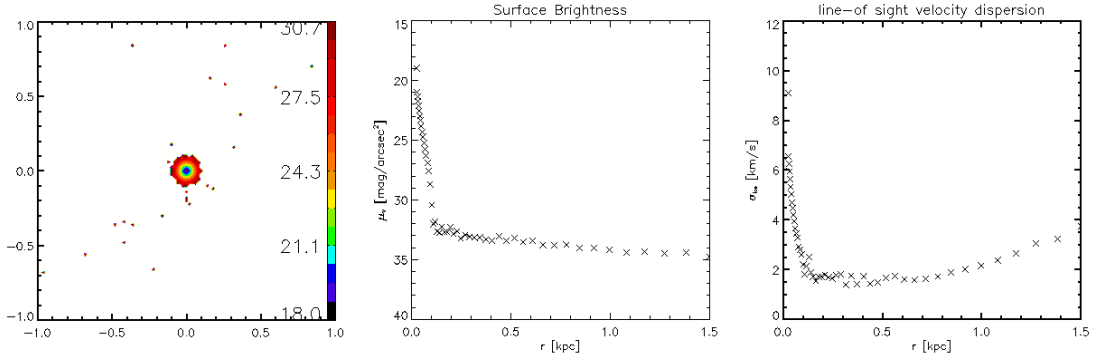

(a) kkk0.5: R_{peri}= 0.5[kpc], T_{int}^{UCD}= 471 [Myr]

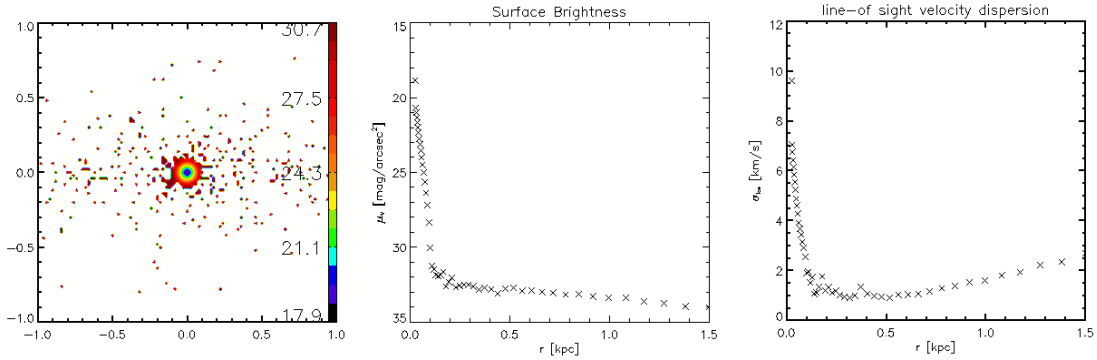

(b) kkk50: R_{peri}= 50[kpc], T_{int}^{UCD}= 3059 [Myr]

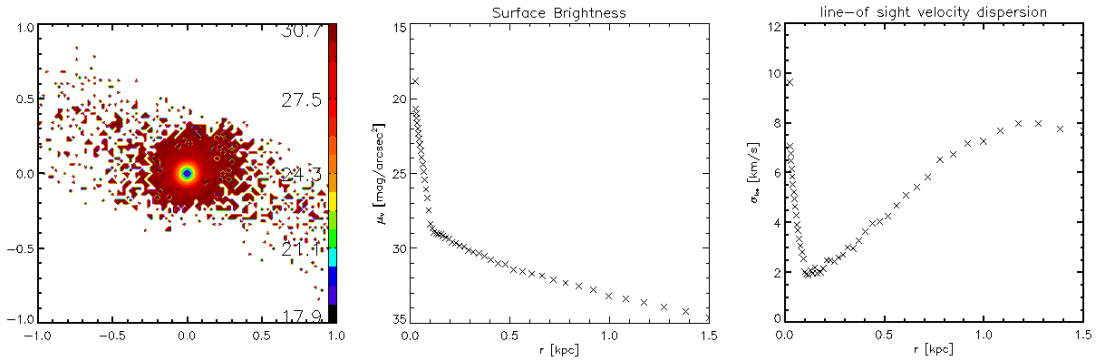

(c) kkk200: R_{peri}= 200[kpc], T_{int}^{UCD}= 8697 [Myr]

Figure 3.5: Properties of the final object up to a radius of 1.5 kpc, the left panel is the shape of the final object with the surface brightness magnitude shown in the colorbar, the center panel is the plot of the surface brightness and the right panel is the velocity dispersion. Set of "kkk" simulations (SL^{DM}=4 [kpc], M^{DM}=10^{10}[$M_\odot$], $R_{eff}^{envelope}$= 1 [kpc], $M^{envelope}$=$10^8 M_\odot$). The pericenter distance of the orbit (R_{peri}) and the simulation time at which the dE transitions into an UCD (T_{int}^{UCD}) are shown under each set of images. Source: this work.

Tails of the Satellite

In the second region (upper part $t_{transform} > 5Gyr$) of Fig. 3.1, where the time it takes for a dE to become an UCD is plotted against the pericenter distance of the orbit, we can notice that for some sets of simulations, orbits with the biggest pericenter distance (100[kpc], 200[kpc] and 240[kpc]), do not appear in the plot because they do not have enough time to transition into an UCD. Simulations with more circular orbits show tails as we can see in Fig 3.6. In this simulations with circular orbit we observe a transition object, which is a partially stripped UCDs with a significant envelope remaining from the dE, in which tails can be observed.
In this Fig we show contour plots of different objects, at left hand side the surface brightens plot and at the right hand side the velocity dispersion plot, under each set of plots are the pericentral distance of the orbit (R_{peri}), the simulation time at which the dE transitions into an UCD (T_{int}^{UCD}), and the position of the nucleus of the object ($Posi_{fin}^{UCD}$).
It is clear that simulations with more circular orbits exhibit a tail at the end of the simulation time, since the interaction between the satellite and the host is still occurring, instead of the ones with more elliptical orbits in where the envelope is more heavily and strongly torn off from the satellite.
Simulations in where we do not obtained a UCD to the pericenter distance or the simulation time, do not result in the formation of a UCD. Instead, we observe a transition object, which is a partially stripped UCDs with a significant envelope remaining from the dE, in which tails can be observed.

Plots for object near to the center of the host display the envelope of the object in the snapshot. However, these envelope particles have clearly been stripped and are now part of the host.
In this figure we present some examples from our more extreme orbits (R_{peri}= 0.5 [kpc] and R_{peri}= 200 [kpc], R_{peri}= 240 [kpc]). Additional examples can be found in Appendix 6.4.

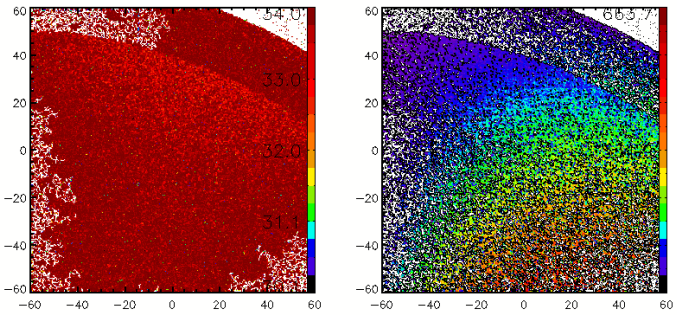

(a) kkk0.5: R_{peri}=0.5[kpc],T_{int}^{UCD}=471[Myr],$Posi_{fin}^{UCD}$=188[kpc]

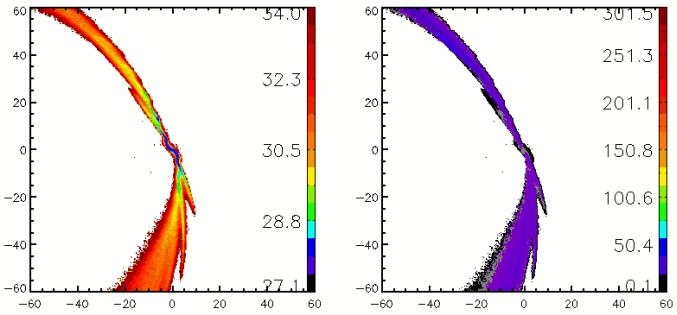

(b) kkk200: R_{peri}=100[kpc], T_{int}^{UCD}=8697[Myr], $Posi_{fin}^{UCD}$=247[kpc]

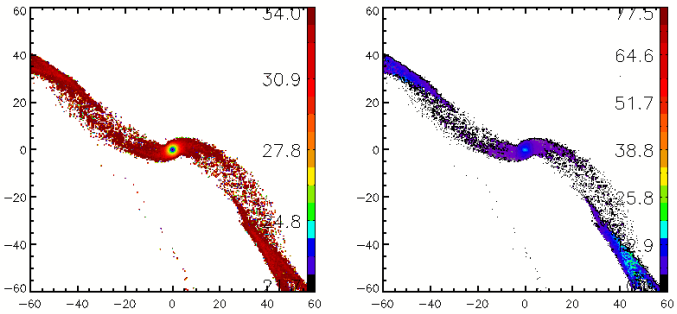

(c) kkk240: R_{peri}=240[kpc], $Posi_{fin}^{UCD}$=250[kpc]

Figure 3.6: Contour plots of different objects at left hand side the surface brightnes plot and at the right hand side the velocity dispersion plot, under each set of images is the pericentral distance of the orbit (R_{peri}), the simulation time at which the dE transitions into an UCD (T_{int}^{UCD}), and the position of the nucleus of the object ($Posi_{fin}^{UCD}$). The axes are in units of kiloparsecs. Set of "kkk" simulations (SL^{DM}=4 [kpc], M^{DM}=10^{10}[$M_{\odot}$], $R_{eff}^{envelope}$= 1 [kpc], $M^{envelope}$=10^{8}[$M_{\odot}$]). Source: this work.

In Table 3.16, Table 3.17, Table 3.18, and Table 3.19, we present the structural parameters of the objects at the end of the simulation. Therefore, after 10 Gyr, some objects may no longer be classified as UCDs. Each table presents the effective radius, central surface brightness, central velocity dispersion, and velocity dispersion at 100 pc for both the nucleus and the baryonic part (which is the nucleus plus the envelope). Additionally, the final position of the object and the number of close pericenter passages are displayed in the last two columns.

Sim	$r_{eff}^{nucleus}$ [pc]	$\Sigma_0^{nucleus}$ [mag/arcsec^2]	$\sigma_0^{nucleus}$ [km/s]	$\sigma_{100}^{nucleus}$ [km/s]	$r_{eff}^{baryonic}$ [pc]	$\Sigma_0^{baryonic}$ [mag/arcsec^2]	$\sigma_0^{baryonic}$ [km/s]	$\sigma_{100}^{baryonic}$ [km/s]	$Posi_{10Gyr}$ [kpc]	CPP
a240$^+$	10	17.978	16.384	9.167	45	17.474	20.01	10.17	250	-
a200$^+$	9	17.969	14.55	9.073	22	17.574	14.878	9.387	244	9
a100$^+$	8	17.928	10.414	9.064	12	17.759	10.623	9.095	247	12
a50	9	17.917	10.044	9.016	11	17.912	10.109	9.06	237	14
a20$^+$	9	17.894	10.157	9.106	11	17.896	10.168	9.11	131	16
a10$^+$	9	17.903	12.462	9.054	9	17.901	11.631	9.067	248	16
a5$^+$	9	17.9	10.107	9.065	9	17.897	10.156	9.096	220	16
a2$^+$	8	17.91	10.104	9.033	8	17.913	10.049	9	120	16
a0.5$^+$	8	17.971	9.721	8.688	8	17.981	9.672	8.66	144	16
b240*	10	17.991	17.333	9.778	130	15.23	24.434	11.702	250	-
b200*	10	17.978	19.142	9.618	110	15.238	23.371	11.147	244	9
b100*	10	17.964	16.508	9.288	48	15.74	16.587	9.813	250	12
b50	8	17.964	15.167	9.135	22	16.142	13.415	9.315	238	14
b20	9	17.927	10.033	9.005	9	17.909	10.033	9	122	16
b10	8	17.916	10.018	9.019	9	17.891	10.099	9.072	244	16
b5	8	17.909	10.111	9.086	8	17.9	10.128	9.097	201	16
b2	7	17.917	10.134	9.086	8	17.917	10.09	9.059	173	16
b0.5	5	17.969	9.755	8.719	8	17.971	9.706	8.689	167	16
c240*	9	17.874	10.286	9.111	39	17.603	9.722	8.606	249	-
c200	9	17.878	10.24	9.089	10	17.843	10.211	9.06	249	9
c100	9	17.87	10.254	9.107	10	17.86	10.257	9.105	239	12
c50	9	17.875	10.239	9.093	9	17.866	10.247	9.096	184	14
c20$^+$	8	17.876	10.226	9.087	10	17.868	10.228	9.086	99	16
c10	7	17.872	10.18	9.051	8	17.865	10.186	9.052	243	16
c5	7	17.885	10.487	9.054	8	17.874	10.568	9.073	249	16
c2	7	17.919	10.127	8.895	8	17.912	10.049	8.971	144	16
c0.5	4	17.981	9.598	8.634	4	17.979	9.726	8.717	243	16

Table 3.16: Effective radius (r_{eff}), central surface brightens (Σ_0), central velocity dispersion (σ_0) and velocity dispersion at 100 pc (σ_{100}), for the nucleus and the baryonic part, final position of the object and the close pericenter passages(CPP). For satellite a, b and c. Source: this work.

Sim	$r_{eff}^{nucleus}$	$\Sigma_0^{nucleus}$	$\sigma_0^{nucleus}$	$\sigma_{100}^{nucleus}$	$r_{eff}^{baryonic}$	$\Sigma_0^{baryonic}$	$\sigma_0^{baryonic}$	$\sigma_{100}^{baryonic}$	$Posi_{10Gyr}$	CPP
	[kpc]	[mag/arcsec^2]	[km/s]	[km/s]	[kpc]	[mag/arcsec^2]	[km/s]	[km/s]	[kpc]	
d240	8	17.857	10.421	9.297	12	17.605	10.128	9.075	250	-
d200	8	17.86	10.402	9.273	17	17.624	10.121	9.035	249	9
d100	8	17.87	10.351	9.211	9	17.865	10.35	9.207	243	12
d50	7	17.866	10.293	9.187	9	17.864	10.329	9.205	200	14
d20$^+$	8	17.873	10.304	9.19	9	17.874	10.306	9.189	105	16
d10$^+$	7	17.873	10.886	9.164	8	17.868	17.886	9.176	246	16
d5$^+$	7	17.887	10.206	9.124	7	17.884	10.238	9.143	248	16
d2$^+$	6	17.905	10.053	8.998	7	17.899	10.138	9.054	245	16
d0.5$^+$	4	17.966	9.768	8.757	5	17.968	9.8	8.776	245	16
e240	10	17.888	10.213	9.059	10	17.873	10.217	9.059	249	-
e200	10	17.884	10.203	9.055	10	17.875	10.199	9.059	249	9
e100	9	17.88	10.207	9.047	9	17.871	10.212	9.052	234	12
e50	9	17.876	10.216	9.059	9	17.867	10.216	9.056	191	14
e20	7	17.877	10.214	9.057	8	17.869	10.219	9.057	105	16
e10	7	17.891	10.606	9.067	8	17.881	21.736	9.075	247	16
e5	7	17.888	10.128	9.029	7	17.881	10.156	9.045	247	16
e2	6	17.914	9.937	8.882	7	17.908	10.051	8.95	242	16
e0.5	4	17.97	9.596	8.624	4	17.969	9.705	8.696	241	16
f240*	11	17.883	10.199	9.052	10	17.879	10.207	9.054	249	9
f200	10	17.878	10.233	9.067	10	17.873	10.229	9.063	249	12
f100	10	17.87	10.207	9.063	10	17.865	10.206	9.06	232	14
f50	9	17.884	10.209	9.064	9	17.88	10.209	9.061	187	16
f20$^+$	9	17.884	10.208	9.066	9	17.884	10.212	9.067	111	16
f10$^+$	9	17.881	10.84	9.063	9	17.871	22.966	9.07	247	16
f5$^+$	8	17.888	10.123	9.017	8	17.885	10.153	9.036	246	16
f2$^+$	7	17.913	9.952	8.879	7	17.907	10.059	8.949	240	16
f0.5$^+$	4	17.977	9.641	8.645	4	17.977	9.715	8.693	236	16

Table 3.17: Similar to the previous Table 3.16 but for the d, e and f satellite. Source: this work.

Sim	$r_{eff}^{nucleus}$ [kpc]	$\Sigma_0^{nucleus}$ [mag/arcsec^2]	$\sigma_0^{nucleus}$ [km/s]	$\sigma_{100}^{nucleus}$ [km/s]	$r_{eff}^{baryonic}$ [kpc]	$\Sigma_0^{baryonic}$ [mag/arcsec^2]	$\sigma_0^{baryonic}$ [km/s]	$\sigma_{100}^{baryonic}$ [km/s]	$Posi_{10Gyr}$ [kpc]	CPP
g240*	8	17.844	10.593	9.562	88	15.118	15.765	10.274	250	-
g200*	8	17.855	11.954	9.53	53	15.216	15.398	9.035	249	9
g100*	8	17.845	10.529	9.441	50	15.51	13.543	9.207	241	12
g50	8	17.867	10.341	9.209	8	17.817	10.337	9.205	196	14
g20	9	17.88	10.313	9.201	10	17.868	10.314	9.201	114	16
g10	10	17.883	10.262	9.191	11	17.857	19.262	9.195	248	16
g5	8	17.88	10.238	9.151	11	17.87	10.258	9.163	243	16
g2	8	17.906	10.635	9.074	9	17.903	10.129	9.054	243	16
g0.5	4	17.968	10.536	8.748	8	17.978	9.719	8.694	233	16
h240*	8	17.864	10.314	9.155	14	15.138	12.899	9.413	250	-
h200*	8	17.864	10.312	9.137	56	15.173	12.136	9.331	249	9
h100	10	17.875	10.241	9.082	11	17.801	10.237	9.331	239	12
h50	10	17.874	10.234	9.08	10	17.844	10.234	9.079	189	14
h20	9	17.876	10.222	9.072	11	17.86	10.227	9.073	113	16
h10	9	17.877	10.495	9.075	11	17.81	16.998	9.08	248	16
h5	10	17.896	10.12	9.033	11	17.873	10.145	9.048	244	16
$h2^+$	8	17.911	9.957	8.898	8	17.898	10.045	8.957	239	16
$h0.5^+$	4	17.965	9.744	8.721	5	17.969	9.743	8.721	229	16
i240*	8	17.866	10.301	9.136	20	15.181	12.251	9.3	250	-
i200*	8	17.865	10.312	9.133	40	15.231	11.629	9.226	249	9
i100	10	17.877	10.216	9.065	10	17.823	10.211	9.062	238	12
i50	10	17.876	10.242	9.078	10	17.858	10.247	9.08	189	14
$i20^+$	9	17.88	10.195	9.064	10	17.868	10.199	9.066	118	16
i10	9	17.873	10.169	9.035	10	17.853	10.175	9.038	248	16
$i5^+$	9	17.886	10.135	9.034	10	17.871	10.158	9.048	244	16
$i2^+$	8	17.912	9.959	8.901	8	17.902	10.06	8.968	238	16
$i0.5^+$	3	17.971	9.679	8.68	4	17.973	9.71	8.699	233	16

Table 3.18: Similar to the previous Table 3.16 but for the g, h and i satellite. Source: this work.

Sim	$r_{eff}^{nucleus}$ [kpc]	$\Sigma_0^{nucleus}$ [mag/arcsec^2]	$\sigma_0^{nucleus}$ [km/s]	$\sigma_{100}^{nucleus}$ [km/s]	$r_{eff}^{baryonic}$ [kpc]	$\Sigma_0^{baryonic}$ [mag/arcsec^2]	$\sigma_0^{baryonic}$ [km/s]	$\sigma_{100}^{baryonic}$ [km/s]	$Posi_{10Gyr}$ [kpc]	CPP
j240*	8	17.859	13.596	9.22	88	15.121	17.712	9.811	250	-
j200*	8	17.863	10.977	9.184	67	15.15	14.685	9.651	248	9
j100*	8	17.866	10.305	9.134	23	15.564	10.473	9.133	250	12
j50	7	17.877	10.229	9.074	11	17.856	10.24	9.079	224	14
j20	7	17.876	10.2	9.069	10	17.863	10.205	9.071	166	16
j10	7	17.881	10.188	9.064	10	17.863	10.199	9.07	246	16
j5	7	17.886	10.144	9.042	8	17.874	10.173	9.059	222	16
j2	7	17.905	9.986	8.929	8	17.898	10.072	8.985	198	16
j0.5	4	17.962	9.806	8.768	4	17.969	9.753	8.735	163	16
k240*	8	17.862	10.316	9.162	57	15.164	18.468	9.588	250	-
k200*	7	17.863	10.873	9.155	31	15.203	14.092	9.468	247	9
k100	7	17.876	10.238	9.068	11	17.466	10.222	9.056	250	12
k50	7	17.873	10.247	9.082	11	17.862	10.23	9.072	220	14
k20	6	17.871	10.53	9.092	9	17.863	10.218	9.081	153	16
k10	7	17.88	10.195	9.061	9	17.866	10.206	9.066	247	16
k5	6	17.89	10.144	9.03	8	17.886	10.16	9.04	222	16
k2	7	17.921	9.961	8.908	7	17.913	10.066	8.973	189	16
k0.5	3	17.956	9.807	8.768	5	17.962	9.757	8.738	188	16

Table 3.19: Similar to the previous Table 3.16 but for the j and k satellite. Source: this work.

In Fig 3.7 we show the effective radius against the pericenter distance of the orbit, for each set of simulations, demarcated by different color lines.

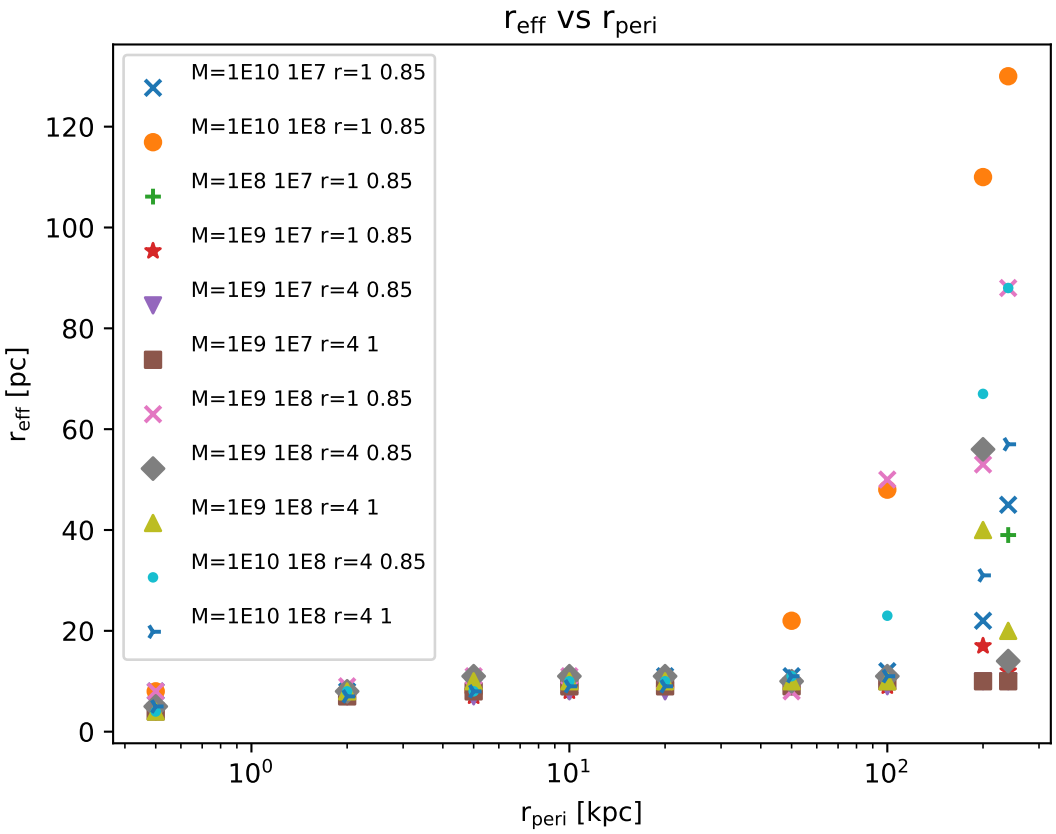

Figure 3.7: Effective radius vs pericenter of the orbit. As in previous figures the label indicates the mass of the dark matter halo, the mass of the Plummer envelope, and the scale length radius of the dark matter, and the Plummer radius of the envelope. Source: this work.

All satellites with small pericenters show small r_{eff} after 10 Gyr, this due the passages by the densest part of the host and also because they have the highest numbers of CPP among all the pericenter simulations, so besides passing closest to the center, they also pass often, compared to the ones with larger pericenter distances, also because of that they transition into an UCD earlier in the simulation, they they have more time to be destroyed completely during the simulation. For more circular orbits, the outcome will depend on the parameters of the satellite. In Fig 3.7, upper right, we can see that simulations with highest values for the mass of the DM halo show bigger effective radius, this corresponds to the ones in the tables where we do not obtained an UCD for example, b240 and b200.

In Fig 3.8 we show the central surface brightness against the pericenter distance of the orbit, for each set of simulations, demarcated by different color lines.

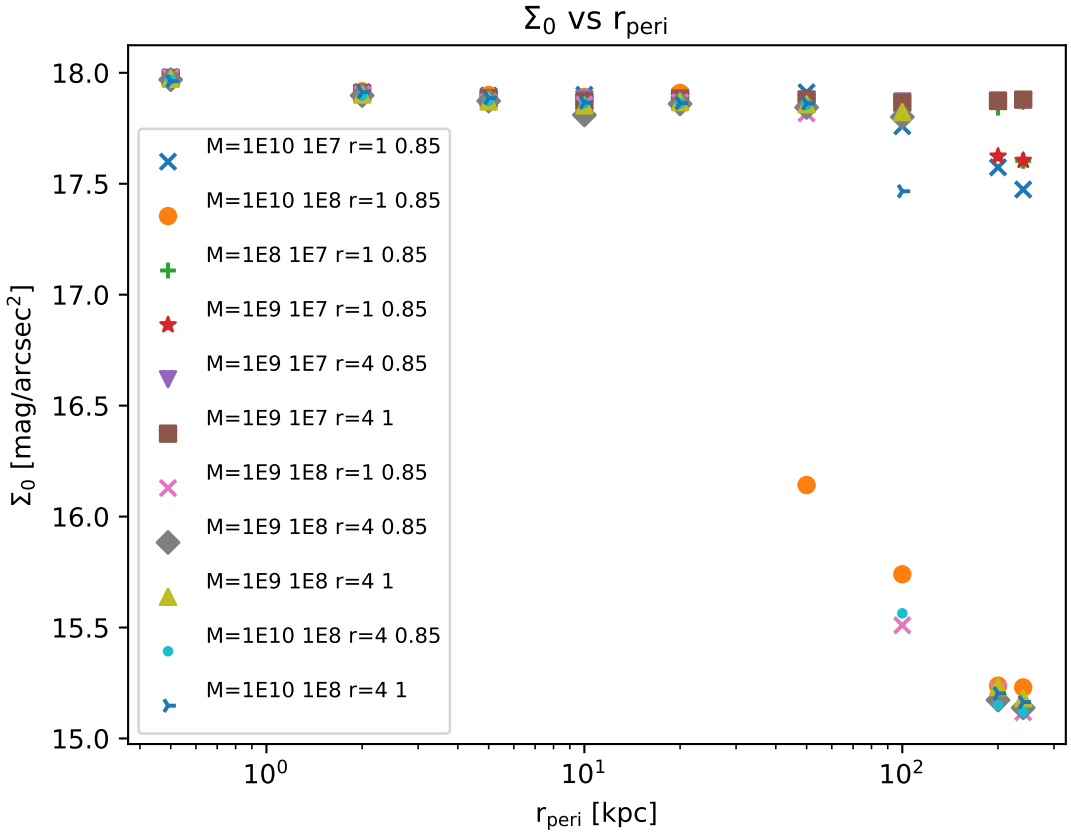

Figure 3.8: Central surface brightness against the pericenter distance of the orbit. Source: this work.

At the end of 10 Gyr simulation, the majority of objects have central surface brightness in the range of 17.0 and 18.0 mag arcsec^{-2}, except for simulations with larger pericenter distances, where we do not obtained an UCD, this correspond to the upper right point of the previous plot in Fig 3.7. Simulations with larger pericenter distances show smaller values, this means they are brighter, this outcome is because of their passages for the less dense areas of the host, the number of CPP and that they transitioned into UCDs later in the simulation, resulting in shorter times remaining to lose mass and become less bright by the end of the simulation, the opposite happens to the satellites with closest pericenter passages.

In Fig 3.9 we present the velocity dispersion within 100 pc measured from the center of the object, vs the pericenter distance of the orbit, for each set of simulations, demarcated by different color lines.

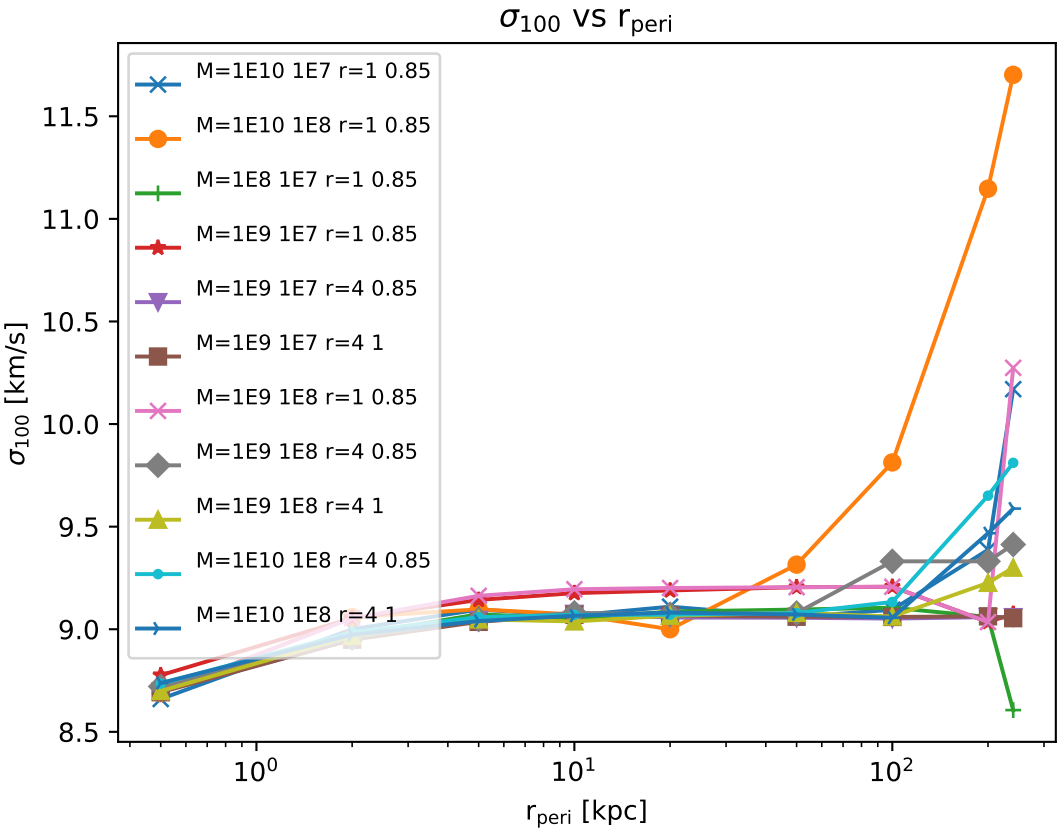

Figure 3.9: Velocity dispersion within 100 pc vs the pericenter distance of the orbit, for each set of simulations, demarcated by different color lines. Source: this work.

If we analyze the plot in Fig 3.9, we can easily notice that again the satellites that do no transition into an UCDs can be distinguished between the ones that did, showing in the upper right side of the plot the biggest velocities dispersion. Among satellites that transition into UCD we can notice that larger pericenter distance for the orbits are directly proportional with the final velocity dispersion within 100 pc. However, this is not that clear between simulations with pericenter passages between 10 pc and 50 pc which show almost the same values.

Chapter 4

Additional Simulations

4.1 Simulations with parameters explored by Pfeffer & Baumgardt(P&B)

The host galaxy parameters for this section are the same of those of the previous section. The parameters of the dE galaxy are shown in Table 4.1. Simulations with satellite l are in agreement with the ones considered in Pfeffer & Baumgardt (2013) simulations, The simulations involving satellites b and e were selected for comparison with the simulations from the previous section. For the nucleus we considered model 2 of Pfeffer & Baumgardt (2013) which has a Plummer radius of $r_{pl} = 10$ [pc] and a mass of $M_{\rm nucleus} = 2.56 \times 10^6$ [$M_\odot$].

One important difference with their simulations is that we add a dark matter halo of M^{DM}=10^9, 10^{10} [$M_\odot$] and a scale length of 1 and 4 [kpc].

We follow the orbit criteria of simulations from Pfeffer & Baumgardt (2013). Elliptical orbits are highly eccentric, with apocenters of 50 kpc and 100 kpc, and pericenters of 20 kpc, 10 kpc, 5 kpc and 2 kpc.

We compute the initial velocities of the dE galaxy as explained in section 3.2.2 to follow an elliptical orbit with these specified apocenter and pericenter distances. The obtained initial velocities are shown in Table 4.2. In these simulations, we use a live, self-consistent objects for both components of dark matter, both for the host and the satellite. Therefore, dynamical friction is correctly taken into account.

	DM halo			Plummer	
Sim	Scale length [kpc]	R_{200} [kpc]	Mass $M_\odot$	r_{pl} [kpc]	Mass $M_\odot$
b	1	45.66	10^{10}	0.85	10^8
e	4	21.19	10^9	0.85	10^7
l	1	45.66	10^{10}	0.85	8.4×10^8

Table 4.1: Parameters of the satellites of P&B simulations. We show, in order, the scale length, the R_{200} and the mass of the DM halo, then the plummer radius (r_{pl}) and the mass of the plummer envelope. Source: this work.

r_a[kpc]	100	100	100	100	50	50	50	50
r_p[kpc]	20	10	5	2	20	10	5	2
Velocity[km s^{-1}]	393.99	219.82	117.1	48.95	624.53	359.74	195.69	83.11

Table 4.2: Initial Velocities of the orbiting object for a elliptical orbit at a fixed apocenter (r_a) and pericenter (r_p) distance. Source: this work.

The simulations names describe the initial parameters, the apocenter and the pericenter distance for the orbit. For example: E10020 has the parameters corresponding to the e-simulations, displayed in table 4.1, an apocenter of 100 [kpc], a pericenter of 20 [kpc] considering the "e" satellite.

Results

To determine when a component of the orbiting dwarf is regarded as completely stripped or destroyed, we follow the same criterion of previous sections, i.e., bound particles determined by SUPERBOX below 10%. We consider a lower mass limit for UCDs of $2\times10^6_\odot$ (Hasegan et al 2005). In order to have the observed mass of an UCD in our simulations, the nucleus has to have at least 78% of the initial mass. In all simulations the dark matter halo of the orbiting galaxy gets stripped first followed by the envelope.
In only one simulation we reach the lower mass limit of an UCD (E502).

The results of the of the P&B simulations are displayed in Table 4.3. We show the time when: the DM halo is destroyed ($T_{0.1}^{DM}$) and when the envelope is destroyed ($T_{0.1}^{env}$). Then the time, mass and position when the dE transition into an UCD. The only case in where we obtained a destroyed Nuclei is simulation E502 at 8242 [Myr].

Sim	haloc $T_{0.1}^{DM}$ [Myr]	Plummer $T_{0.1}^{env}$ [Myr]	Initial T [Myr]	UCDs Mass $M_\odot$	Posi [kpc]
E10020	85	277	277	6.3×10^6	94
E10010	252	185	185	10^8	99
E1005	80	114	114	3.3×10^7	4
E1002	80	112	112	2.3×10^7	2
E5020	27	43	43	6.3×10^7	33
E5010	26	38	38	6.3×10^7	32
E505	26	37	37	6.3×10^7	31
E502	26	37	37	6.3×10^7	31
B10020	286	696	696	322.5×10^6	97
B10010	260	647	647	322.5×10^6	90
B1005	248	436	436	742.5×10^6	99
B1002	236	316	316	132.5×10^6	13
B5020	147	378	378	272.5×10^6	48
B5010	133	244	244	502.5×10^6	45
B505	125	228	228	552.5×10^6	48
B502	120	204	204	372.5×10^6	49
L10020	309	2482	2482	215.7×10^6	80
L10010	269	1282	1282	220.3×10^6	93
L1005	246	906	906	220.7×10^6	83
L1002	227	676	676	226.5×10^6	92
L5020	155	1151	1151	229×10^6	47
L5010	136	508	508	226.5×10^6	9
L505	123	375	375	230.5×10^6	6
L502	115	329	329	226.5×10^6	46

Table 4.3: Results of the P&B simulations, we present the time when: the DM halo is destroyed ($T_{0.1}^{DM}$) and the envelope is destroyed ($T_{0.1}^{env}$). Then the time, mass and position when the dE transition into an UCD. Source: this work.

In Fig. 4.1, we show the initial time when we obtain an UCD in the simulations

against the pericenter of the orbit of the dE. Simulations with an apocenter for the orbit of 50 [kpc] are displayed in with points, and those with 100 [kpc] are displayed with "+". Different colors represent the three satellites studied. The time increases first with the apocenter and then with the pericenter. Simulations with an apocenter distance of 50 [kpc] transition into a UCD at the very beginning of the simulation, almost independently of the pericenter. However, simulations with an apocenter distance of 100 [kpc] take slightly longer to become UCDs, and their orbital pericenters start to make a difference on the outcome. With larger pericenters, it takes longer for the satellite to transition into a UCD

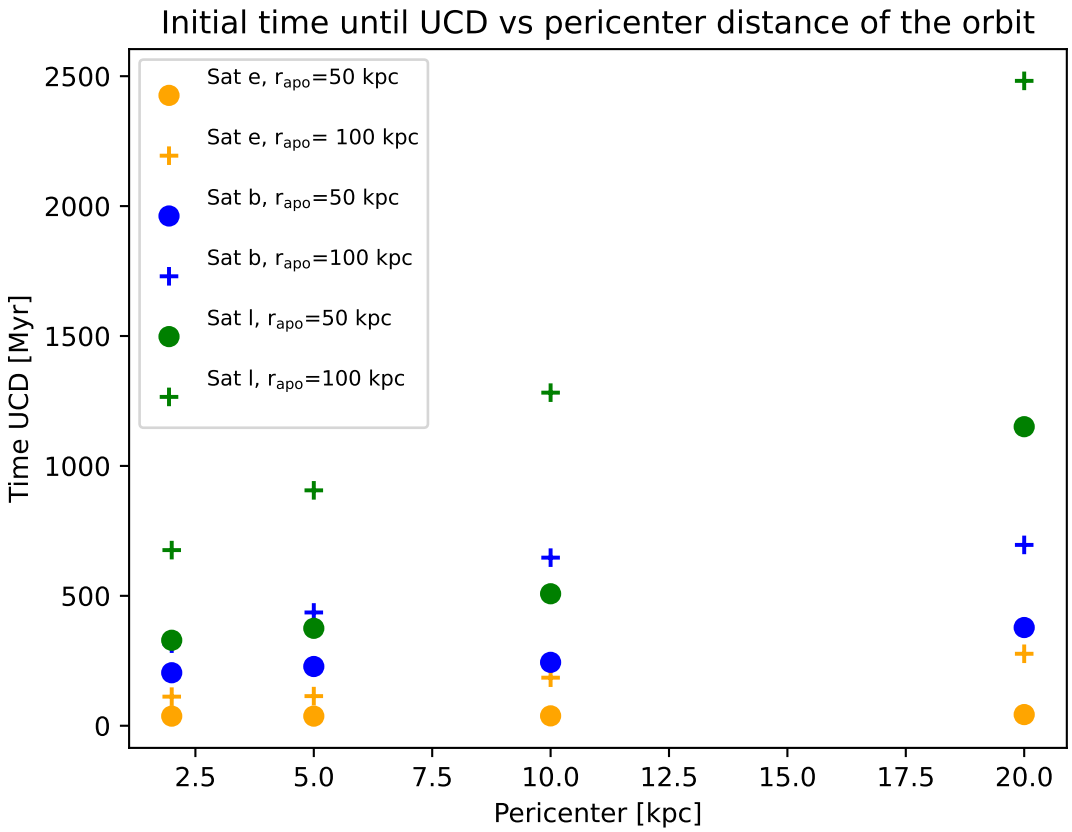

Figure 4.1: Time when the dE transition into an UCD in the simulations against the pericenter of the orbit. Data from Table 4.3, different markers represent the apocenter of the orbit and the satellites are displayed with different colors. Source: this work.

Assuming the UCDs are born with DM halos as predicted by LCDM theory (Behroozi et al., 2013), these halos can undergo stripping processes, resulting in the observed dis-

tances of UCDs. By considering orbits with apocenters between 100 to 50 kpc and pericenters between 2 and 20 kpc, the dark matter halo is stripped within the first Gyr for close orbits leading to the stripping of the envelope within the next few hundred Myr. This conclusion mainly applies to orbits near the center of the host and involves satellite e, b and l.

4.2 From dE to UCD in MOND

In this section, we study the evolution of the orbital parameters of simulations when instead of considering a dark matter halo within the framework of LCDM, we adopt the MOND treatment for the particles (see Section 1.6).

4.2.1 Setup

The simulations of this section were performed with Phantom of Ramses (see Chapter 2.2) using 32 nodes. The parameters of the simulations are displayed in Table 4.4. As explained in section 3.2.1 we consider the correlation between the masses of the nucleus and envelope parts of the satellite we consider the relation showed in fig 19 of R.Capuzzo-Dolcetta & I. Tosta e Melo 2017, were a relation of the order of 1:100 is also observed.

In Table 4.4 columns are the number of particles, Mass and Plummer radius of : Host, Envelope and Nucleus. Last three columns are the orbital parameters: the apocenter, pericenter of the orbit and the initial velocity of the satellite.
The simulation end-time is 10 Gyr and are performed using the AMR parameters displayed in Table 4.5.

	Host			Envelope			Nucleus			Orbit		
Sim	$N_{particles}$	M	r_{pl}	$N_{particles}$	M	r_{pl}	$N_{particles}$	M	r_{pl}	R_{apo}	R_{peri}	v_0
	10^3	[$M_\odot$]	[pc]	10^3	[$M_\odot$]	[pc]	10^3	[$M_\odot$]	[pc]	[kpc]	[kpc]	[km s^{-1}]
1	200	10^{14}	16220	200	10^8	1000	100	2.56×10^6	10	250	2	387.57
2	2	10^{12}	16220	2	10^8	1000	1	2.56×10^6	10	250	20	22.5
3	2	10^{12}	16220	2	10^8	1000	1	2.56×10^6	10	290	250	387.57
4	20	10^{12}	16220	20	10^8	1000	10	2.56×10^6	10	250	75	190.52
5	20	10^{12}	16220	20	10^8	1000	10	2.56×10^6	10	250	35	103.7
6	20	10^{12}	16220	20	10^8	1000	10	2.56×10^6	10	250	30	54.41

Table 4.4: Parameters of the MOND simulations. Columns are the number of particles, mass and Plummer radius of : Host, Envelope and Nucleus. Last columns are the apocenter and pericenter of the orbit, followed by the initial velocity of the satellite. Source: this work.

AMR PARAMS	
levelmin	5
levelmax	12
ngridmax	2000000
boxlen	1024.0
npartmax	2000000

Table 4.5: AMR parameters. Source: this work.

4.2.2 Results

Simulation number 1 gets completely destroyed before the first Gyr, this due to the strong potential of the host ($10^{14}M_{\odot}$). However, this mass is completely out of range with reality and was chosen to explore the behavior of a satellite orbiting a host with the mass of the 'dark matter' halo of a Virgo-like galaxy cluster.

Also, initial velocities equal to the ones used in the previous section for satellites with the same mass for the nucleus and the envelope do not follow the same orbits. The same velocities in PoR turn into orbits with larger pericenters than in the previous sections.

In Fig. 4.6 we present some orbital outcomes of simulations from Table 4.4. We show the dynamical evolution of the orbit depending on the initial velocity of the satellite, the apocenter and pericenter distances, the number of close passages, the number of apocenter passages, and finally, the azimuthal periods.

Sim	Apocenter [kpc]	Pericenter [kpc]	CPP N	CAP N	Azimuthal periods N
2	250	20	6	5	4
3	290	250	3	3	3
4	250	75	5	5	3
5	250	35	6	5	4
6	250	30	6	6	4

Table 4.6: Results of MOND simulations. Dynamical evolution of the orbit: the apocenter and pericenter distances, the number of close passages, number of apocenter passages, and finally, the azimuthal periods. Source: this work.

In Table 4.7 we show, the apocenter and pericenter of the orbit. Then the time when the dE transition into an UCD, the position at that time and the last column show the final position of the satellite in the simulation

Sim	Apocenter [kpc]	Pericenter [kpc]	$T_{0.1}^{UCD}$ [Myr]	$Position_{T_{0.1}^{UCD}}$ [kpc]	Final position [kpc]
2	250	20	1300	194	200
3	290	250	-	-	263
4	250	75	5600	206	250
5	250	35	3600	237	170
6	250	30	2600	32	188

Table 4.7: Results of UCDs in MOND simulations. We show, the apocenter and pericenter of the orbit. Then the time when the dE transition into an UCD, the position at that time and the last column show the final position of the satellite in the simulation . Source: this work.

In Fig 4.2 we show times when we obtained an UCD of the object b,j and k from the section 3.2.1. This are the ones that most closely resemble a dE as explained before. In this plot comparison we include the times for the UCDs with MOND simulations in red stars.

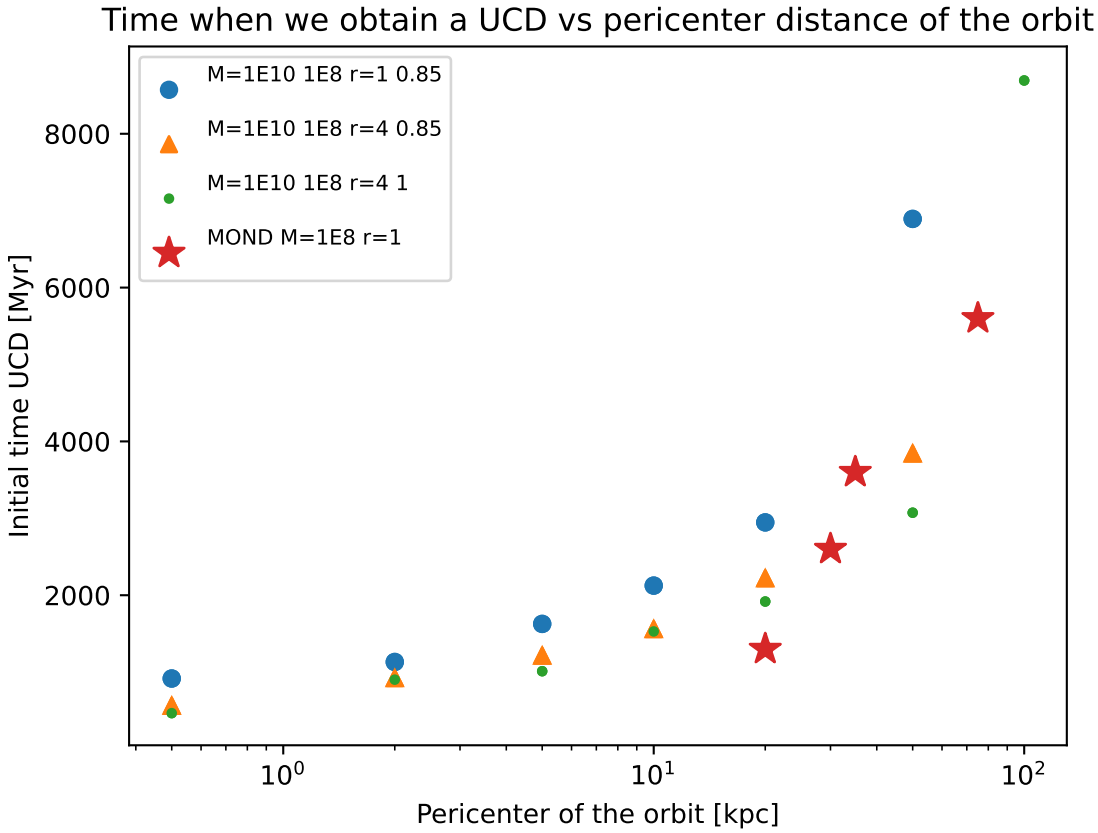

Figure 4.2: In this figure we show the evolution of simulation number 5. Each subplot represents a snapshot separated by a 100 Myr interval. Source: this work.

Simulations performed with PoR using MONDian dynamics do not show large differences compared to the ones performed considering LCDM. In Fig 4.2 we show that the data points from MOND simulations and LCDM simulations lie in the same region.

We present some examples of the first 5 Gyr of two simulations with very different orbits. First in Fig 4.3 the object follow a high eccentric orbit with a pericenter of 35 kpc (Sim5 from Table 4.4) and then in Fig. 4.10 the orbit is more circular (Sim3 from Table 4.4).

Fig 4.3 the satellite experience 6 close pericenter passages during the 10 [Gyr] simulation and transition into a UCD at 3600 [Myr] of simulation. In Fig. 4.4 , 4.5 and **??** we show the mass of the nucleus, the nucleus plus the envelope in $M_{\odot}kpc^{-2}$ and the surface brightness in mag kpc^{-2}, when the object transition into an UCD (3600 [Myr]).

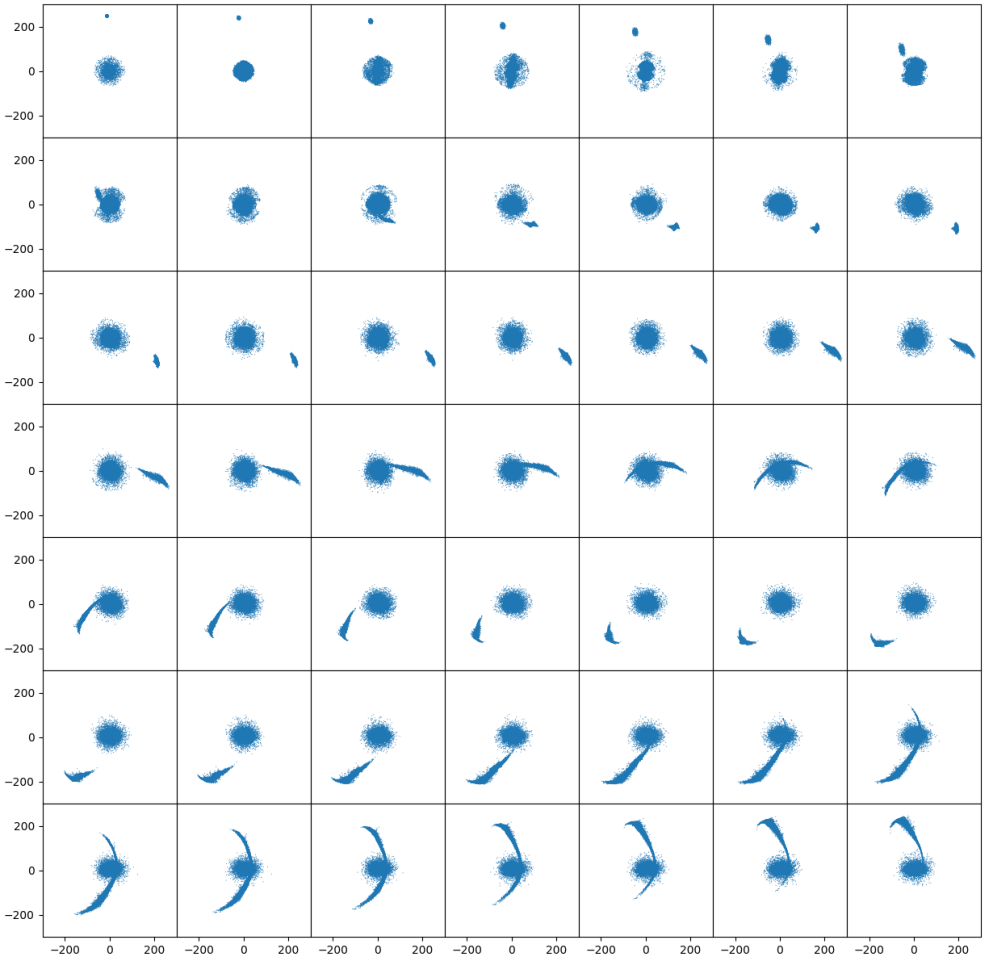

Figure 4.3: In this figure we show the evolution of simulation number 5. Each subplot represents a snapshot separated by a 100 Myr interval. Source: this work.

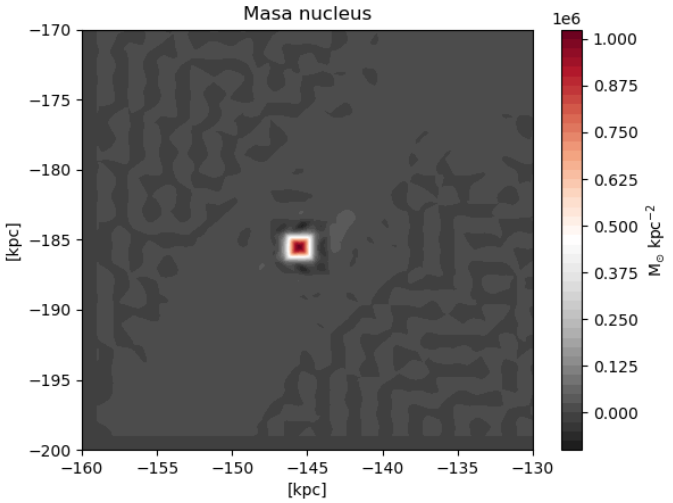

Figure 4.4: Nucleus of simulation number 5 after transitionate into an UCD. The color bar shows the mass in units of $M_{\odot}kpc^{-2}$. Source: this work.

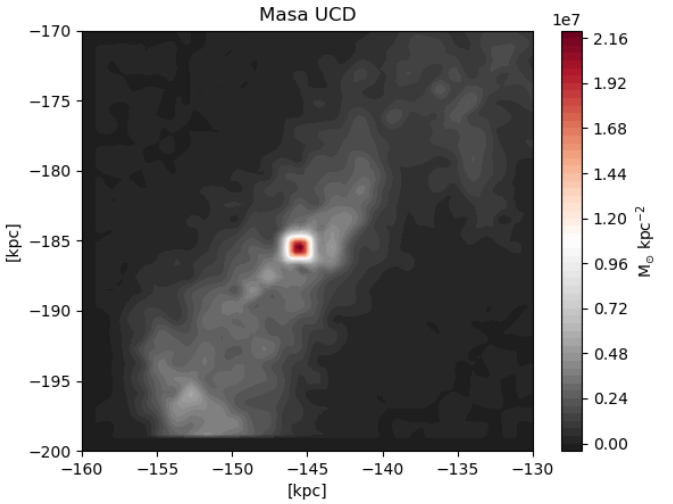

Figure 4.5: Satellite of simulation number 5 after transitionate into an UCD. The object shown in the image is the nucleus and the envelope. The color bar shows the mass in units of $M_{\odot}kpc^{-2}$. Source: this work.

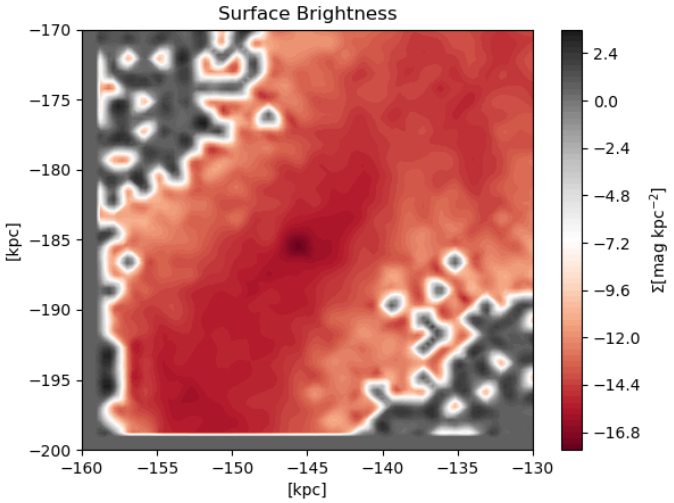

Figure 4.6: Surface Brightness of satellite from simulation number 5 after transitionate into an UCD. The object shown in the image is the nucleus and the envelope. The color bar shows the mass in units of mag kpc^{-2}. Source: this work.

And in 4.7 , 4.8 and **??** we show the same contor plots but now for the satellite at the end of the simulation (10 [Gyr]).

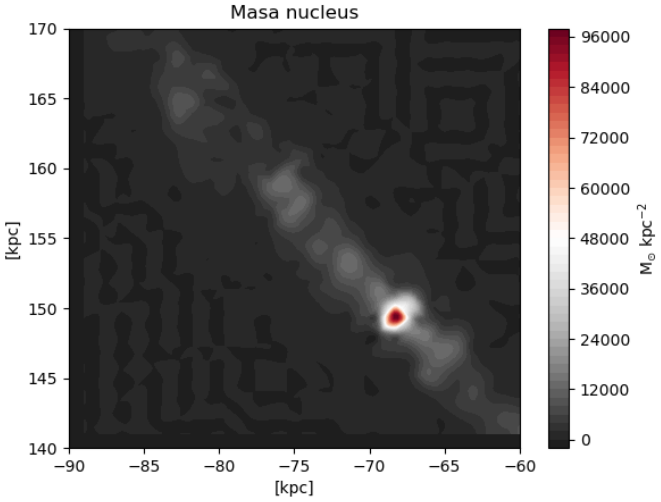

Figure 4.7: Nucleus of simulation number 5 at the end of the simulation. The color bar shows the mass in units of $M_\odot kpc^{-2}$. Source: this work.

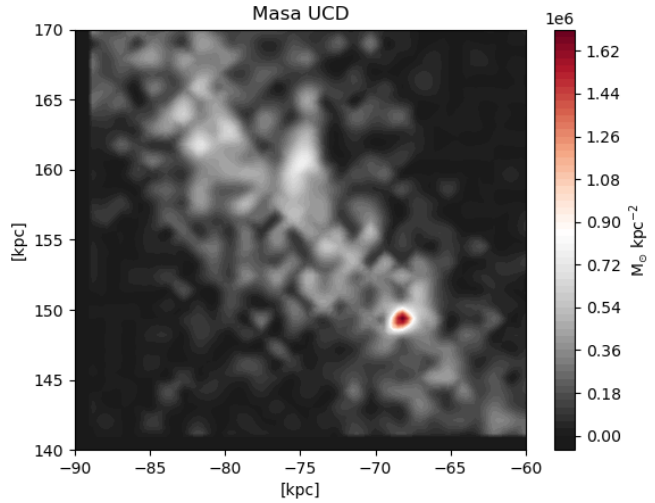

Figure 4.8: Satellite of simulation number 5 at the end of the simulation. The object shown in the image is the nucleus and the envelope. The color bar shows the mass in units of $M_\odot kpc^{-2}$. Source: this work.

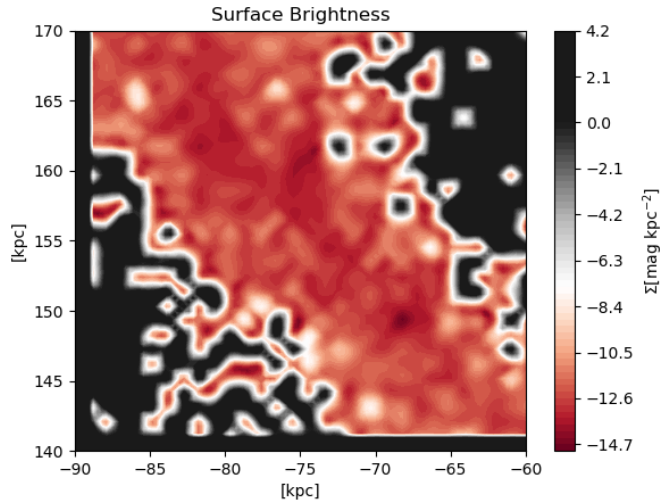

Figure 4.9: Surface Brightness of satellite from simulation number 5 at the end of the simulation. The object shown in the image is the nucleus and the envelope. The color bar shows the mass in units of mag kpc^{-2}. Source: this work.

Fig 4.10 show the evolution of simulation number 3, this simulations starts in their pericenter at 250 [kpc] from the center of the host, and follow an orbit with an apocenter

of 290 [kpc]. This satellite goes through three azimuthal periods during the 10 [Gyr]. And since the first 1.5 Gyr start to show tails of stars. After 10 Gyr of simulation the object have the properties shown in Fig. 4.11. Similar to the previous simulation in Fig. 4.12 we show the mass of the nucleus plus the envelope of the object, in units of $M_{\odot}kpc^{-2}$, and in 4.13 we present the surface brightness of the object in unities of mag kpc^{-2}. This object do not transition into UCD in the 10 Gyr of the simulation due to the small eccentricity of their orbit (as discussed in previous sections).

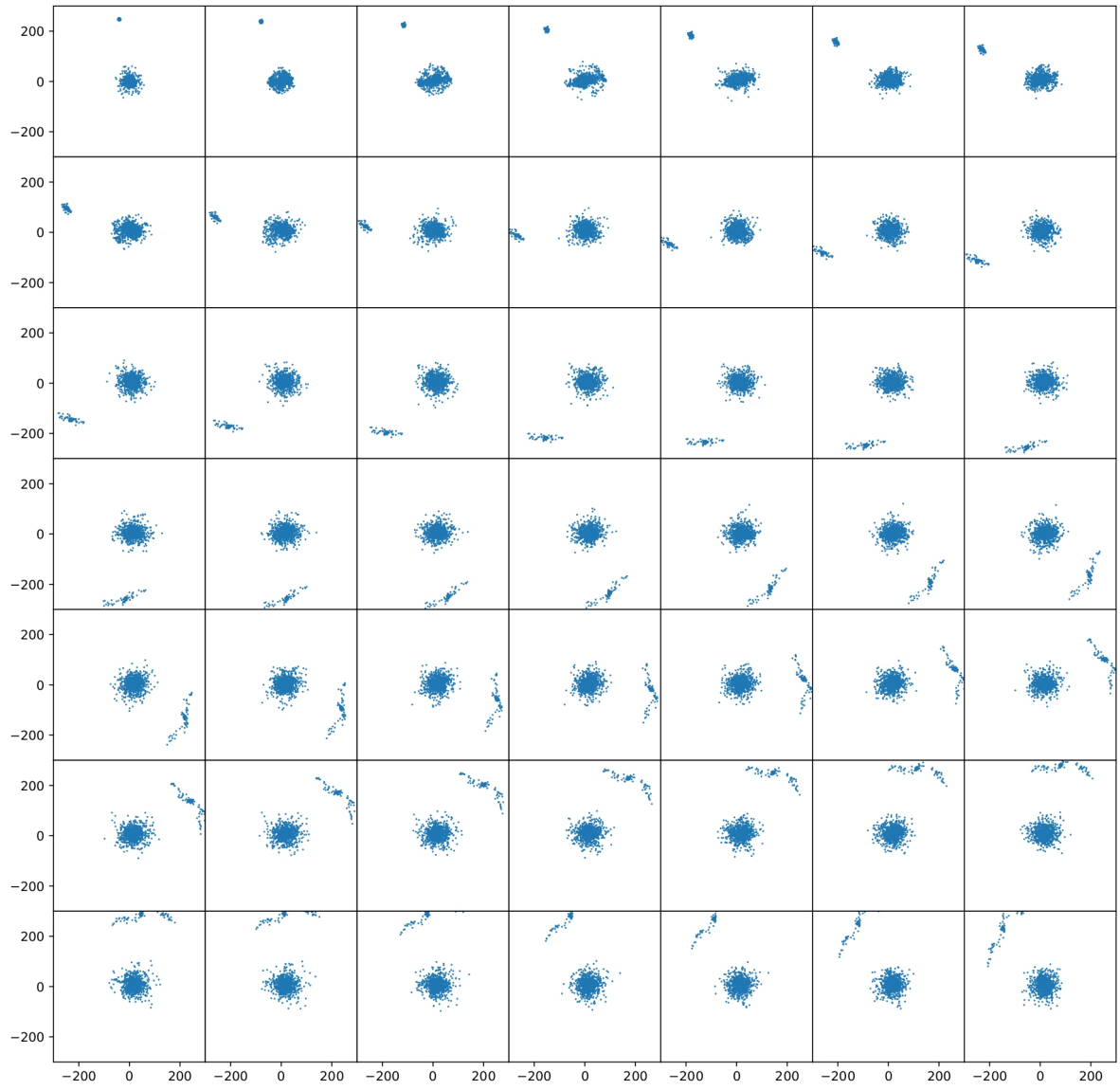

Figure 4.10: In this figure we show the evolution of simulation number 3. Each subplot represents a snapshot separated by a 100 [Myr] interval. Source: this work.

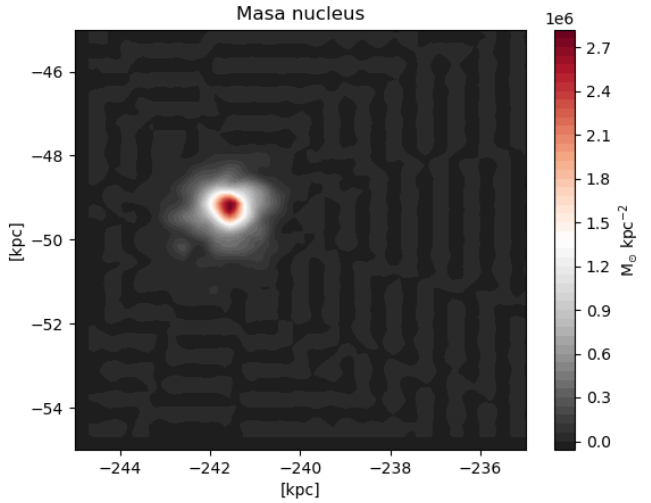

Figure 4.11: Nucleus number 3 after 10 [Gyr] of simulation. The color bar shows the mass in units of $M_{\odot}kpc^{-2}$. Source: this work.

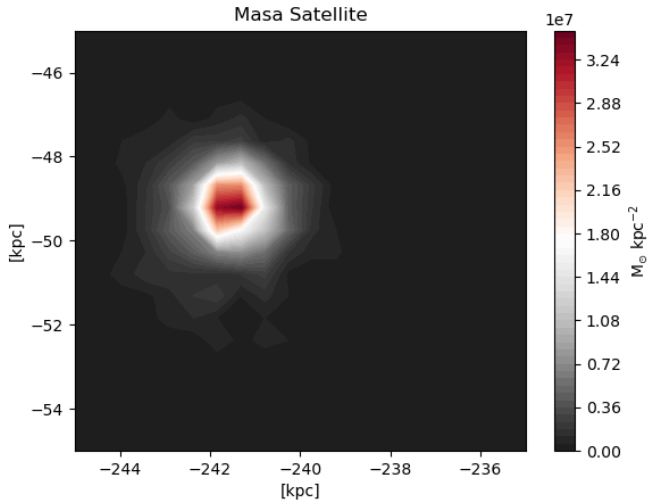

Figure 4.12: Satellite of simulation number 3 after 10 [Gyr] of simulation. The object shown in the image is the nucleus and the envelope. The color bar shows the mass in units of $M_{\odot}kpc^{-2}$. Source: this work.

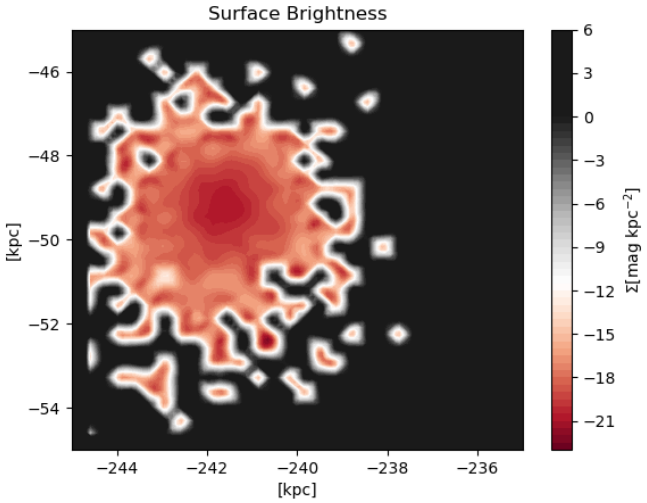

Figure 4.13: Surface Brightness of satellite from simulation number 3 after 10 [Gyr] of simulation. The object shown in the image is the nucleus and the envelope. The color bar shows the mass in units of mag kpc^{-2}. Source: this work.

In Figures 4.14 the percentage of bound particles within the envelope part is illustrated along the simulation. Different pericenters are represented by distinct colored lines.

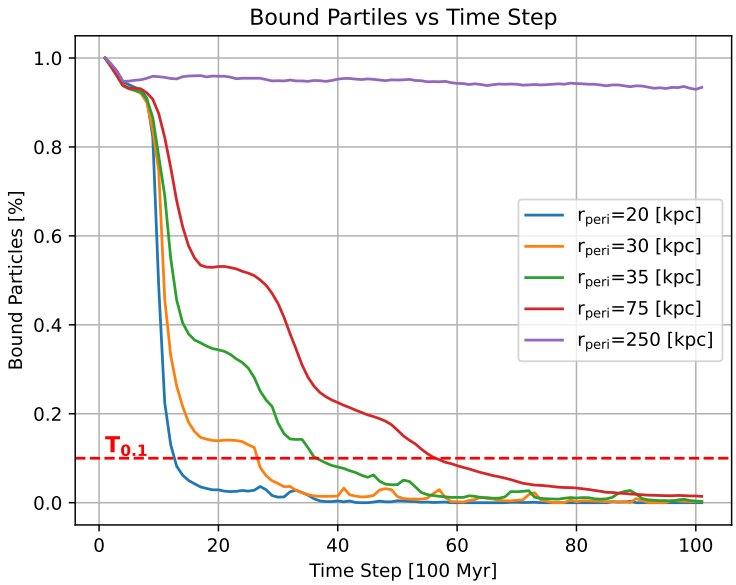

Figure 4.14: Bound particles of envelope along the simulation. Different pericenters are delineated by distinct colored lines. Source: this work.

Most of the mass stripping from the envelope occurs during close passages. The initial diminishing along each pericenter line corresponds to the satellite's first passage through its pericenter. In addition, it is evident that this decline is more pronounced when the pericenter value is smaller. This suggests that the object loses the most mass when passing near the center, where the host's density is greater.

4.3 Extreme Orbits(Kroupa)

To study how fast the dark matter envelope gets stripped from the satellite we present the study of some interesting extreme orbits. For this study we choose to place the object outside the host and then throw the object with different angles to the center of the host. In Fig. 4.15, a scheme of the extreme orbits is shown. Here, the blue filled circle represents the host, the pink filled circle the satellite, and the different dashed-lines represent the different tested orbits.

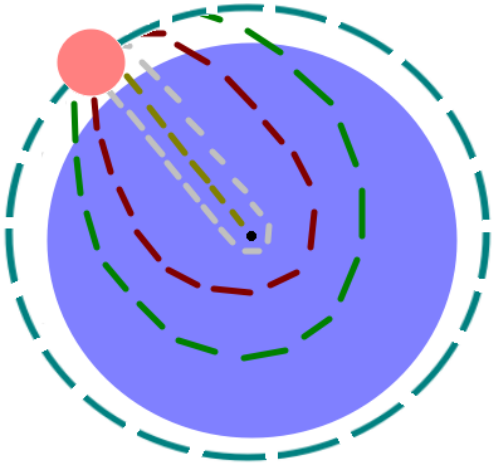

Figure 4.15: Scheme of the extreme orbits is shown. Here, the blue filled circle represents the host, the pink filled circle the satellite, and the different dashed-lines represent the different tested orbits. Source: this work.

4.3.1 Setup

We perform simulations considering two objects, similar to Chapter 3.1, the host is built by the dark matter halo and the baryonic part, and the satellite(dE) built by the dark matter halo, the envelope of stars and the nucleus.
The host has the same parameters as the previous sections is live so the dynamical friction of the satellite (UCD+DM halo + DM halo of the host) is computed self-consistently.

The satellite follows the characteristics of the "b" , "j" and "k" sets of simulations

from Table 3.10, which most closely resemble dEs, and are in good mass ratios of their components. These ratios are derived from studies by Behroozi, Wechsler, & Conroy (2013), providing the baryonic mass-to-dark matter halo mass ratio, and R. Capuzzo-Dolcetta & I. Tosta e Melo (2017), which determines the nucleus-to-envelope ratio. These parameters were discussed in detail in previous sections. We consider 5 different pericenter distances for the orbit in order to obtain diferent insertion angles for the satellite into the host, 0, 250, 500, 750 and 1050 [kpc]. The more extreme cases are the ones for the 0 [kpc], where the satellite goes directly to the center of the host and one case in where the satellite goes in a obtuse angle starting at 1050 [kpc] and reaching 1125 [kpc].
The initial velocities of the satellite are displayed in Table 4.8

r_a[kpc]	1050	1050	1050	1050	1125
r_p[kpc]	0	250	500	750	1050
Velocity[km s^{-1}]	0	334.63	480.66	572.91	643.28

Table 4.8: Initial Velocities of the orbiting object for extreme orbits at a fixed apocenter (r_a) and pericenter (r_p) distance. Source: this work.

The parameters of the simulation are displayed in Table 4.9. Here the dark matter part and 'envelope' of the dwarf galaxy are built by 2.000.000 particles each, while the nucleus is built by 1.000.000 particles. The Plummer radius of the nucleus is set to $r_{nucleus,pl}$ = 0.01 [kpc], while the nucleus mass is set to $M_{nucleus} = 2.56 \times 10^6$ $M_\odot$ in all simulations. Also for all sets of parameters we perform simulations with 5 different pericenter distances for the orbits: 0, 250, 500, 750, 1050 [kpc]. The apocenter distance is 1050 [kpc] in all orbits, except the last one in where the pericenter is 1050 [kpc] and the apocenter is 1125 [kpc]. An additional simulation was performed for the "b" set using instead of 2.000.000 particles for each component of the host, 10.000.000 particles to explore the behavior of the number of particles.

Sim	haloc			Plummer		Orbit
	Scale length [kpc]	R_{200} [kpc]	Mass $M_\odot$	r_{pl} [kpc]	Mass $M_\odot$	R_{peri} [kpc]
b0	1	45.66	10^{10}	0.85	10^8	0
b250	1	45.66	10^{10}	0.85	10^8	250
b500	1	45.66	10^{10}	0.85	10^8	500
b750	1	45.66	10^{10}	0.85	10^8	750
b1125	1	45.66	10^{10}	0.85	10^8	1050
j0	4	45.66	10^{10}	0.85	10^8	0
j250	4	45.66	10^{10}	0.85	10^8	250
j500	4	45.66	10^{10}	0.85	10^8	500
j750	4	45.66	10^{10}	0.85	10^8	750
j1125	4	45.66	10^{10}	0.85	10^8	1050
k0	4	45.66	10^{10}	1	10^8	0
k250	4	45.66	10^{10}	1	10^8	250
k500	4	45.66	10^{10}	1	10^8	500
k750	4	45.66	10^{10}	1	10^8	750
k1125	4	45.66	10^{10}	1	10^8	1050

Table 4.9: Initial conditions of the simulations., the dark matter part and 'envelope' of the dwarf galaxy are built by 2.000.000 particles each, while the nueclei is built by 1.000.000 particles. The Plummer radius is $r_{nucleus,pl} = 0.01$ [kpc] and the mass is $M_{nucleus} = 2.56 \times 10^6 M_\odot$ in all simulations. Also for all sets of parameters we perform different simulations with 5 pericenter distances for the orbits: 0, 250, 500, 750, 1050 [kpc]. The apocenter distance is 1050 [kpc] in all orbits except the last one that reaches 1125 [kpc].Source: this work.

4.3.2 Results

In Fig. 4.10 we show the properties of the final UCDs in the cases where we obtain them, which only happen to those simulations with the closest pericenters, i.e., where the

satellite is aimed directly to the center of the host.

Columns shown are, in order, the simulation time when the dark matter halo gets destroyed, the percent of the baryonic part when the dark matter halo is destroyed , the time when the Plummer envelope gets destroyed, then time when the object begins to be an UCD in the simulation, the mass of the object, the position, mass to light ratio and % of the dark matter content of the object.

Sim	haloc			Envelope	Initial	UCDs			
	$T_{0.1}^{DM}$	$M_{T_{0.1}^{DM}}^{envelope}$	$M_{T_{0.1}^{DM}}^{Plummer}$	$T_{0.1}^{envelope}$	T	M	Posi	M/L	% DM_0
	[Myr]	%	%	[Myr]	[Myr]	$M_\odot$	[kpc]		%
b0	1875	21	23	5466	5466	112.4	22	9.06	0.1
j0	1870	56	57	2137	2137	112.5	411	6.58	0.07
k0	1870	49	50	1980	1980	112.5	234	8.98	0.1

Table 4.10: Results of simulations from Table 4.9. Columns shown are, in order, the simulation time when the dark matter halo gets destroyed, the percent of the envelope part when the dark matter halo is destroyed and then the same but for the baryonic part (envelope plus nucleus), the time when the Plummer envelope gets destroyed. Then time when the object begins to be an UCDs in the simulation, the mass of the object, the position, mass to light ratio and % of the dark matter content of the object. Source: this work.

Orbits

The orbits of the satellite for different pericenters are shown in Fig. 4.16, 4.18, 4.20 and 4.22. Their respective apocenters along the simulations are shown in Fig 4.17, 4.19, 4.21 and Fig 4.23 (different satellites are shown in different colors).

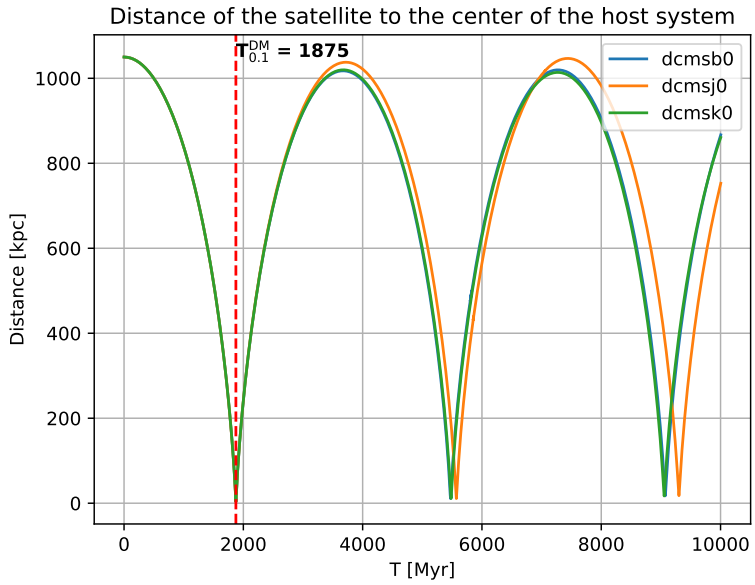

Figure 4.16: Orbits of the satellites in the b0 simulation. In this plot it is possible to observe that the apocenter diminishes for the first two Gyr (specially for the b and k satellite), with the DM halo getting destroyed. As this is the most massive object in the satellite, the mass that remains inside is not enough to show a dynamical friction effect. Source: this work.

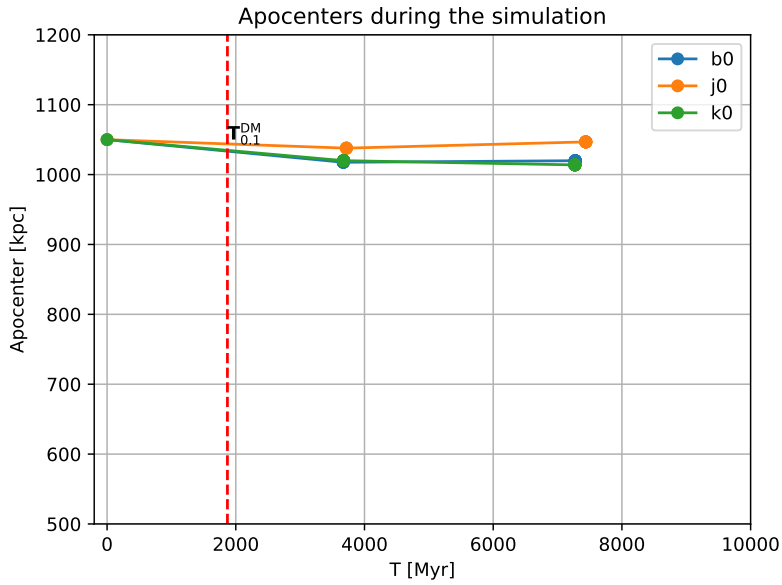

Figure 4.17: Apocenters of the simulations where the satellite passes through the center, i.e., those with pericenter equal to 0. The apocenter diminishes for the first two Gyr (specially for the b and k satellite), with the DM halo getting destroyed. Source: this work.

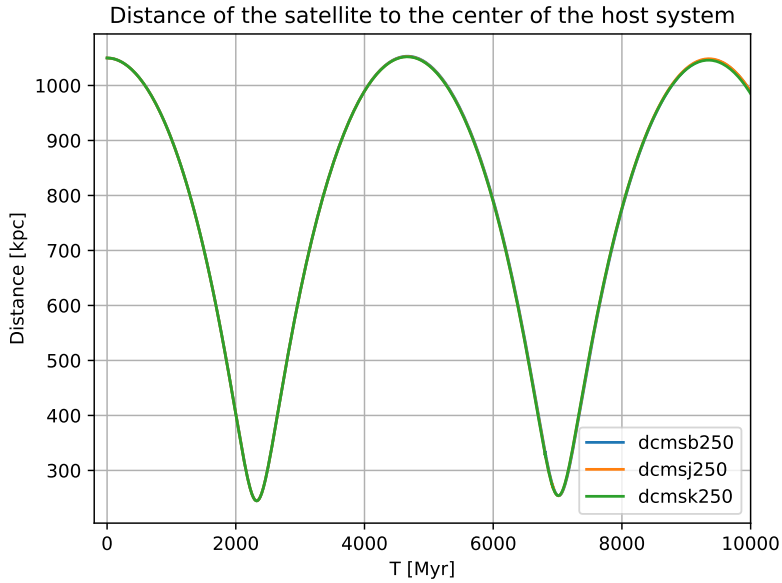

Figure 4.18: Orbit of the satellite in simulations with pericenters of 250 [kpc]. Source: this work.

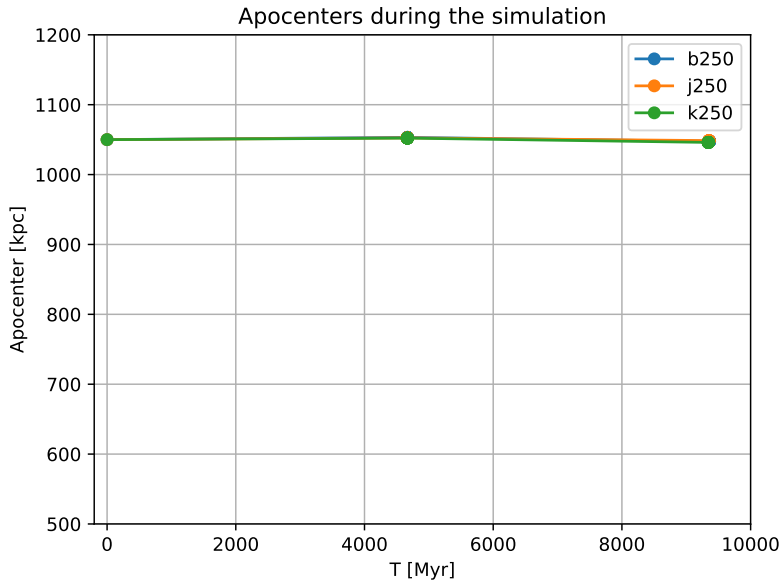

Figure 4.19: Apocenters along the simulations with 250[kpc] of pericenters. Source: this work.

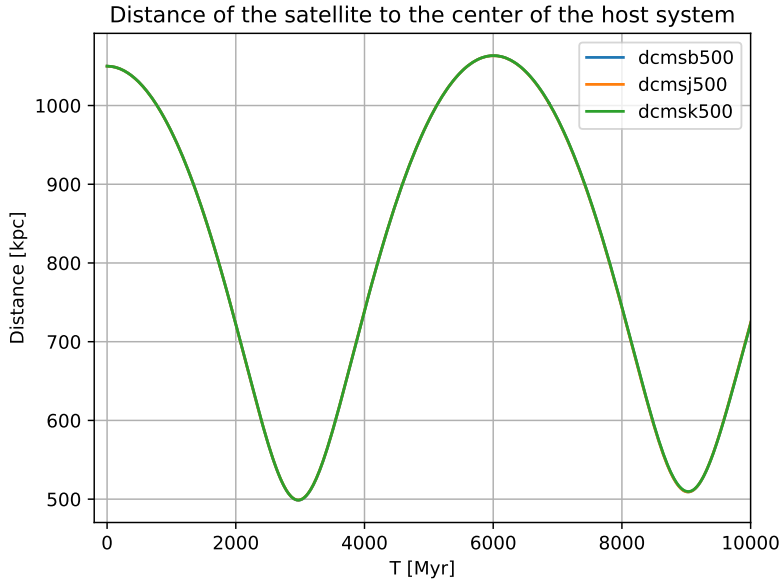

Figure 4.20: Orbit of the satellite in simulations with pericenters of 500 [kpc] Source: this work.

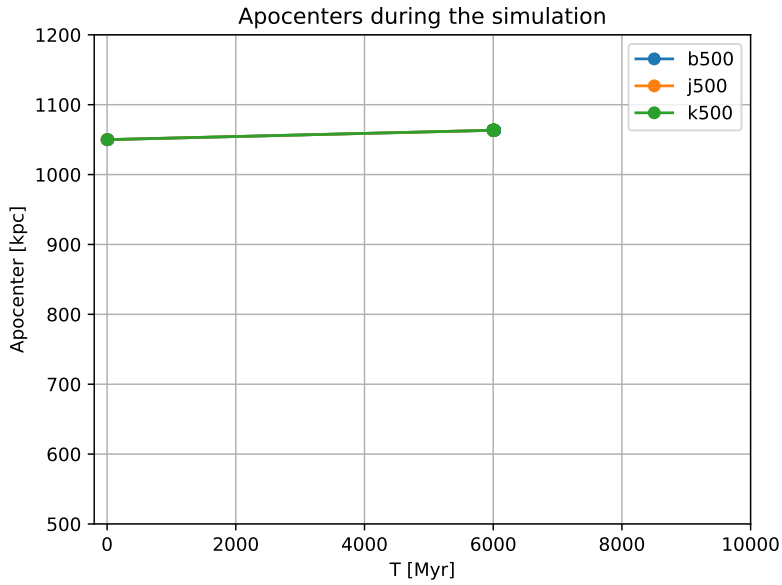

Figure 4.21: .

Source: this work.]Apocenters along the simulations with pericenters of 500 [kpc].

Source: this work.

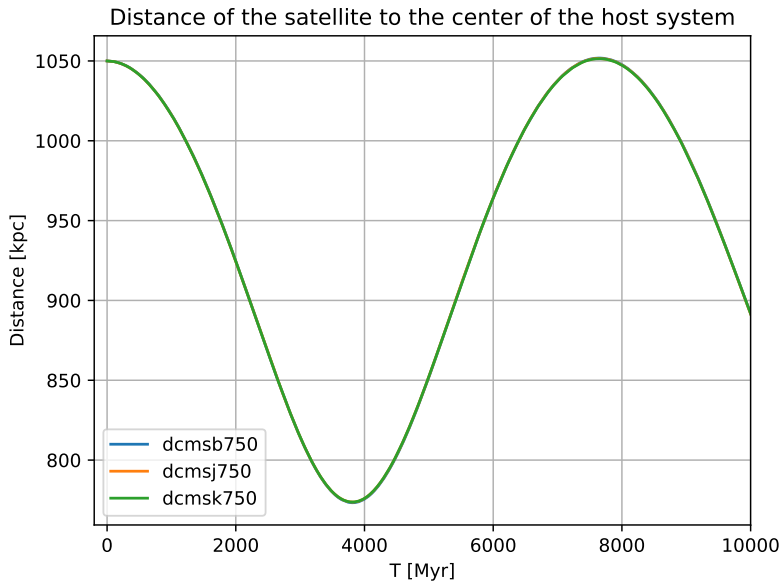

Figure 4.22: Orbits of the satellite in simulations with pericenters of 750 [kpc]. Source: this work.

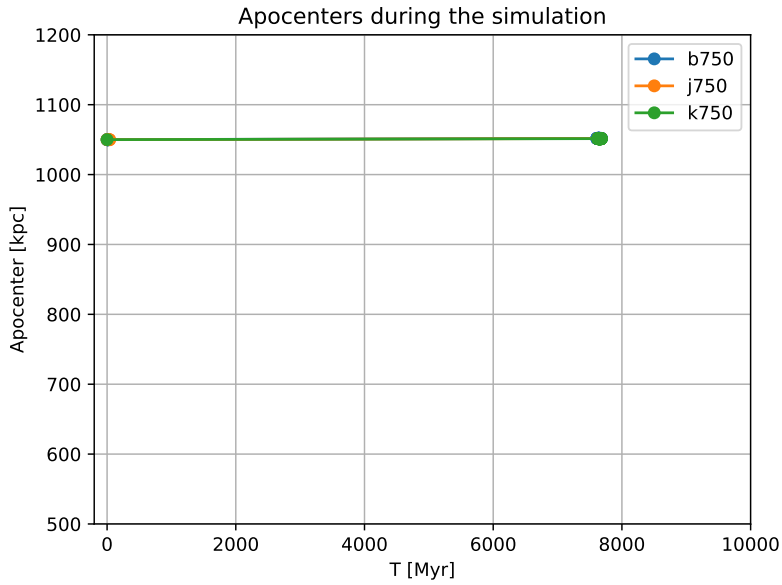

Figure 4.23: Apocenters along the simulations with pericenters of 750[kpc]. Source: this work.

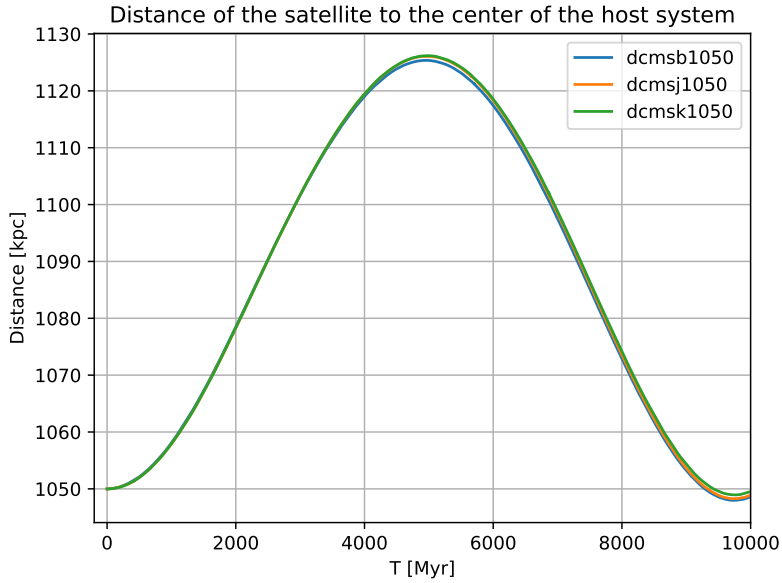

Figure 4.24: Orbit of the satellite in simulations with pericenters of 1050 [kpc]. Source: this work.

We can observe that there is no clear difference between simulations with different satellites (b,j,k). Also, the effects of dynamical friction are not clearly evident in the

simulations, except in the simulation where the object is directly in direction of the center of the host (see Fig. 4.16 and more clearly in Fig. 4.17). In this simulation we can observe that the apocenter diminishes for the first two Gyr, with the DM halo getting destroyed. This diminishes of the apocenter is from 1050 [kpc] to 1017 [kpc], so due to the dynamical friction the orbit shrink 33 [kpc] in the first close pericenter passage, then the dark matter halo gets destroyed. As this is the most massive object in the satellite, the mass that remains inside is not enough to show a dynamical friction effect.
The inability to observe the effect of dynamical friction for larger pericenters is due to the higher density of the host at its center. In the case where the pericenter is 0, the object passes directly through the point where the host is densest. All other orbits pass outside the scale radius of the host's dark matter halo.

Stripping of the dark matter halo

In Figures 4.25, 4.26 and 4.27, the percentage of bound particles within the dark matter (DM) halo is illustrated along the simulation trajectories of satellites b, j, and k, respectively. Different pericenters are represented by distinct colored lines.

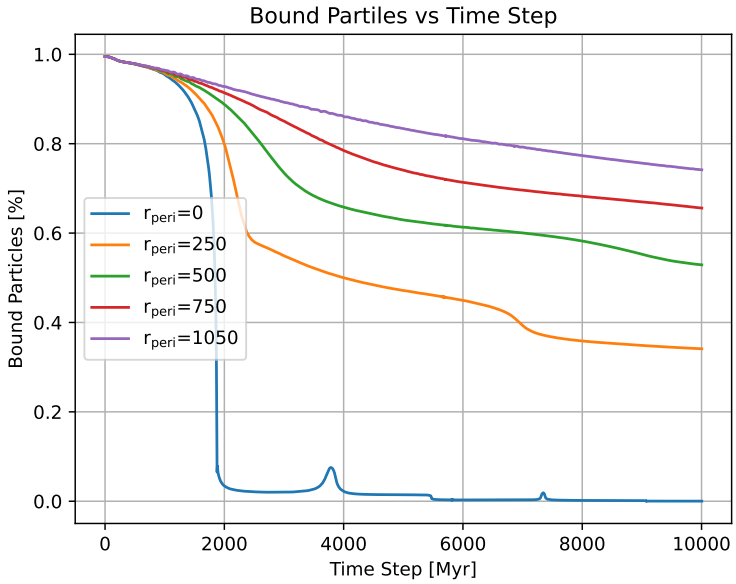

Figure 4.25: Bound particles of the DM halo along the simulation with satellite b. Different pericenters are delineated by distinct colored lines. Source: this work.

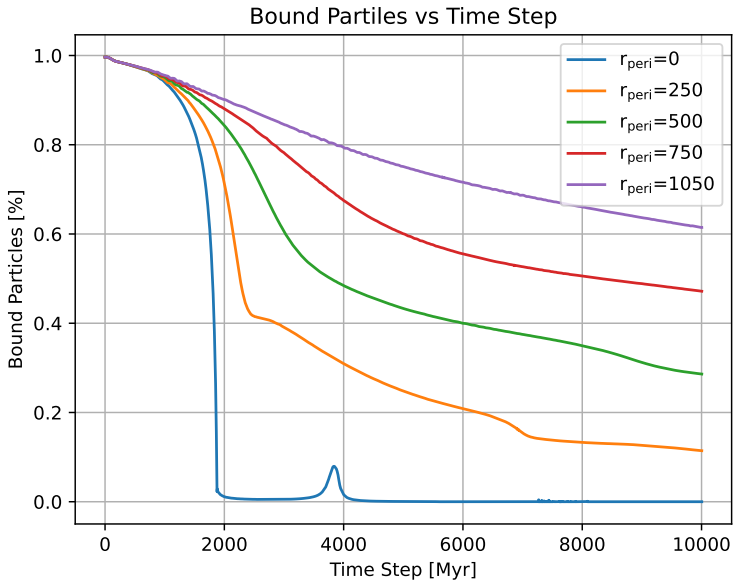

Figure 4.26: Bound particles of the DM halo along the simulation with satellite j. Different pericenters are delineated by distinct colored lines. Source: this work.

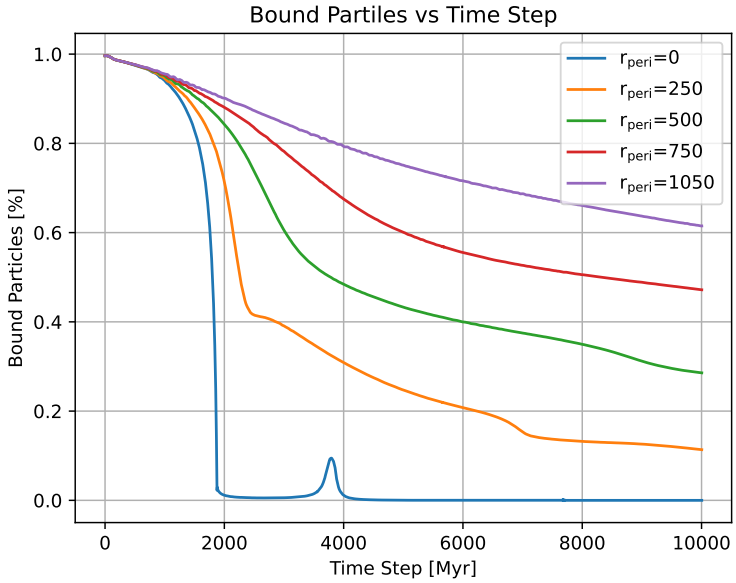

Figure 4.27: Bound particles of the DM halo along the simulation with satellite k. Different pericenters are delineated by distinct colored lines. Source: this work.

The majority of the mass stripping from the dark matter halo occurs during close passages. The initial diminishing along each pericenter line corresponds to the satellite's

first passage through its pericenter. In addition, it is evident that this decline is more pronounced when the pericenter value is smaller. This suggests that the object loses the most mass when passing near the center, where the host's density is greater and the dynamical friction effect is greater and more visible, as in the case of the pericenter at 0 kpc.

To examine how the structural parameters of the DM halo affect the velocity at which it loses mass, we can analyze Figures 4.28, 4.29, 4.30, 4.31 and 4.32. These figures show the bound particles of the DM halo along the simulation for various pericenters, with the three satellites represented by different colored lines.

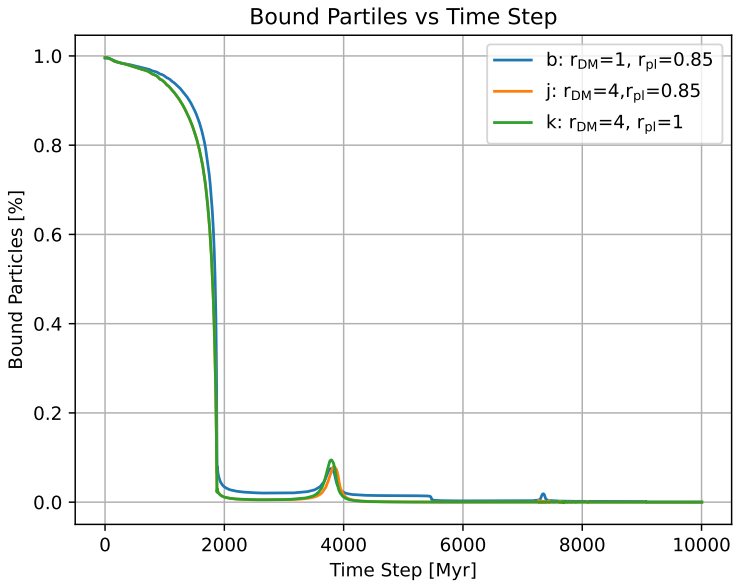

Figure 4.28: Bound particles of the DM halo along the simulation for the 0 pericenter, different satellites are shown in different color lines. Source: this work.

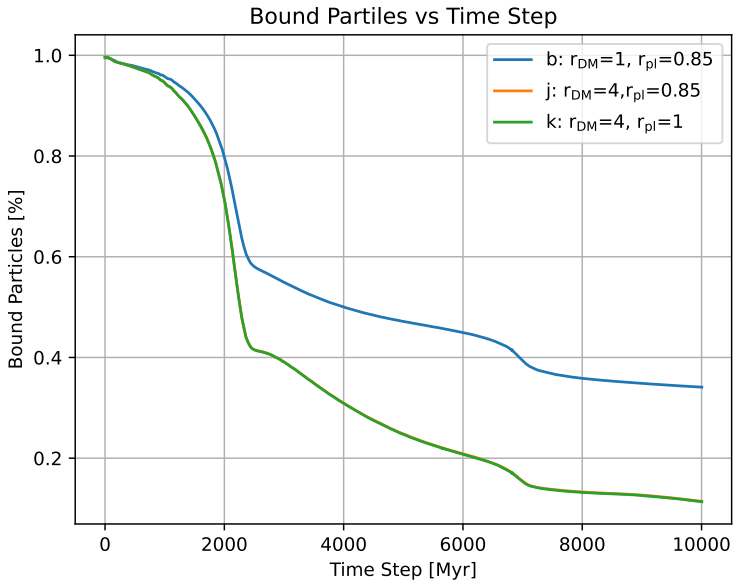

Figure 4.29: Bound particles of the DM halo along the simulation for the 250 pericenter, different satellites are shown in different color lines. Source: this work.

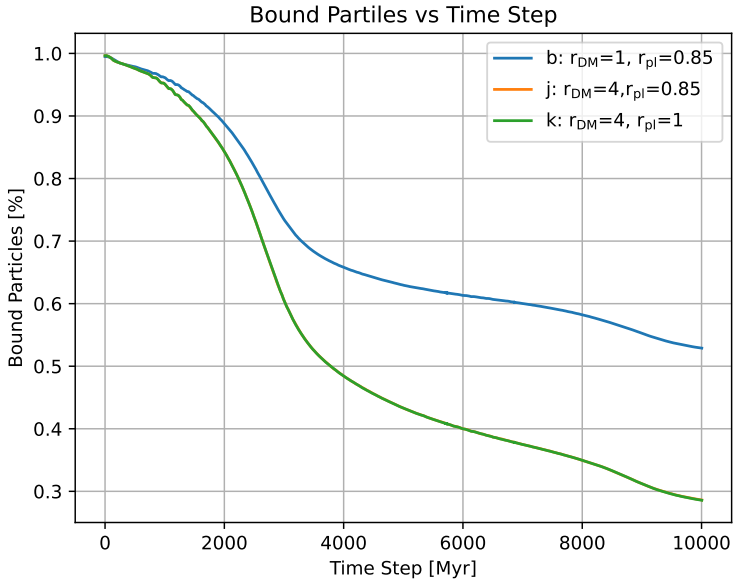

Figure 4.30: Bound particles of the DM halo along the simulation for the 500 pericenter, different satellites are shown in different color lines. Source: this work.

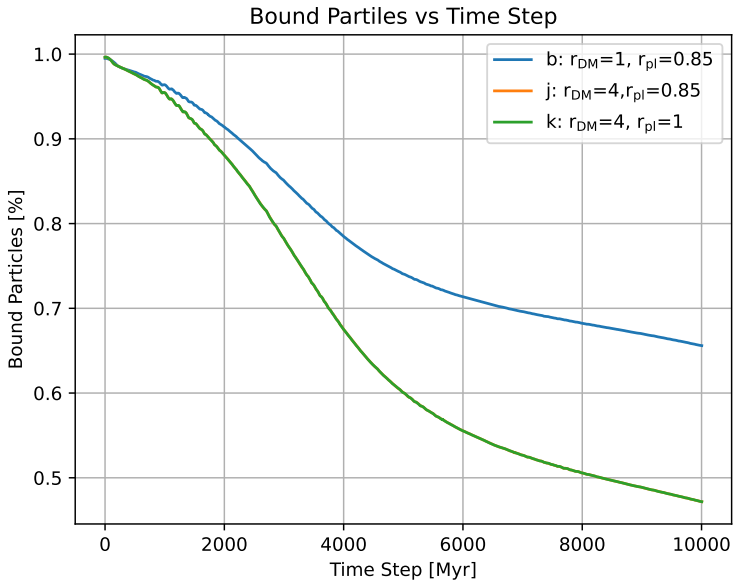

Figure 4.31: Bound particles of the DM halo along the simulation for the 750 pericenter, different satellites are shown in different color lines. Source: this work.

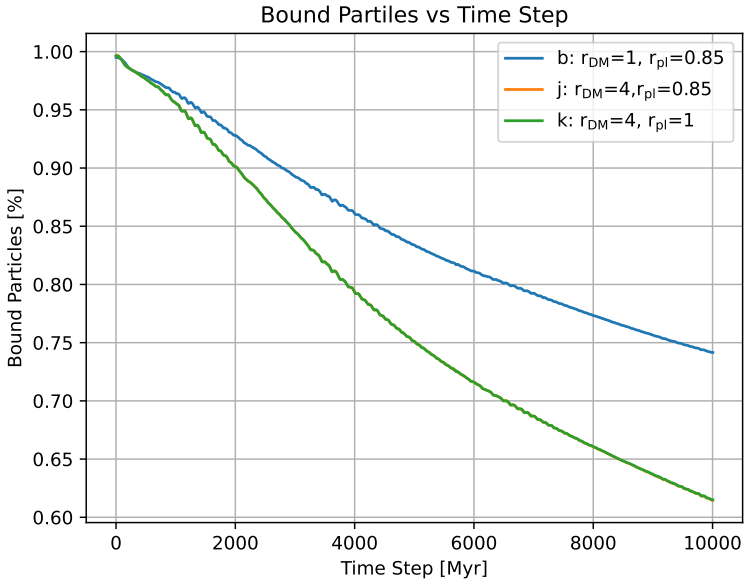

Figure 4.32: Bound particles of the DM halo along the simulation for the 1050 pericenter, different satellites are shown in different color lines. Source: this work.

In the simulation where the object hits the center directly, appears to be little difference between the three satellites. However, if we analyze the other four plots Fig 4.29, Fig 4.30,

Fig 4.31 and Fig 4.32 we can clearly observe that simulations with larger dark matter halos experience faster destruction compared to those with smaller dark matter halos. Thus, as observed in the previous sections, the destruction time and the density of the halos are propotional.

Chapter 5

Summary and Conclusions

In almost all simulations of this study, the dark matter halo of the orbiting galaxy is stripped by the host galaxy, followed by the baryonic part. As the dark matter halo is stripped first in the majority of simulations, the crucial parameters influencing the outcome are those associated with the baryonic envelope. Simulations with smaller masses tend to be more susceptible to destruction.

If we analyze time of the dE transition to an UCD vs the pericenters of the orbits, it is apparent that, among the initial 9 sets of simulations with different pericenters, those with pericenter distances of 0.5, 2, 5, 10, 20, and 50 kpc consistently evolve into UCDs. However, as we reach pericenter distances of 100, 200, and 240 kpc, more massive satellites do not have sufficient time to undergo the UCD transformation. This observation implies that simulations with the highest mass values for the satellite and those with the most circular orbits (larger pericenter distance) do not transform into UCDs over a 10 Gyr simulation period. We can conclude that the pericenter is the most influential parameter in the outcome of our simulations. Also, it is useful to demarcate 3 regions in the plot of pericenter vs time when the dE transition into a UCD. First, in the lower segment, we encounter objects exhibiting smaller effective radii similar to globular clusters, potentially leading to misidentification. Second, satellites situated in the outer upper parts of the plot have not enough time to transition into UCDs within the 10 Gyr simulation period. Finally, the central objects at the center of the plot can be designated as UCDs.

If we analyze the importance of the sizes of different satellite components on the

outcome of the simulation, the Plummer part is the most important for the evolution of the simulation, followed by the dark matter part. Larger sizes contribute to a less compact object, making it more susceptible to earlier destruction during the simulation. Therefore, the order of importance for the parameters is as follows: the mass of the Plummer envelope (larger masses require more time for UCD formation), followed by the size of the Plummer envelope (larger sizes result in a less compact object that is more easily destroyed), and finally, the size of the dark matter part.

One of the most important result of our work is that in most of the simulations the satellite turns into an UCD at two distances: first, close to the center of the simulation -due to the strong potential in that area-, and second, in the outer part of the orbit, this is near to the apocenter values, this is because according to the second law of Kepler the velocity of the object is smaller near to the apocenter so the probability to obtain the object is larger in that position, because objects spend most of their time around apocenter.

If we analyze the destruction of different components of the satellite :

- For the dark matter halo an evident trend is apparent with larger pericenter values in the orbit, where we observe a late destruction of the DM halo of the satellite. This delay can be attributed to the fact that, similar to the envelope, most of the destruction occurs near the host where the density is higher. Then, the mass of the halo is the second more important parameter to determinate the time when the halo gets destroyed. Higher masses result in later destruction of the halo. Additionally, the scale length of the halo becomes important; larger scale lengths (4 [kpc]) lead to earlier destruction compared to smaller scale lengths (1 [kpc]). This is due to the fact that, the two objects have the same mass, so objects with larger scale lengths have lower densities compared to the ones with smaller scale lengths.

- For the nuclei: Simulations where the nuclei gets destroyed are simulations with pericenter distance of 0.5 [kpc]. Positions when the object UCDs are all near to the center. This is because most particles in the nuclei are very bound and the loss of the particles (so the mass) occurs mostly when the satellite passes near the

center of the potential, i.e. is in pericenter distance. Further away the object loses considerably less particles, per time.

When our objects have masses below the UCDS threshold we note that the DM particles are 100% stripped implying a M/L ratio of 1.

Regarding to the structural parameters of the object at the end of the simulation satellites with closest pericenter passages after 10 Gyr, show all very small effective radii this due the passages by the densest part of the host and also because they have the highest number of close pericenter passages (CPP) among all the simulations with different pericenters, so besides passing closest to the center, they also pass more often, than the ones with larger pericenter distances, also because of that they transition into an UCD early in the simulation, they have more time to be destroyed completely during the simulation. In the cases of more circular orbits, it depends on the parameters of the satellite. Simulations with highest values for the mass of the DM halo show bigger effective radius. At the end of 10 Gyr simulation, the majority of objects have central surface brightness in the range of 17.0 and 18.0 mag arcsec^{-2}, except for simulations with larger pericenter distances, objects that did not transition into an UCD show smaller values, this means they are brighter, this outcome is because of their passages for the less dense areas of the host, the number of CPP and that they became UCDs later in the simulation, this results into smaller times to losses the remain mass and became less brighter, the opposite happens to the satellites with closest pericenter passages. Studing the velocity dispersion, satellites that do no transition into an UCDs are distinguished between the ones that did, showing the biggest velocities dispersion. Among the satellites that transition into UCD we can notices that larger pericenter distance for the orbits are directly proportional with the final velocity dispersion within 100 pc.

So, in summary we can say that: in most simulations, the dE,N turns into an UCD and the DM halo gets stripped first. The further evolution is governed by the parameters of the stellar envelope. Massive dE,N either need close pericenter passages or very long evolution times to turn into UCDs. On eccentric orbits, objects spend most of their orbital period close to apo-center. So even though it is the pericentric passages that do

the damage to our objects, the objects need time to lose mass and transform into UCDs further out i.e. closer to their apocenter. Also most UCDs are found close to the apocenter distance today. We see the following order of importance of our starting parameters:
- pericentre distance
- mass of stellar envelope
- size of stellar envelope
- mass of the DM halo
- size of DM halo.

In relation to the sections 4.3 and 4.1 of additional simulations chapter, we conducted simulations for the first time, taking into account a self-consistent treatment of dynamical friction and accurate DM halo masses.

In simulations with parameters inspired by Pfeffer & Baumgardt (2013), assuming the UCDs are born with DM halos as predicted by LCDM theory (Behroozi et al., 2013), these halos can undergo stripping processes, resulting in the observed distances of UCDs. By considering orbits with apocenters between 100 to 50 kpc and pericenters between 2 and 20 kpc, the dark matter halo is stripped within the first Gyr for close orbits leading to the stripping of the envelope within the next few hundred Myr. But this apply only for the closest orbits and satellites studied that section.

In simulations with extreme orbits, where the object starts outside the dark matter halo of the host and enters with varying angles, we observe that there is no significant difference between simulations involving different satellites (b, j, k). Also, the effects of dynamical friction are not clearly evident in the simulations, except in the simulation where the object is directly in direction of the center of the host. In this simulation we can observe that the apocenter diminishes for the first two Gyr, with the DM halo getting destroyed. This diminishes of the apocenter is from 1050 [kpc] to 1017 [kpc], so due to the dynamical friction the orbit shrink 33 [kpc] in the first close pericenter passage, then the dark matter halo gets destroyed. As this is the most massive object in the satellite, the mass that remains inside is not enough to show a dynamical friction effect.
The inability to observe the effect of dynamical friction for larger pericenters is due to the higher density of the host at its center. In the case where the pericenter is 0, the object

passes directly through the point where the host is densest. All other orbits pass outside the scale radius of the host's dark matter halo.

The dark matter halo gets the majority of its mass stripped during the first close passage as we can observe the first big decline in mass in each pericenter line coincides with the satellite's first passage through its pericenter. Also, this decline is stronger the smaller the value for the pericenter is. This probes that the object looses most mass, passing near to the center where the density of the host is higher and also where the dynamical friction effect is stronger and visible, as is in the case for the pericenter of 0 kpc. In the simulation where the object hits the center, appears to be no significant difference between the three satellites. But if we analyze the other 4 cases with different angles, we can observe clearly that simulations with the larger dark matter halo get their dark matter halo destroyed faster than simulations with smaller dark matter halo.

Thus, according to the LCDM theory, in many orbits, the dE (composed of a nucleus, an envelope, and a dark matter halo) evolves by first stripping the DM halo, then the envelope of the dE, resulting in the nucleus remaining as a UCD on an orbit comparable to observed UCDs. This process occurs over the 10 Gyr duration of the simulation. However, this behavior is not observed in all the orbits studied in this thesis. Some orbits, due to the pericenter distance or the simulation time, do not result in the formation of a UCD. Instead, we observe a transition object, which is a partially stripped UCDs with a significant envelope remaining from the dE, in which tails can be observed.

In a kinematic study of the UCD population around M87 Zhang et al. (2015) have shown that UCDs follow radially biased orbital structure at large galactocentric distances. This is in good agreement with our results. In our study we find most UCDs in the apocenter and a few in the pericenter but almost nothing in between. In conclusion UCDs nearest to the apocenter of an orbit with high eccentricity could correspond to an UCD that is the result of a stripping and truncation scenario, as confirmed by the observation.

In the context of MOND simulations, satellites with the same mass for the nucleus and the envelope do not follow the same orbits. The same velocities in PoR turn into orbits with larger pericenters than in the previous sections. Nevertheless we do obtain

UCDs in the new orbits explored in that section.

Also similar to the conclusion for the LCDM sections, the envelope gets the majority of its mass stripped during the first close passage as we can observe the first big decline in mass in each pericenter line coincides with the satellite's first passage through its pericenter. Also, this decline is stronger the smaller the value for the pericenter is. This probes that the object looses most mass, passing near to the center where the density of the host is higher.

An important conclusion is drawn from the plot depicting the initial time of the UCD relative to the pericenter of the orbit: simulations conducted in PoR using MONDian dynamics, and those performed considering LCDM, show no significant differences as the data points from MOND simulations and LCDM simulations lie in the same region.

Chapter 6

Appendix

6.1 Parameters simulations

In this section we show tables with the exact parameters of all simulations. The parameters of the dwarf elliptical galaxy in each simulation and the orbit that it follows are displays in Table 6.1, Table 6.2,Table 6.3, Table 6.4, Table 6.5, Table 6.6 and Table 6.7. In principle, all the columns in the different tables represent the same, but simulations with their names in uppercase have the dark matter part and 'envelope' of the dwarf galaxy built by 10.000.000 particles, and the nucleus by 1.000.000. On the other hand, simulations where the name is in lowercase have the dark matter part and 'envelope' of the dwarf galaxy built by 2.000.000 particles, and the nucleus by 1.000.000. Also the number in the simulations name represent the pericenter distance of the orbit.
We perform a single simulation for those with uppercase names, whereas for simulations with lowercase names, we perform three repetitions for statistical purposes, each with a different seed number.

Sim	haloc			Plummer		nucleus		Orbit	
	Scale length [kpc]	R_{200} [kpc]	Mass $M_\odot$	r_{pl} [kpc]	Mass $M_\odot$	r_{pl} [kpc]	Mass $M_\odot$	apo [kpc]	peri [kpc]
C240	1	9.83	10^8	0.85	10^7	0.01	2.56×10^6	250	240
C200	1	9.83	10^8	0.85	10^7	0.01	2.56×10^6	250	200
C100	1	9.83	10^8	0.85	10^7	0.01	2.56×10^6	250	100
C50	1	9.83	10^8	0.85	10^7	0.01	2.56×10^6	250	50
C20	1	9.83	10^8	0.85	10^7	0.01	2.56×10^6	250	20
C10	1	9.83	10^8	0.85	10^7	0.01	2.56×10^6	250	10
C5	1	9.83	10^8	0.85	10^7	0.01	2.56×10^6	250	5
C2	1	9.83	10^8	0.85	10^7	0.01	2.56×10^6	250	2
C0.5	1	9.83	10^8	0.85	10^7	0.01	2.56×10^6	250	0.5

Table 6.1: Parameters simulations, different columns show the parameters of the components of the satellite: the dark matter part as 'haloc' the envelope part as 'Plummer' and de nucleus. Also the apo distance and peri distance of the orbit are displayed in the 'Orbit' column. The dark matter part and 'envelope' of the dwarf galaxy is built by 10.000.000 particles and the nucleus by 1.000.000. Source: this work.

Sim	haloc			Plummer		nucleus		Orbit	
	Scale length [kpc]	R_{200} [kpc]	Mass $M_\odot$	r_{pl} [kpc]	Mass $M_\odot$	r_{pl} [kpc]	Mass $M_\odot$	apo [kpc]	peri [kpc]
D240	1	21.19	10^9	0.85	10^7	0.01	2.56×10^6	250	240
D200	1	21.19	10^9	0.85	10^7	0.01	2.56×10^6	250	200
D100	1	21.19	10^9	0.85	10^7	0.01	2.56×10^6	250	100
D50	1	21.19	10^9	0.85	10^7	0.01	2.56×10^6	250	50
D20	1	21.19	10^9	0.85	10^7	0.01	2.56×10^6	250	20
D10	1	21.19	10^9	0.85	10^7	0.01	2.56×10^6	250	10
D5	1	21.19	10^9	0.85	10^7	0.01	2.56×10^6	250	5
D2	1	21.19	10^9	0.85	10^7	0.01	2.56×10^6	250	2
D0.5	1	21.19	10^9	0.85	10^7	0.01	2.56×10^6	250	0.5
E240	4	21.19	10^9	0.85	10^7	0.01	2.56×10^6	250	240
E200	4	21.19	10^9	0.85	10^7	0.01	2.56×10^6	250	200
E100	4	21.19	10^9	0.85	10^7	0.01	2.56×10^6	250	100
E50	4	21.19	10^9	0.85	10^7	0.01	2.56×10^6	250	50
E20	4	21.19	10^9	0.85	10^7	0.01	2.56×10^6	250	20
E10	4	21.19	10^9	0.85	10^7	0.01	2.56×10^6	250	10
E5	4	21.19	10^9	0.85	10^7	0.01	2.56×10^6	250	2
E2	4	21.19	10^9	0.85	10^7	0.01	2.56×10^6	250	5
E0.5	4	21.19	10^9	0.85	10^7	0.01	2.56×10^6	250	0.5
F240	4	21.19	10^9	1	10^7	0.01	2.56×10^6	250	240
F200	4	21.19	10^9	1	10^7	0.01	2.56×10^6	250	200
F100	4	21.19	10^9	1	10^7	0.01	2.56×10^6	250	100
F50	4	21.19	10^9	1	10^7	0.01	2.56×10^6	250	50
F20	4	21.19	10^9	1	10^7	0.01	2.56×10^6	250	20
F10	4	21.19	10^9	1	10^7	0.01	2.56×10^6	250	10
F5	4	21.19	10^9	1	10^7	0.01	2.56×10^6	250	5
F2	4	21.19	10^9	1	10^7	0.01	2.56×10^6	250	2
F0.5	4	21.19	10^9	1	10^7	0.01	2.56×10^6	250	0.5

Table 6.2: Parameters simulations, same columns as the previous Table 6.1. Source: this work.

Sim	haloc			Plummer		nucleus		Orbit	
	Scale length [kpc]	R_{200} [kpc]	Mass $M_\odot$	r_{pl} [kpc]	Mass $M_\odot$	r_{pl} [kpc]	Mass $M_\odot$	apo [kpc]	peri [kpc]
G240	1	21.19	10^9	0.85	10^8	0.01	2.56×10^6	250	200
G200	1	21.19	10^9	0.85	10^8	0.01	2.56×10^6	250	200
G100	1	21.19	10^9	0.85	10^8	0.01	2.56×10^6	250	100
G50	1	21.19	10^9	0.85	10^8	0.01	2.56×10^6	250	50
G20	1	21.19	10^9	0.85	10^8	0.01	2.56×10^6	250	20
G10	1	21.19	10^9	0.85	10^8	0.01	2.56×10^6	250	10
G5	1	21.19	10^9	0.85	10^8	0.01	2.56×10^6	250	5
G2	1	21.19	10^9	0.85	10^8	0.01	2.56×10^6	250	2
G0.5	1	21.19	10^9	0.85	10^8	0.01	2.56×10^6	250	0.5
H240	4	21.19	10^9	0.85	10^8	0.01	2.56×10^6	250	240
H200	4	21.19	10^9	0.85	10^8	0.01	2.56×10^6	250	200
H100	4	21.19	10^9	0.85	10^8	0.01	2.56×10^6	250	100
H50	4	21.19	10^9	0.85	10^8	0.01	2.56×10^6	250	50
H20	4	21.19	10^9	0.85	10^8	0.01	2.56×10^6	250	20
H10	4	21.19	10^9	0.85	10^8	0.01	2.56×10^6	250	10
H5	4	21.19	10^9	0.85	10^8	0.01	2.56×10^6	250	5
H2	4	21.19	10^9	0.85	10^8	0.01	2.56×10^6	250	2
H0.5	4	21.19	10^9	0.85	10^8	0.01	2.56×10^6	250	0.5
I240	4	21.19	10^9	1	10^8	0.01	2.56×10^6	250	240
I200	4	21.19	10^9	1	10^8	0.01	2.56×10^6	250	200
I100	4	21.19	10^9	1	10^8	0.01	2.56×10^6	250	100
I50	4	21.19	10^9	1	10^8	0.01	2.56×10^6	250	50
I20	4	21.19	10^9	1	10^8	0.01	2.56×10^6	250	20
I10	4	21.19	10^9	1	10^8	0.01	2.56×10^6	250	10
I5	4	21.19	10^9	1	10^8	0.01	2.56×10^6	250	5
I2	4	21.19	10^9	1	10^8	0.01	2.56×10^6	250	2
I0.5	4	21.19	10^9	1	10^8	0.01	2.56×10^6	250	0.5

Table 6.3: Parameters simulations, same columns as the previous Table 6.1 and Table 6.2. Source: this work.

	haloc			Plummer		nucleus		Orbit	
Sim	Scale length [kpc]	R_{200} [kpc]	Mass $M_\odot$	r_{pl} [kpc]	Mass $M_\odot$	r_{pl} [kpc]	Mass $M_\odot$	apo [kpc]	peri [kpc]
a240	1	45.66	10^{10}	0.85	10^7	0.01	2.56×10^6	250	240
a200	1	45.66	10^{10}	0.85	10^7	0.01	2.56×10^6	250	200
a100	1	45.66	10^{10}	0.85	10^7	0.01	2.56×10^6	250	100
a50	1	45.66	10^{10}	0.85	10^7	0.01	2.56×10^6	250	50
a20	1	45.66	10^{10}	0.85	10^7	0.01	2.56×10^6	250	20
a10	1	45.66	10^{10}	0.85	10^7	0.01	2.56×10^6	250	10
a5	1	45.66	10^{10}	0.85	10^7	0.01	2.56×10^6	250	5
a2	1	45.66	10^{10}	0.85	10^7	0.01	2.56×10^6	250	2
a0.5	1	45.66	10^{10}	0.85	10^7	0.01	2.56×10^6	250	0.5
b240	1	45.66	10^{10}	0.85	10^8	0.01	2.56×10^6	250	240
b200	1	45.66	10^{10}	0.85	10^8	0.01	2.56×10^6	250	200
b100	1	45.66	10^{10}	0.85	10^8	0.01	2.56×10^6	250	100
b50	1	45.66	10^{10}	0.85	10^8	0.01	2.56×10^6	250	50
b20	1	45.66	10^{10}	0.85	10^8	0.01	2.56×10^6	250	20
b10	1	45.66	10^{10}	0.85	10^8	0.01	2.56×10^6	250	10
b5	1	45.66	10^{10}	0.85	10^8	0.01	2.56×10^6	250	5
b2	1	45.66	10^{10}	0.85	10^8	0.01	2.56×10^6	250	2
b0.5	1	45.66	10^{10}	0.85	10^8	0.01	2.56×10^6	250	0.5
c240	1	9.83	10^8	0.85	10^7	0.01	2.56×10^6	250	240
c200	1	9.83	10^8	0.85	10^7	0.01	2.56×10^6	250	200
c100	1	9.83	10^8	0.85	10^7	0.01	2.56×10^6	250	100
c50	1	9.83	10^8	0.85	10^7	0.01	2.56×10^6	250	50
c20	1	9.83	10^8	0.85	10^7	0.01	2.56×10^6	250	20
c10	1	9.83	10^8	0.85	10^7	0.01	2.56×10^6	250	10
c5	1	9.83	10^8	0.85	10^7	0.01	2.56×10^6	250	5
c2	1	9.83	10^8	0.85	10^7	0.01	2.56×10^6	250	2
c0.5	1	9.83	10^8	0.85	10^7	0.01	2.56×10^6	250	0.5

Table 6.4: Parameters simulations, same columns as the previous Table 6.1, Table 6.2 and Table 6.3. But in these simulations the dark matter part and 'envelope' of the dwarf galaxy is built by 2.000.000 particles and the nucleus by 1.000.000. Source: this work.

	haloc			Plummer		nucleus		Orbit	
Sim	Scale length	R_{200}	Mass	r_{pl}	Mass	r_{pl}	Mass	apo	peri
	[kpc]	[kpc]	$M_\odot$	[kpc]	$M_\odot$	[kpc]	$M_\odot$	[kpc]	[kpc]
d240	1	21.19	10^9	0.85	10^7	0.01	2.56×10^6	250	240
d200	1	21.19	10^9	0.85	10^7	0.01	2.56×10^6	250	200
d100	1	21.19	10^9	0.85	10^7	0.01	2.56×10^6	250	100
d50	1	21.19	10^9	0.85	10^7	0.01	2.56×10^6	250	50
d20	1	21.19	10^9	0.85	10^7	0.01	2.56×10^6	250	20
d10	1	21.19	10^9	0.85	10^7	0.01	2.56×10^6	250	10
d5	1	21.19	10^9	0.85	10^7	0.01	2.56×10^6	250	5
d2	1	21.19	10^9	0.85	10^7	0.01	2.56×10^6	250	2
d0.5	1	21.19	10^9	0.85	10^7	0.01	2.56×10^6	250	0.5
e240	4	21.19	10^9	0.85	10^7	0.01	2.56×10^6	250	240
e200	4	21.19	10^9	0.85	10^7	0.01	2.56×10^6	250	200
e100	4	21.19	10^9	0.85	10^7	0.01	2.56×10^6	250	100
e50	4	21.19	10^9	0.85	10^7	0.01	2.56×10^6	250	50
e20	4	21.19	10^9	0.85	10^7	0.01	2.56×10^6	250	20
e10	4	21.19	10^9	0.85	10^7	0.01	2.56×10^6	250	10
e5	4	21.19	10^9	0.85	10^7	0.01	2.56×10^6	250	5
e2	4	21.19	10^9	0.85	10^7	0.01	2.56×10^6	250	2
e0.5	4	21.19	10^9	0.85	10^7	0.01	2.56×10^6	250	0.5
f240	4	21.19	10^9	1	10^7	0.01	2.56×10^6	250	240
f200	4	21.19	10^9	1	10^7	0.01	2.56×10^6	250	200
f100	4	21.19	10^9	1	10^7	0.01	2.56×10^6	250	100
f50	4	21.19	10^9	1	10^7	0.01	2.56×10^6	250	50
f20	4	21.19	10^9	1	10^7	0.01	2.56×10^6	250	20
f10	4	21.19	10^9	1	10^7	0.01	2.56×10^6	250	10
f5	4	21.19	10^9	1	10^7	0.01	2.56×10^6	250	5
f2	4	21.19	10^9	1	10^7	0.01	2.56×10^6	250	2
f0.5	4	21.19	10^9	1	10^7	0.01	2.56×10^6	250	0.5

Table 6.5: Parameters simulations, same columns as the previous Table 6.4. Source: this work.

	haloc			Plummer		nucleus		Orbit	
Sim	Scale length [kpc]	R_{200} [kpc]	Mass $M_\odot$	r_{pl} [kpc]	Mass $M_\odot$	r_{pl} [kpc]	Mass $M_\odot$	apo [kpc]	peri [kpc]
g240	1	21.19	10^9	0.85	10^8	0.01	2.56×10^6	250	240
g200	1	21.19	10^9	0.85	10^8	0.01	2.56×10^6	250	200
g100	1	21.19	10^9	0.85	10^8	0.01	2.56×10^6	250	100
g50	1	21.19	10^9	0.85	10^8	0.01	2.56×10^6	250	50
g20	1	21.19	10^9	0.85	10^8	0.01	2.56×10^6	250	20
g10	1	21.19	10^9	0.85	10^8	0.01	2.56×10^6	250	10
g5	1	21.19	10^9	0.85	10^8	0.01	2.56×10^6	250	5
g2	1	21.19	10^9	0.85	10^8	0.01	2.56×10^6	250	2
g0.5	1	21.19	10^9	0.85	10^8	0.01	2.56×10^6	250	0.5
h240	4	21.19	10^9	0.85	10^8	0.01	2.56×10^6	250	240
h200	4	21.19	10^9	0.85	10^8	0.01	2.56×10^6	250	200
h100	4	21.19	10^9	0.85	10^8	0.01	2.56×10^6	250	100
h50	4	21.19	10^9	0.85	10^8	0.01	2.56×10^6	250	50
h20	4	21.19	10^9	0.85	10^8	0.01	2.56×10^6	250	20
h10	4	21.19	10^9	0.85	10^8	0.01	2.56×10^6	250	10
h5	4	21.19	10^9	0.85	10^8	0.01	2.56×10^6	250	5
h2	4	21.19	10^9	0.85	10^8	0.01	2.56×10^6	250	2
h0.5	4	21.19	10^9	0.85	10^8	0.01	2.56×10^6	250	0.5
i240	4	21.19	10^9	1	10^8	0.01	2.56×10^6	250	240
i200	4	21.19	10^9	1	10^8	0.01	2.56×10^6	250	200
i100	4	21.19	10^9	1	10^8	0.01	2.56×10^6	250	100
i50	4	21.19	10^9	1	10^8	0.01	2.56×10^6	250	50
i20	4	21.19	10^9	1	10^8	0.01	2.56×10^6	250	20
i10	4	21.19	10^9	1	10^8	0.01	2.56×10^6	250	10
i5	4	21.19	10^9	1	10^8	0.01	2.56×10^6	250	5
i2	4	21.19	10^9	1	10^8	0.01	2.56×10^6	250	2
i0.5	4	21.19	10^9	1	10^8	0.01	2.56×10^6	250	0.5

Table 6.6: Parameters simulations, same columns as the previous Table 6.4 and Table 6.5. Source: this work.

Sim	haloc			Plummer		nucleus		Orbit	
	Scale length [kpc]	R_{200} [kpc]	Mass $M_\odot$	r_{pl} [kpc]	Mass $M_\odot$	r_{pl} [kpc]	Mass $M_\odot$	apo [kpc]	peri [kpc]
j240	4	45.66	10^{10}	0.85	10^8	0.01	2.56×10^6	250	240
j200	4	45.66	10^{10}	0.85	10^8	0.01	2.56×10^6	250	200
j100	4	45.66	10^{10}	0.85	10^8	0.01	2.56×10^6	250	100
j50	4	45.66	10^{10}	0.85	10^8	0.01	2.56×10^6	250	50
j20	4	45.66	10^{10}	0.85	10^8	0.01	2.56×10^6	250	20
j10	4	45.66	10^{10}	0.85	10^8	0.01	2.56×10^6	250	10
j5	4	45.66	10^{10}	0.85	10^8	0.01	2.56×10^6	250	5
j2	4	45.66	10^{10}	0.85	10^8	0.01	2.56×10^6	250	2
j0.5	4	45.66	10^{10}	0.85	10^8	0.01	2.56×10^6	250	0.5
k240	4	45.66	10^{10}	1	10^8	0.01	2.56×10^6	250	240
k200	4	45.66	10^{10}	1	10^8	0.01	2.56×10^6	250	200
k100	4	45.66	10^{10}	1	10^8	0.01	2.56×10^6	250	100
k50	4	45.66	10^{10}	1	10^8	0.01	2.56×10^6	250	50
k20	4	45.66	10^{10}	1	10^8	0.01	2.56×10^6	250	20
k10	4	45.66	10^{10}	1	10^8	0.01	2.56×10^6	250	10
k5	4	45.66	10^{10}	1	10^8	0.01	2.56×10^6	250	5
k2	4	45.66	10^{10}	1	10^8	0.01	2.56×10^6	250	2
k0.5	4	45.66	10^{10}	1	10^8	0.01	2.56×10^6	250	0.5

Table 6.7: Parameters simulations, same columns as the previous Table 6.4, Table 6.5 and Table 6.6. Source: this work.

6.2 Simulations results

In this section we present in Tables the results of all simulations from Table 6.1. Columns shown (in order), simulation time when the dark matter halo gets destroyed, the percent of the baryonic part when the dark matter halo is destroyed , the time when the Plummer envelope gets destroyed. Then time when the object begins to be an UCDs in the

simulation, the mass of the object, the position, mass to light ratio and % of the dark matter content of the object.

Sim	haloc $T_{0.1}^{DM}$ [Myr]	$M_{T_{0.1}^{DM}}^{envelope}$ %	$M_{T_{0.1}^{DM}}^{Plummer}$ %	Envelope $T_{0.1}^{envelope}$ [Myr]	Initial T [Myr]	UCDs M $M_\odot$	Posi [kpc]	M/L	% DM_0 %
C240*	1491	40	52						
C200	1295	38	50	7850	7850	5.5×10^6	248	1.56	2
C100	951	31	45	1890	1890	5.5×10^6	183	1.56	2
C50	791	23	38	1036	1036	5.5×10^6	54	1.56	2
$C20^+$	694	18	35	923	923	5.5×10^6	76	1.56	2
C10	643	11	29	663	663	11.5×10^6	247	3.26	8
C5	305	26	41	459	459	10.5×10^6	196	2.98	7
C2	305	24	39	311	311	6.5×10^6	3	1.84	3
C0.5	305	24	39	310	310	5.5×10^6	1	1.56	2

Table 6.8: Results of simulations from Table 6.1. Columns shown (in order), simulation time when the dark matter halo gets destroyed, the percent of the baryonic part when the dark matter halo is destroyed , the time when the Plummer envelope gets destroyed. Then time when the object begins to be an UCDs in the simulation, the mass of the object, the position, mass to light ratio and % of the dark matter content of the object. Source: this work.

Sim	haloc			Envelope	Initial	UCDs			
	$T_{0.1}^{DM}$	$M_{T_{0.1}^{DM}}^{envelope}$	$M_{T_{0.1}^{DM}}^{Plummer}$	$T_{0.1}^{envelope}$	T	M	Posi	M/L	% DM_0
	[Myr]	%	%	[Myr]	[Myr]	$M_\odot$	[kpc]		%
D240	1729	28	42	6595	6595	23.5×10^6	238	6.65	2
D200	1374	22	38	4204	4204	23.5×10^6	230	6.65	2
D100	989	19	35	1772	1772	40.5×10^6	231	9.48	3
D50	841	14	31	1019	1019	33.5×10^6	69	9.48	3
D20	733	11	29	834	834	43.5×10^6	176	12.31	4
$D10^+$	689	8	27	493	689	103.3×10^6	241	30.99	10
$D5^+$	665	4	23	471	665	102.9×10^6	245	35.07	10
$D2^+$	648	2	22	306	648	102.7×10^6	247	37.57	10
$D0.5^+$	307	8	27	306	307	103.3×10^6	7	30.99	10
E240	997	59	67	5103	5103	7.5×10^6	248	2.13	0.4
E200	936	55	64	3358	3358	10.5×10^6	248	2.98	0.7
E100	874	38	50	1586	1586	43.5×10^6	244	12.31	4
E50	808	30	44	1426	1426	93.5×10^6	248	26.46	9
$E20^+$	1339	4	23	1272	1339	102.9×10^6	243	35.07	4
$E10^+$	724	6	25	656	724	103.1×10^6	231	32.90	10
$E5^+$	705	2	22	551	705	102.7×10^6	236	37.57	10
$E2^+$	710	0.6	21	311	710	102.5×10^6	233	39.54	10
$E0.5^+$	695	0.3	20	310	695	102.5×10^6	238	39.99	10
F240	989	50	60	3526	3526	10.5×10^6	250	2.99	0.7
F200	923	45	56	2483	2483	12.5×10^6	229	3.54	0.9
F100	874	27	42	1229	1229	11.5×10^6	99	3.26	0.8
F50	807	20	36	1351	1351	83.5×10^6	246	23.63	8
$F20^+$	1291	5	24	799	1291	103×10^6	249	33.95	10
$F10^+$	723	3	23	610	723	102.8×10^6	231	36.28	10
$F5^+$	705	1	21	312	705	102.6×10^6	236	38.95	10
$F2^+$	709	0.4	20	309	709	102.5×10^6	233	39.84	10
$F0.5^+$	695	0.2	20	309	695	102.5×10^6	238	40.14	10

Table 6.9: Same columns as the previous Table 6.8 . But results of simulations from Table 6.2. Source: this work.

Sim	haloc $T_{0.1}^{DM}$ [Myr]	$M_{T_{0.1}^{DM}}^{envelope}$ %	$M_{T_{0.1}^{DM}}^{Plummer}$ %	Envelope $T_{0.1}^{envelope}$ [Myr]	Initial T [Myr]	UCDs M $M_\odot$	Posi [kpc]	M/L	% DM_0 %
G240*									
G200	4848	69	70						
G100	1669	58	59						
G50	984	58	59	5798	5798	28.5×10^6	190	1.79	1
G20	765	50	51	2234	2234	29.5×10^6	26	1.79	1
G10	693	41	42	1565	1565	30.5×10^6	9	1.79	1
G5	640	32	34	1229	1229	32.5×10^6	248	2.59	2
G2	310	37	39	926	926	22.5×10^6	10	1.79	1
G0.5	309	40	41	489	489	42.5×10^6	215	3.39	3
H240*	1836	87	87						
H200*	1431	85	85						
H100	931	76	77	5743	5743	18.5×10^6	248	1.47	0.6
H50	768	64	65	2117	2117	31.5×10^6	248	1.79	1
H20	1308	13	15	1385	1385	82.5×10^6	229	6.58	7
H10	572	40	41	1006	1006	19.5×10^6	116	1.55	0.7
H5	731	13	15	819	819	22.5×10^6	169	1.79	1
$H2^+$	711	2	4	555	711	104.5×10^6	232	23.05	10
$H0.5^+$	695	0.9	3	352	695	103.4×10^6	237	30.11	10
I240*	1812	81	81						
I200*	1421	80	80						
I100	923	69	70	3930	3930	20.3×10^6	208	1.55	0.7
I50	766	55	56	1727	1727	19.5×10^6	62	1.55	0.7
$I20^+$	1308	7	9	1264	1308	109.5×10^6	247	11.48	10
I10	599	30	32	929	929	19.5×10^6	27	1.55	0.7
$I5^+$	731	6	8	662	731	108.9×10^8	225	12.71	10
$I2^+$	682	2	4	479	682	104.5×10^6	241	23.05	10
$I0.5^+$	695	0.6	3	329	695	103.2×10^6	237	32.90	10

Table 6.10: Same columns as the previous Table 6.8 and Table 6.9. But results of simulations from Table 6.3. Source: this work.

Sim	haloc			Envelope	Initial	UCDs			
	$T_{0.1}^{DM}$	$M_{T_{0.1}^{DM}}^{envelope}$	$M_{T_{0.1}^{DM}}^{Plummer}$	$T_{0.1}^{envelope}$	T	M	Posi	M/L	% DM_0
	[Myr]	%	%	[Myr]	[Myr]	$M_\odot$	[kpc]		%
a240$^+$	9995	7	23	4946	9995	10^9	250	342.62	10
a200$^+$	4526	8	26	3038	4526	10^9	249	307.97	10
a100$^+$	1232	8	27	1137	1232	10^9	99	300.9	10
a50	924	11	29	990	990	803.5×10^6	101	227.34	8
a20$^+$	772	8	27	541	772	10^9	214	300.9	10
a10$^+$	701	5	24	296	701	10^9	236	330.55	10
a5$^+$	667	3	23	292	667	10^9	242	353.8	10
a2$^+$	639	2	22	292	639	10^9	245	366.71	10
a0.5$^+$	310	1	21	292	310	10^9	1	369.4	10
b240	-								
b200	7443	50	51						
b100	1649	48	49						
b50	999	48	49	6903	6903	102.3×10^6	216	8.26	0.9
b20	797	47	48	2951	2951	92.5×10^6	129	7.39	0.8
b10	707	38	40	2126	2126	92.5×10^6	100	7.39	0.8
b5	668	28	30	1632	1632	92.5×10^6	143	7.38	0.8
b2	375	22	24	1137	1137	112.5×10^6	229	8.97	1
b0.5	310	18	20	917	917	112.5×10^6	12	8.97	1
c240	1486	40	52						
c200	1292	38	50	7637	7637	5.5×10^6	241	1.56	2
c100	949	31	45	1875	1875	6.3×10^6	205	1.56	2
c50	790	23	38	1036	1036	6.3×10^6	54	1.56	2
c20$^+$	1304	3	23	923	1304	12.8×10^6	248	4.52	10
c10	643	11	29	663	663	11.5×10^6	246	3.26	8
c5	305	26	41	457	457	10.5×10^6	194	2.98	7
c2	305	24	39	311	311	6.5×10^6	3	1.84	3
c0.5	305	24	39	310	310	6.4×10^6	1	1.56	2

Table 6.11: Same columns as the previous Table 6.8, Table 6.9 and Table 6.10. But results of simulations from Table 6.4. Source: this work.

Sim	haloc			Envelope	Initial	UCDs			
	$T_{0.1}^{DM}$	$M_{T_{0.1}^{DM}}^{envelope}$	$M_{T_{0.1}^{DM}}^{Plummer}$	$T_{0.1}^{envelope}$	T	M	Posi	M/L	% DM_0
	[Myr]	%	%	[Myr]	[Myr]	$M_\odot$	[kpc]		%
d240	1745	27	42	5442	5442	23.5×10^6	249	6.65	2
d200	1381	22	38	3933	3933	23.5×10^6	199	6.65	2
d100	991	19	35	1750	1750	43.55×10^6	237	12.31	4
d50	841	14	31	1017	1017	33.5×10^6	71	9.48	3
d20	734	11	29	833	833	43.5×10^6	176	12.31	4
$d10^+$	689	8	27	493	689	103.3×10^6	241	30.99	10
$d5^+$	664	4	23	471	664	102.9×10^6	245	35.07	10
$d2^+$	648	2	22	306	648	103.5×10^6	247	30.11	10
$d0.5^+$	307	0.8	21	306	307	103.4×10^6	7	30.11	10
e240	1011	59	67	4748	4748	8.5×10^6	249	2.42	0.5
e200	953	54	63	3233	3233	11.5×10^6	245	3.26	0.8
e100	877	38	50	1522	1522	43.5×10^6	242	12.31	4
e50	808	29	43	1425	1425	93.5×10^6	248	26.46	9
$e20^+$	1292	8	27	1270	1292	103.3×10^6	248	30.99	10
$e10^+$	723	6	25	657	723	103.1×10^6	231	32.9	10
$e5^+$	705	2	22	548	705	102.7×10^6	236	37.57	10
$e2^+$	688	0.9	21	311	688	102.6×10^6	240	39.10	10
$e0.5^+$	694	0.3	20	310	694	102.5×10^6	238	39.99	10
f240	1003	50	60	3385	3385	10.5×10^6	250	2.98	0.7
f200	943	45	56	2396	2396	13.5×10^6	240	3.82	1
f100	876	27	42	1220	1220	11.5×10^6	99	3.26	0.8
f50	808	19	35	936	936	23.5×10^6	154	6.65	2
$f20^+$	1292	5	24	796	1292	103×10^6	248	33.95	10
$f10^+$	723	3	23	611	723	102.8×10^6	231	36.28	10
$f5^+$	705	1	21	312	705	102.6×10^6	236	38.95	10
$f2^+$	688	0.7	21	309	688	102.6×10^6	239	39.39	10
$f0.5^+$	694	0.2	20	309	694	102×10^6	238	40.14	10

Table 6.12: Same columns as previous Tables from this section showing results of simulations from Table 6.5. Source: this work.

Sim	haloc			Envelope	Initial	UCDs			
	$T_{0.1}^{DM}$	$M_{T_{0.1}^{DM}}^{envelope}$	$M_{T_{0.1}^{DM}}^{Plummer}$	$T_{0.1}^{envelope}$	T	M	Posi	M/L	% DM_0
	[Myr]	%	%	[Myr]	[Myr]	$M_\odot$	[kpc]		%
g240*									
g200*	4892	69	70						
g100*	1673	58	59						
g50	985	58	59	5836	5836	29.52×10^6	163	1.79	1
g20	766	49	50	2235	2235	29.5×10^6	25	1.79	1
g10	693	41	42	1565	1565	30.5×10^6	9	1.79	1
g5	426	39	40	1232	1232	32.5×10^6	248	2.59	2
g2	310	37	39	926	926	22.5×10^6	10	1.79	1
g0.5	309	40	41	488	488	42.5×10^6	214	3.39	3
h240*	1855	86	86						
h200*	1441	85	85						
h100	937	76	77	5783	5783	18.5×10^6	249	1.47	0.6
h50	771	64	65	2123	2123	32.5×10^6	247	2.59	2
h20	1309	13	15	1389	1389	72.5×10^6	227	5.78	6
h10	783	40	41	1019	1019	19.5×10^6	132	1.55	0.7
h5	730	13	15	813	813	22.5×10^6	173	1.79	1
$h2^+$	682	3	5	554	682	105.5×10^6	241	19.06	10
$h0.5^+$	695	0.9	3	352	695	103.4×10^6	237	30.11	10
i240*	1841	81	81						
i200*	1430	79	79						
i100	928	69	70	3965	3965	20.5×10^6	221	1.63	0.8
i50	769	55	56	1729	1729	19.5×10^6	60	1.55	0.7
$i20^+$	1308	7	9	1265	1308	109.5×10^6	247	11.48	10
i10	604	30	32	929	929	19.5×10^6	37	1.55	0.7
$i5^+$	730	6	8	662	730	108.5×10^6	225	12.71	10
$i2^+$	682	2	4	479	682	104.5×10^6	240	23.05	10
$i0.5^+$	696	0.6	3	329	696	103.1×10^6	237	32.9	10

Table 6.13: Same columns as previous Tables from this section showing results of simulations from Table 6.6. Source: this work.

Sim	haloc			Envelope	Initial	UCDs			
	$T_{0.1}^{DM}$	$M_{T_{0.1}^{DM}}^{envelope}$	$M_{T_{0.1}^{DM}}^{Plummer}$	$T_{0.1}^{envelope}$	T	M	Posi	M/L	% DM_0
	[Myr]	%	%	[Myr]	[Myr]	$M_\odot$	[kpc]		%
j240*	1639	74	75						
j200*	1349	73	74						
j100*	959	72	73						
j50	810	69	70	3848	3848	22.5×10^6	50	1.79	0.1
j20	710	65	66	2222	2222	22.5×10^6	32	1.79	0.1
j10	668	60	61	1561	1561	13.2×10^6	10	1.05	0.007
j5	637	49	50	1221	1221	212.5×10^6	246	16.95	2
j2	306	55	56	923	923	22.5×10^6	5	1.79	0.1
j0.5	306	55	56	562	562	412.5×10^6	241	32.91	4
k240*	1630	67	68						
k200*	1339	67	68						
k100	956	65	66	8663	8663	22.5×10^6	135	1.79	0.1
k50	809	61	62	3085	3085	22.5×10^6	108	1.79	0.1
k20	710	57	58	1917	1917	212.5×10^6	248	16.95	2
k10	668	51	52	1528	1528	22.5×10^6	67	1.79	0.1
k5	639	39	40	1016	1016	62.5×10^6	142	4.98	0.5
k2	306	47	48	903	903	312.5×10^6	50	2.59	0.2
k0.5	306	47	48	467	467	32.5×10^6	201	24.93	3

Table 6.14: Same columns as previous Tables from this section showing results of simulations from Table 6.7. Source: this work.

Sim	haloc $T_{0.1}^{DM}$ [Myr]	$M_{T_{0.1}^{DM}}^{envelope}$ %	$M_{T_{0.1}^{DM}}^{Plummer}$ %	Envelope $T_{0.1}^{envelope}$ [Myr]	Initial T [Myr]	UCDs M 10^6 $M_\odot$	Posi [kpc]	M/L	% DM_0 %
aa240$^+$	9995	7	23	4891	9995	10^9	250	342.62	10
aa200$^+$	4530	8	26	3002	4530	10^9	249	307.97	10
aa100$^+$	1233	7	26	1154	1233	10^9	98	310.17	10
aa50	923	10	27	970	970	803×10^6	122	227.34	8
aa20$^+$	771	8	27	524	771	10^9	215	300.9	10
aa10$^+$	700	4	24	294	700	10^9	236	341.78	10
aa5$^+$	667	3	23	292	667	10^9	242	353.8	10
aa2$^+$	325	2	22	291	325	10^9	35	366.71	10
aa0.5$^+$	310	1	21	292	310	10^9	1	366.71	10
bb240*	-								
bb200*	7426	50	51						
bb100*	1648	48	49						
bb50	998	48	49	6900	6900	102.3×10^6	216	8.26	0.9
bb20	797	47	48	2948	2948	92.5×10^6	120	7.39	0.8
bb10	706	37	39	2124	2124	92.5×10^6	120	7.39	0.8
bb5	667	28	30	1626	1626	92.5×10^6	137	7.38	0.8
bb2	312	22	24	1133	1133	112.5×10^6	227	8.97	1
bb0.5	310	19	21	917	917	112.5×10^6	15	8.97	1
cc240*	1489	40	52						
cc200	1293	38	50	7671	7671	5.5×10^6	244	1.56	2
cc100	950	31	45	1888	1888	5.5×10^6	183	1.56	2
cc50	791	24	39	1036	1036	5.5×10^6	55	1.56	2
cc20$^+$	1310	2	22	923	1310	12.7×10^6	247	4.65	10
cc10	642	11	29	663	663	11.5×10^6	247	3.26	8
cc5	305	26	41	460	460	10.5×10^6	196	2.98	7
cc2	305	25	40	311	311	7.5×10^6	2	2.13	4
cc0.5	305	24	39	310	310	7.5×10^6	1	2.13	4

Table 6.15: Same columns as previous Tables from this section showing the second sets of results of simulations from Table 6.4. Source: this work.

Sim	haloc			Envelope	Initial	UCDs			
	$T_{0.1}^{DM}$	$M_{T_{0.1}^{DM}}^{envelope}$	$M_{T_{0.1}^{DM}}^{Plummer}$	$T_{0.1}^{envelope}$	T	M	Posi	M/L	% DM_0
	[Myr]	%	%	[Myr]	[Myr]	10^6 $M_\odot$	[kpc]		%
dd240	1745	27	42	5429	5429	23.5×10^6	249	6.65	2
dd200	1380	22	38	3952	3952	23.5×10^6	200	6.65	2
dd100	992	19	35	1745	1745	43.5×10^6	239	12.31	4
dd50	842	15	32	1017	1017	33.5×10^6	73	9.48	3
dd20	734	11	29	838	838	43.5×10^6	172	12.31	4
dd10$^+$	689	8	27	491	689	103.3×10^6	241	30.99	10
dd5$^+$	665	4	23	472	665	102.9×10^6	245	35.07	10
dd2$^+$	648	2	22	306	648	102.7×10^6	247	37.57	10
dd0.5$^+$	307	9	27	306	307	103.5×10^6	10	30.11	10
ee240	1007	59	67	4606	4606	8.5×10^6	250	2.42	0.5
ee200	949	54	63	3261	3261	11.5×10^6	247	3.26	0.8
ee100	876	38	50	1583	1583	43.5×10^6	243	12.31	4
ee50	808	30	44	1425	1425	93.5×10^6	248	26.46	9
ee20$^+$	1342	4	23	1250	1342	102.9×10^6	243	35.07	10
ee10$^+$	724	6	25	656	724	103.1×10^6	231	32.9	10
ee5$^+$	705	2	22	551	705	102.7×10^6	236	37.57	10
ee2$^+$	688	0.9	21	311	688	102.6×10^6	239	39.10	10
ee0.5$^+$	695	0.3	20	310	695	102.5×10^6	238	39.99	10
ff240	1000	50	60	3424	3424	10.5×10^6	250	2.98	0.7
ff200	939	44	55	2432	2432	13.5×10^6	235	3.82	1
ff100	876	27	42	1217	1217	11.5×10^6	101	3.26	0.8
ff50	808	20	36	938	938	23.5×10^6	153	6.65	2
ff20$^+$	1341	2	22	794	1341	102.7×10^6	243	37.57	10
ff10$^+$	723	3	23	609	723	102.8×10^6	231	36.28	10
ff5$^+$	705	1	21	312	705	102.6×10^6	236	38.95	10
ff2$^+$	688	0.6	21	309	688	102.5×10^6	240	39.54	10
ff0.5$^+$	694	0.2	20	309	694	102.5×10^6	238	40.14	10

Table 6.16: Same columns as previous Tables from this section showing the second sets of results of simulations from Table 6.5. Source: this work.

Sim	haloc $T_{0.1}^{DM}$ [Myr]	$M_{T_{0.1}^{DM}}^{envelope}$ %	$M_{T_{0.1}^{DM}}^{Plummer}$ %	Envelope $T_{0.1}^{envelope}$ [Myr]	Initial T [Myr]	UCDs M 10^6 $M_\odot$	Posi [kpc]	M/L	% DM_0 %
gg240*									
gg200*	4880	69	70						
gg100*	1674	58	59						
gg50	985	58	59	5842	5842	29.5×10^6	158	1.79	1
gg20	766	49	50	2235	2235	30.5×10^6	26	1.79	1
gg10	693	41	42	1563	1563	30.5×10^6	11	1.79	1
gg5	427	39	40	1230	1230	32.5×10^6	248	2.59	2
gg2	310	37	39	926	926	22.5×10^6	13	1.79	1
gg0.5	309	40	41	488	488	42.5×10^6	214	3.39	3
hh240*	1849	86	86						
hh200*	1439	85	85						
hh100	936	76	77	5790	5790	18.5×10^6	249	1.47	0.6
hh50	771	64	65	2125	2125	32.5×10^6	247	2.59	2
hh20	1309	13	15	1388	1388	82.5×10^6	228	6.58	7
hh10	572	40	41	1007	1007	19.5×10^6	115	1.55	0.7
hh5	730	13	15	819	819	22.5×10^6	170	1.79	1
$hh2^+$	710	2	4	555	710	104.4×10^6	233	23.05	10
$hh0.5^+$	696	0.9	3	353	696	103.4×10^6	237	30.11	10
ii240*	1835	81	81						
ii200*	1427	80	80						
ii100	927	69	70	3959	3959	20.5×10^6	219	1.63	0.8
ii50	768	55	56	1729	1729	19.5×10^6	60	1.55	0.7
$ii20^+$	1308	7	9	1264	1308	109.5×10^6	247	11.48	10
ii10	599	30	32	929	929	19.5×10^6	29	1.55	0.7
$ii5^+$	698	7	9	662	698	109.5×10^6	237	11.48	10
$ii2^+$	682	2	4	480	682	104.5×10^6	241	23.05	10
$ii0.5^+$	696	0.7	3	329	696	103.2×10^6	237	31.91	10

Table 6.17: Same columns as previous Tables from this section showing the second sets of results of simulations from Table 6.6. Source: this work.

Sim	haloc $T_{0.1}^{DM}$ [Myr]	$M_{T_{0.1}^{DM}}^{envelope}$ %	$M_{T_{0.1}^{DM}}^{Plummer}$ %	Envelope $T_{0.1}^{envelope}$ [Myr]	Initial T [Myr]	UCDs M 10^6 $M_\odot$	Posi [kpc]	M/L	% DM_0 %
jj240*	1638	73	74						
jj200*	1349	73	74						
jj100*	958	72	73						
jj50	809	69	70	3846	3846	22.5×10^6	51	1.79	0.1
jj20	710	64	65	2219	2219	22.5×10^6	39	1.79	0.1
jj10	668	59	60	1561	1561	14.5×10^6	10	1.15	00.2
jj5	638	49	50	1210	1210	112.5×10^6	246	8.97	1
jj2	306	55	56	923	923	22.5×10^6	7	1.79	0.1
jj0.5	306	55	56	566	566	412.5×10^6	242	32.91	4
kk240*	1631	67	68						
kk200*	1341	66	67						
kk100	955	65	66	8720	8720	22.5×10^6	107	1.79	0.1
kk50	808	61	62	3075	3075	22.5×10^6	118	1.79	0.1
kk20	710	57	58	1913	1913	212.5×10^6	248	16.95	2
kk10	668	51	52	1531	1531	22.5×10^6	61	1.79	0.1
kk5	639	38	40	1011	1011	52.5×10^6	138	4.19	0.4
kk2	306	48	49	901	901	22.5×10^6	55	1.79	0.1
kk0.5	306	47	48	462	462	312.5×10^6	197	24.93	3

Table 6.18: Same columns as previous Tables from this section showing the second sets of results of simulations from Table 6.7. Source: this work.

Sim	haloc			Envelope	Initial	UCDs			
	$T_{0.1}^{DM}$	$M_{T_{0.1}^{DM}}^{envelope}$	$M_{T_{0.1}^{DM}}^{Plummer}$	$T_{0.1}^{envelope}$	T	M	Posi	M/L	% DM_0
	[Myr]	%	%	[Myr]	[Myr]	10^6 $M_\odot$	[kpc]		%
aaa240$^+$	9995	7	23	4976	9995	10^9	250	342.62	10
aaa200$^+$	4521	8	26	2872	4521	10^9	250	307.97	10
aaa100$^+$	1234	7	26	1107	1234	10^9	99	310.17	10
aaa50	925	10	28	985	985	803×10^6	105	227.34	8
aaa20$^+$	771	8	27	513	771	10^9	214	300.9	10
aaa10$^+$	700	5	24	293	700	10^9	236	330.55	10
aaa5$^+$	667	3	23	289	667	10^9	242	353.8	10
aaa2$^+$	642	1	21	289	642	10^9	245	380.59	10
aaa0.5$^+$	310	1	21	289	310	10^9	1	380.59	10
bbb240*	-								
bbb200*	7378	50	51						
bbb100*	1649	48	49						
bbb50	998	48	49	6876	6876	102×10^6	204	8.26	0.9
bbb20	797	46	47	2943	2943	92.5×10^6	122	7.39	0.8
bbb10	706	37	39	2125	2125	92.5×10^6	100	7.39	0.8
bbb5	668	28	30	1624	1624	92.5×10^6	136	7.38	0.8
bbb2	369	23	25	1127	1127	112.5×10^6	225	8.97	1
bbb0.5	311	14	16	917	917	112.5×10^6	14	8.97	1
ccc240*	1485	40	52						
ccc200	1290	38	50	7706	7706	5.5×10^6	247	1.56	2
ccc100	950	31	45	1876	1876	5.5×10^6	190	1.56	2
ccc50	789	23	38	1036	1036	5.5×10^6	54	1.56	2
ccc20$^+$	1299	3	23	921	1299	12.8×10^6	249	4.52	10
ccc10	643	11	29	662	662	11.5×10^6	247	3.26	8
ccc5	305	26	41	455	455	10.5×10^6	192	2.98	7
ccc2	305	25	40	311	311	6.5×10^6	3	1.84	3
ccc0.5	305	24	39	310	310	5.5×10^6	1	1.56	2

Table 6.19: Same columns as previous Tables from this section showing the third sets of results of simulations from Table 6.4. Source: this work.

Sim	haloc			Envelope	Initial	UCDs			
	$T_{0.1}^{DM}$	$M_{T_{0.1}^{DM}}^{envelope}$	$M_{T_{0.1}^{DM}}^{Plummer}$	$T_{0.1}^{envelope}$	T	M	Posi	M/L	% DM_0
	[Myr]	%	%	[Myr]	[Myr]	10^6 $M_\odot$	[kpc]		%
ddd240	1750	28	42	5426	5426	23.5×10^6	249	6.65	2
ddd200	1380	22	38	3999	3999	23.5×10^6	202	6.65	2
ddd100	992	19	35	1723	1723	43.5×10^6	243	12.31	4
ddd50	843	14	31	1016	1016	33.5×10^6	73	9.48	3
ddd20	734	11	29	833	833	43.5×10^6	176	12.31	4
ddd10$^+$	689	8	27	494	689	103.3×10^6	241	30.99	10
ddd5$^+$	665	4	23	471	665	102.0×10^6	245	35.04	10
ddd2$^+$	647	2	22	307	647	102.7×10^6	247	37.57	10
ddd0.5$^+$	307	9	27	306	307	103.4×10^6	7	30.11	10
eee240	1012	59	67	4860	4860	8.5×10^6	249	2.42	0.5
eee200	955	55	64	3222	3222	11.5×10^6	244	3.26	0.8
eee100	877	38	50	1582	1582	43.5×10^6	244	12.31	4
eee50	808	29	36	1424	1424	93.5×10^6	248	26.46	9
eee20$^+$	1341	4	23	1267	1341	102.9×10^6	243	35.07	10
eee10$^+$	723	5	24	653	723	103×10^6	231	33.95	10
eee5$^+$	705	1	21	545	705	102.6×10^6	236	38.95	10
eee2$^+$	688	0.9	21	311	688	102.6×10^6	240	39.10	10
eee0.5$^+$	695	0.3	20	310	695	102.5×10^6	238	39.99	10
fff240	1004	50	60	3418	3418	10.5×10^6	249	2.98	0.7
fff200	947	45	56	2447	2447	13.5×10^6	234	3.82	1
fff100	877	27	42	1218	1218	11.5×10^6	100	3.26	0.8
fff50	808	19	35	936	936	23.5×10^6	154	6.65	2
fff20$^+$	1341	2	22	795	1341	102.7×10^6	243	37.57	10
fff10$^+$	723	3	23	608	723	102.8×10^6	231	36.28	10
fff5$^+$	705	1	21	312	705	102.6×10^6	235	38.95	10
fff2$^+$	688	0.6	21	309	688	103.4×10^6	239	30.11	10
fff0.5$^+$	695	0.2	20	309	695	102.5×10^6	238	40.14	10

Table 6.20: Same columns as previous Tables from this section showing the third sets of results of simulations from Table 6.5. Source: this work.

Sim	haloc			Envelope	Initial	UCDs			
	$T_{0.1}^{DM}$	$M_{T_{0.1}^{DM}}^{envelope}$	$M_{T_{0.1}^{DM}}^{Plummer}$	$T_{0.1}^{envelope}$	T	M	Posi	M/L	% DM_0
	[Myr]	%	%	[Myr]	[Myr]	10^6 $M_\odot$	[kpc]		%
ggg240*									
ggg200*	4881	69	70						
ggg100*	1676	58	59						
ggg50	986	58	59	5836	5836	29.5×10^6	163	1.79	1
ggg20	766	49	50	2234	2234	30.5×10^6	25	1.79	1
ggg10	693	41	42	1565	1565	30.5×10^6	9	1.79	1
ggg5	640	32	34	1230	1230	32.5×10^6	248	2.59	2
ggg2	310	36	38	926	926	22.5×10^6	10	1.79	1
ggg0.5	309	40	41	496	496	42.5×10^6	218	3.39	3
hhh240*	1846	86	86						
hhh200*	1440	85	85						
hhh100	935	76	77	5783	5783	18.5×10^6	249	1.47	0.6
hhh50	771	64	65	2125	2125	32.5×10^6	248	2.59	2
hhh20	1309	13	15	1386	1386	82.5×10^6	229	6.58	7
hhh10	571	40	41	1006	1006	19.5×10^6	116	1.55	0.7
hhh5	730	13	15	813	813	22.5×10^6	174	1.79	1
$hhh2^+$	681	3	5	552	681	105.5×10^6	241	19.06	10
$hhh0.5^+$	696	0.9	3	352	696	103.4×10^6	237	30.11	10
iii240*	1836	81	81						
iii200*	1427	80	80						
iii100	926	69	70	3953	3953	20.5×10^6	217	1.63	0.8
iii50	768	55	56	1731	1731	19.5×10^6	58	1.55	0.7
$iii20^+$	1308	7	9	1264	1308	109.5×10^6	247	11.48	10
iii10	600	30	31	929	929	19.5×10^6	27	1.55	0.7
$iii5^+$	730	6	8	663	730	108.5×10^6	225	12.71	10
$iii2^+$	682	2	4	480	682	104.5×10^6	225	23.05	10
$iii0.5^+$	695	0.7	3	329	695	103.2×10^6	237	31.91	10

Table 6.21: Same columns as previous Tables from this section showing the third sets of results of simulations from Table 6.6. Source: this work.

Sim	haloc			Envelope	Initial	UCDs			
	$T_{0.1}^{DM}$	$M_{T_{0.1}^{DM}}^{envelope}$	$M_{T_{0.1}^{DM}}^{Plummer}$	$T_{0.1}^{envelope}$	T	M	Posi	M/L	% DM_0
	[Myr]	%	%	[Myr]	[Myr]	10^6 $M_\odot$	[kpc]		%
jjj240*	1636	74	75						
jjj200*	1348	73	74						
jjj100*	958	72	73						
jjj50	809	69	70	3834	3834	22.5×10^6	58	1.79	0.1
jjj20	710	64	65	2223	2223	22.5×10^6	30	1.79	0.1
jjj10	668	59	60	1558	1558	14.5×10^6	9	1.15	0.02
jjj5	639	49	50	1214	1214	112.5×10^6	246	8.97	1
jjj2	306	55	56	922	922	22.5×10^6	5	1.79	0.1
jjj0.5	306	55	56	562	562	412.5×10^6	240	32.91	4
kkk240*	1628	67	68						
kkk200*	1340	66	67						
kkk100	955	65	66	8697	8697	13.3×10^6	119	1.06	0.0008
kkk50	808	61	62	3059	3059	22.5×10^6	132	1.79	0.1
kkk20	710	57	58	1923	1923	212.5×10^6	244	16.95	2
kkk10	668	51	52	1529	1529	22.5×10^6	63	1.79	0.1
kkk5	641	38	40	1009	1009	52.5×10^6	135	4.19	0.4
kkk2	306	47	48	903	903	22.5×10^6	49	1.79	0.1
kkk0.5	306	47	48	471	471	312.5×10^6	204	24.93	3

Table 6.22: Same columns as previous Tables from this section showing the third sets of results of simulations from Table 6.7. Source: this work.

The following tables display the final values along with their corresponding error values, derived from the statistical analysis of three simulations. These tables feature the same columns as those found throughout this chapter.

Sim	haloc $T_{0.1}^{DM}$ [Myr]	$M_{T_{0.1}^{DM}}^{envelope}$ %	$M_{T_{0.1}^{DM}}^{Plummer}$ %	Envelope $T_{0.1}^{envelope}$ [Myr]	Initial T [Myr]	UCDs M 10^6 $M_\odot$	Posi [kpc]	M/L	% DM_0 %
a240$^+$	9995	7	23	4938±43	9995	10^3	250	342.62	10
a200$^+$	4526±5	8	26	2971±87	4526±5	10^3	249±1	307.97	10
a100$^+$	1233±1	7±1	26±1	1133±24	1233±1	10^3	99±1	307.1±5.4	10
a50	924±1	10±1	28±1	982±10	982±10	803.2 ± 0.3	109±11	227.34	8
a20$^+$	771±1	8	27	526±14	771±1	10^3	214±1	300.9	10
a10$^+$	700±1	5±1	24	294±2	700±1	10^3	236	334.3±6.5	10
a5$^+$	667	3	23	291±2	667	10^3	242	353.8	10
a2$^+$	535±182	2±1	22±1	291±2	535±182	10^3	175±121	371.3±8	10
a0.5$^+$	310	1	21	291±2	310	10^3	1	372.2±7.3	10
b240*	-								
b200*	7416±33	50	51						
b100*	1649±1	48	49						
b50	998±1	48	49	6893±15	6893±15	102.2 ± 0.2	212±7	8.26	0.9
b20	797	47±1	48±1	2947±4	2947±4	92.5	124±5	7.39	0.8
b10	706±1	37±1	39±1	2125±1	2125±1	92.5	107±12	7.39	0.8
b5	668±1	28	30	1627±4	1627±4	92.5	139±4	7.38	0.8
b2	352±35	22±1	24±1	1132±5	1132±5	112.5	227±2	8.97	1
b0.5	310±1	17±3	19±3	917	917	112.5	14±2	8.97	1
c240*	1487±2	40	52						
c200	1292±2	38	50	7671±35	7671±35	5.5	244±3	1.56	2
c100	950±1	31	45	1879±7	1879±7	5.8 ± 0.5	193±11	1.56	2
c50	790±1	23±1	38±1	1036	1036	5.8 ± 0.5	54±1	1.56	2
c20$^+$	1304±6	3±1	23±1	922±1	1304±6	12.8 ± 0.1	248±1	4.6±0.1	10
c10	643±1	11	29	663±1	663±1	11.5	247±1	3.26	8
c5	305	26	41	457±3	457±3	10.5	194±2	2.98	7
c2	305	25±1	40±1	311	311	6.8 ± 0.6	3±1	1.9±0.2	3.3±0.6
c0.5	305	24	39	310	310	6.5 ± 1	1	1.8±0.3	2.7±1.2

Table 6.23: Same columns as previous Tables from this section showing final values with their corresponding error values, derived from the statistical analysis of three exact simulations but with different seed number from Table 6.4. Source: this work.

Sim	haloc $T_{0.1}^{DM}$ [Myr]	$M_{T_{0.1}^{DM}}^{envelope}$ %	$M_{T_{0.1}^{DM}}^{Plummer}$ %	Envelope $T_{0.1}^{envelope}$ [Myr]	Initial T [Myr]	UCDs M 10^6 $M_\odot$	Posi [kpc]	M/L	% DM_0 %
d240	1747±3	27±1	42	5432±9	5432±9	23.53	249	6.65	2
d200	1380±1	22	38	3961±34	3961±34	23.5	200±2	6.65	2
d100	992±1	19	35	1739±14	1739±14	43.5	240±3	12.31	4
d50	842±1	14±1	31±1	1017±1	1017±1	33.5	72±1	9.48	3
d20	734	11	29	835±3	835±3	43.5	175±2	12.31	4
d10$^+$	689	8	27	493±2	689	103.3	241	30.99	10
d5$^+$	665±1	4	23	471±1	665±1	102.6 ± 0.5	245	35.1	10
d2$^+$	648±1	2	22	306±1	648±1	103 ± 0.5	247	34.4±3.9	10
d0.5$^+$	307	9	25±3	306	307	103.4 ± 0.1	8±2	30.11	10
e240	1010±3	59	67	4738±127	4738±127	8.5	249±1	2.42	0.5
e200	952±3	54±1	63±1	3238±20	3238±20	11.5	245±2	3.26	0.8
e100	877±1	38	50	1562±35	1562±35	43.5	243±1	12.31	4
e50	808	29±1	41±4	1424±1	1424±1	93.5	248	26.46	9
e20$^+$	1325±29	5±2	24±2	1262±11	1325±29	103 ± 0.2	245±3	35.7±2.4	10
e10$^+$	723±1	6±1	25±1	655±2	723±1	103.1 ± 0.1	231	33.2±0.6	10
e5$^+$	705	2±1	22±1	548±3	705	102.7 ± 0.1	236	38±0.8	10
e2$^+$	688	0.9	21	311	688	102.6	240±1	39.10	10
e0.5$^+$	695±1	0.3	20	310	695±1	102.5	238	39.99	10
f240	1002±2	50	60	3409±21	3409±21	10.5	249±1	2.98	0.7
f200	943±4	45±1	56±1	2425±26	2425±26	13.5	236±3	3.82	1
f100	876±1	27	42	1218±2	1218±2	11.5	100±1	3.26	0.8
f50	808	19±1	35±1	937±1	937±1	23.5	154±1	6.65	2
f20$^+$	1325±28	3±2	23±1	795±1	1325±28	102.8±0.2	245±3	36.4±2.1	10
f10$^+$	723	3	23	609±2	723	102.8	231	36.28	10
f5$^+$	705	1	21	312	705	102.6	236±1	38.95	10
f2$^+$	688	0.6	21	309	688	102.8±0.5	239±1	36.3±5.4	10
f0.5$^+$	694±1	0.2	20	309	694±1	102.3±0.3	238	40.14	10

Table 6.24: Same columns as previous Tables from this section showing final values with their corresponding error values, derived from the statistical analysis of three exact simulations but with different seed number from Table 6.5. Source: this work.

Sim	haloc $T_{0.1}^{DM}$ [Myr]	$M^{envelope}_{T_{0.1}^{DM}}$ %	$M^{Plummer}_{T_{0.1}^{DM}}$ %	Envelope $T_{0.1}^{envelope}$ [Myr]	Initial T [Myr]	UCDs M 10^6 $M_\odot$	Posi [kpc]	M/L	% DM_0 %
g240*									
g200*	4884±7	69	70						
g100*	1674±2	58	59						
g50	985±1	58	59	5838±3	5838±3	29.5	161±3	1.79	1
g20	766	49	50	2235±1	2235±1	30.2±0.6	25±1	1.79	1
g10	693	41	42	1564±1	1564±1	30.5	10±1	1.79	1
g5	498±123	37±4	38±3	1231±1	1231±1	32.5	248	2.59	2
g2	310	37±1	39±1	926	926	22.5	11±2	1.79	1
g0.5	309	40	41	491±5	491±5	42.5	215±3	3.39	3
h240*	1850±5	86	86						
h200*	1440±1	85	85						
h100	936±1	76	77	5785±4	5785±4	18.5	249	1.47	0.6
h50	771	64	65	2124±1	2124±1	32.5	247±1	2.59	2
h20	1309	13	15	1388±2	1388±2	79.2±5.8	228±1	6.3±0.5	6.7±0.6
h10	575±7	40	41	1011±7	1011±7	19.5	121±10	1.55	0.7
h5	730	13	15	815±3	815±3	22.5	172±2	1.79	1
h2$^+$	691±16	3±1	5±1	554±2	691±16	104.1 ± 1.5	238±5	20.4±2.3	10
h0.5$^+$	696±1	0.9	3	352±1	696±1	103.4	237	30.11	10
i240*	1837±3	81	81						
i200*	1428±2	80±1	80±1						
i100	927±1	69	70	3959±6	3959±6	20.5	219±2	1.63	0.8
i50	768±1	55	56	1730±1	1730±1	19.5	59±1	1.55	0.7
i20$^+$	1308	7	9	1264±1	1308	109.5	247	11.48	10
i10	601±3	30	32±1	929	929	19.5	31±5	1.55	0.7
i5$^+$	719±18	6±1	8±1	662±1	719±18	108.8 ± 0.6	229±7	12.3±0.7	10
i2$^+$	682	2	4	480±1	682	104.5	235±9	23.05	10
i0.5$^+$	696±1	0.7	3	329	696±1	103.2 ± 0.1	237	32.2±0.6	10

Table 6.25: Same columns as previous Tables from this section showing final values with their corresponding error values, derived from the statistical analysis of three exact simulations but with different seed number from Table 6.6. Source: this work.

Sim	haloc $T_{0.1}^{DM}$ [Myr]	$M_{T_{0.1}^{DM}}^{envelope}$ %	$M_{T_{0.1}^{DM}}^{Plummer}$ %	Envelope $T_{0.1}^{envelope}$ [Myr]	Initial T [Myr]	UCDs M 10^6 $M_\odot$	Posi [kpc]	M/L	% DM_0 %
j240*	1638±2	74±1	75±1						
j200*	1349±1	73	74						
j100*	958±1	72	73						
j50	809±1	69	70	3843±8	3843±8	22.5	53±4	1.79	0.1
j20	710	64±1	65±1	2221±2	2221±2	22.5	34±5	1.79	0.1
j10	668	59±1	60±1	1560±2	1560±2	13.7 ± 0.7	10±1	1.1±0.1	0.02
j5	638±1	49	50	1215±6	1215±6	145.8 ± 57.7	246	11.6±4.6	1.3±0.6
j2	306	55	56	923±1	923±1	22.5	6±1	1.79	0.1
j0.5	306	55	56	563±2	563±2	412.5	241±1	32.91	4
k240*	1630±2	67	68						
k200*	1340±1	67±1	67						
k100	955±1	65	66	8693±29	8693±29	19.4 ± 5.3	120±14	1.5±0.4	0.07±0.06
k50	808±1	61	62	3073±13	3073±13	22.5	119±12	1.79	0.1
k20	710	57	58	1918±5	1918±5	212.5	247±2	16.95	2
k10	668	51	52	1529±2	1529±2	22.5	64±3	1.79	0.1
k5	640±1	38±1	40	1012±4	1012±4	55.8 ± 5.8	138±4	4.5±0.5	0.4±0.1
k2	306	47±1	48±1	902±1	902±1	25.8 ± 5.8	51±3	2.1±0.5	0.1±0.1
k0.5	306	47	48	467±5	467±5	312.5	201±4	24.93	3

Table 6.26: Same columns as previous Tables from this section showing final values with their corresponding error values, derived from the statistical analysis of three exact simulations but with different seed number from Table 6.7. Source: this work.

The following tables as the previous ones show the final values along with their corresponding error values, but now derived from the statistical analysis of not three but four simulations (except the case of the "a", "b", "j" and "k" set of simulations), including now the simulations with initial number of particles for the the dark matter part and 'envelope' of the dwarf galaxy of 10.000.000, so the result from Table 6.8, Table 6.9 and Table 6.10. These tables feature the same columns as those found throughout this chapter.

Sim	haloc $T_{0.1}^{DM}$ [Myr]	$M_{T_{0.1}^{DM}}^{envelope}$ %	$M_{T_{0.1}^{DM}}^{Plummer}$ %	Envelope $T_{0.1}^{envelope}$ [Myr]	Initial T [Myr]	UCDs M 10^6 $M_\odot$	Posi [kpc]	M/L	% DM_0 %
a240$^+$	9995	7	23	4938±43	9995	10^3	250	342.62	10
a200$^+$	4526±5	8	26	2971±87	4526±5	10^3	249±1	307.97	10
a100$^+$	1233±1	7±1	26±1	1133±24	1233±1	10^3	99±1	307.1±5.4	10
a50	924±1	10±1	28±1	982±10	982±10	803.2 ± 0.3	109±11	227.34	8
a20$^+$	771±1	8	27	526±14	771±1	10^3	214±1	300.9	10
a10$^+$	700±1	5±1	24	294±2	700±1	10^3	236	334.3±6.5	10
a5$^+$	667	3	23	291±2	667	10^3	242	353.8	10
a2$^+$	535±182	2±1	22±1	291±2	535±182	10^3	175±121	371.3±8	10
a0.5$^+$	310	1	21	291±2	310	10^3	1	372.2±7.3	10
b240*	-								
b200*	7416±33	50	51						
b100*	1649±1	48	49						
b50	998±1	48	49	6893±15	6893±15	102.2 ± 0.2	212±7	8.26	0.9
b20	797	47±1	48±1	2947±4	2947±4	92.5	124±5	7.39	0.8
b10	706±1	37±1	39±1	2125±1	2125±1	92.5	107±12	7.39	0.8
b5	668±1	28	30	1627±4	1627±4	92.5	139±4	7.38	0.8
b2	352±35	22±1	24±1	1132±5	1132±5	112.5	227±2	8.97	1
b0.5	310±1	17±3	19±3	917	917	112.5	14±2	8.97	1
c240*	1488±3	40	52						
c200	1293±2	38	50	7716±94	7716±94	5.5	245±3	1.56	2
c100	950±1	31	45	1882±8	1882±8	5.7 ± 0.4	190±10	1.56	2
c50	790±1	23±1	38±1	1036	1036	5.7 ± 0.4	54±1	1.56	2
c20$^+$	1151±305	7±8	26±6	923±1	1151±305	11 ± 3.6	205±86	3.8±1.5	8±4
c10	643±1	11	29	663±1	663±1	11.5	247±1	3.26	8
c5	305	26	41	458±2	458±2	10.5	195±2	2.98	7
c2	305	25±1	40±1	311	311	6.8 ± 0.5	3±1	1.9±0.1	3.3±0.5
c0.5	305	24	39	310	310	6.2 ± 1	1	1.7±0.3	3±1

Table 6.27: Same columns as previous Tables from this section showing final values with their corresponding error values, derived from the statistical analysis of three (for the "a" and b" set) and four (for the "c" set) exact simulations but with different seed number from Table 6.4. And for the "c" set one simulation have different initial number of particles from the dark matter and envelope part (10.000.000). Source: this work.

Sim	haloc $T_{0.1}^{DM}$ [Myr]	$M_{T_{0.1}^{DM}}^{envelope}$ %	$M_{T_{0.1}^{DM}}^{Plummer}$ %	Envelope $T_{0.1}^{envelope}$ [Myr]	Initial T [Myr]	UCDs M 10^6 $M_\odot$	Posi [kpc]	M/L	% DM_0 %
d240	1742±9	28±1	42	5723±581	5723±581	23.5	246±6	6.65	2
d200	1379±3	22	38	4022±124	4022±124	23.5	208±15	6.65	2
d100	991±1	19	35	1748±20	1748±20	42.8 ± 1.5	238±5	11.6±1.4	3.8±0.5
d50	842±1	14±1	31±1	1017±1	1017±1	33.5	72±2	9.48	3
d20	734±1	11	29	835±2	835±2	43.5	175±2	12.31	4
d10$^+$	689	8	27	493±1	689	103.3	241	30.99	10
d5$^+$	665±1	4	23	471±1	665±1	102.7 ± 0.5	245	35.1	10
d2$^+$	647±1	2	22	306±1	647±1	102.9 ± 0.4	247	35.2±3.5	10
d0.5$^+$	307	7±4	26±3	306	307	103.4 ± 0.1	8±2	30.3±0.4	10
e240	1007±7	59	67	4829±210	4829±210	8.3 ± 0.5	249±1	2.3±0.1	0.5±0.1
e200	948±9	55±1	64±1	3269±62	3269±62	11.3 ± 0.5	246±2	3.2±0.1	0.8±0.1
e100	876±1	38	50	1568±31	1568±31	43.5	243±1	12.31	4
e50	808	30±1	42±4	1425±1	1425±1	93.5	248	26.46	9
e20$^+$	1329±24	5±2	24±2	1265±10	1329±24	103 ± 0.2	244±3	34.1±2	10
e10$^+$	724±1	6±1	25±1	656±2	724±1	103.1 ± 0.1	231	33.2±0.5	10
e5$^+$	705	2±1	22±1	549±3	705	102.7 ± 0.1	236	37.9±0.7	10
e2$^+$	694±11	0.8	21	311	694±11	102.6 ± 0.1	238±3	39.2±0.2	10
e0.5$^+$	695±1	0.3	20	310	695±1	102.5	238	39.99	10
f240	999±7	50	60	3438±61	3438±61	10.5	250±1	3	0.7
f200	938±11	45±1	56±1	2440±36	2440±36	13.3 ± 0.5	235±5	3.8±0.1	1±0.1
f100	876±1	27	42	1221±5	1221±5	11.5	100±1	3.26	0.8
f50	808±1	20±1	36±1	1040±207	1040±207	38.5±30	177±46	10.9±8.5	3.5±3
f20$^+$	1316±29	4±2	23±1	796±2	1316±29	102.9±0.2	246±3	35.8±2.1	10
f10$^+$	723	3	23	610±1	723	102.8	231	36.28	10
f5$^+$	705	1	21	312	705	102.6	236±1	38.95	10
f2$^+$	693±11	0.6	21±1	309	693±11	102.8±0.4	238±3	37.2±4.7	10
f0.5$^+$	695±1	0.2	20	309	695±1	102.4±0.3	238	40.14	10

Table 6.28: Same columns as previous Tables from this section showing final values with their corresponding error values, derived from the statistical analysis of four exact simulations but with different seed number from Table 6.5. One simulation have different initial number of particles from the dark matter and envelope part (10.000.000). Source: this work.

Sim	haloc $T_{0.1}^{DM}$ [Myr]	$M_{T_{0.1}^{DM}}^{envelope}$ %	$M_{T_{0.1}^{DM}}^{Plummer}$ %	Envelope $T_{0.1}^{envelope}$ [Myr]	Initial T [Myr]	UCDs M 10^6 $M_\odot$	Posi [kpc]	M/L	% DM_0 %
g240*									
g200*	4875±19	69	70						
g100*	1673±19	58	59						
g50	985±1	58	59	5828±20	5828±20	29.3 ± 0.5	169±15	1.79	1
g20	766±1	49±1	50±1	2235±1	2235±1	30±0.6	26±1	1.79	1
g10	693	41	42	1565±1	1565±1	30.5	10±1	1.79	1
g5	533±123	36±4	37±3	1230±1	1230±1	32.5	248	2.59	2
g2	310	37±1	39±1	926	926	22.5	11±2	1.79	1
g0.5	309	40	41	490±4	490±4	42.5	215±2	3.39	3
h240*	1847±8	86±1	86±1						
h200*	1415±50	85	85						
h100	935±3	76	77	5775±21	5775±21	18.5	249±1	1.47	0.6
h50	770±2	64	65	2123±4	2123±4	32.3±0.5	248±1	2.4±0.4	1.8±0.5
h20	1309±1	13	15	1387±2	1387±2	80±5	228±1	6.4±0.4	6.8±0.5
h10	574±7	40	41	1010±6	1010±6	19.5	120±8	1.55	0.7
h5	730±1	13	15	816±3	816±3	22.5	172±2	1.79	1
h2$^+$	696±17	3±1	5±1	554±1	696±17	104.2 ± 1.3	237±5	21.1±2.3	10
h0.5$^+$	696±1	0.9	3	352±1	696±1	103.4	237	30.11	10
i240*	1831±13	81	81						
i200*	1426±4	80±1	80±1						
i100	926±2	69	70	3952±15	3952±15	20.5 ± 0.1	191±56	1.6	0.8±0.1
i50	768±1	55	56	1729±2	1729±2	19.5	60±2	1.55	0.7
i20$^+$	1308	7	9	1264±1	1308	109.5	247	11.48	10
i10	601±2	30	32±1	929	929	19.5	30±5	1.55	0.7
i5$^+$	722±16	6±1	8±1	662±1	722±16	108.9 ± 0.5	228±6	12.4±0.6	10
i2$^+$	682	2	4	480±1	682	104.5	237±8	23.05	10
i0.5$^+$	696±1	0.7	3	329	696±1	103.2 ± 0.1	237	33.4±0.6	10

Table 6.29: Same columns as previous Tables from this section showing final values with their corresponding error values, derived from the statistical analysis of four exact simulations but with different seed number from Table 6.6. One simulation have different initial number of particles from the dark matter and envelope part (10.000.000). Source: this work.

6.3 Structural parameters of final objects.

In this section we present some examples for the characteristics of the nucleus at the end of the simulation, until a radius of 1.5 kpc, the left panel is the shape of the final object with a color bar for the magnitude of the surface Brightness, the center panel is the plot of the surface brightness and the right panel is the velocity dispersion. Under each set of images, is the pericenter distance of the orbit (R_{peri}) and the simulation time at which the dE transitions into an UCD (T_{int}^{UCD}).

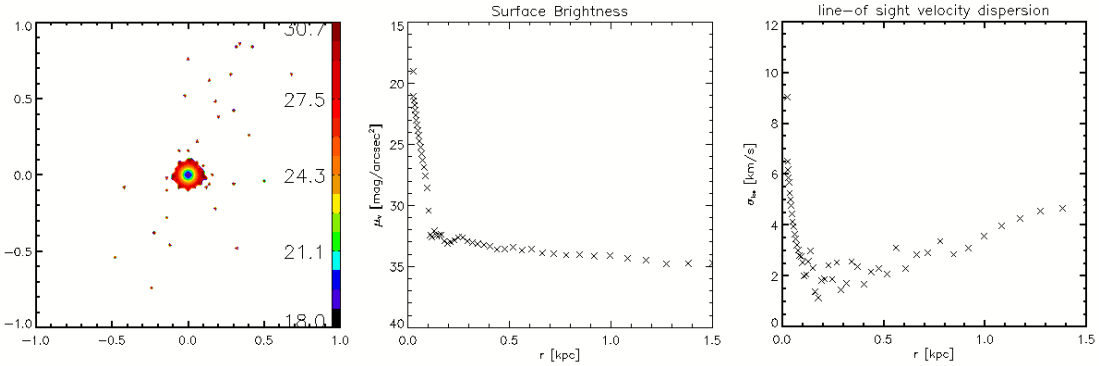

(a) aaa0.5: R_{peri}= 0.5[kpc], T_{int}^{UCD}= 310[Myr]

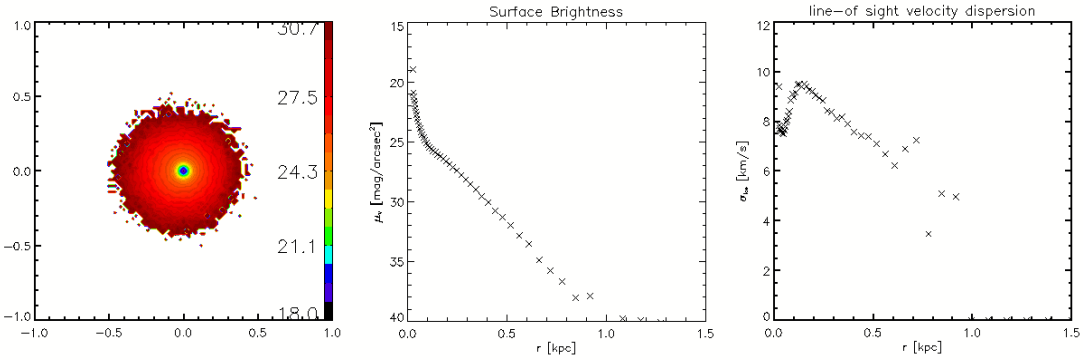

(b) aaa200: R_{peri}= 200[kpc], T_{int}^{UCD}= 4521[Myr]

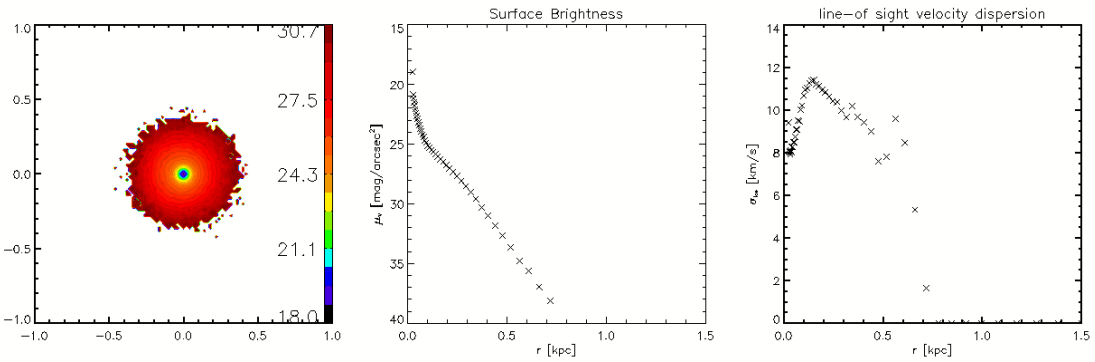

(c) aaa240: R_{peri}= 240[kpc], T_{int}^{UCD}= 9995[Myr]

Figure 6.1: Properties of the final object up to a radius of 1.5 kpc, the left panel is the shape of the final object with a color bar for the magnitude of the surface Brightness, the center panel is the plot of the surface brightness and the right panel is the velocity dispersion. Set of "aaa" simulations (SL^{DM}=1 [kpc], M^{DM}=10^{10}[$M_\odot$], $R_{eff}^{envelope}$=0.85[kpc], $M^{envelope}$=$10^7 M_\odot$). Under each set of images, is the pericenter distance of the orbit (R_{peri}) and the simulation time at which the dE transitions into an UCD (T_{int}^{UCD}). Source: this work.

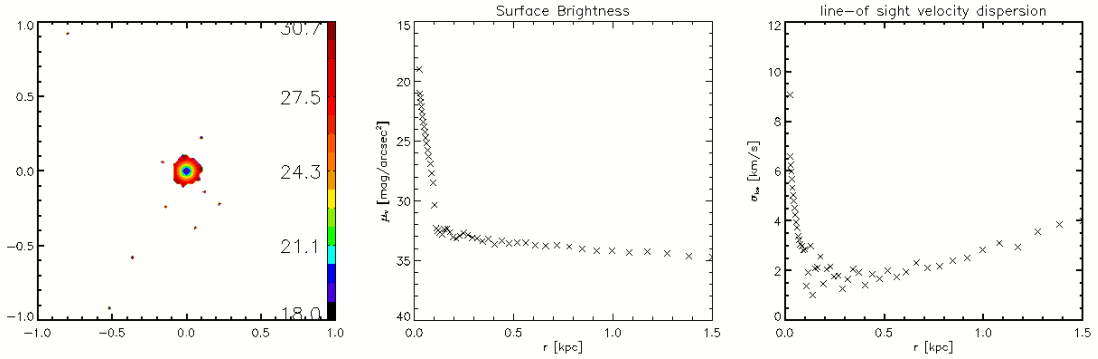

(a) bbb0.5: R_{peri}= 0.5[kpc], T_{int}^{UCD}= 917[Myr]

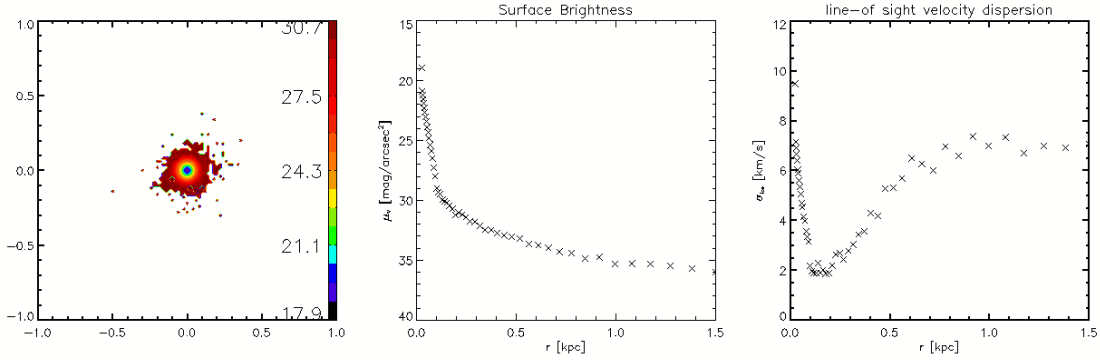

(b) bbb2: R_{peri}= 2[kpc], T_{int}^{UCD}= 1127[Myr]

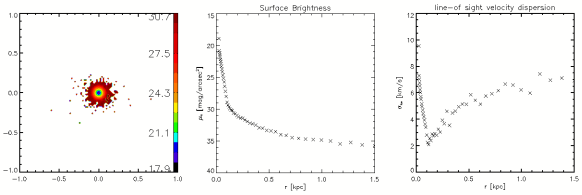

(c) bbb5: R_{peri}= 5[kpc], T_{int}^{UCD}= 1624[Myr]

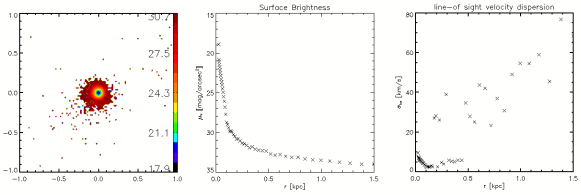

(d) bbb10: R_{peri}= 10[kpc], T_{int}^{UCD}= 2125[Myr]

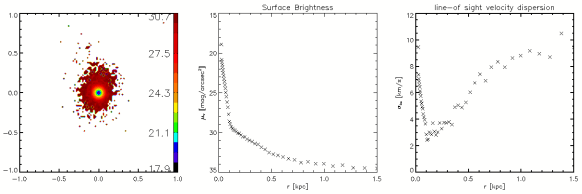

(e) bbb20: R_{peri}= 20[kpc], T_{int}^{UCD}= 2943[Myr]

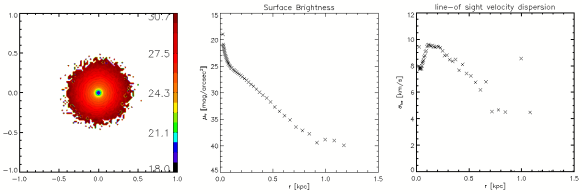

(f) bbb50: R_{peri}= 50[kpc], T_{int}^{UCD}= 6876[Myr]

Figure 6.2: Similar to previous Fig 6.1. Set of "bbb" simulations (SL^{DM}=1 [kpc], M^{DM}=10^{10}[$M_\odot$], $R_{eff}^{envelope}$=0.85[kpc], $M^{envelope}$=$10^{8}M_\odot$). Source: this work.

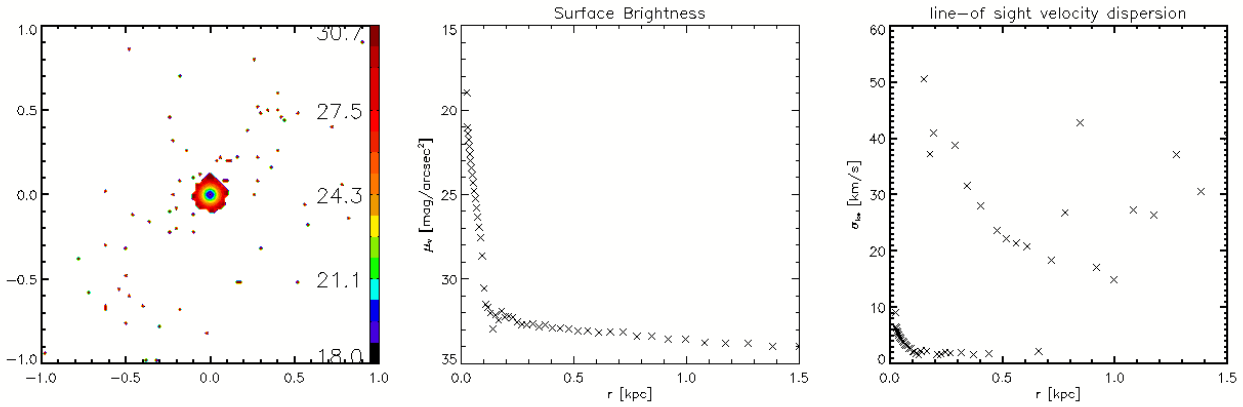

(a) ccc0.5: R_{peri}= 0.5[kpc], T_{int}^{UCD}= 310[Myr]

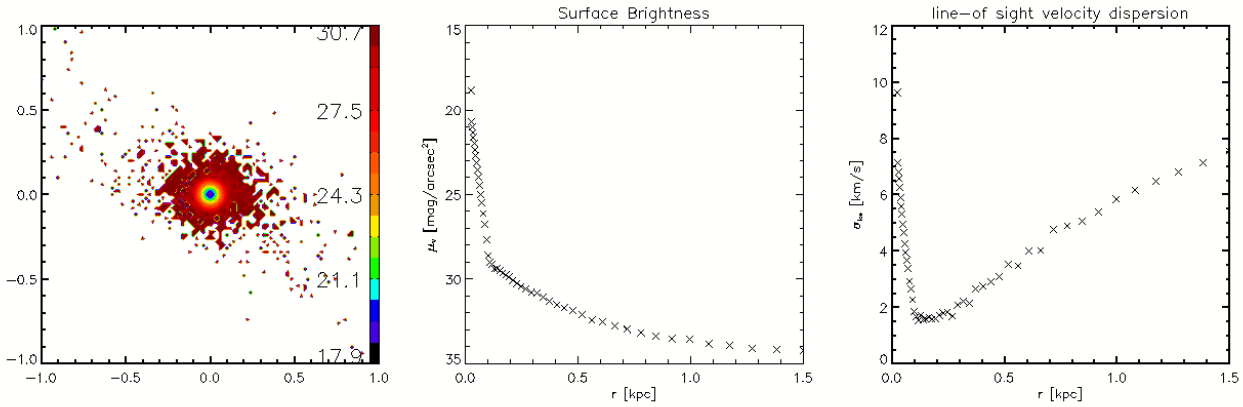

(b) ccc200: R_{peri}= 200[kpc], T_{int}^{UCD}= 7706[Myr]

Figure 6.3: Similar to previous Fig 6.1. Set of "ccc" simulations (SL^{DM}=1 [kpc], M^{DM}=10^8[$M_\odot$], $R_{eff}^{envelope}$=0.85[kpc], $M^{envelope}$=$10^7M_\odot$). Source: this work.

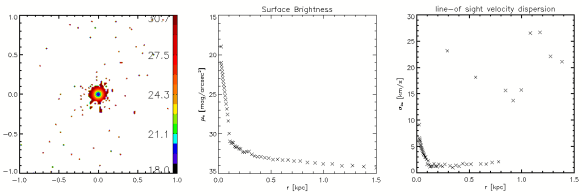

(a) ddd0.5: R_{peri}= 0.5[kpc], T_{int}^{UCD}= 307[Myr]

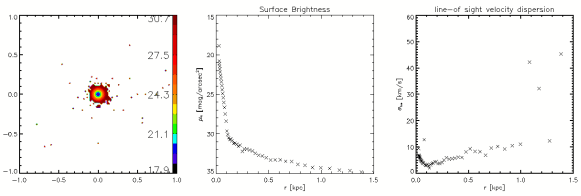

(b) ddd2: R_{peri}= 2[kpc], T_{int}^{UCD}= 647[Myr]

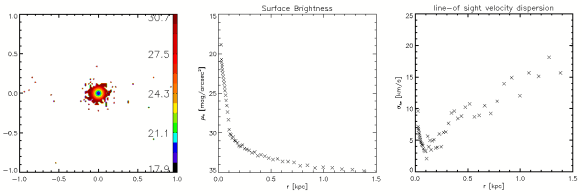

(c) ddd5: R_{peri}= 5[kpc], T_{int}^{UCD}= 665[Myr]

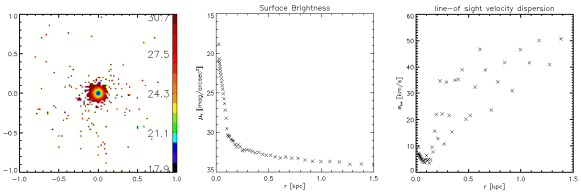

(d) ddd10: R_{peri}= 10[kpc], T_{int}^{UCD}= 689[Myr]

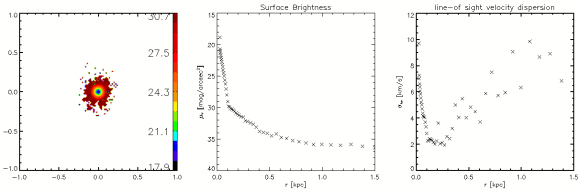

(e) ddd20: R_{peri}= 20[kpc], T_{int}^{UCD}= 833[Myr]

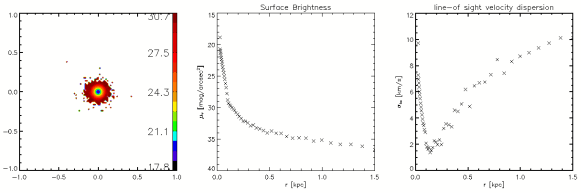

(f) ddd50: R_{peri}= 50[kpc], T_{int}^{UCD}= 1016[Myr]

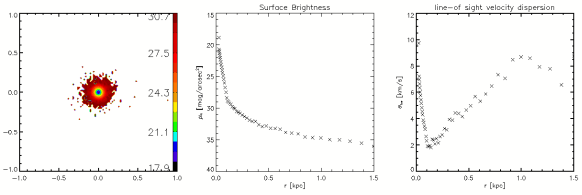

(g) ddd100: R_{peri}= 100[kpc], T_{int}^{UCD}= 1723[Myr]

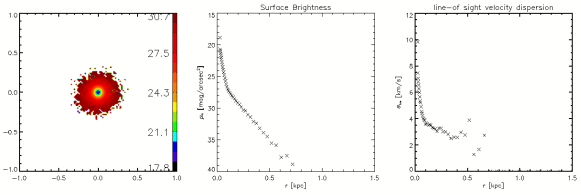

(h) ddd200: R_{peri}= 200[kpc], T_{int}^{UCD}= 3999[Myr]

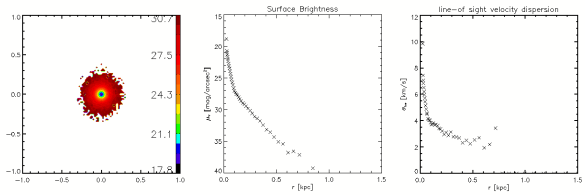

(i) ddd240: R_{peri}= 240[kpc], T_{int}^{UCD}= 5426[Myr]

Figure 6.4: Similar to previous Fig 6.1. Set of "ddd" simulations (SL^{DM}=1 [kpc], M^{DM}=10^9[$M_\odot$], $R_{eff}^{envelope}$=0.85[kpc], $M^{envelope}$=$10^7M_\odot$). Source: this work.

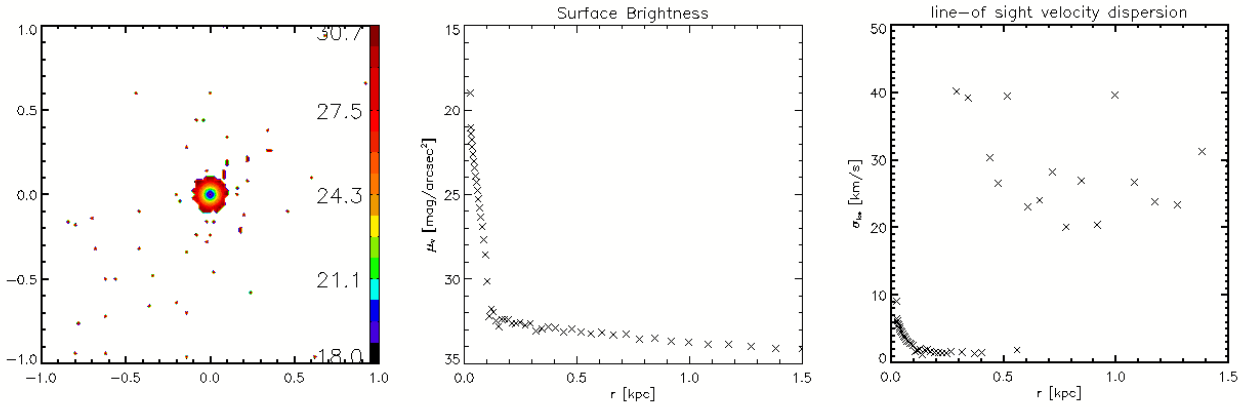

(a) eee0.5: R_{peri}= 0.5[kpc], T_{int}^{UCD}= 695[Myr]

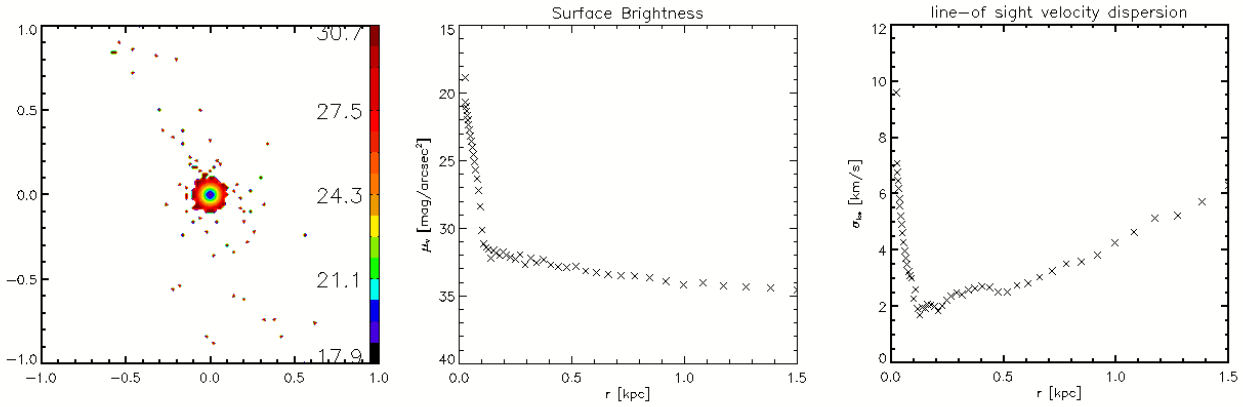

(b) ddd200: R_{peri}= 200[kpc], T_{int}^{UCD}= 3222[Myr]

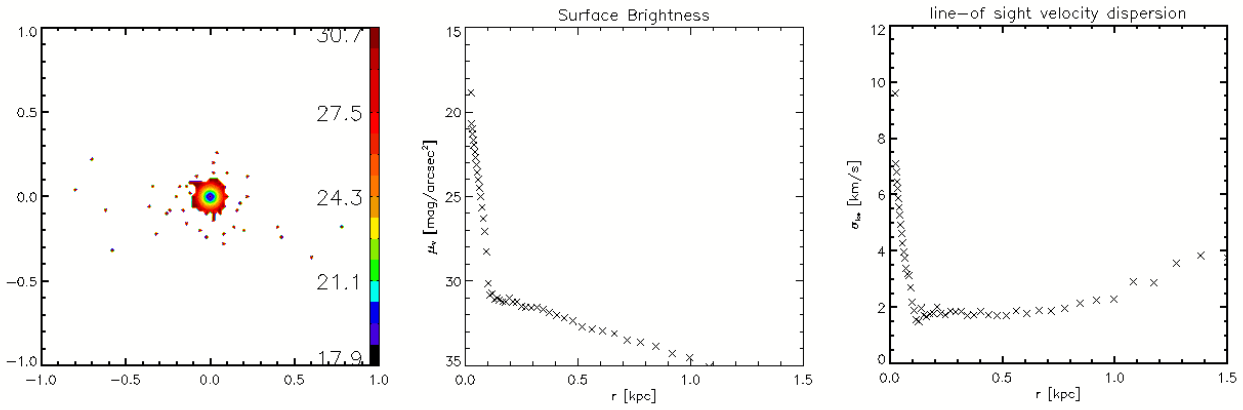

(c) ddd240: R_{peri}= 240[kpc], T_{int}^{UCD}= 4860[Myr]

Figure 6.5: Similar to previous Fig 6.1. Set of "eee" simulations (SL^{DM}=4 [kpc], M^{DM}=10^9[$M_\odot$], $R_{eff}^{envelope}$=0.85[kpc], $M^{envelope}$=$10^7 M_\odot$). Source: this work.

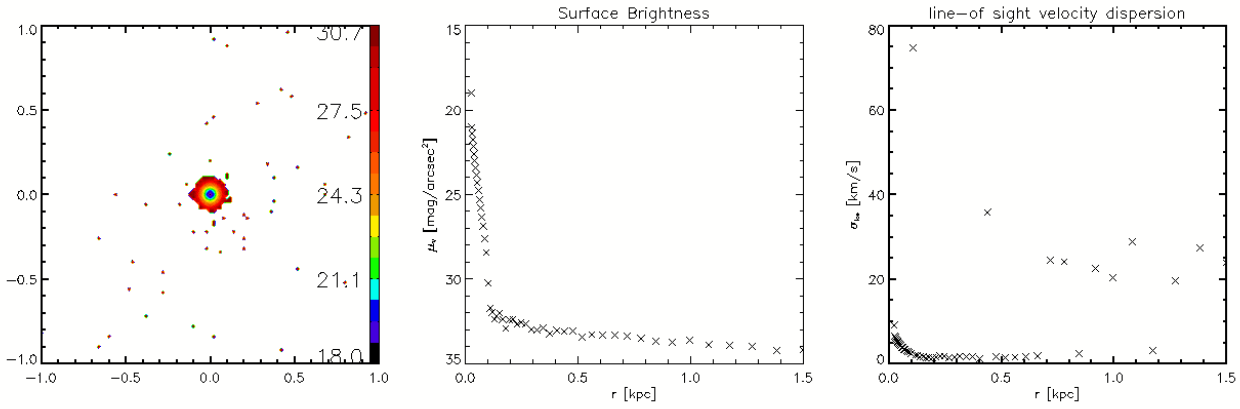

(a) fff0.5: R_{peri}= 0.5[kpc], T_{int}^{UCD}= 695[Myr]

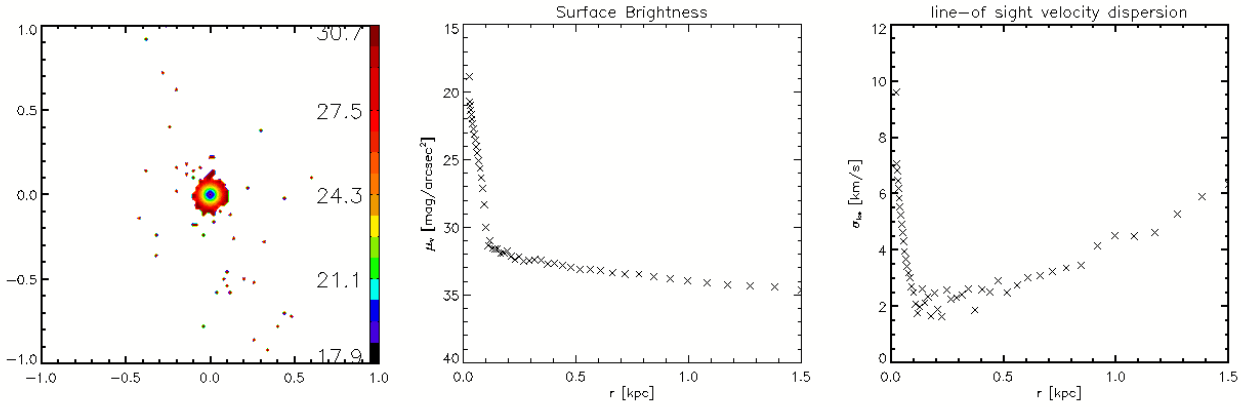

(b) fff200: R_{peri}= 200[kpc], T_{int}^{UCD}= 2447[Myr]

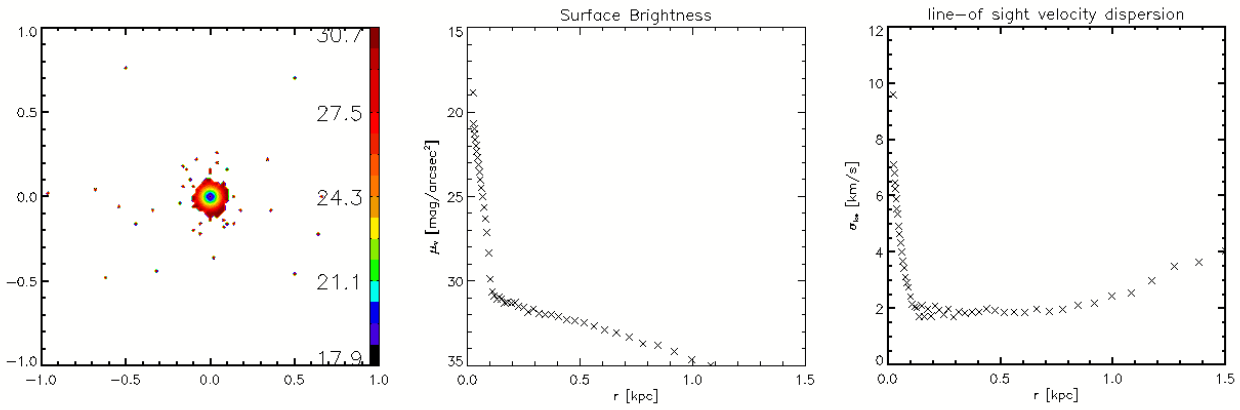

(c) fff240: R_{peri}= 240[kpc], T_{int}^{UCD}= 3418[Myr]

Figure 6.6: Similar to previous Fig 6.1. Set of "fff" simulations (SL^{DM}=4 [kpc], M^{DM}=10^9[$M_\odot$], $R_{eff}^{envelope}$= 1[kpc], $M^{envelope}$=$10^7 M_\odot$). Source: this work.

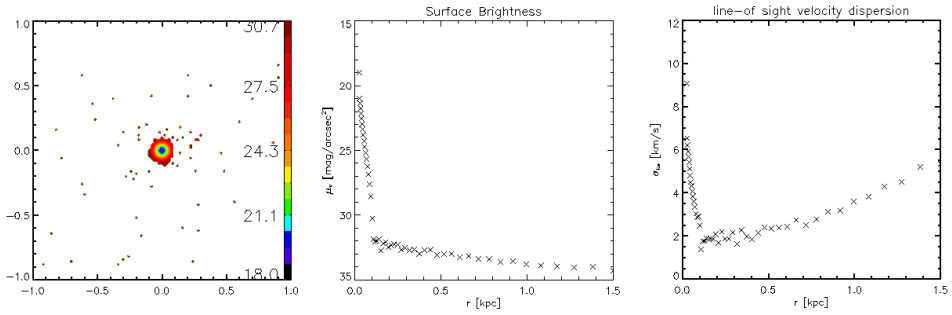

(a) ggg0.5: R_{peri}= 0.5[kpc], T_{int}^{UCD}= 496 [Myr]

Figure 6.7: Similar to previous Fig 6.1. Set of "ggg" simulations (SL^{DM}=1 [kpc], M^{DM}=10^9[$M_\odot$], $R_{eff}^{envelope}$= 0.85[kpc], $M^{envelope}$=$10^8M_\odot$). Source: this work.

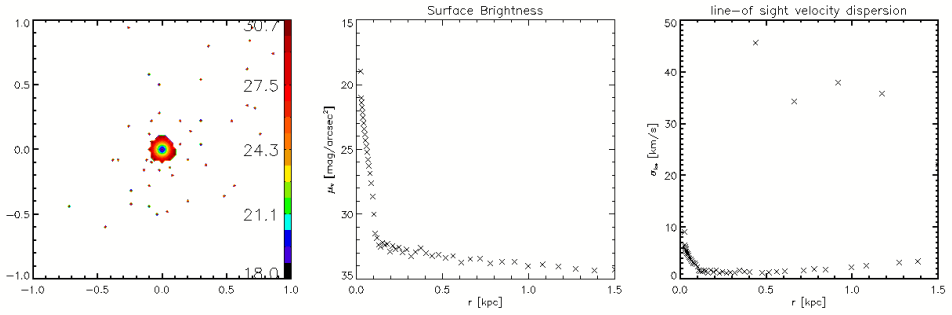

(a) hhh0.5: R_{peri}= 0.5[kpc], T_{int}^{UCD}= 696 [Myr]

Figure 6.8: Similar to previous Fig 6.1. Set of "hhh" simulations (SL^{DM}=4 [kpc], M^{DM}=10^9[$M_\odot$], $R_{eff}^{envelope}$= 0.85[kpc], $M^{envelope}$=$10^8M_\odot$). Source: this work.

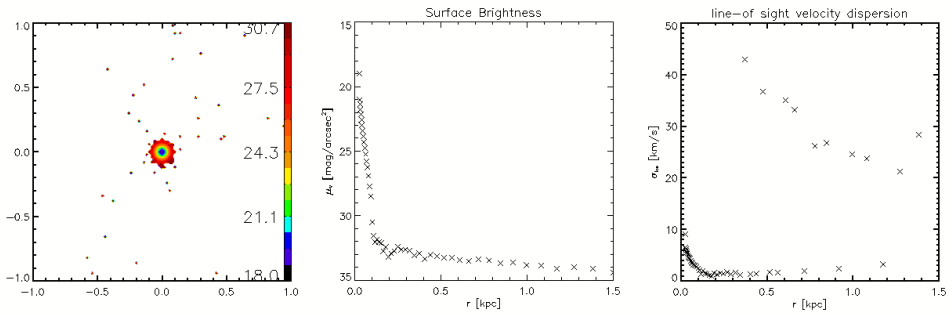

(a) iii0.5: R_{peri}= 0.5[kpc], T_{int}^{UCD}= 695 [Myr]

Figure 6.9: Similar to previous Fig 6.1. Set of "iii" simulations (SL^{DM}=4 [kpc], M^{DM}=10^9[$M_\odot$], $R_{eff}^{envelope}$= 1 [kpc], $M^{envelope}$=$10^8M_\odot$). Source: this work.

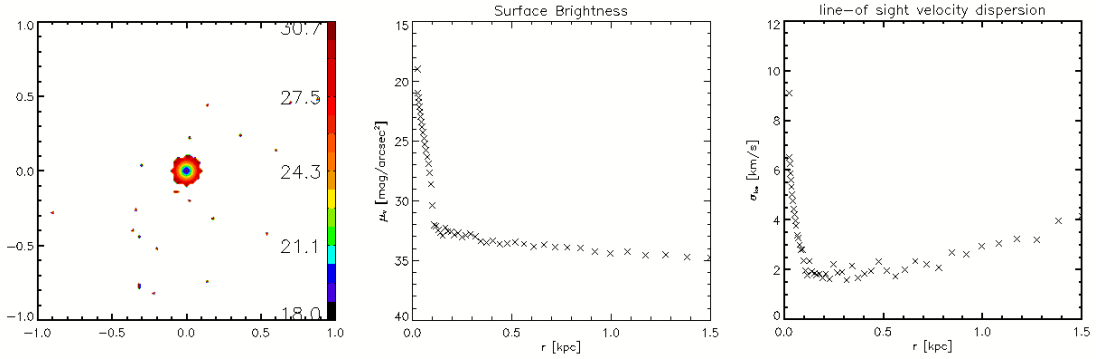

(a) jjj0.5: R_{peri}= 0.5[kpc], T_{int}^{UCD}= 562 [Myr]

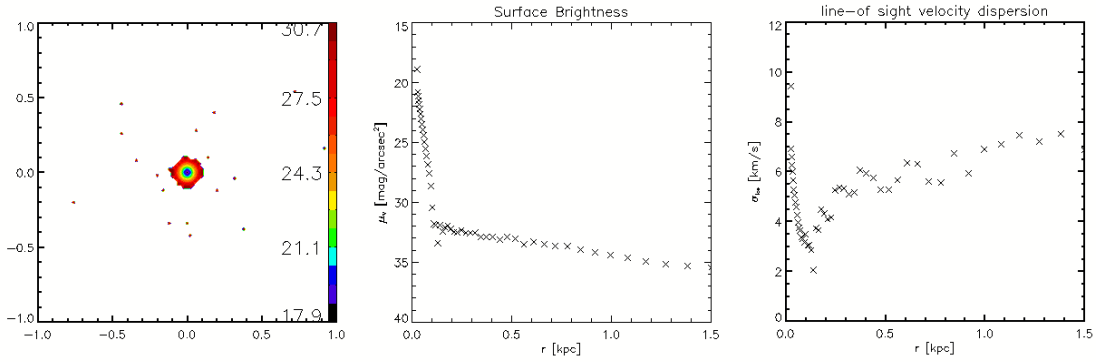

(b) jjj2: R_{peri}= 2[kpc], T_{int}^{UCD}= 922 [Myr]

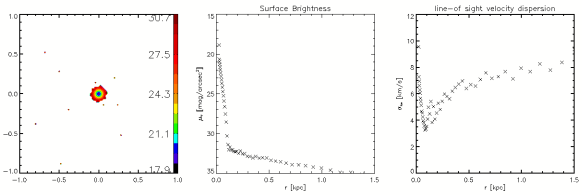

(c) jjj5: R_{peri}= 5[kpc], T_{int}^{UCD}= 1214 [Myr]

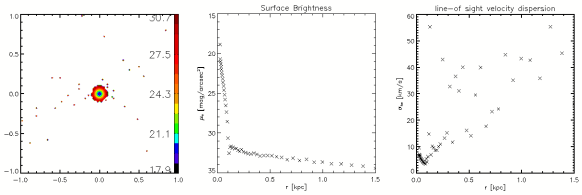

(d) jjj10: R_{peri}= 10[kpc], T_{int}^{UCD}= 1558 [Myr]

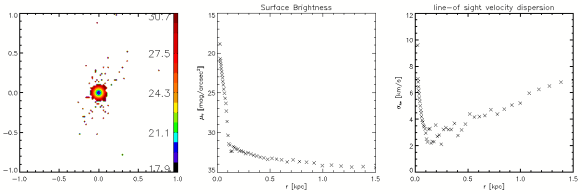

(e) jjj20: R_{peri}= 20[kpc], T_{int}^{UCD}= 2223 [Myr]

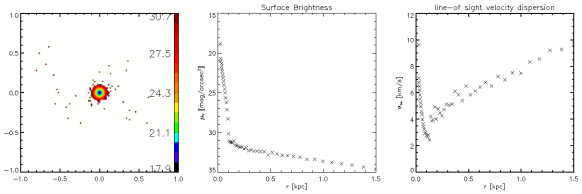

(f) jjj50: R_{peri}= 50[kpc], T_{int}^{UCD}= 3834 [Myr]

Figure 6.10: Similar to previous Fig 6.1. Set of "jjj" simulations (SL^{DM}=4 [kpc], M^{DM}=10^{10}[$M_{\odot}$], $R_{eff}^{envelope}$= 0.85 [kpc], $M^{envelope}$=$10^{8}M_{\odot}$). Source: this work.

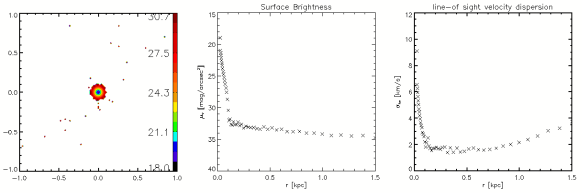

(a) kkk0.5: R_{peri}= 0.5[kpc], T_{int}^{UCD}= 471 [Myr]

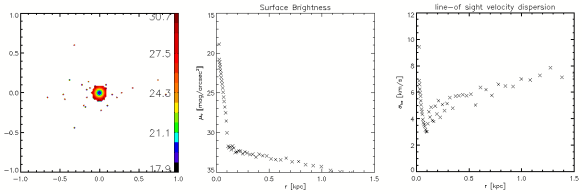

(b) kkk2: R_{peri}= 2[kpc], T_{int}^{UCD}= 903 [Myr]

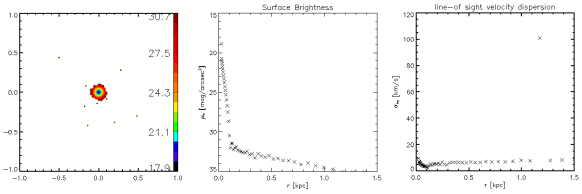

(c) kkk5: R_{peri}= 5[kpc], T_{int}^{UCD}= 1009 [Myr]

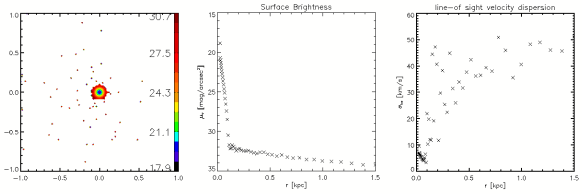

(d) kkk10: R_{peri}= 10[kpc], T_{int}^{UCD}= 1529 [Myr]

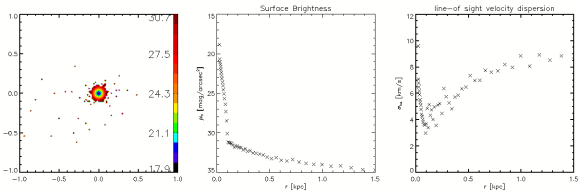

(e) kkk20: R_{peri}= 20[kpc], T_{int}^{UCD}= 1923 [Myr]

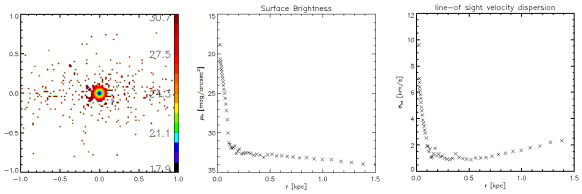

(f) kkk50: R_{peri}= 50[kpc], T_{int}^{UCD}= 3059 [Myr]

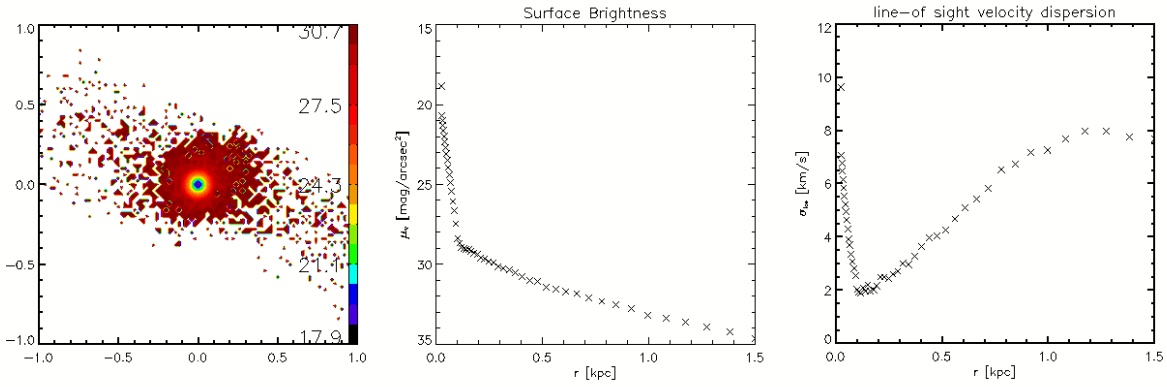

(g) kkk100: R_{peri}= 100[kpc], T_{int}^{UCD}= 8697 [Myr]

Figure 6.11: Similar to previous Fig 6.1. Set of "kkk" simulations (SL^{DM}=4 [kpc], M^{DM}=10^{10}[$M_\odot$], $R_{eff}^{envelope}$= 1 [kpc], $M^{envelope}$=$10^8 M_\odot$). Source: this work.

6.4 Tails

In this section we presentcontour plots of different objects, at left hand side the surface brightens plot and at the right hand side the velocity dispersion plot, under each set of plots are the pericentral distance of the orbit (R_{peri}), the simulation time at which the dE transitions into an UCD (T_{int}^{UCD}), and the position of the nuclei of the object ($Posi_{fin}^{UCD}$).

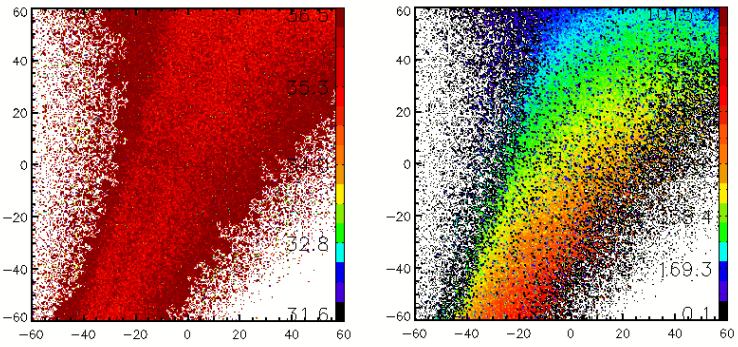

(a) aaa0.5: R_{peri}= 0.5[kpc], T_{int}^{UCD}= 310 [Myr], $Posi_{fin}^{UCD}$= 144 [kpc]

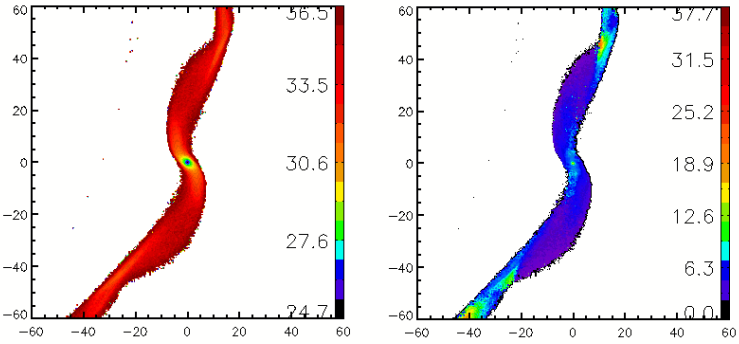

(b) aaa200: R_{peri}= 200[kpc], T_{int}^{UCD}= 4521 [Myr], $Posi_{fin}^{UCD}$= 244[kpc]

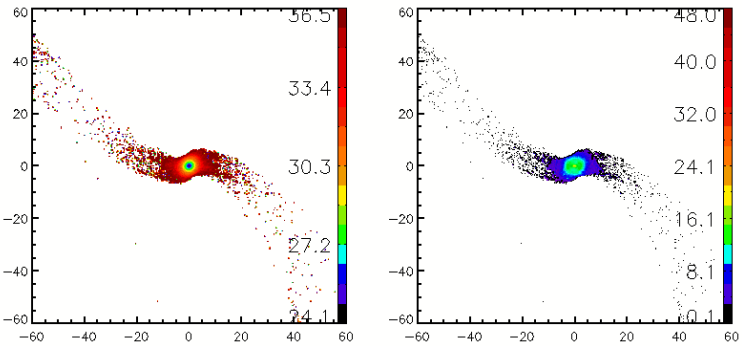

(c) aaa240: R_{peri}= 240[kpc], T_{int}^{UCD}= 9995 [Myr], $Posi_{fin}^{UCD}$= 250[kpc]

Figure 6.12: Contour plots of different objects at left hand side the surface brightnes plot and at the right hand side the velocity dispersion plot, under each set of images is the pericentral distance of the orbit (R_{peri}), the simulation time at which the dE transitions into an UCD (T_{int}^{UCD}), and the position of the nuclei of the object ($Posi_{fin}^{UCD}$). Source: this work. Set of "aaa" simulations (SL^{DM}=1 [kpc], M^{DM}=10^{10}[$M_{\odot}$], $R_{eff}^{envelope}$=0.85[kpc], $M^{envelope}$=$10^{7}M_{\odot}$) Source: this work.

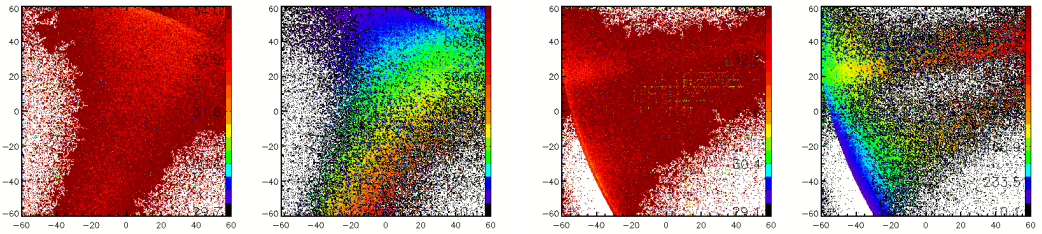

(a) bbb0.5:R_{peri}=0.5[kpc],T_{int}^{UCD}=917[Myr],$Posi_{fin}^{UCD}$=167[kpc] (b) bbb2:R_{peri}=2[kpc],T_{int}^{UCD}=1127[Myr],$Posi_{fin}^{UCD}$=173[kpc]

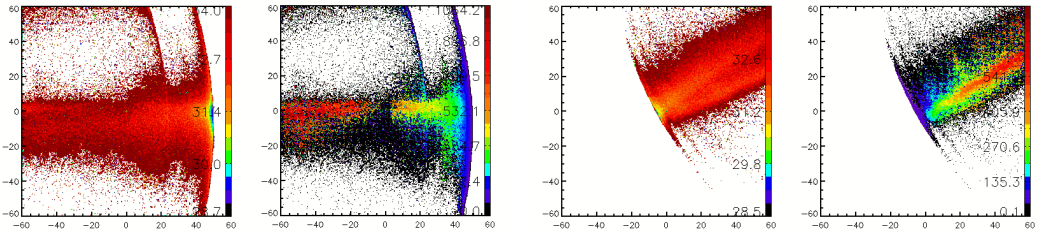

(c) bbb5:R_{peri}=5[kpc],T_{int}^{UCD}=1624[Myr], (d) bbb10:R_{peri}=10[kpc],T_{int}^{UCD}=2125[Myr],$Posi_{fin}^{UCD}$=244[kpc],$Posi_{fin}^{UCD}$=201[kpc]

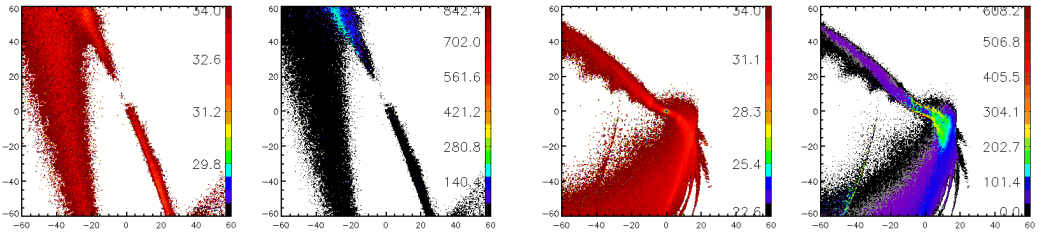

(e) bbb20:R_{peri}=20[kpc],T_{int}^{UCD}=2943[Myr],$Posi_{fin}^{UCD}$=122[kpc] (f) bbb50:R_{peri}=50[kpc],T_{int}^{UCD}=6876[Myr],$Posi_{fin}^{UCD}$=238[kpc]

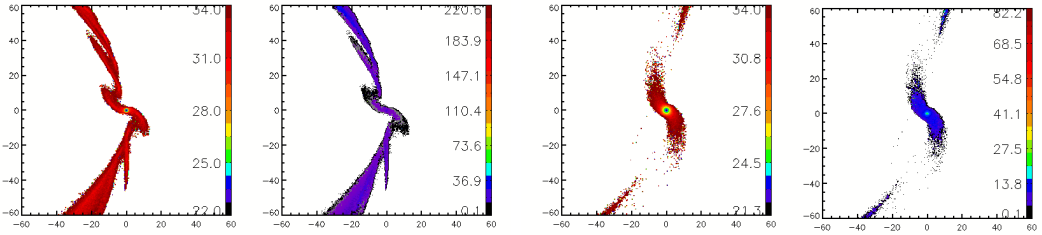

(g) bbb100:R_{peri}=100[kpc], $Posi_{fin}^{UCD}$=250[kpc] (h) bbb200:R_{peri}=200[kpc], $Posi_{fin}^{UCD}$=244[kpc]

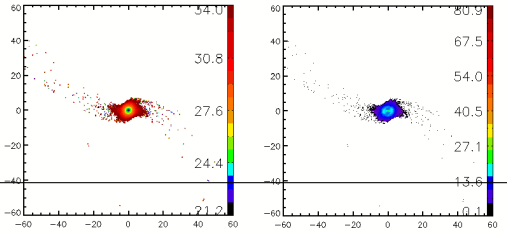

(i) bbb240:R_{peri}=240[kpc], $Posi_{fin}^{UCD}$=250[kpc]

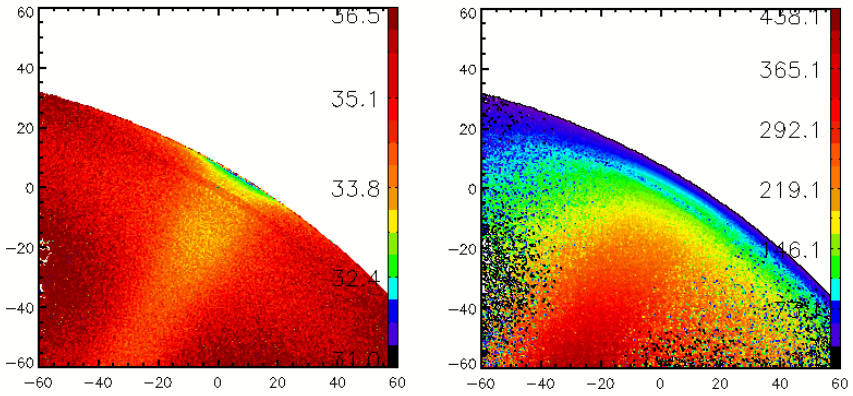

(a) ccc0.5: R_{peri}= 0.5[kpc], T_{int}^{UCD}= 310 [Myr], $Posi_{fin}^{UCD}$=243[kpc]

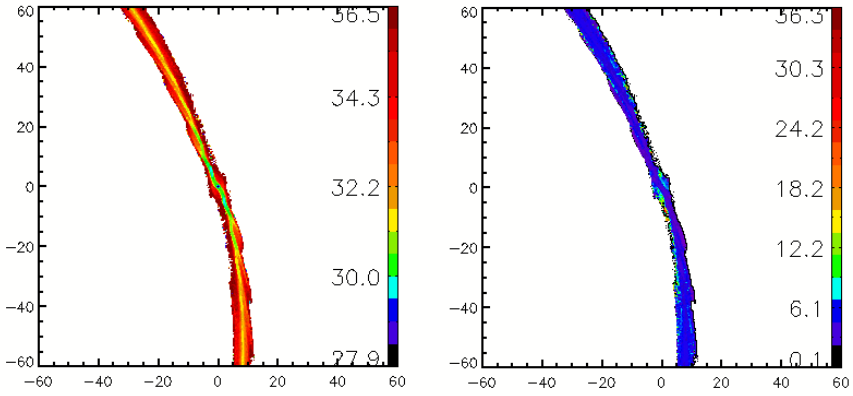

(b) ccc200: R_{peri}= 200[kpc], T_{int}^{UCD}= 7706 [Myr], $Posi_{fin}^{UCD}$=249[kpc]

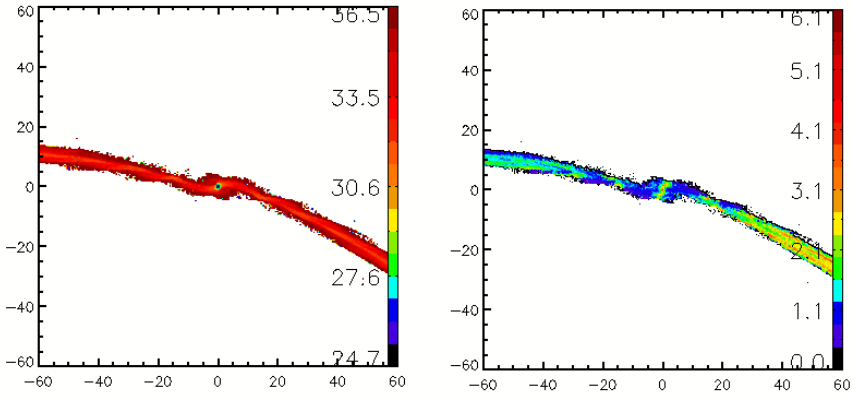

(c) ccc240: R_{peri}= 240[kpc], $Posi_{fin}^{UCD}$=249[kpc]

Figure 6.14: Similar to previous Fig 6.12. Set of "ccc" simulations (SL^{DM}=1 [kpc], M^{DM}=10^8[$M_\odot$], $R_{eff}^{envelope}$=0.85[kpc], $M^{envelope}$=10^7[$M_\odot$]) Source: this work.

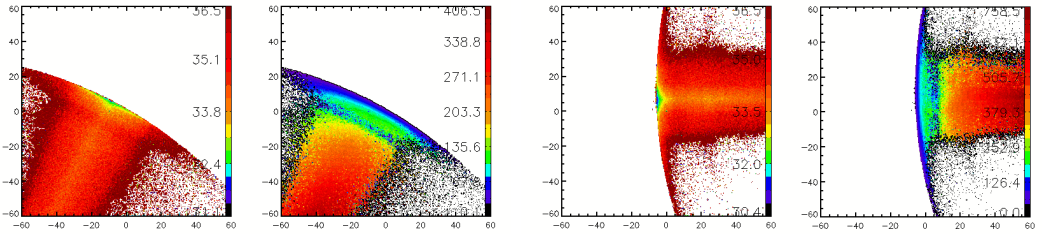

(a) ddd0.5:R_{peri}=0.5[kpc],T_{int}^{UCD}=307[Myr],$Posi_{fin}^{UCD}$=245[kpc] (b) ddd2:R_{peri}=2[kpc],T_{int}^{UCD}=647[Myr],$Posi_{fin}^{UCD}$=245[kpc]

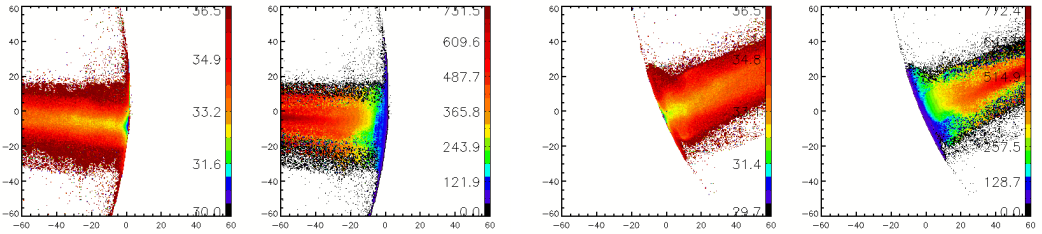

(c) ddd5:R_{peri}=5[kpc],T_{int}^{UCD}=665[Myr],$Posi_{fin}^{UCD}$=248[kpc] (d) ddd10:R_{peri}=10[kpc],T_{int}^{UCD}=689[Myr],$Posi_{fin}^{UCD}$=246[kpc]

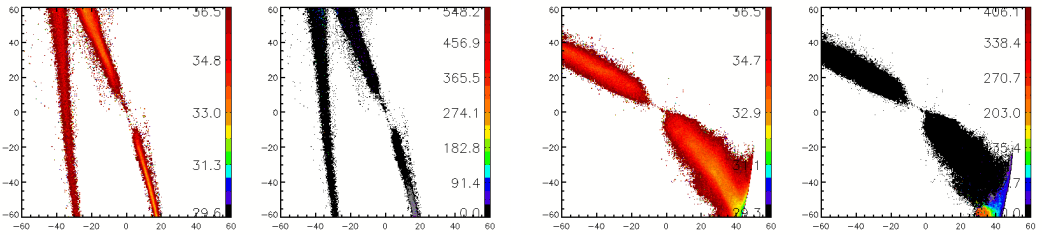

(e) ddd20:R_{peri}=20[kpc],T_{int}^{UCD}=833[Myr],$Posi_{fin}^{UCD}$=105[kpc] (f) ddd50:R_{peri}=50[kpc],T_{int}^{UCD}=1016[Myr],$Posi_{fin}^{UCD}$=200[kpc]

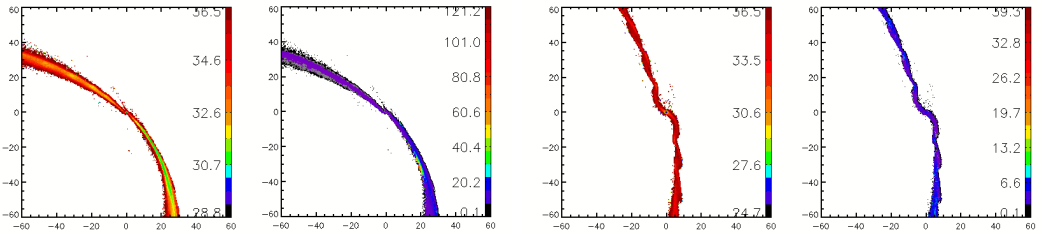

(g) ddd100:R_{peri}=100[kpc],T_{int}^{UCD}=1723[Myr],$Posi_{fin}^{UCD}$=243[kpc] (h) ddd200:R_{peri}=200[kpc],T_{int}^{UCD}=3999[Myr],$Posi_{fin}^{UCD}$=249[kpc]

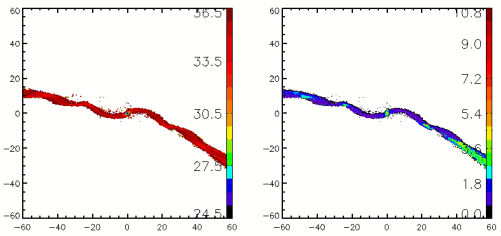

(i) ddd240:R_{peri}=240[kpc],T_{int}^{UCD}=5426[Myr],$Posi_{fin}^{UCD}$=250[kpc]

Figure 6.15: Similar to previous Fig 6.12. Set of "ddd" simulations (SL^{DM}=1 [kpc], M^{DM}=10^9[$M_\odot$], $R_{eff}^{envelope}$=0.85[kpc], $M^{envelope}$=10^7[$M_\odot$]) Source: this work.

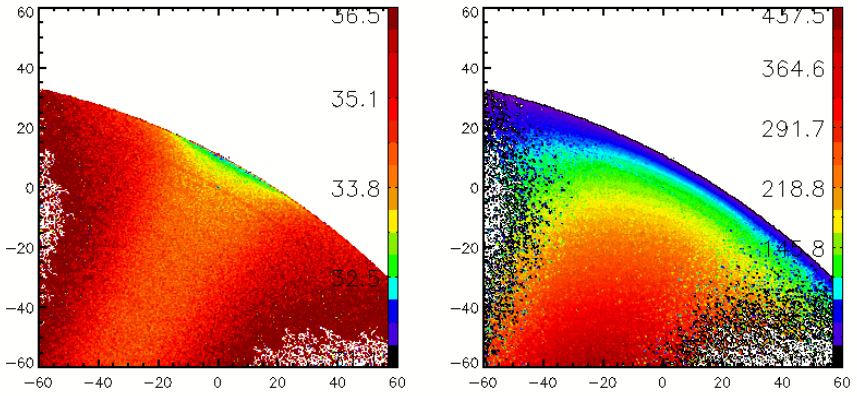

(a) eee0.5: R_{peri}= 0.5[kpc], T_{int}^{UCD}= 695 [Myr], $Posi_{fin}^{UCD}$=241[kpc]

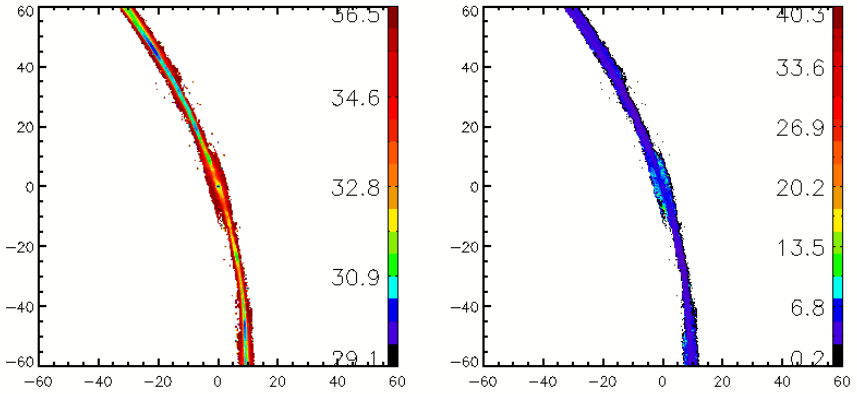

(b) eee200: R_{peri}= 200[kpc], T_{int}^{UCD}= 3222 [Myr], $Posi_{fin}^{UCD}$=249[kpc]

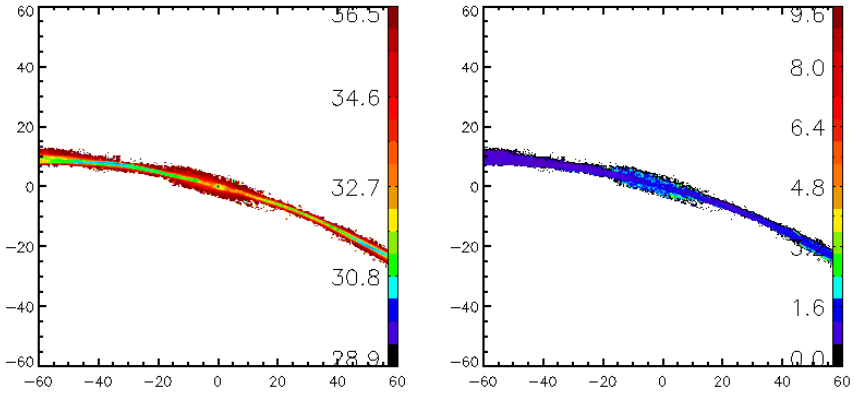

(c) eee240: R_{peri}= 240[kpc], T_{int}^{UCD}= 4860 [Myr], $Posi_{fin}^{UCD}$=249[kpc]

Figure 6.16: Similar to previous Fig 6.12. Set of "eee" simulations (SL^{DM}=4 [kpc], M^{DM}=10^9[$M_\odot$], $R_{eff}^{envelope}$=0.85[kpc], $M^{envelope}$=10^7[$M_\odot$]). Source: this work.

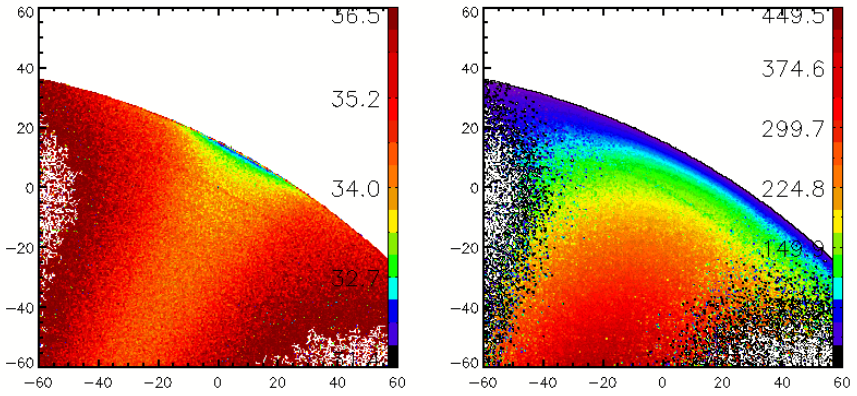

(a) fff0.5: R_{peri}= 0.5[kpc], T_{int}^{UCD}= 695 [Myr], $Posi_{fin}^{UCD}$=236[kpc]

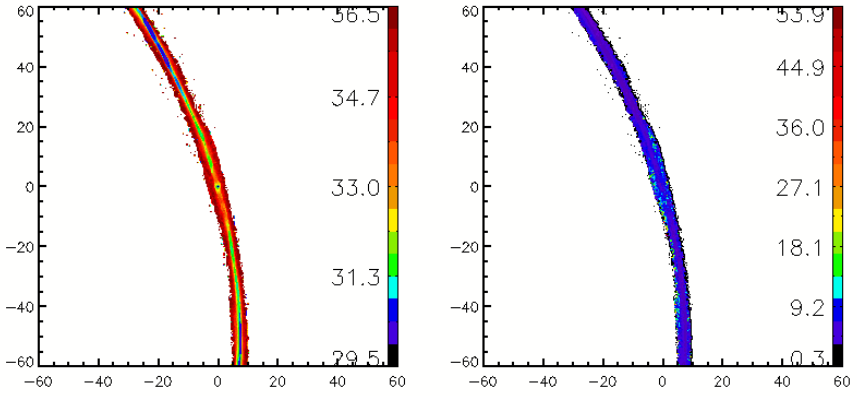

(b) fff200: R_{peri}= 200[kpc], T_{int}^{UCD}= 2447 [Myr], $Posi_{fin}^{UCD}$=249[kpc]

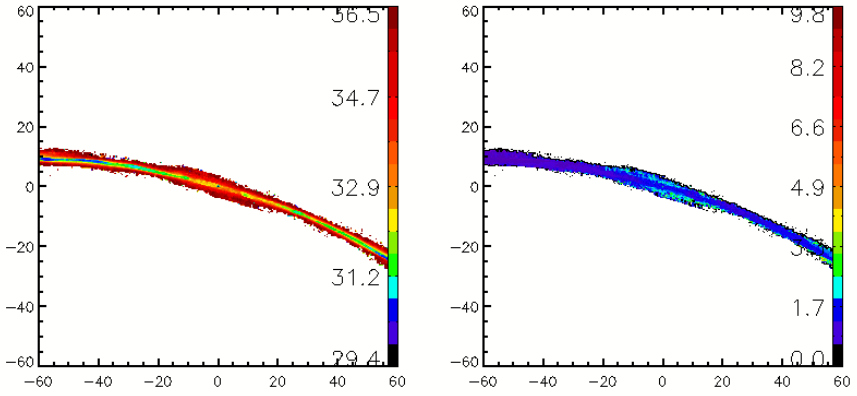

(c) fff240: R_{peri}= 240[kpc], T_{int}^{UCD}= 3418 [Myr], $Posi_{fin}^{UCD}$=249[kpc]

Figure 6.17: Similar to previous Fig 6.12. Set of "fff" simulations (SL^{DM}=4 [kpc], M^{DM}=10^9[$M_\odot$], $R_{eff}^{envelope}$= 1[kpc], $M^{envelope}$=10^7[$M_\odot$]). Source: this work.

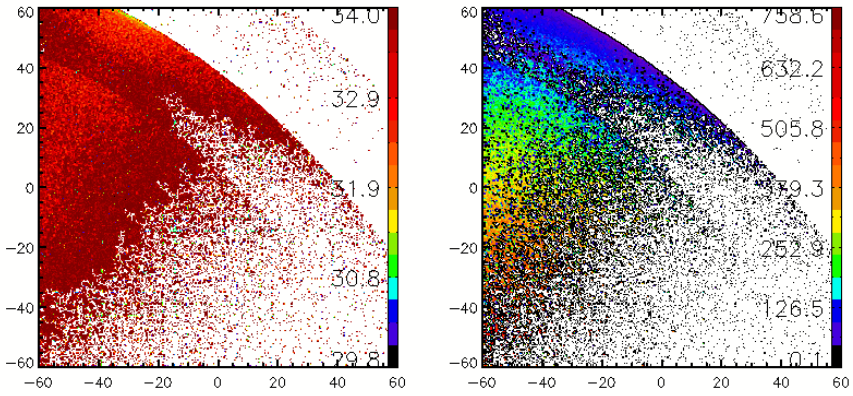

(a) ggg0.5: R_{peri}= 0.5[kpc], T_{int}^{UCD}= 496 [Myr], $Posi_{fin}^{UCD}$=233[kpc]

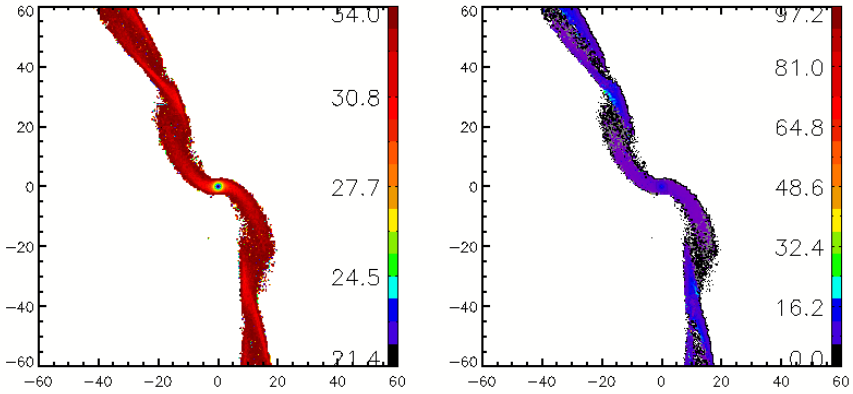

(b) ggg200: R_{peri}= 200[kpc], $Posi_{fin}^{UCD}$=249[kpc]

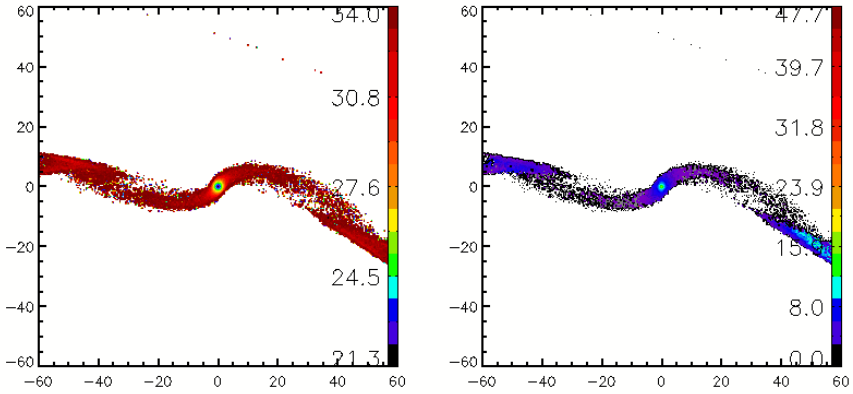

(c) ggg240: R_{peri}= 240[kpc], $Posi_{fin}^{UCD}$=250[kpc]

Figure 6.18: Similar to previous Fig 6.12. Set of "ggg" simulations (SL^{DM}=1 [kpc], M^{DM}=10^9[$M_\odot$], $R_{eff}^{envelope}$= 0.85 [kpc], $M^{envelope}$=10^8[$M_\odot$]). Source: this work.

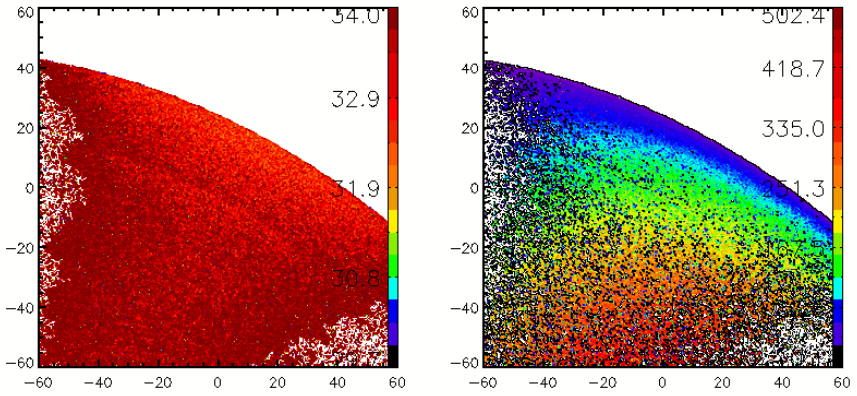

(a) hhh0.5: R_{peri}= 0.5[kpc], T_{int}^{UCD}= 696 [Myr], $Posi_{fin}^{UCD}$=229[kpc]

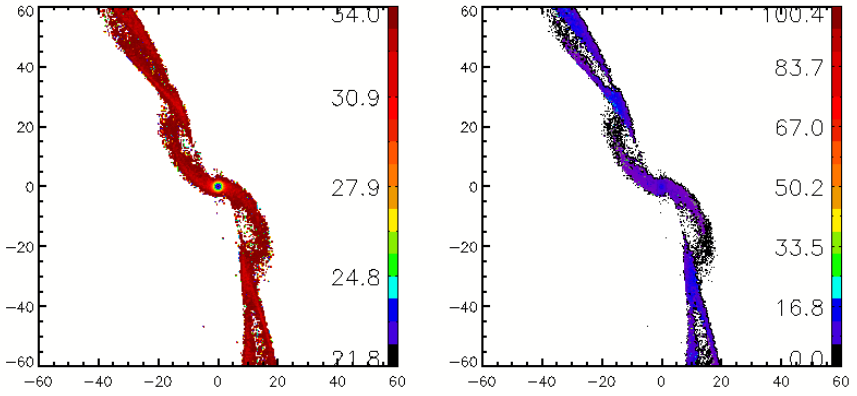

(b) hhh200: R_{peri}= 200[kpc], $Posi_{fin}^{UCD}$=249[kpc]

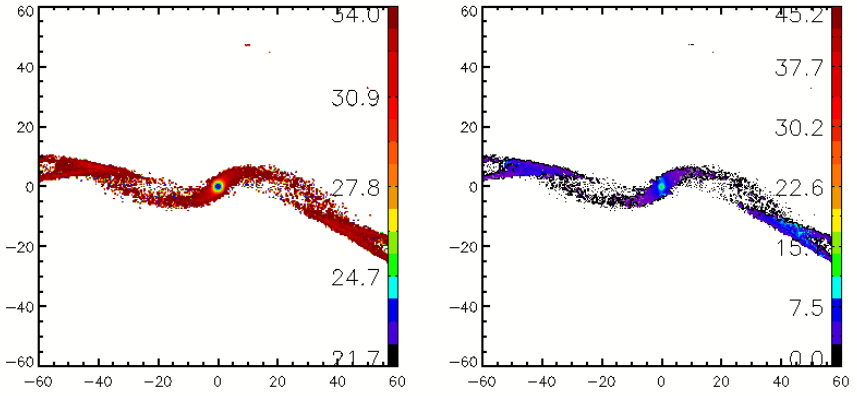

(c) hhh240: R_{peri}= 240[kpc], $Posi_{fin}^{UCD}$=250[kpc]

Figure 6.19: Similar to previous Fig 6.12. Set of "hhh" simulations (SL^{DM}=4 [kpc], M^{DM}=10^9[$M_\odot$], $R_{eff}^{envelope}$= 0.85[kpc], $M^{envelope}$=10^8[$M_\odot$]). Source: this work.

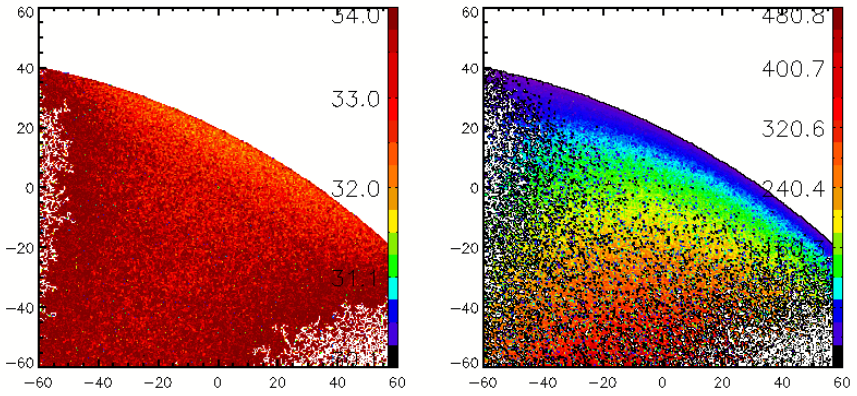

(a) iii0.5: R_{peri}= 0.5[kpc], T_{int}^{UCD}= 695 [Myr], $Posi_{fin}^{UCD}$=233[kpc]

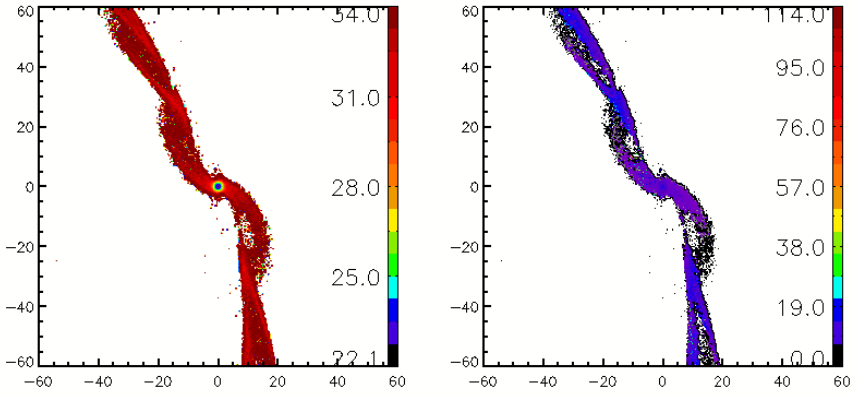

(b) iii200: R_{peri}= 200[kpc], $Posi_{fin}^{UCD}$=249[kpc]

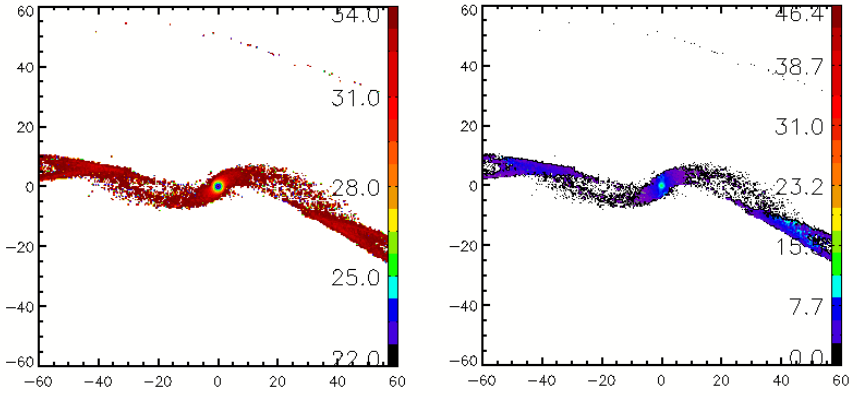

(c) iii240: R_{peri}= 240[kpc], $Posi_{fin}^{UCD}$=250[kpc]

Figure 6.20: Similar to previous Fig 6.12. Set of "iii" simulations (SL^{DM}=4 [kpc], M^{DM}=10^{10}[$M_\odot$], $R_{eff}^{envelope}$= 0.85 [kpc], $M^{envelope}$=10^{8}[$M_\odot$]). Source: this work.

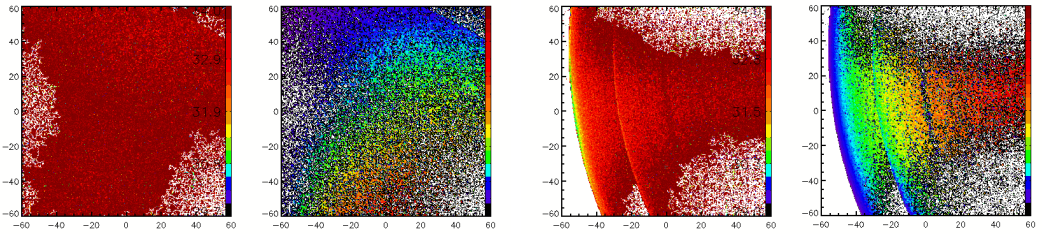

(a) jjj0.5:R_{peri}=0.5[kpc],T_{int}^{UCD}=562[Myr],$Posi_{fin}^{UCD}$=163[kpc] (b) jjj2:R_{peri}=2[kpc],T_{int}^{UCD}=922[Myr],$Posi_{fin}^{UCD}$=198[kpc]

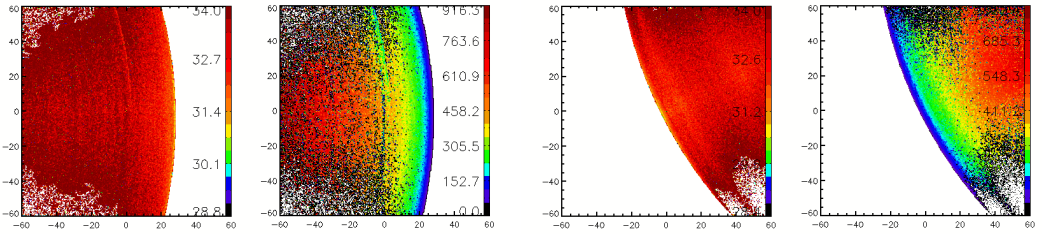

(c) jjj5:R_{peri}=5[kpc],T_{int}^{UCD}=1214[Myr],$Posi_{fin}^{UCD}$=222[kpc] (d) jjj10:R_{peri}=10[kpc],T_{int}^{UCD}=1558[Myr],$Posi_{fin}^{UCD}$=246[kpc]

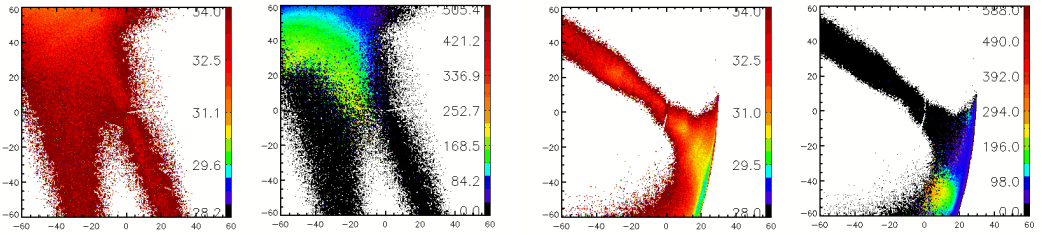

(e) jjj20:R_{peri}=20[kpc],T_{int}^{UCD}=2223[Myr],$Posi_{fin}^{UCD}$=166[kpc] (f) jjj50:R_{peri}=50[kpc],T_{int}^{UCD}=3834[Myr],$Posi_{fin}^{UCD}$=224[kpc]

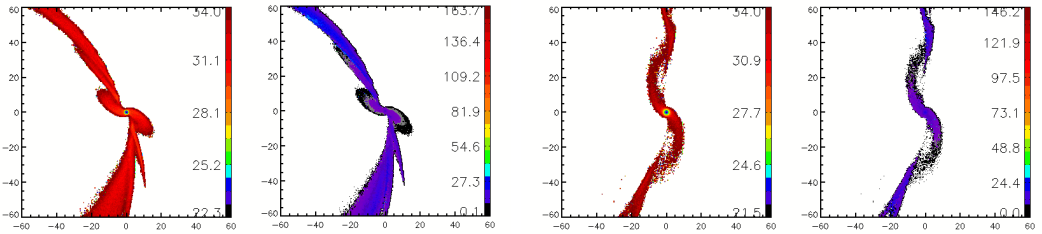

(g) jjj100:R_{peri}=100[kpc], $Posi_{fin}^{UCD}$=250[kpc] (h) jjj200:R_{peri}=200[kpc], $Posi_{fin}^{UCD}$=248[kpc]

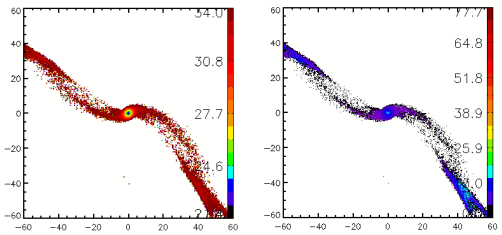

(i) jjj240:R_{peri}=240[kpc], $Posi_{fin}^{UCD}$=250[kpc]

Figure 6.21: Similar to previous Fig 6.12. Set of "jjj" simulations (SL^{DM}=4 [kpc], M^{DM}=10^{10}[$M_\odot$], $R_{eff}^{envelope}$= 0.85 [kpc], $M^{envelope}$=10^{8}[$M_\odot$]). Source: this work.

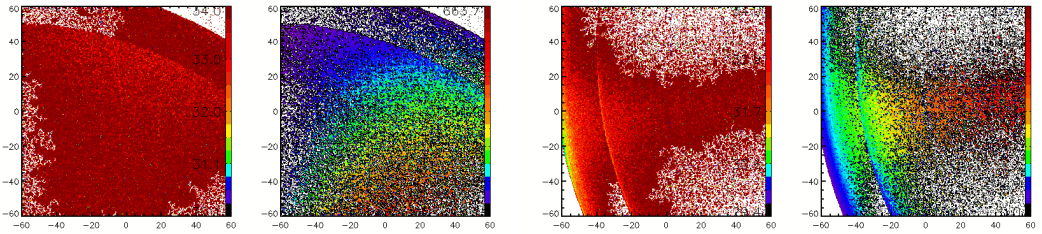

(a) kkk0.5:R_{peri}=0.5[kpc],T_{int}^{UCD}=471[Myr],$Posi_{fin}^{UCD}$=188[kpc] (b) kkk2:R_{peri}=2[kpc],T_{int}^{UCD}=903[Myr],$Posi_{fin}^{UCD}$=189[kpc]

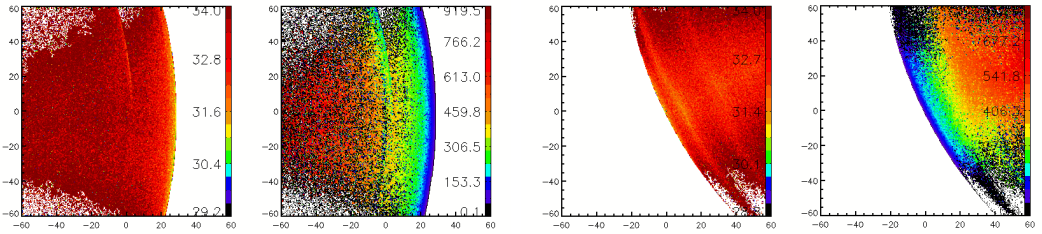

(c) kkk5:R_{peri}=5[kpc],T_{int}^{UCD}=1009[Myr],$Posi_{fin}^{UCD}$=222[kpc] (d) kkk10:R_{peri}=10[kpc],T_{int}^{UCD}=1529[Myr],$Posi_{fin}^{UCD}$=247[kpc]

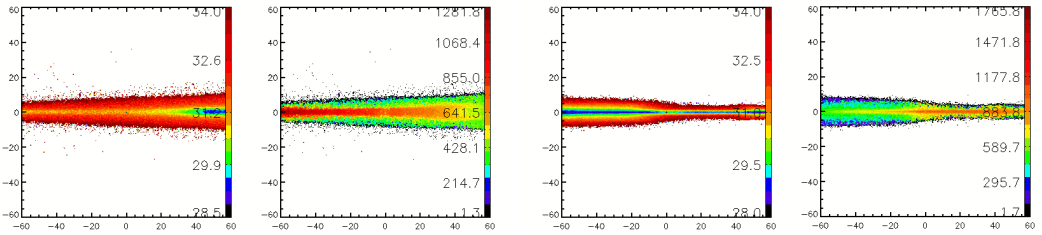

(e) kkk20:R_{peri}=20[kpc],T_{int}^{UCD}=1923[Myr],$Posi_{fin}^{UCD}$=153[kpc] (f) kkk50:R_{peri}=50[kpc],T_{int}^{UCD}=3059[Myr],$Posi_{fin}^{UCD}$=220[kpc]

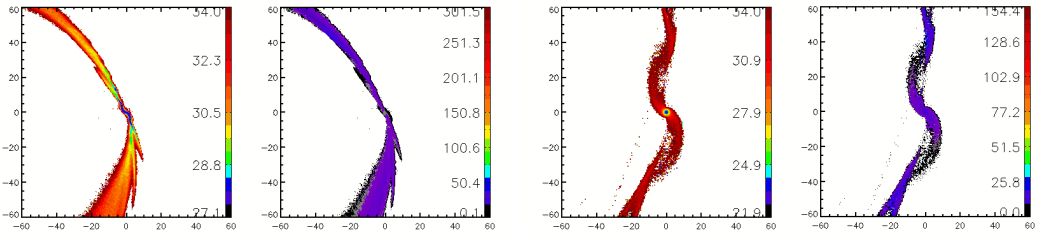

(g) kkk100:R_{peri}=100[kpc],T_{int}^{UCD}=8697[Myr],$Posi_{fin}^{UCD}$=250[kpc] (h) kkk200:R_{peri}=200[kpc],$Posi_{fin}^{UCD}$=247[kpc]

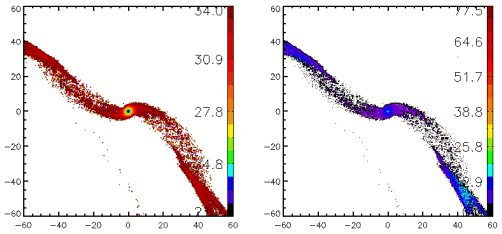

(i) kkk240:R_{peri}=240[kpc],$Posi_{fin}^{UCD}$=250[kpc]

Figure 6.22: Similar to previous Fig 6.12. Set of "kkk" simulations (SL^{DM}=4 [kpc], M^{DM}=10^{10}[$M_\odot$], $R_{eff}^{envelope}$= 1 [kpc], $M^{envelope}$=10^{8}[$M_\odot$]). Source: this work.

Chapter 7

Bibliography

Arp H., 1966, ApJS, 14, 1

Bastian, N., Gieles, M., Efremov, Y. N., Lamers, H. J. G. L. M. 2005, A&A, 443, 79

Bastian, N., Schweizer, F., Goudfrooij, P., Larsen, S. S., Kissler-Patig, M. 2013, MNRAS, 431, 1252

Behroozi P. S., Wechsler R. H., Conroy C., 2013, ApJ, 770, 57.

Bekenstein J., Milgrom M., 1984, ApJ, 286, 7

Bekki K., Couch W. J., Drinkwater M. J., Gregg M. D., 2001, ApJ, 557, L39

Bekki, K., Couch, W. J., Drinkwater, M. J.,& Shioya, Y. 2003, MNRAS, 344, 399

Binggeli B., Cameron L. M., 1991, A&A, 252, 27.

Binggeli B., Sandage A., Tarenghi M., 1984, AJ, 89, 64

Brada R., Milgrom M., 1999, ApJ, 519, 590 Brodie, J. P., Larsen S. S. 2002 AJ, 124, 1410

Brüns, R. C., Kroupa, P., Fellhauer, M. 2009, ApJ, 702, 1268

Brüns, R. C., Kroupa, P. 2011, ApJ, 729, 69

Brüns, R. C., Kroupa, P., Fellhauer, M., Metz, M., & Assmann, P. 2011, A&A, 529, 138

Brüns, R. C., Kroupa, P. 2012, A&A, 547, 65

Brüns 2013 PhD thesis, University of Bonn.

Bruzual, G., Charlot, S., 2003, MNRAS, 344, 1000

Burkert, A., Brodie, J., Larsen, S. 2005, AJ, 628, 231

Capuzzo-Dolcetta, R. ; Tosta e Melo, I., 2017, MNRAS, 472,4013.

Candlish, G. N.; Smith, R.; Fellhauer, M., 2015, MNRAS, 446, 1060.

Chandrasekhar S., 1943, ApJ, 97, 255

Chies-Santos,A. L., Santiago, B. X., Pastoriza, M. G., 2007, A&A, 467, 1003

Dabringhausen J., Kroupa P., 2013, MNRAS, 429, 1858

Drinkwater, M. J., Jones, J. B., Gregg, M. D., Phillipps, S. 2000, PASA, 17, 227

Drinkwater M., J, 2004, PASA, 21, 375

Duc P.-A., Renaud F., 2013, in Souchay J., Mathis S., Tokieda T., eds, Lecture Notes in Physics, Vol. 861, Tides in Colliding Galaxies. Springer-Verlag, Berlin, p. 327.

Evstigneeva, E. A., Drinkwater, M. J., Peng, C. Y., et al. 2008, AJ, 136, 461

Evstigneeva, E. A., Gregg, M. D., Drinkwater, M. J., Hilker, M. 2007, AJ, 133, 1722

Faber S. M., 1973, ApJ, 179, 423

Faber S. M., Lin D. M. C., 1983, ApJ, 266, L17.

Fellhauer M., Baumgardt H., Kroupa P., Spurzem R., 2002, CeMDA, 82, 113

Fellhauer M., Kroupa P., Baumgardt H., Bien R., Boily C. M., Spurzem R., Wassmer N., 2000, New Astron., 5, 305

Fellhauer, M., Kroupa, P., 2002a, MNRAS, 330, 642

Fellhauer, M., Kroupa, P. 2002b, AJ, 124, 2006

Fellhauer, M., Kroupa, P., 2005, MNRAS, 359, 223

Ferré-Mateu,A., Forbes, D. A., Romanowsky, A. J., Janz, J., Dixon, C. 2017, MNRAS, 473, 1819

Forbes D. A. et al 2013 , MNRAS, 435

Graham, A. W. 2002, MNRAS, 334, 859

Graham, A. W. 2005, in IAU Coll. 198, Near-fields Cosmology with Dwarf Elliptical Galaxies, ed. H. Jerjen & B. Binggeli (Cambridge: Cambridge University Press), 303.

Hilker, M., Infante, L., Vieira, G., Kissler-Patig, M., Richtler, T. 1999, A&AS, 134, 75

Holmberg E., 1941, ApJ, 94, 385

Huxor A. P., Phillipps S., Price J., Harniman R., 2011, MNRAS, 414, 3557

Huxor,A. P., Phillipps,S. , Price, J., 2013, MNRAS, 430, 1956

Hwang, N., Lee, M. G., Lee, J. C., et al. 2011, ApJ, 738, 58

Janz J. et al., 2016, MNRAS, 456, 617

Khokhlov A. M., 1998, J. Chem. Phys., 143, 519 King, I. 1962, AJ, 67, 471

Kissler-Patig, M. 2004, in Astronomical Society of the Pacific Conference Series, Vol. 322, The Formation and Evolution of Massive Young Star Clusters, ed. H. J. G. L. M. Lamers, L. J. Smith, A. Nota, 535

Kormendy, J., Bender, R., 2012, ApJS, 198, 2

Kormendy, J., Fisher, D. B., Cornell, M. E., Bender, R., 2009, ApJS, 182, 216

Kroupa, P.,1998 , MNRAS, 300, 200

Kroupa P., 2012, PASA, 29, 395

Larsen, Brodie, 2000, AJ, 120, 2938

Lee, M. G., Chandar, R., Whitmore, B. C. 2005, AJ, 130, 2128

Lüghausen F., Famaey B., Kroupa P., 2014a, Lüghausen, F, Famaey, B, Kroupa, P., 2015, Canadian Journal of Physics, 93, 232.

Mieske, S., Hilker, M., Infante, L., 2002, A&A, 383, 823

Mieske, S., Hilker, M., Jordán, A., et al. 2008, A&A, 487, 921

Milgrom M., 1983, ApJ, 270, 365.

Milgrom M., 2010, MNRAS, 403, 886.

Monachesi, A., Trager, S. C., Lauer, T. R., et al. 2012, ApJ, 745, 97

Navarro, J. F., Frenk, C. S., White, S. D. M., 1996, The Astrophysical Journal. 462, 563.

Navarro, J. F., Frenk, C. S., White, S. D. M., 1995c, MNRAS, 275, 720.

Norris, M. A., Kannappan, S. J., 2011, MNRAS, 414, 739

Oehm, W., Thies, I. and Kroupa, P., 2017, MNRAS, 467, 273.

Petsch H. P., Theis C., 2008, Astron. Nachr., 329, 1046

Pfeffer J., Baumgardt H., 2013, MNRAS, 433, 1997

Ploeckinger S., Hensler G., Recchi S., Mitchell N., Kroupa P., 2014, MNRAS, 437, 3980

Ploeckinger S., Recchi S., Hensler G., Kroupa P., 2015, MNRAS, 447, 2512

Plummer, H. C. 1911, MNRAS, 71, 460

Press W. H., Schechter P. L., 1974, ApJ, 187, 425.

Pryor, C., Meylan, G. 1993, in ASP Conf. Ser. 50, Structure and Dynamics of Globular Clusters, ed. S. G. Djorgovski & G. Meylan (San Francisco, CA:ASP), 357

Renaud F., Boily C. M., Fleck J.-J., Naab T., Theis C., 2008, MNRAS, 391, L98.

Renaud F., Boily C. M., Naab T., Theis C., 2009, ApJ, 706, 67.

Renaud F., Bournaud F., Kraljic K., Duc P.-A., 2014, MNRAS, 442, L33.

Renaud, F., Famaey, B., & Kroupa, P. 2016, MNRAS, 463, 3637

Renaud F., Bournaud F., Duc P.-A., 2015a, MNRAS, 446, 2038

Sandage, A., & Binggeli, B. 1984, AJ, 89, 919

Sandage A., Binggeli B., Tammann G. A., 1985b, AJ, 90, 1759.

Teyssier R., 2002, A&A, 385, 337

Toomre A., Toomre J., 1972, ApJ, 178, 623

Tran, H. D., Sirianni, M., Ford, H. C., et al. 2003, ApJ, 585, 750

Urrutia Zapata, F., et al, 2019, MNRAS, 489, 2746.

Urrutia Zapata, F. 2018, Master thesis, University of Concepcion.

van den Bergh, Mackey, 2004,MNRAS, 354, 713

de Vaucouleurs G., 1948, Ann. d'Astrophys., 11, 247

de Vaucouleurs G., 1959, in Handbuch der Physik, Flügge S. ed. Springer-Verlag, Berlin, p. 275

Whitmore, B. C., Chandar, R., Schweizer, F., et al. 2010, AJ, 140, 75

Whitmore, B. C. & Schweizer, F. 1995, AJ, 109, 960

Whitmore, B. C., Zhang, Q., Leitherer, C., et al. 1999, AJ, 118, 1551

Wirth A., Gallagher, III J. S., 1984, ApJ, 282, 85

Zhang, H.-X., Peng, E. W., Côté, P., et al. 2015, ApJ, 802, 30